UNIVERSITA' DEGLI STUDI DI BOLOGNA

FACOLTA' DI SCIENZE MATEMATICHE FISICHE E NATURALI

An experimental and theoretical approach to correct for the scattered radiation in an X-ray computer tomography system for industrial applications

Dissertation submitted in partial satisfaction of the requirements for the degree of

DOCTOR OF PHILOSOPHY IN PHYSICS

by

ALICE MICELI

2008

Keywords: Monte Carlo simulation; Cone beam computed tomography; GEANT4; Scatter; X-ray spectra

Coordinator: Prof. Fabio Ortolani
Supervisor: Prof. Franco Casali
Co-supervisor: Dr. Urs Sennhauser

Dottorato di Ricerca in Fisica XX Ciclo FIS / 07

Table of Contents

Abstract

The main problem connected to cone beam computed tomography (CT) systems for industrial applications employing 450 kV X-ray tubes is the high amount of scattered radiation which is added to the primary radiation (signal). This stray radiation leads to a significant degradation of the image quality. A better understanding of the scattering and methods to reduce its effects are therefore necessary to improve the image quality. Several studies have been carried out in the medical field at lower energies, whereas studies in industrial CT, especially for energies up to 450 kV, are lacking. Moreover, the studies reported in literature do not consider the scattered radiation generated by the CT system structure and the walls of the X-ray room (environmental scatter). In order to investigate the scattering on CT projections a GEANT4-based Monte Carlo (MC) model was developed. The model, which has been validated against experimental data, has enabled the calculation of the scattering including the environmental scatter, the optimization of an anti-scatter grid suitable for the CT system, and the optimization of the hardware components of the CT system. The investigation of multiple scattering in the CT projections showed that its contribution is 2.3 times the one of primary radiation for certain objects. The results of the environmental scatter showed that it is the major component of the scattering for aluminum box objects of front size 70 x 70 mm^2 and that it strongly depends on the thickness of the object and therefore on the projection. For that reason, its correction is one of the key factors for achieving high quality images. The anti-scatter grid optimized by means of the developed MC model was found to reduce the scatter-to-primary ratio in the reconstructed images by 20 %. The object and environmental scatter calculated by means of the simulation were used to improve the scatter correction algorithm which could be patented by Empa. The results showed that the cupping effect in the corrected image is strongly reduced. The developed CT simulation is a powerful tool to optimize the design of the CT system and to evaluate the contribution of the scattered radiation to the image. Besides, it has offered a basis for a new scatter correction approach by which it has been possible to achieve images

with the same spatial resolution as state-of-the-art well collimated fan-beam CT with a gain in the reconstruction time of a factor 10. This result has a high economic impact in non-destructive testing and evaluation, and reverse engineering.

1 Introduction

The mathematical principle of computed tomography (CT) was developed in the early 20th century by Radon [1]. CT found its first commercial application in the early 1970s when Cormack and Hounsfield, who received the Nobel Price for Medicine in 1979, built the first computed tomography (CT) scanner [2-4]. These early developments mainly focused on medical diagnostic imaging, but by the end of the 1970s special efforts had been made towards the application of computed tomography in the industrial environment. Since then, the potential of CT as a non-destructive tool to investigate parts of interest of automotive and aerospace industry became evident. Nowadays, the application of industrial CT goes from the detection of defects (i.e. cracks, flaws) and wall thickness analysis of cast parts to reverse engineering [5-8]. A wide variety of XCT systems for industrial applications is available on the market. Scanners equipped with linear accelerators investigate parts of steel up to 300 mm of thickness. CT systems using X-ray tubes scan automotive and aircraft parts (i.e. cylinder heads and turbine blades). Micro-CT systems, with a resolution limit of about 1 µm employing micro-focus X-ray tubes or using synchrotron light with a resolution limit in the sub-micrometer range, analyze microelectronic parts.

1.1 Motivation, strategy, and objectives

Cone-beam computed tomography (CT) systems for industrial applications equipped with 450 kV X-ray tubes represent a novel CT approach by application of full-field area detectors that increase volume coverage, allow isotropic data sampling and fast data acquisition, thereby providing advantages over conventional fan-beam CT. The larger irradiated area in cone-beam CT geometry compared to fan beam CT geometry is responsible for the creation of a large amount of scattered radiation, which causes cupping and streak artifacts, and CT number inaccuracies in the reconstructed images

[9-12]. The evaluation and correction of the scattering are therefore essential to improve the image quality [13]. Figure 1.1 shows the effects of the scattered radiation on a cylinder head. Blurring of the image, reconstruction artifacts, and underestimation of the attenuation are clearly visible.

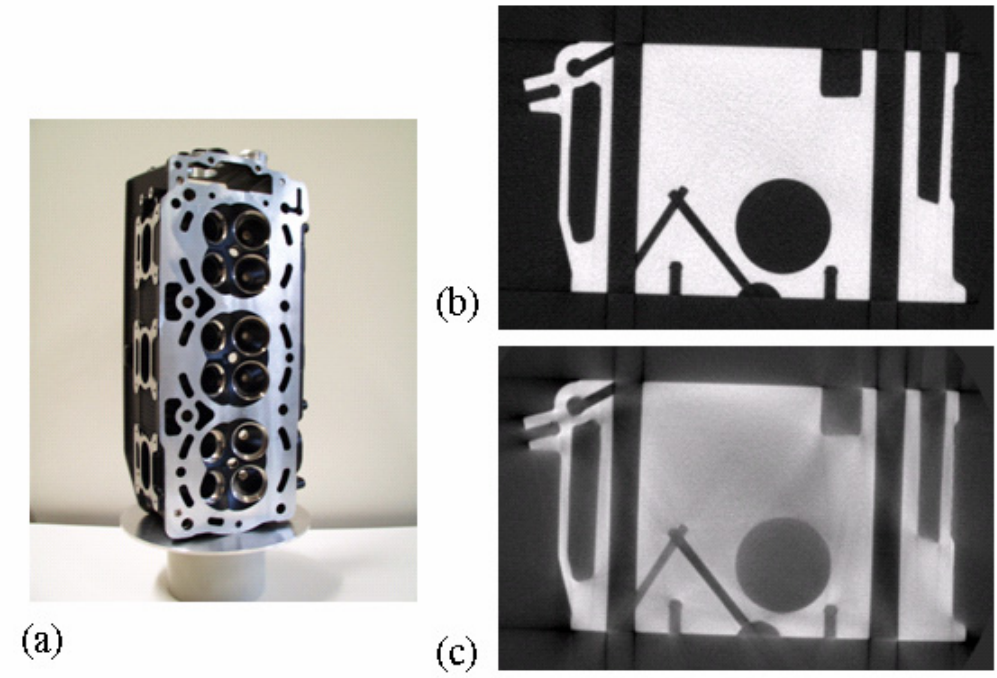

Figure 1.1 (a) Cylinder head made of aluminum of dimensions 60 x 30 x 20 cm^3. (b) A reconstructed image of the object obtained using a fan-beam CT system (well collimated), where the scattered radiation is negligible. (c) A reconstructed slice of the object obtained using a cone-beam CT system, where the scattered radiation is not negligible.

Scattering and methods to reduce its effects are well known in medical CT [11, 12, 14, 15], whereas studies in industrial CT (energies up to 450 keV) are rather limited [16]. Besides, the studies reported in literature deal with the scattering generated by the object, neglecting completely the scattered radiation created by the CT system structure and walls (environmental scatter). The scatter correction methods reported for medical CT can be classified in mechanical and numerical techniques. Mechanical techniques, such as anti-scatter grids, attempt to prevent scatter from reaching the detector. Numerical techniques are based on the estimation and subtraction of the scatter contribution in acquisition data. Anti-scatter grids and their effectiveness in reducing scattered radiation are well known for energies encountered in medical CT (30-140 keV) [17, 18], while studies extending to “high energy” (up to 450 keV) as

required in industrial applications are lacking. The numerical methods proposed to evaluate the scattered radiation in medical CT are based on the calculation of the first-order scattering and on the evaluation of the multiple scattering as scaling or convolution of single scattering [19-21]. These methods do not provide an accurate solution when the multiple order of scattering is the predominant contribution to the image formation, as when large objects (15+cm) have to be investigated. Besides, these methods are not able to simulate complex CT geometries, as for instance, post-filters or supports of the scintillator.

Objectives of this thesis work are the investigation and reduction of the scattering in an industrial cone-beam CT system working with a 450 kV X-ray tube, and its optimization. The scattering generated by the object as well as the environmental scatter were considered.

To achieve the objectives we developed a model of the CT system based on the GEANT4 Monte Carlo (MC) code. The full simulation of the X-ray tube, object, and area detector was considered. The model, which takes into account single and multiple scattering, was validated against experimental data. The developed MC model has enabled the (1) optimization of the CT system, (2) investigation of the scattering generated by the object as well as the scattering created by the CT system structure and the walls of the experimental room, and (3) the investigation and optimization of an anti-scatter grid suitable for the studied CT system. The results of the scattering calculation were used to reduce the artifacts in the reconstructed images for a test case using the reconstruction and scattering correction method patented by Empa [22, 23]. In addition, the optimization of the scanning parameters of the CT system was carried out and the performance of the CT system investigated for some test objects. Besides, a simulation of a complex object "*real object"* defined by an STL-file was also performed.

Our choice of simulating the energy spectrum of the X-ray source of the CT system is based on the fact that the measurement of the energy spectrum of the X-ray tube is time consuming, is vulnerable to alignment errors, needs special equipment, and requires a correction for spurious detector effects and detector efficiency. Besides that, the use of a different source setting and or filtration requires a new measurement and correction. The simulation of the X-ray spectrum is obtained on a personal computer within a few hours for any combination of source energy and filter. The validation of the simulated energy spectrum was performed by comparison with X-ray energy spectra measured using a cadmium telluride detector. The energy and efficiency calibration of the detector, the evaluation of the spurious effects, and the correction of the pulse height distributions were carried out.

An additional source of artifacts in CT with polyenergetic sources is the beam hardening. Standard methods to correct the beam-hardening are the use of layers of absorbing material (filters) to remove the soft part of the X-ray spectrum and numerical corrections based on the information of the spectral shape of the X-ray source and the material passed through. In this thesis we investigated experimentally several filters to find the most effective in reducing the beam-hardening. Moreover, we corrected the reconstructed data with the algorithm of beam hardening correction patented by Dr. R. Thierry [22, 24]. The spectral shape of the X-ray tube that is an input to the algorithm was generated by the author of this thesis with a GEANT4-based MC simulation.

The industrial cone-beam CT system studied in this work was developed during the *DETECT* project by the Department of Physics of the University of Bologna in Italy, the Department of Electronics, Metrology, and Reliability of the Swiss Laboratories for Materials Testing and Research (Empa) in Switzerland, and Hans Wälischmiller GmbH in Germany. In addition to the cone beam geometry and the working energy of the X-ray tube, the particular configuration of the system, namely, the short source-detector distance and the CT system structure, and the size of the X-ray room contribute to the generation of a considerable amount of scattered radiation.

1.2 Structure of the thesis

We describe basic principles of the interaction of photons with matter and of X-ray CT in Chapter 2. The main sources of artifacts in CT are also presented. Moreover, an overview of the different kinds of industrial CT systems available on the market is given. Chapter 3 describes the methodology and approaches to validate the MC simulation of the CT system, to optimize the CT system, to investigate the scattering, and to optimize the anti-scatter grid. An example of the application of the reduction of the artifacts using the evaluated quantities of the scattering is also shown. The description of the equipments and of the developed MC simulation is provided in sections 3.1 and 3.2. In addition, the simulation of a *real object* is described. Extracts from the code are presented in appendix 3. The results and discussions are included in chapter 4. Finally the conclusions and the future work are presented in Chapter 5.

1.3 References

1. Radon, J., *Über die Bestimmung von Funktionen durch ihre Integralwerte längs gewisser Mannigfaltigkeiten.* Math.-Phys., 1917. **69**.
2. Cormack, A.M., *Representation of a Function by Its Line Integrals with Some Radiological Applications.* Journal of Applied Physics, 1963. **34**(9).
3. Cormack, A.M., *Representation of Function by Its Line Integrals with Some Radiological Applications .2.* Journal of Applied Physics, 1964. **35**(10).
4. Hounsfield, G.N., *Computerized Transverse Axial Scanning (Tomography) .1. Description of System.* British Journal of Radiology, 1973. **46**(552): p. 1016-1022.
5. Buynak, C.F. and R.H. Bossi, *Applied X-Ray Computed-Tomography.* Nuclear Instruments & Methods in Physics Research Section B-Beam Interactions with Materials and Atoms, 1995. **99**(1-4): p. 772-774.
6. Flisch, A. and J. Wirth, *Industrial computed tomography in reverse engineering applcations.* Int. symposium on computerized tomography for industrial applications and image processing in radiology, Berlin, 1999.
7. Obrist, A., et al., *3D digitising based on x-ray computed tomography: state of the art and evolution.* Congress numerisation 3D (scanning 2002), Paris, France, 2002.
8. Flisch, A., *Computer tomography for 3-D volume acquisition and defect analysis.* Casting Plant & Technology International, 2006(3): p. 10-17.
9. Endo, M., et al., *Effect of scattered radiation on image noise in cone beam CT.* Medical Physics, 2001. **28**(4): p. 469-474.
10. Glover, G.H., *Compton Scatter Effects in Ct Reconstructions.* Medical Physics, 1982. **9**(6): p. 860-867.
11. Johns, P.C. and M. Yaffe, *Scattered Radiation in Fan Beam Imaging-Systems.* Medical Physics, 1982. **9**(2): p. 231-239.
12. Joseph, P.M. and R.D. Spital, *The Effects of Scatter in X-Ray Computed-Tomography.* Medical Physics, 1982. **9**(4): p. 464-472.
13. Rinkel, J., et al., *A new method for x-ray scatter correction: first assessment on a cone-beam CT experimental setup.* Physics in Medicine and Biology, 2007. **52**(15): p. 4633-4652.
14. Colijn, A.P., et al., *Experimental validation of a rapid Monte Carlo based micro-CT simulator.* Physics in Medicine and Biology, 2004. **49**(18): p. 4321-4333.
15. Inanc, F., *Analysis of X-ray and gamma ray scattering through computational experiments.* Journal of Nondestructive Evaluation, 1999. **18**(2): p. 73-82.
16. Rinkel, J., F. Estève, and J.-M. Dinten. *Evaluation of a physical based approach of scattered radiation correction in cone beam CT for Non Destructive Testing applications*. in *ECNDT*. 2006. Berlin.
17. Chan, H.P. and K. Doi, *Investigation of the performance of antiscatter grids: Monte Carlo simulation studies.* Phys.Med.Biol., 1982. **27**(6): p. 785-803.
18. Kalender, W., *Calculation of x-ray grid characteristics by Monte Carlo methods.* Physics in Medicine and Biology, 1982. **27**(3): p. 353-361.

19. Hopkins, F., et al., *Analytical corrections for beam-hardeing and object scatter in volumetric computed tomography systems.* 16th WCNDT - World Conference on NDT, Montreal, Canada, 2004.
20. Kyriakou, Y., T. Riedel, and W.A. Kalender, *Combining deterministic and Monte Carlo calculations for fast estimation of scatter intensities in CT.* Physics in Medicine and Biology, 2006. **51**(18): p. 4567-4586.
21. Wiegert, J., et al., *Model based scatter correction for cone-beam copmuted tomography.* Proceedings of SPIE, 2005. **5745**: p. 271-282.
22. Thierry, R., *A Statistical Beam Hardening Correction for polychromatic X-ray CT device, PATENT 246/06, 2006*.
23. Thierry, R., Miceli, A., Hofmann, J., Flisch, A., Sennhauser, U., *Hybrid Simulation of Scatter Intensity in Industrial Cone Beam Computed Tomography.* Nuclear Instruments & Methods in Physics Research Section A, 2007(Submitted).
24. Thierry, R., et al., *Statistical Beam-Hardening Correction for Industrial X-ray Computed Tomography.* Conference Proceedings We.3.7.2, ECNDT, Berlin (D), 2006.

2 XCT for industrial application

In this chapter we illustrate the interaction of photons with matter, the principles of X-ray computed tomography (CT), as well as the main sources of artifacts in CT images and the CT systems for industrial applications.

2.1 Interaction of photons with matter

Although a large number of possible interaction mechanisms are known for photons with matter, only two major types play an important role for the energies used in XCT for industrial application (up to 450keV): photoelectric absorption and Compton scattering. These processes lead to the full or partial transfer of the photon energy to the electron energy. The photon either disappears or is scattered by a significant angle.

A third interaction can occur in the energy range considered: Rayleigh scattering. In this case the photon scatters without an appreciable loss of energy. The Rayleigh scatter has a minor importance compared to the photoelectric and Compton effects. In the next paragraphs the notion of the cross section and the linear attenuation coefficient will be introduced and the photoelectric, Compton and Rayleigh effects will be explained in more detail. If not specified otherwise, the information given in this chapter is taken from textbooks, papers and thesis [1-10].

2.1.1 Cross section and linear attenuation coefficient

Consider a monochromatic photon beam of energy E that impinges on a homogeneous slab of some material. After passing through a material thickness dl the ratio between dI , the intensity removed from the beam by scattering and absorption and the initial intensity I is given by:

$$\frac{dI(E,x)}{I(E,x)} = -\sigma(E)ndx \qquad \text{Eq. 2.1}$$

where $\sigma(E)$ is the total interaction cross section and n is the number of atoms per unit of volume. The product of $\sigma(E)n$ is defined as the linear attenuation coefficient $\mu(E)$, representing the probability of interaction per unit path length. For energies up to 450 keV, the linear attenuation coefficient is the sum of the linear attenuation coefficient of photoelectric effect $\tau(E)$, Compton effect $\sigma_c(E)$ and Rayleigh effect $\sigma_{coh}(E)$:

$$\mu(E) = \tau(E) + \sigma_c(E) + \sigma_{coh}(E) \qquad \text{Eq. 2.2}$$

By integrating Eq. 2.1 we obtain the equation that gives the transmitted photon intensity I(E) for a monochromatic pencil photon beam after passing through a thickness of material X (see figure 2.1 for visualization):

$$I(E) = I_o(E)e^{-\int_X \mu(x,E)dx} \qquad \text{Eq. 2.3}$$

The Eq. 2.3 is also called Lambert-Beer law. In case of polychromatic source, as X-ray tubes, the equation becomes:

$$I = \int_0^{E_{max}} I_o(E)e^{-\int_X \mu(x,E)dx} dE \qquad \text{Eq. 2.4}$$

where E_{max} is the maximum photon energy of the beam.

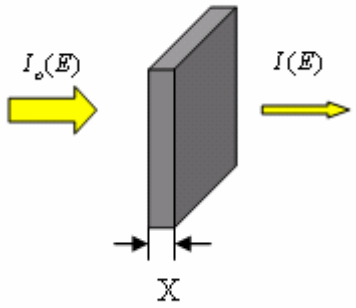

Figure 2.1 A monochromatic pencil photon beam is shown here illuminating a slab of homogeneous material. The beam is measured after the passage inside the slab to determine the attenuation of the object.

2.1.2 Photoelectric absorption

In the photoelectric absorption process, a photon undergoes an interaction with an absorber atom in which the photon completely disappears. In its place, an energetic electron is ejected by the atom from one of its bound shells. The interaction is with the atom as a whole and cannot take place with free electrons. For photons of sufficient energy, the most probable origin of the electron is the most tightly bound or the K shell of the atom. The electron appears with an energy E_{e-} given by:

$$E_{e-} = h\nu - E_b \qquad \text{Eq. 2.5}$$

where E_b represents the binding energy of the electron, $h\nu$ the energy of the photon.

In addition to the electron, the interaction also creates an ionized absorber atom with a vacancy in one of its bound shells. This vacancy is quickly filled by rearrangement of electrons from other shells of the atom. Therefore, one or more characteristic X-ray photons may also be generated. In some cases, the emission of an Auger electron may substitute for the characteristic X-ray in carrying away the atomic excitation energy.

The photoelectric process is the predominant mode of interaction for photons of relatively low energy. The process is enhanced for absorber materials of high atomic number Z. The probability of photoelectric absorption per atom τ is given by the rough approximation:

$$\tau \propto \frac{Z^n}{(h\nu)^{3.5}} \quad n \in [4,5] \qquad \text{Eq. 2.6}$$

2.1.3 Compton effect

The interaction process of Compton scattering takes place between the incident photon and an electron in the absorbing material. It is the predominant interaction mechanism for aluminum at the energies of X-ray tubes for industrial applications (up to 450 keV).

In Compton scattering, the incoming photon is deflected through an angle θ with respect to its original direction. The photon transfers a portion of its energy to the electron (recoil electron). The energy transferred to the electron can vary from zero to a large fraction of the photon energy. The expression that relates the energy transfer and the scattering angle for any given interaction is derived by the equations for the conservation of energy and momentum:

$$h\nu' = \frac{h\nu}{1 + \frac{h\nu}{m_o c^2}(1 - \cos\theta)} \qquad \text{Eq. 2.7}$$

where *hν'* is the energy of the photon after the interaction, *hν* is the energy of the incident photon, θ is the scattering angle and m_0c^2 is the rest-mass energy of 511 keV of the electron. For small scattering angles, very little energy is transferred.

The probability of Compton scattering per atom of the absorber depends on the number of electrons available as scattering targets and therefore increases linearly with Z. The angular distribution of scattered photons is given by the Klein-Nishina formula for the differential scattering cross section $d\sigma_c / d\Omega$:

$$\frac{d\sigma_c}{d\Omega} = Zr_o^2 \left(\frac{1}{1 + \alpha(1 - \cos\theta)}\right)^2 \left(\frac{1 + \cos^2\theta}{2}\right)\left(1 + \frac{\alpha^2(1 - \cos\theta)^2}{(1 + \cos^2\theta)\left[1 + \alpha(1 - \cos\theta)\right]}\right) \qquad \text{Eq. 2.8}$$

where $\alpha = h\nu / m_0c^2$ and r_o is the classical electron radius. The angular distribution of the scattered radiation is shown in figure 2.2. The radial distance represents the energy scattered through an angle θ. At very low energies the scattering is symmetrical about 90°, and as the energy increases the scattering tends to be more and more in the forward direction.

Eq. 2.8 assumes that the electron is initially free. For low energy X-rays or small scatter angles this assumption is not valid because the recoil energy of the electron is comparable or smaller than the electron binding energy. To take into account the binding energy of the electrons Eq. 2.8 is replaced by:

$$\frac{d\sigma_{lowEn}}{d\Omega} = SF(q, Z)\frac{d\sigma_c}{d\Omega} \qquad \text{Eq. 2.9}$$

where $d\sigma_c / d\Omega$ is the Klein-Nishina differential cross section, $SF(q, Z)$ the scattering function and q the momentum transfer given by $E \sin^2(\theta/2)$.

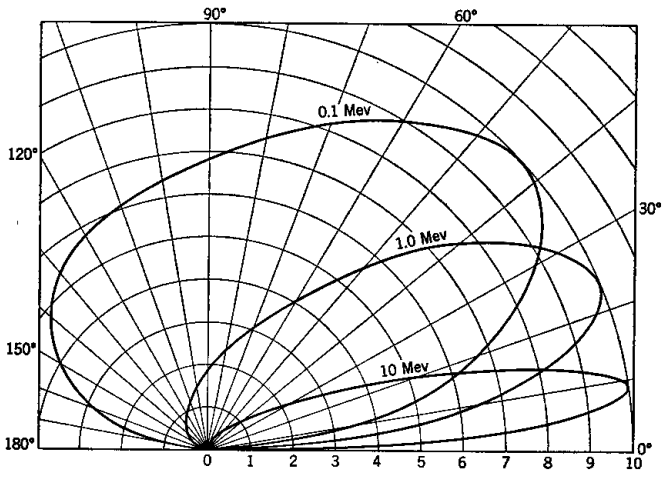

Figure 2.2 Angular distribution of Compton scattered photons (relative energy per unit interval of angle).

2.1.4 Rayleigh scattering

In a Rayleigh or coherent scatter interaction the incident photon interacts with the atom. The photon scatters without appreciable loss of energy. The cross section for coherent scattering σ_{coh} is:

$$\sigma_{coh} \propto \frac{Z^{2.5}}{E_\gamma^2} \qquad \text{Eq. 2.10}$$

The percentage of Rayleigh scattering of the total attenuation cross section in aluminum at energies above 80 keV is below 5%.

2.1.5 Relative importance of photoelectric, Compton and Rayleigh effects

A plot of the photoelectric absorption cross section, Compton cross section and Rayleigh cross section for aluminum in the energy range 0 – 500 keV is shown in figure 2.3a. It shows that the photoelectric effect predominates at low energies (up to 50 keV) while the Compton effect predominates at intermediate energies. The Rayleigh scatter does not play an important role. Figure 2.3b illustrates the ratio of scattering cross-section to absorption cross-section for aluminum. As the incident energy of the X-ray beam increases, the probability of scattering over absorption increases dramatically: the probability of scattering is 26, 180, and 370 times higher than the probability of absorption at 150, 300, and 400 keV, respectively. It becomes evident that the effects of the scattering will be much more severe when we deal with

CT system equipped with 450 kV X-ray tubes compared to CT systems employing 250 kV X-ray tubes.

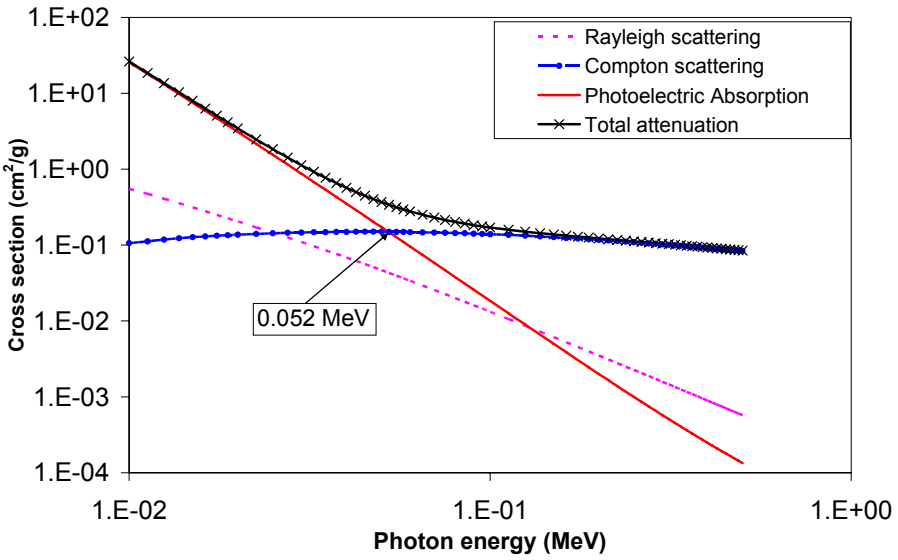

(a)

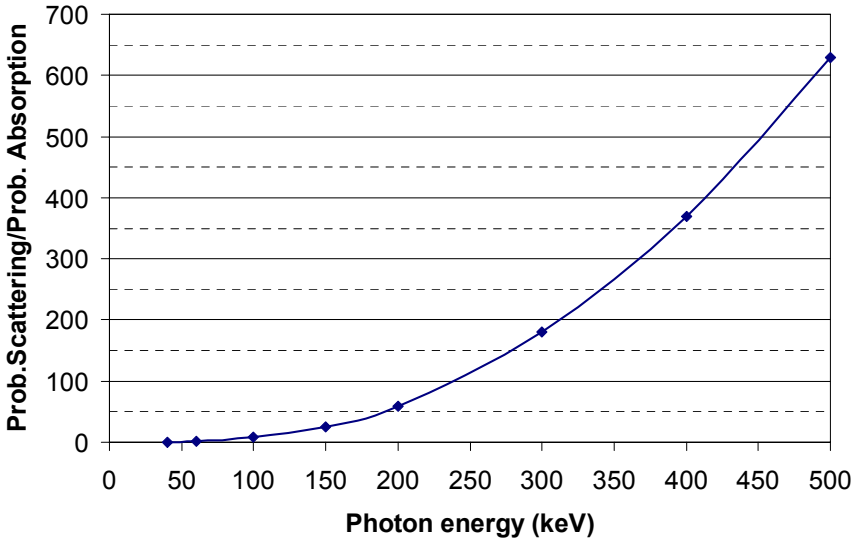

(b)

Figure 2.3 (a) Energy dependence of the various photon interaction processes in aluminum (from NIST database). (b) The photoelectric effect predominates at low energies. Ratio of scattering cross-section to absorption cross-section for aluminum.

2.2 Principles of X-ray computed tomography

This section gives a brief summary of the principles of X-ray Computed Tomography. The result of an X-ray CT measurement is an image which gives the distribution of the local linear attenuation coefficient. The image is obtained by a two step process. First, the transmission of X-ray photons through the object is measured at many different angles. Subsequently, these transmission profiles are reconstructed into an image.

2.2.1 Data acquisition

A typical industrial CT system comprises an X-ray source, a detector, a mechanical system to rotate and move the object relative to the source and detector, and a computer system to perform the reconstruction of the data. The X-ray source and the area detector are fixed. The X-ray source emits a cone beam of photons in the direction of the object. The detector measures the photons transmitted through the object. The measured intensity for a definite angular position of the object is called projection. A projection thus consists of the measured transmitted X-ray photons for each individual ray path.

2.2.2 The Radon transform and the projection data

The Radon transform is the relation between projection data $P_\theta(t)$ and a parametric function f representing the object, where θ is the angle with respect to a reference direction and *t* is the distance of a particular ray path from the origin. Figure 2.4 visualizes the projection $P_\theta(t)$ of an object function *f (l, m)* for a parallel beam configuration. Radon demonstrated that a two dimensional object function could be uniquely reconstructed from an infinite set of projections. In the case of X-ray CT, this object function is the distribution of the linear attenuation *μ (l, m)*. The value for $P_\theta(t)$ for a particular *t* and θ is called ray sum. The ray sum $P_\theta(t)$ can be expressed as the integral of *f (l, m)* along a ray path *s (θ, t)*:

$$P_\theta(t) = \int_{s(\theta,t)} f(l,m)ds \qquad \text{Eq. 2.11}$$

This equation is equivalent to a Radon transform. Consequently *f (l, m)* is completely determined by $P_\theta(t)$ if an infinite number of projections is considered. During a CT scan, we measure at a finite number of projection angles. Therefore, some information about the object function will be lost.

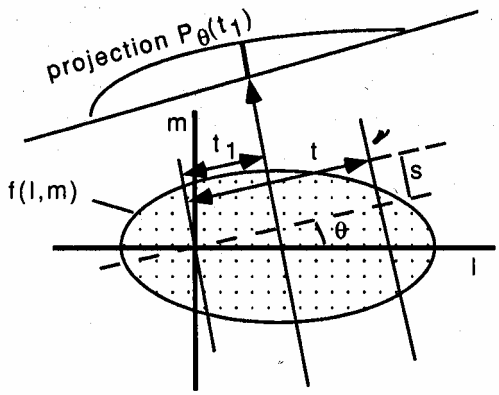

Figure 2.4 An object represented by a two dimensional object function f (l, m), and its projection, $P_\theta(t_1)$, are shown for an angle θ and a distance t_1.

In case of a narrow monochromatic beam, the attenuation can be expressed by the Lambert-Beer equation introduced in section 2.1.1:

$$I = I_o e^{-\int_L \mu(l,m)ds} \qquad \text{Eq. 2.12}$$

where $\mu\ (l, m)$ is the linear attenuation coefficient, I_0 is the initial intensity of the X-ray beam and I is the intensity after passing through the material of thickness L. The X-ray beam intensity is diminished by absorption and scatter. If we rewrite Eq. 2.12 into:

$$\ln(\frac{I_o}{I}) = \int_L \mu(l,m)ds \qquad \text{Eq. 2.13}$$

we see that the natural logarithm of the ratio of the measured initial and transmitted intensities is equal to the integrated linear attenuation along a ray path. By substitution of the linear attenuation $\mu\ (l, m)$ as object function in Eq. 2.11 we obtain

$$P_\theta(t) = \ln(\frac{I_o}{I}) = \int_{L(\theta,t)} \mu(l,m)ds \qquad \text{Eq. 2.14}$$

According to Eq. 2.13, the reconstruction problem consists of the inversion of the Radon transform to find the distribution of linear attenuation coefficients $\mu\ (l, m)$ in the image plane.

2.2.3 Image reconstruction

A large number of inversion or reconstruction methods is available to obtain an image from the measured projection data. The most widely used reconstruction methods in industrial CT are Filtered Back Projection (FBP) and Feldkamp David Kreiss (FDK) algorithm [11]. The use of alternative methods, such as statistical algorithms (SR), is rare and often restricted to discrete tomography or to the truncated data case [12, 13]. The main reason why statistical reconstruction has not yet penetrated massively in X-ray CT, although widely used in nuclear medicine (PET and SPECT), is that data sets in CT are much larger than in nuclear medicine, then iterative reconstruction becomes computationally very intensive [14]. However, since the statistical reconstruction reduces the reconstruction artifacts by improving failure detectability and quantitative accuracy it can be a good candidate for industrial CT.

2.3 Main sources of artifacts in computed tomography

2.3.1 Beam hardening

The X-ray sources used in industrial computed tomography are polychromatic. The attenuation of different energies is not uniform because the attenuation coefficient depends on the energy. The X-ray beam will be depleted in energy ranges with higher attenuation coefficients. The beam hardening is the process of selective removal of soft X-rays (low energy) from the X-ray beam. As these X-rays are removed due to the passage in matter, the beam becomes harder and more penetrating. The amount of beam hardening depends on the initial X-ray spectrum and on the composition of the material traversed. This effect causes the reduction of the reconstructed attenuation coefficient toward the centre of a large object (cupping artifacts) in a CT image [15].

2.3.2 Scattered radiation

An X-ray beam traveling through an object can be attenuated by photoelectric absorption or by scattering. Attenuation by scattering occurs because some of the original energy in the beam is deflected onto a new path. When the intensity scattered from the object reaches the detector, the object will appear to be less attenuating than in reality (figure 2.5).

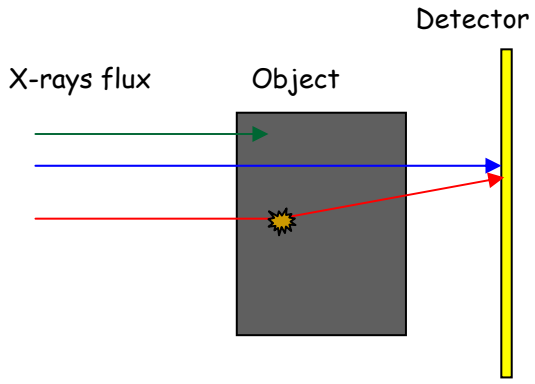

Figure 2.5 Interaction of X-ray photons with the object. The photon can be absorbed by the object (green arrow), can pass through it without interacting and be absorbed by the detector (primary radiation), i.e. signal (blue arrow) or can interact within the object, being deflected from its original path and be absorbed within the detector generating a wrong count on the detector, i.e. noise (red arrow).

Moreover, in some experimental conditions scattered radiation generated by the CT system structure and by the walls of the room (environmental scatter) reaches the detector leading to a further underestimation of the attenuating.

Therefore, the intensity measured by the detector can be decomposed in three components as described in the formula:

$$I_{measured}(x,y) = I_{primary}(x,y) + I_{ScattObj}(x,y) + I_{EnvScatt}(x,y) \quad \text{Eq. 2.15}$$

where *(x,y)* are the pixels on the detector and $I_{primary}(x,y)$, $I_{ScattObj}(x,y)$, and $I_{EnvScatt}(x,y)$ are the contributions to the measured value due to primary radiation, radiation scattered by the object, and radiation scattered by the walls of the room and CT system structure, respectively. The first component represents the signal, whereas the second and the third components represent the noise.

The projection data $P_\theta(t)$ given by:

$$P_\theta(t) = \ln\left(\frac{I_0}{I_{measured}}\right) \quad \text{Eq. 2.16}$$

can be express as:

$$P_\theta(t) = \ln\left(\frac{I_0}{I_{prim} + I_{ScattObj} + I_{EnvScatt}}\right) \leq \ln\left(\frac{I_0}{I_{prim}}\right) \quad \text{Eq. 2.17}$$

Therefore, the ray sum $P_\theta(t)$ from regions where the detected scattered intensity is not negligible will be underestimated. For rays through the object where the primary intensity is very small, the effect of scatter will be large, while for other rays where the primary beam is large, scattered X-rays will not lead to a large error. Consequently, the scattered energy causes larger errors in some projections than others. Thus instead of spreading the error energy over the entire image, there is a directional dependence that leads to streaks in reconstruction and cupping artifacts in CT images. On the radiographic images it will lead to a reduction of the contrast.

The amount of scattering generated by the object depends on many factors, namely, material, size, and shape of the object, position of the object with respect to the detector, X-ray imaging system (geometry and material) and settings (energy and filtration) of the X-ray tube. The environmental scatter in addition to the parameters mentioned above depends also on the characteristics of the X-ray room (dimensions of the room and materials of the walls) and on the area on the detector irradiated by the X-ray tube.

2.4 Industrial CT systems

CT systems for industrial applications are mainly used to analyze the internal and external object structure, detect and characterize material defects (non destructive testing), describe or control matter density differences, and for the 3D digitization for CT to CAD comparison and reverse engineering into CAD.

Industrial CT systems can be divided in two categories: fan-beam and cone-beam CT systems. Fan beam (or 2D) CT systems are composed of X-ray source, collimator, manipulator, and linear detector (figure 2.6a). The collimator focuses the X-ray beam to a fan beam so that only a slice of the object is irradiated by the X-ray beam. The manipulator translates vertically the object to acquire the full volume. The main advantage of this kind of system is the low amount of scatter and consequently the high image quality due to the well collimated geometry. The disadvantage is the long acquisition time and the anisotropy of the 3D data due to the slice-by-slice acquisition process. Cone beam (or 3D) CT systems are composed of X-ray source, manipulator and area detector, which can be a flat panel, a CMOS or a scintillator screen coupled with a CCD camera (figure 2.6b). The advantage of this system is the short acquisition time and the isotropy of the 3D data due to the fact that the radiography of the whole object is acquired at a time. The main drawback is the high level of scattering that causes a severe degradation of the image quality.

Industrial CT systems equipped with 450 kV X-ray tubes are mostly 2D CT systems with a scintillator line. The number of individual detector channels varies from tens to thousands. The scanning of an object is done slice-by-slice translating vertically the object. CT systems with flat panel detectors are used with X-ray tubes of lower energies only (usually up to 250 kV), because of the high amount of scattering at higher energies. Common flat panel systems are based on a photo diode matrix read out by transistors made of amorphous silicon. The X-rays are converted to light by scintillators. Other flat panels use complementary metal oxide silicon (CMOS) or a combination of amorphous selenium/silicon [16].

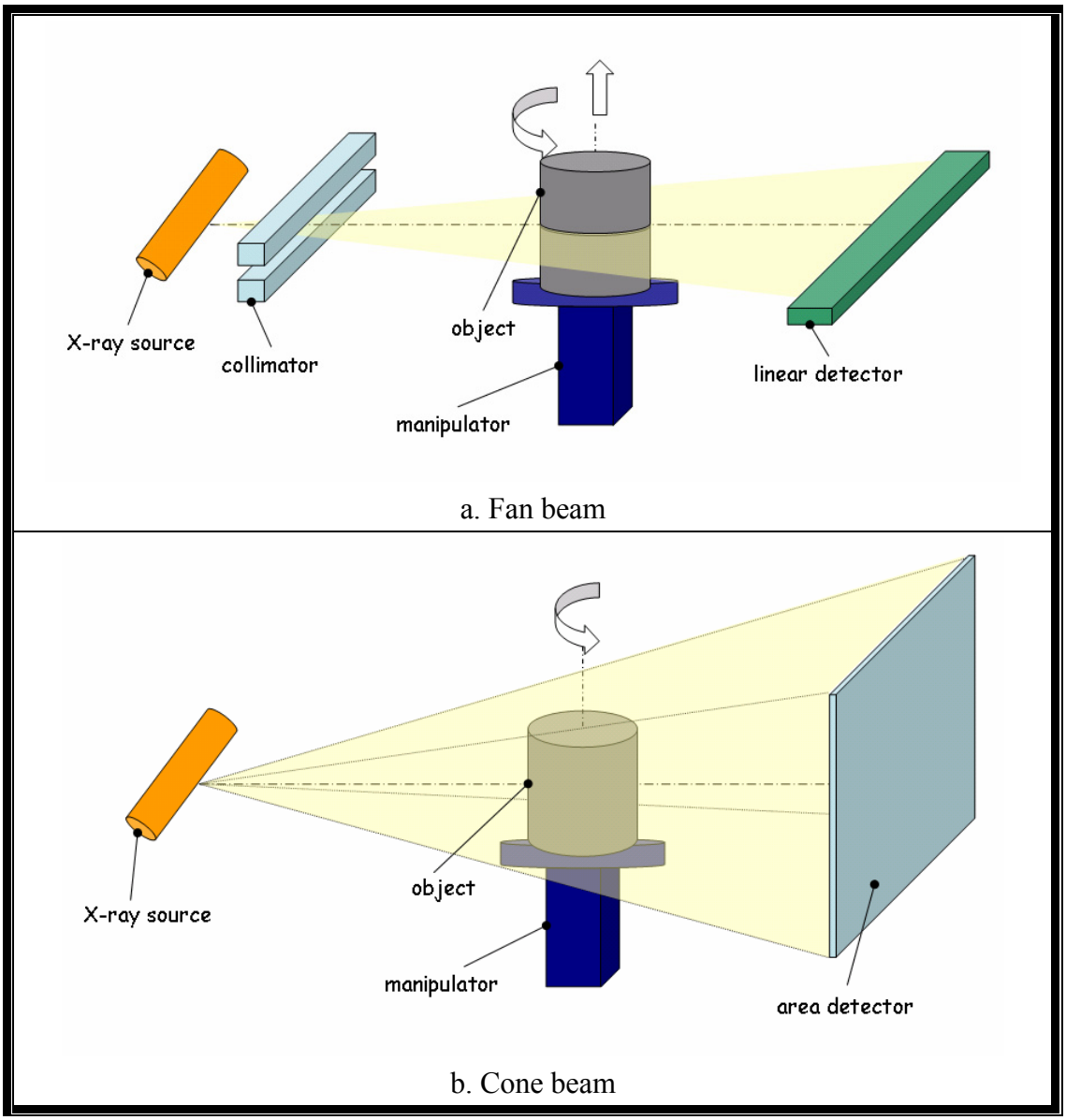

Figure 2.6 (a) Fan beam acquisition system. The X-ray beam is collimated to a fan beam that irradiates only a thin slice of the object. The data are retrieved by a linear detector. (b) Cone beam CT system. The object is fully illuminated by the X-ray beam. The data are retrieved by an area detector.

2.5 References

1. Bradley, D. and D.C. Creagh, *Physical Techniques in the Study of Art, Archaeology and Cultural Heritage, 1*. 2006: Elsevier Science.
2. Copley, D.C., J.W. Eberhard, and G.A. Mohr, *Computed-Tomography .1. Introduction and Industrial Applications.* Jom-Journal of the Minerals Metals & Materials Society, 1994. **46**(1): p. 14-26.
3. Dyson, N.A., *X-rays in atomic and nuclear physics* London, Longman, 1973.
4. Evans, R.D., *The atomic nucleus*. 1955, New York: McGraw-Hill.
5. Glover, G.H., *Compton Scatter Effects in Ct Reconstructions.* Medical Physics, 1982. **9**(6): p. 860-867.
6. Joseph, P.M. and R.D. Spital, *The Effects of Scatter in X-Ray Computed-Tomography.* Medical Physics, 1982. **9**(4): p. 464-472.
7. Kak, A.C. and M. Slaney, *Principles of computerized tomographic imaging*. 1988, New York: The institute of electrical and electronics engineers, Inc.
8. Knoll, G.F., *Radiation detection and measurement*, ed. Second. 1989: John Wiley & Sons, Inc.
9. Leliveld, C.J., *A fast Monte Carlo simulator for scattering in X-ray computerized tomography*. 1996, Delft Technische Universiteit Delft: Delft.
10. Segrè, E., *Nuclei and particles*. 1977, New York: Benjamin.
11. Feldkamp, I.A., L.C. Davis, and J.W. Kress, *Practical cone-beam algorithm.* Journal of the Optical Society of America A, 1984. **1**(6): p. 612–619.
12. Krimmel, S., et al., *Discrete tomography for reconstruction from limited view angles in non-destructive testing.* Electronic Notes in Discrete Mathematics 2005. **20**: p. 455-474.
13. Vengrinovich, V., et al., *New techniques for resolution enhancement in 3D X-ray toomgraphic imaging from incomplete data* Conference Proceeding, International symposium on CT for industrial applications and image processing in radiology Berlin, March 15-17, 1999.
14. Thierry, R., et al., *Statistical Beam-Hardening Correction for Industrial X-ray Computed Tomography.* Conference Proceedings We.3.7.2, ECNDT, Berlin (D), 2006.
15. http://www.medcyclopaedia.com.
16. Obrist, A., et al., *3D digitising based on x-ray computed tomography: state of the art and evolution.* Congress numerisation 3D (scanning 2002), Paris, France, 2002.

3 Materials and Methods

3.1 Detectors: X-and γ-ray spectrometer and Computed Tomography system

In this section we describe the X-and γ-ray spectrometer used to acquire the energy spectrum of the X-ray tube for the validation of the GEANT4-based simulation of the X-ray spectrum of the source and the X-ray imaging system studied and optimized in this thesis work.

3.1.1 X-and γ-ray spectrometer

Among the semiconductor detectors for spectrometry, the CdTe detector is an excellent candidate for the measurement of X-ray tube spectra because of the large bandgap energy (1.47 eV) that permits room temperature operation and of the high density (6.06 g/cm^3) and relatively high atomic numbers Z (48 and 52) that provide high detection efficiency. The drawback of the CdTe, as of most high-Z semiconductors with wide bandgaps is the low mobility (particularly for holes) of the charge carriers. As a result, the effects of trapping and recombination are enhanced, and it is very difficult to achieve complete charge collection over distances greater than 1 mm. The measurement then depends strongly on detector geometry and irradiation conditions [1]. To overcome the problem of incomplete charge collection we used a CdTe detector (XR-100T-CdTe-Stack) produced by AMPTEK Inc., consisting of a stack of three 5 x 5 x 0.75 mm^3 CdTe diode detectors. The advantage of this detector stack over a single detector of the same volume is the significant improvement in charge transport. The charges are transported across 0.75 mm, so the hole tailing is equal to that seen with a single 0.75 mm thick detector, but for radiation interaction purposes, the entire volume is used, to enable the detection of photons with

energies of hundreds of keV. Charge collection efficiency is much higher than in a single, planar element of equal volume since the travel distance to the collecting electrode is short. In addition, to facilitate the electron/hole collection a bias voltage of up to 1500 V can be applied. The detector is cooled by a thermoelectric cooler to avoid excessive leakage and eventually a breakdown when high voltages are applied [2, 3]. The properties of the CdTe are listed in table 3.1.

Table 3.1 Properties of the CdTe [1].

Atomic numbers	48-52
Energy per Electron / Hole Pair	4.43 eV
Band gap at 300K	1.47 eV
Density	6.06 g/cm^3
Electron mobility at 300K	1000 cm^2/Vsec
Hole mobility at 300K	80 cm^2/Vsec
Lifetime electrons, holes	10^{-6} sec

The XR-100T-CdTe-Stack detector consists of an X-and γ-ray detector and a preamplifier. It was used together with the shaping amplifier and multichannel analyzer Amptek PX4. The output of the spectrometer was read by a computer. The software used for the acquisition and analysis of the data was the Amptek ADMCA software.

XR-100T-CdTe-Stack detector

The X-and γ-ray detector is composed of a stack of three 5 x 5 x 0.75 mm^3 CdTe diode detectors mounted on a thermoelectric cooler. The detector and the preamplifier are built as an integral assembly. The internal components are kept at approximately -30° C. The package of the detector has a light and vacuum tight 250 μm beryllium (Be) window. Figure 3.1 shows a picture of the detector and a drawing of the internal components.

Preamplifier. The preamplifier is a charge sensitive preamplifier with a Field-Effect Transistor (FET) input stage. The FET and the feedback components are cooled by the thermoelectric cooler. The sensitivity, defined as the ratio of output voltage produced by the preamplifier to the energy of the incident radiation, is 140 mV/MeV. This type of preamplifier with a FET input stage provides low noise and stable sensitivity.

(a) (b)

Figure 3.1 (a) XR-100T-CdTe-Stack detector. (b) Drawing of the internal components.

PX4

The PX4 is the interface between detector and computer (figure 3.2a). The PX4 includes three major components: shaping amplifier, multichannel analyzer, and power supply. The PX4 filters and digitizes the preamplifier signals, implements the trapezoidal shaping, detects the peak amplitude, and bins this value in its memory, generating an energy spectrum. The spectrum is then transmitted via USB interface to the computer. The performance of the PX4 is listed in table 3.2. Figure 3.2b displays the block diagram of the PX4. Each component of the PX4 is briefly described.

(a)

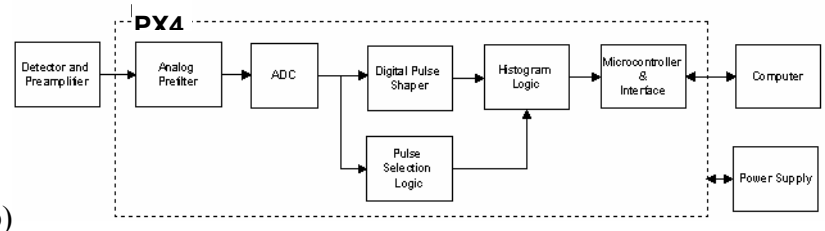

(b)

Figure 3.2 (a) Shaping amplifier and multichannel analyzed PX4. (b) Block diagram of the PX4 in the complete system.

Analog Prefilter. The input to the analog prefilter is the output of the charge sensitive preamplifier. The analog prefilter circuit (high-pass filter, time constant: 3.2 μs) prepares this signal for the digitization.

Analog-to-Digital Converter. The 13-bit analog-to-digital converter (ADC) digitizes the output of the analog prefilter at a rate of 20 MHz. The digitized values are sent into the digital pulse shaper.

Digital Pulse Shaper. The ADC output is processed continuously using a pipeline architecture to generate a real time shaped pulse. The peak value of the digital shaped pulse is determined by a peak detect circuit in the pulse shaper. The peak value for each pulse, a single digital quantity, is the primary output of the pulse shaper. The DP uses trapezoidal pulse shaping.

Pulse Selection Logic. The pulse selection logic rejects pulses for which an accurate measurement cannot be made. It includes pile-up rejection and risetime discrimination.

Histogram logic. When a pulse occurs with a particular peak value, a counter in a corresponding memory location is incremented. The result is a histogram with each cell containing the number of events with the corresponding peak value. This is the energy spectrum and is the output of the PX4.

Table 3.2 Performance of the digital pulse processor.

Gain	x10.8, x20.7, x55.4, x106.2
Fine gain	0.75 - 1.25
Pulse shape	Trapezoidal
Peaking time (μsec)	0.8 - 102.4
Flat top time	16 flat top durations available > 0.2 μsec
Max count rate	Cycle time: 1 μsec. With a peaking time of 0.8 μsec, a 1 MHz periodic signal can be acquired
Dead time	1.25 x peaking time
Pile-up reject	Pulses separated by more than the fast channel resolving time, 600 nsec, and less than 1.25 x peaking time are rejected

3.1.2 CT system

The CT system prototype developed in the framework of the European project DETECT consists of an X-ray source, an X-ray source-collimator, a four axis manipulator, an anti-scatter grid, and an area detector (figure 3.3). The detector is composed of a scintillator, a mirror and a CCD camera. The CCD camera is connected via USB to a data acquisition PC and a data reconstruction PC cluster located in the control room. The mirror and the CCD camera are placed inside a shielding box (detector box). The removable focused one-dimensional (1D) anti-scatter grid is placed on a support in front of the detector at 1390 mm from the source. The source-detector distance is 1500 mm. The X-ray room is 3.6 m wide, 2.9 m high, and 3.7 m deep. Two of the four walls are made of concrete, the other two of a sandwich of steel (3mm), lead (25 mm), and steel (3mm). A detailed description of the CT system components is given below.

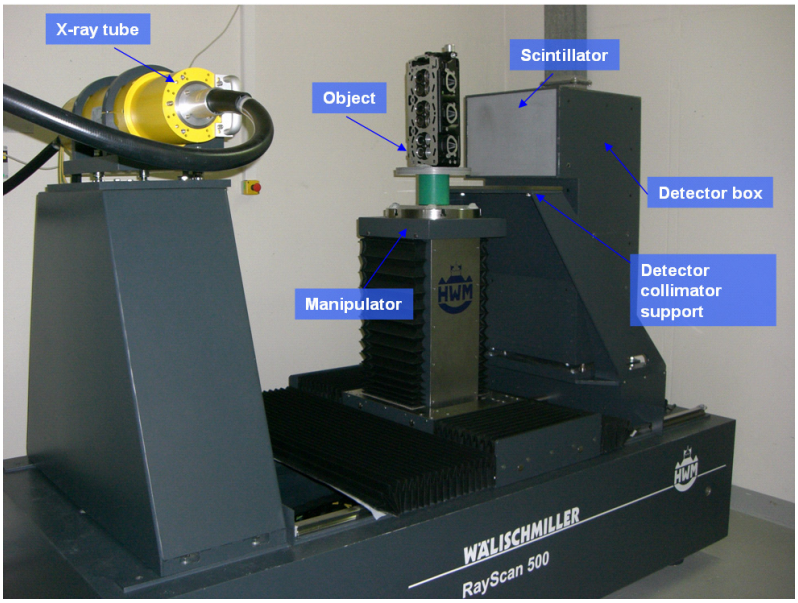

Figure 3.3 CT system prototype. The CT system structure was designed by Hans Wälischmiller GmbH (Germany).

X-ray source

In this thesis work we used two X-ray tubes: a MXR-451 tube (COMET) and an MXR-451 HP/11/Y tube (COMET). The MXR-451 tube has a nominal voltage of 450 kV and effective focal spots of 5.0 mm (large focal spot) and 2.5 mm (small focal spot), respectively. The small focal spot was selected to perform the measurements. The inherent filtration is 2.3 mm iron and 1.0 mm copper. The angle of the tungsten

target is 30°. The emission cone of the X-ray source is 40°. An additional lead housing was placed on the X-ray tube to reduce the leakage through the X-ray tube housing. The MXR-451 HP/11/Y tube has a nominal voltage of 450 kV and effective focal spots of 1.0 mm (large focal spot) and 0.4 mm (small focal spot), respectively. The maximum tube current at 450 kV is 3.3 mA (large focal spot) and 1.6 mA (small focal spot). Both focal spots were used in the experiments. The target material is tungsten and the inherent filtration of the tube is 5.0 mm Be plus 3 mm Al (removable). The Al filter was removed to acquire the data. The angle of the anode is 11°. The beam emission angle is 40° x 30°. A schematic view of an X-ray tube is shown in figure 3.4.

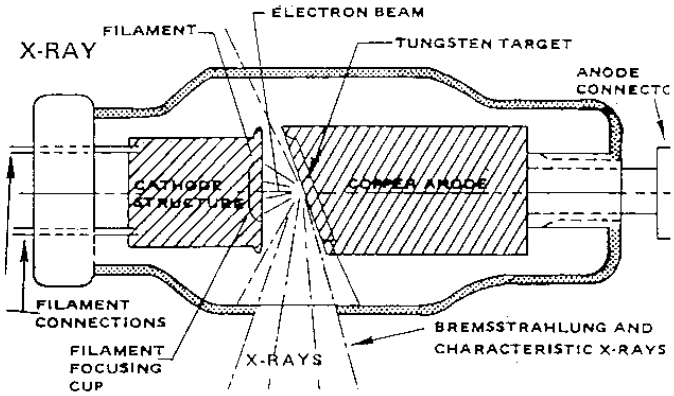

Figure 3.4 Schematic view of an X-ray tube [4].

X-ray source collimator

Several rectangular and slit X-ray source collimators were employed to narrow the beam aperture of the X-ray source and therefore to reduce the unwanted scattered radiation from the CT structure and from the walls of the X-ray room (environmental scatter). We manufactured a rectangular lead source collimator, which illuminates the full area of the scintillator, and three collimators made of brass to be inserted inside the lead collimator. The material chosen for the three collimators was brass, because it was readily available, cheap, and easy to manufacture. Figure 3.5 shows a picture of one of the brass source collimators and its drawings. The slit collimator was composed of two bricks of lead 100 mm thick and spacers of thicknesses 2 mm, 4 mm, 5mm, and 12 mm. The characteristics of the collimators are listed in table 3.3.

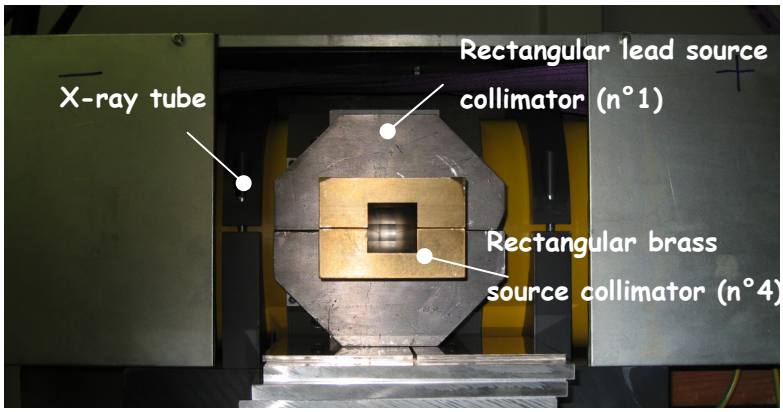

(a)

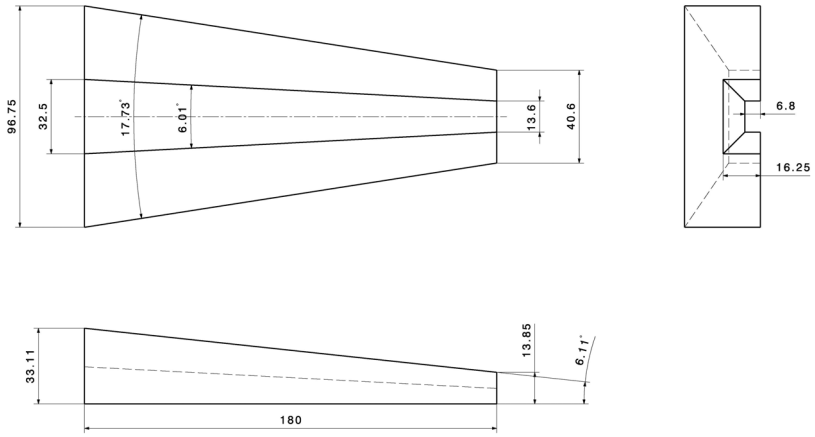

(b)

Figure 3.5 (a) Brass source collimator n° 4 inserted into the rectangular lead source collimator. (b) Drawing of the source collimator n°4.

Table 3.3 Characteristics of the source collimators.

Collimator n°	Geometry	Material	Thickness (mm)	Area illuminated on the scintillator screen (mm^2)
1	Rectangular	Pb	100	Full area
2	Rectangular	brass	180	273 x 270
3	Rectangular	brass	180	337 x 220
4	Rectangular	brass	180	150 x 142
5	Slit (2 mm)	Pb	100	450 x13
6	Slit (4 mm)	Pb	100	450 x 26
7	Slit (5 mm)	Pb	100	450 x 33
8	Slit (12 mm)	Pb	100	450 x 78

Pre-filter

Four different pre-filters were used to cut off the low energy part of the X-ray spectrum: (i) 0.5 mm of tungsten (alloy: HPM1750), (ii) 1.0 mm of tungsten (alloy: HPM1750), (iii) 2.0 mm of brass, and (iv) 2.0 mm of copper.

Post-filter

In some experiments we used 1 mm silver as a post-filter. It was placed in front of the scintillator at a distance of 1461 mm from the source.

Anti-scatter grid

Based on MC simulation studies of one-dimensional (1D) anti-scatter grids (§ 3.7) a 1D grid was manufactured. The grid was composed of tungsten strips focused in the direction of the X-ray beam. The height *h* and the thickness *d* of the strips are 39.7 mm and 5.0 mm, respectively. The thickness of the interspace (*D*) was 7.5 mm (figure 3.6a). The strips were fitted into the groove of a steel frame (figure 3.6b).

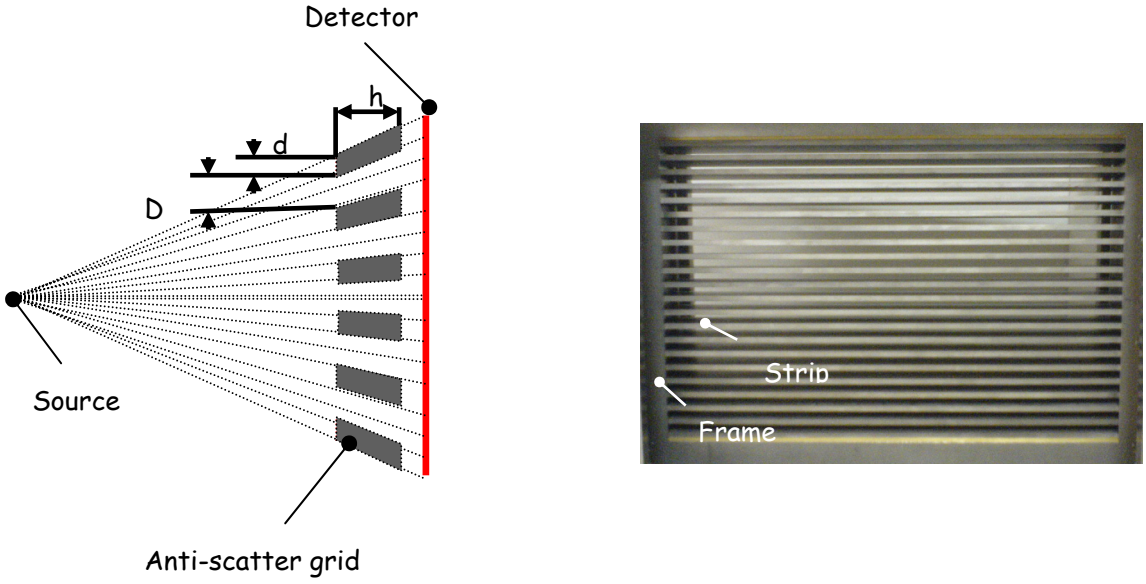

(a) (b)

Figure 3.6 (a) Sketch of the anti-scatter grid. (b) Anti-scatter grid.

Detector

Detector box. The structure, which houses the mirror and the CCD camera, is a box of overall dimensions of 490 x 510 x 1000 mm^3 (width x height x depth). Originally it was composed of a layer of steel of 3 mm (inner layer), a layer of lead of 3 mm, and a layer of steel of 5 mm thickness. For the measurements we removed the inner layer of steel, which was found to significantly degrade the contrast of the CT images (§ 4.2.1). The CCD camera is further shielded by a shielding coffin. The visible photons enter the shielding coffin through a hole in which a lead glass can be inserted.

Scintillator. The detector is a flat thallium doped cesium iodine, CsI(Tl), scintillator 2 mm thick manufactured by Hamamatsu. The thickness of the screen was chosen after simulating screens of 1 and 2 mm (§ 4.2.1). The effective scintillator area is 428 x 280 mm^2. The density is 4.52 g/cm^3. The support of the CsI is aluminum of 1 mm thickness. The material properties of the CsI(Tl) are listed in table 3.4.

Table 3.4 Material properties of CsI (Tl).

Atomic number	53 - 55
Density	4.51 g/cm^3
Wavelength of max. emission	550 nm
Refractive index at max. emission	1.79
Primary decay time	1.0 μs

Mirror. To preserve the CCD camera from the X-ray direct radiation, the photons converted by the scintillator are projected on a high reflectivity front surface of a 3 mm thick mirror tilted to 45° with respect to the direction of the X-ray beam.

CCD camera. The CCD camera is an Apogee Alta U32 CCD camera with a 3-megapixel Kodak Blue Plus full-frame sensor (figure 3.7). The CCD camera has high quantum efficiency, excellent dynamic range and low noise. The specifications of the CCD camera are listed in table 3.5. An uninterruptible power system (UPS–PW 5115) was installed to protect the CCD camera from power failures, power sags, power surges, brownouts, and line noise.

Figure 3.7Apogee Alta U32 CCD camera.

Table 3.5 Specifications of the CCD camera.

CCD	Kodak KAF-3200ME
Digital resolution	12 bits at 10 MHz and 16 bits at 1 MHz
Array size (pixels)	2184 x 1472
Pixel size	6.8 x 6.8 μm
Image area	14.85 x 10.01 mm
Dynamic range	77 dB
Quantum efficiency at 550 nm	70%
Max. quantum efficiency	86% (at 610 nm)

Lens. A Linos 25 mm f/1.6 lens with C-mount adapter (figure 3.8) was mounted on the CCD camera. The field of view was 524 x 353 mm^2 and the pixel size on the scintillator screen was 0.24 x 0.24 mm^2. Several apertures were available; among them we selected f/1.6, f/2.8 and f/5.6.

Figure 3.8 Linos 25 mm f/1.6 lens with C-mount adapter.

Manipulator

The 4-axis manipulator (3 translation, 1 rotation axis), on which the investigated object is placed, is made of RHENOCAST mineral casting basis. The specifications of the manipulator are listed in table 3.6.

Table 3.6 Specifications of the manipulator.

Diameter of rotary table	340 mm
Max. height	1050 mm
Maximum object weight	50 kg
Max. object diameter	315 mm
Max. object height	1000 mm
Path length X (source detector), Max	850 mm
Path length Y (transversal), Max	+ / - 250 mm
Path length Z (vertical), Max	500 mm

Computer hardware

The computer hardware consists of a data acquisition PC (HP xw6200, 3.6 GHz, 1GB RAM), directly connected with the CCD camera by USB2.0, and a data reconstruction PC cluster (5 dual processor workstation HP xw6200, 3.6 GHz, 2 GB RAM).

Software for acquisition, reconstruction, and data correction

Acquisition. The software used to set the parameters of the CCD camera, the manipulator, and the X-ray rube and to acquire the data is “RayScan” developed by Hans Wälischmiller GmbH, Germany (a tutorial of the software can be found in appendix A.1).

Reconstruction. Two reconstruction softwares were considered. The former, provided together with the acquisition software of Hans Wälischmiller GmbH, is based on a three-dimensional cone-beam version of the filtered backprojection (FBP), namely the Feldkamp-David-Kreiss (FDK) algorithm [5] [6]. No beam-hardening or scatter correction are implemented in this software. The latter, developed and patented by Dr. R. Thierry (Empa) [7], is based on a statistical image reconstruction (SR) accelerated by an iterative method called ordered subsets (OS) [8] [9]. The algorithm includes also the statistical correction for beam-hardening in cone-beam geometry. This approach models the object attenuation as a linear combination of the attenuation properties of two base substances. The spectrum of the X-ray source that is a priori information of the algorithm was simulated with the MC method (§ 3.2) [9] [7]. As mentioned in

chapter 2, the statistical reconstruction compared to the FDK algorithm reduces the reconstruction artifacts by improving failure detectability and qualitative accuracy.

Scatter correction. To correct for the scattered radiation generated by the object as well as the scattered radiation created by the CT system structure and walls of the room, we utilized the scatter correction method patented by Empa [10, 11] [12] [13]. The method that requires a priori knowledge of the investigated object is based on the subtraction of the scattering contribution from the original sinograms. The scattering contribution is evaluated with the Monte Carlo method (§ 3.2).

3.2 Monte Carlo simulation

In this section we introduce the MC code GEANT4 and describe the elements of a GEANT4-based simulation. In addition, we illustrate the MC simulation developed in this thesis work.

3.2.1 MC simulations and CT

Main advantage of the simulation is the ability of studying the interaction of the radiation with each of the components of the Computed Tomography (CT) system and analyzing the contribution of different orders of scattering to the formation of the image. For that reason, the simulation is an excellent and powerful tool for the optimization of the geometry of the CT system, as well as for the study and correction of the scattered radiation that is responsible for the creation of artifacts in the reconstructed images.

The application of simulations in medical CT has started already many years ago, whereas the application in industrial CT is still quite infrequent. Some authors use deterministic simulations to investigate the scattering in medical CT [14-16]. These models can be used with some success, but give only an approximate estimate of the true scatter distribution since they stop the calculation of the scattered photons to first order scattering. In industrial cone-beam CT, the contribution of multiple scattering is often higher then the primary radiation and can not be neglected (§ 4.3). For that reason, our studies are based on Monte Carlo (MC) simulations that enable accurate models of the geometry of the system and the calculation of multiple order scattering. The drawback of the MC method is the high computing time compared to deterministic simulations. The widespread availability of high performance parallel computing and Grid technology in addition to the popularity of variance reduction techniques can be a solution.

Among the MC codes for the simulation of the interaction of radiation with matter (i.e. MCNP, EGS, etc.) we chose the GEANT4 toolkit for the accuracy of the models implemented, the energy range of validity, and the openness due to the object-oriented technology.

3.2.2 GEANT4

The GEANT4 (GEometry ANd Tracking) code was developed at CERN, Switzerland, in the framework of a worldwide collaboration. Nowadays, GEANT4 is largely used by the scientific community for the accuracy of the models implemented and for the wide energy range of validity. The main applications are in the medical field, as well as in the high energy and astrophysics [17, 18]. The code is written in C++. GEANT4 implements two electromagnetic models: standard that covers the energy range [10 keV, 1 TeV] and low energy, which was used in this thesis work, that is valid in the energy range [250 eV, 100 GeV]. The cross sections, scattering functions, form factors, binding energies of the electrons, and transition probabilities for fluorescence and Auger effect are retrieved from the Evaluated Atomic Data Library (EADL), Evaluated Electrons Data Library (EEDL), and Evaluated Photons Data Library (EPDL97) [19].

The main concept of GEANT4 is the use of the MC method to simulate the interactions of particles with matter [20]. The term "Monte Carlo method" means that the code is based on repeated random sampling. The input is chosen from a range of possible inputs. The procedure is repeated several times and the combined value of the simulated inputs creates the final results.

GEANT4 transports the particles step-by-step (step-wise manner). Figure 3.9 shows how the path of a photon in matter is composed of several steps. The next paragraph explains how the step is determined.

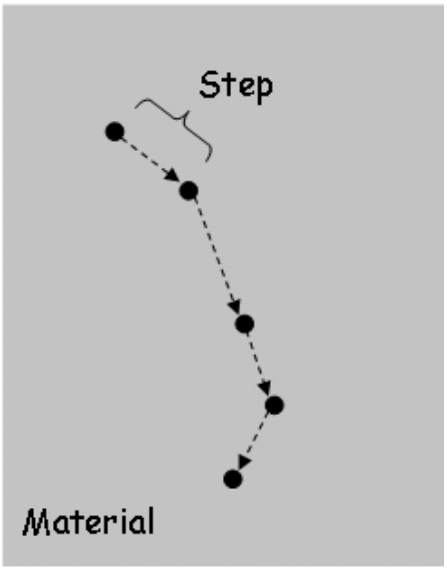

Figure 3.9 Path of a photon in matter.

Determination of the step

The probability of interaction of a particle traveling in a certain material at the position X is given by:

$$\int_0^X \mu e^{-\mu x} dx = 1 - e^{-\mu X} = \alpha , \quad \alpha \in [0,1] \qquad \text{Eq. 3.1}$$

where μ is the linear attenuation coefficient of the material. The number α can be randomly sampled from a uniform distribution and the interaction length X can be retrieved by simply inverting Eq. 3.1

$$X = -\frac{\ln(1-\alpha)}{\mu} \qquad \text{Eq. 3.2}$$

A random number α_i in the range [0, 1] is generated by the code for each physical process *i* associated with the particle. Then, the interaction length X_i is calculated from Eq. 3.2. The physical process corresponding to the smallest interaction length applies. The procedure is repeated until the kinetic energy of the particle is zero, the particle disappears due to an interaction, or the particle reaches the end of the simulated region.

GEANT4 Version

We used the version 4.7.0 with the low energy electromagnetic extension version 2.3 for all the simulations presented in this thesis work except the simulation of complex objects. For that simulation we used the version 4.8.2 with the low energy electromagnetic extension version 4.2 because of the presence of a new kind of solid called *Tessellated Solid* necessary to implement methods to read STL-files (files describing the surface geometry of an object).

3.2.3 Elements of a GEANT4-based simulation

In GEANT4 it is mandatory to define random engine, particles and physical processes associated with the particles, energy and angular distribution of the initial beam, elements and materials employed, detector geometry, and to retrieve the quantities of interest. The input or configuration data have to be embedded directly into the source code of the program. The user is also responsible for the creation of the *main* program module.

Random engine

The generation of random numbers is essential for a MC simulation to sample cross-sections, interaction lengths, probability distributions, etc. It is very important to avoid correlations arising from the periodicity of random number sequences. The random numbers are created by algorithms which generate uniform sequences with measured stochastic properties called Random Engines. The sequences of random numbers (pseudo-random) are undistinguishable from true stochastic distributions in nature [21]. Great care should be given to the choice of the random engine especially if one wants to parallelize the simulation. The random engine should be defined in the *main()* using the class *HepRandom* (extracts from the code are in appendix A.3.1). After testing the random engines *Ranecu* [22] and *HepJamesRandom* [22] we concluded that the random engine *HepJamesRandom* is more suitable for the parallelization of the simulation because it generates longer sequences of pseudo-random numbers.

Particles and physical processes

The particles and their physical processes are defined in the PhysicsList class. For our simulation we considered photons and electrons. We defined low energy bremsstrahlung, low energy ionization, and multiple scattering for electrons, low energy photoelectric effect, low energy Rayleigh scattering, and low energy Compton scattering for the interaction of the photons.

The term “low energy” refers to the fact that the low energy electromagnetic physics model of GEANT4 was employed to simulate the interaction of radiation with matter [19]. The description of the theory, model or parameterization of the physics interactions provided by GEANT4 can be found in [23]. In the Physic List it is also necessary to define a threshold below which the secondary particles will not be generate. This threshold is defined as a distance. This distance is internally converted to energy for each material [24]. We set the cut to 0.1 mm. Extracts from the code are in appendix A.3.2.

Initial beam

To define the incident beam we utilized the *G4GeneralParticleSource* [25] developed at ESA [26] instead of the default generator of GEANT4. The *G4GeneralParticleSource* allows the user to define energy, angular and spatial distributions of the source. We replaced the *G4ParticleGun* with the *G4GeneralParticleSource* in the *PrimaryGeneratorAction* class and we defined the characteristics of the beam in a macro file (simulation of the CdTe detector and of the X-ray spectrum) or we implemented the code in the *main()* of the program (generation

of the radiography) (appendix A.3.3). The characteristics of the initial beam for each simulation are described in the following sections together with the geometry.

Elements and materials

The elements and materials that we have defined are listed in tables 4.7 and 4.8, respectively. The elements were defined in *DetectorConstruction* class using their atomic number and atomic weight retrieved from the NIST Database [27], the materials using density and chemical composition (extracts from are code is in appendix A.3.4).

Detector geometry

A detector geometry is composed of several geometrical elements or volumes defined in the *DetectorConstruction* class. The largest volume (*World volume),* containing all the other volumes, represents the experimental room. Each volume is described by its shape, its physical properties, and its position inside a containing volume (*mother volume*). The shape and the dimensions of the volume are described using the concept of *solid*. The physical properties (i.e. material) and the position of the volume are defined in the *logical volume* and in the *physical volume*, respectively [24].

Solids available in GEANT4 are *Constructive Solid Geometry* (CSG) and *Boundary Represented Solids* (BREPs). The former, which comprises boxes, tubes, cones, spheres, wedges, and tori, is defined as three-dimensional primitives and can be combined using Boolean operations (union, intersection or subtraction). The latter are defined by describing their boundaries [24].

Starting from the version 4.8.2 it is available another kind of solid called *Tessellated Solids* defined by the number of facets. This solid can be used to implement methods to read STL-files [28].

Table 3.7 Elements defined in the simulation.

Element	Atomic number	Atomic weight (g/mole)
Be	4	9.0122
C	6	12.01
N	7	14.01
O	8	16.00
Mg	12	24.31
Al	13	26.98
Si	14	28.09
P	15	30.97
S	16	32.07
Ar	18	39.95
Ti	22	47.87
Cr	24	52.00
Mn	25	54.94
Fe	26	55.85
Ni	28	58.69
Cu	29	63.55
Zn	30	65.39
Ag	47	107.87
Cd	48	112.41
Sb	51	121.76
Te	52	127.6
I	53	126.90
Cs	55	132.91
W	74	183.84
Au	79	196.97
Pb	82	207.20

Table 3.8 Materials defined in the simulation.

Material	Composition	Density (g/cm^3)
Vacuum		$1.00*10^{-25}$
Air	N 76%, O 23 %, Ar 1%	$1.21*10^{-3}$
SiO_2	Si 33.3%, O 66.7%	2.2
AlMgSi1	Si 1%, Fe 0.5%, Cu 0.1%, Mn 0.7 %, Mg 0.9%, Cr 0.25%, Zn 0.2 %, Ti 0.1 %, Al 96.25 %	2.70
CsI	I 50%, Cs 50%	4.52
CdTe	Cd 50%, Te 50%	6.06
Bronze	Sn 10 %, Cu 90%	7.7
LaserFormST-100	Bronze 40%, 420StainlessSteel 60%	7.7
420StainlessSteel	S 0.03%, C 0.15%, Cr 14%, Fe 83.3%, Mn 1%, P 0.04%, Si 0.1%, Ni 0.5%	7.75
Steel	Fe 99.82 %, C 0.18%	7.87
Brass	Zn 39%, Pb 3%, Cu 58%	8.47

Physical quantities

In order to retrieve the physical quantities of interest the user has to implement three action classes: *RunAction*, *EventAction*, and *SteppingAction*. In these classes the user has to implement the actions to take at the beginning and at the end of a *run*, an *event*, and a *step*, respectively. A *run* is a collection of *events* which share the same detector conditions, an *event* is a primary particle, and a *step* is the trajectory of a particle between two subsequent interactions. At the beginning of a *run*, the geometry is fixed and the tables of the cross-sections are calculated for the defined materials considering the cut-off values [29].

Examples of the actions that can be taken in the *RunAction* class are the collection, sum and storage of the data generated by the processors working in parallel (appendix A.3.5); in the *EventAction* class are the retrieving of energy and position of production of the electrons within the scintillator generated by the interaction of photons (appendix A.3.6); and in the *SteppingAction* class are the classification of the photons reaching the detector as primary photons, first, second, and higher order of scattering photons (appendix A.3.7).

3.2.4 Monte Carlo simulation of the CT system

In this thesis work, we developed a MC model for the industrial X-ray CT system described in § 3.1.2. The simulation was designed to describe the image formation in CT starting from the generation of the X-ray photons up to their absorption in the sensitive detector. Detailed simulation of the X-ray tube, source collimator, pre-filters, test objects, post-filter, and detector were considered [30]. The model was validated by comparison with experimental data (§ 3.3). The CT model was used to optimize the hardware components of the CT system, to study the scattering generated by the investigated objects and by the environment (CT system structure and walls of the room), and to study and optimize anti-scatter grids. Moreover, the results of the MC simulation were used in the scatter correction algorithm patented by EMPA [31] to reduce the artifacts in CT images due to the scattered radiation generated by the investigated object and by the environment [9].

The X-ray spectrum of the tube was simulated taking into account the anode angle and the inherent and external filtration of the tube. The spectrum was used as input to the simulation of the full CT system for the generation of the projection of the object (i.e. image of the energy deposited within the detector) [30]. The simulated X-ray spectrum was also used in the statistical reconstruction for the beam-hardening correction.

Some simulations were run on a Pentium-IV-based personal computer with a 2.80 GHz microprocessor and some others, in order to reduce the computing time, were parallelized on the data reconstruction PC cluster (10 CPUs, § 3.1.2). The software used for the parallelization was developed at Empa by J. Hofmann. The software uses the Message Passing Interface (MPI) for the inter-communications of the computers [32]. The number of events to simulate was divided by the number of CPUs available and in each CPU the program was executed using a different value of the random engine (§ 3.2.3). The simulations were performed with primary photon histories ranging from 10^6 to $2*10^9$ depending on the simulated object, geometry, and quantities investigated. The computing time to reach a good statistics strongly depends on the number of primary photon histories and the X-ray beam aperture. It goes from several minutes to several hours, when the PC cluster is used.

3.2.4.1 X-ray spectrum

The generation of the spectrum involves the simulation of a monochromatic pencil electron beam hitting the tungsten target at an angle θ with respect to the normal of the anode surface (anode angle) and the passage of the produced X-ray spectrum through inherent and external filtration. The radiation is retrieved within an angle of 20° with respect to the central axis of the beam and with an energy bin of 1 keV. The anode angle, inherent filtration, and material of the anode were simulated according to the parameters provided by the X-ray tube manufacturer. Figure 3.10 shows the setup of the MC simulation. The validation of the simulated spectra has been assessed through comparison with experimental data (§ 3.3.1) [33]. An extract of the code is provided in appendix A.3.8.

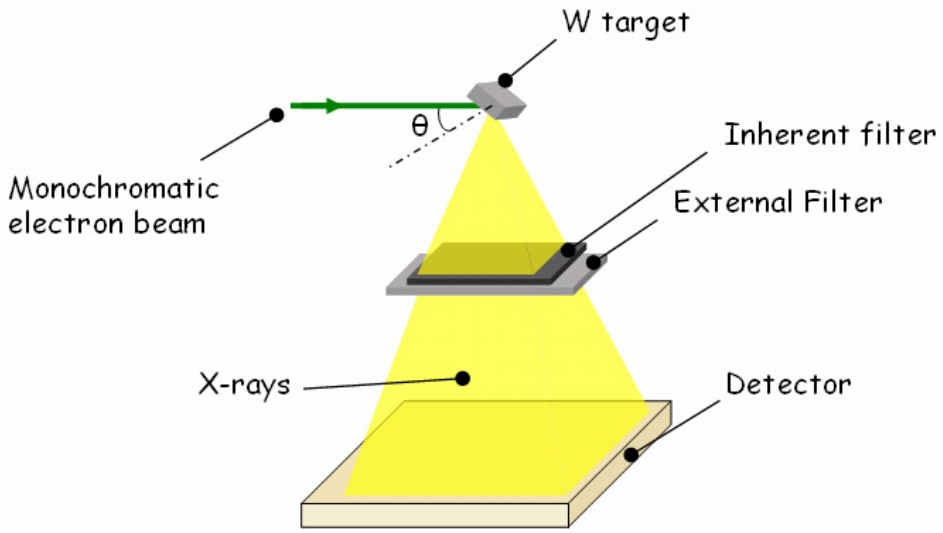

Figure 3.10 Simulation setup for the generation of the X-ray spectrum. The detector is a box made of vacuum. The photon energy is retrieved on the front side of the detector.

3.2.4.2 Image of the energy deposited within the detector

The X-ray photons are emitted from the focal spot of diameter D, with energy sampled randomly from the simulated X-ray spectrum, towards the object. Their direction is selected randomly from an isotropic distribution of angles in a cone of selected aperture (§ 3.3.1 illustrates the verification of the hypothesis of the isotropy of the angular distribution). When the X-ray photons reach the object they can undergo photoelectric absorption, single Compton scattering, multiple Compton scattering, and Rayleigh scattering. The X-ray photons that leave the object in the direction of the detector are filtered by the post-filter and the support of the scintillator. If the anti-scatter grid is simulated, the photons can interact with the grid before interacting with the post-filter. The photons interact with the scintillator by releasing energy to the material with production of electrons. When simulating the detector box or the mirror, the photons that are not absorbed by the scintillator can interact with the detector box or the mirror and backscatter into the scintillator. The images of the energy deposited within the scintillator generated by the primary photons, first, second, and higher order of scattering photons were obtained retrieving the energy and the position of production of the electrons within the scintillator together with the number of Compton and Rayleigh interactions of the parent photon within the object.

The scatter images were de-noised using the Richardson-Lucy fit. The procedure, which has been used by Colijn [12], utilizes a maximum likelihood algorithm to retrieve the original noise-free signal blurred by a Gaussian kernel. Smooth estimates of scatter projections can be obtained from a simulation with a low number of photons. This allows reducing the time needed for MC simulations [34]. The projections were de-noised using 10 iterations of the Richardson-Lucy fit and a standard deviation of the Gaussian kernel of 30 detector pixels, if not otherwise specified.

3.2.4.3 Geometry models of the X-ray CT system

In this paragraph we describe all the components of the CT system (§ 3.1.2) simulated with the GEANT4-based MC code. Dimensions, materials, and spatial positioning of the components were simulated according to the ones of the CT system prototype. The simulation setup is shown in figure 3.11 [30].

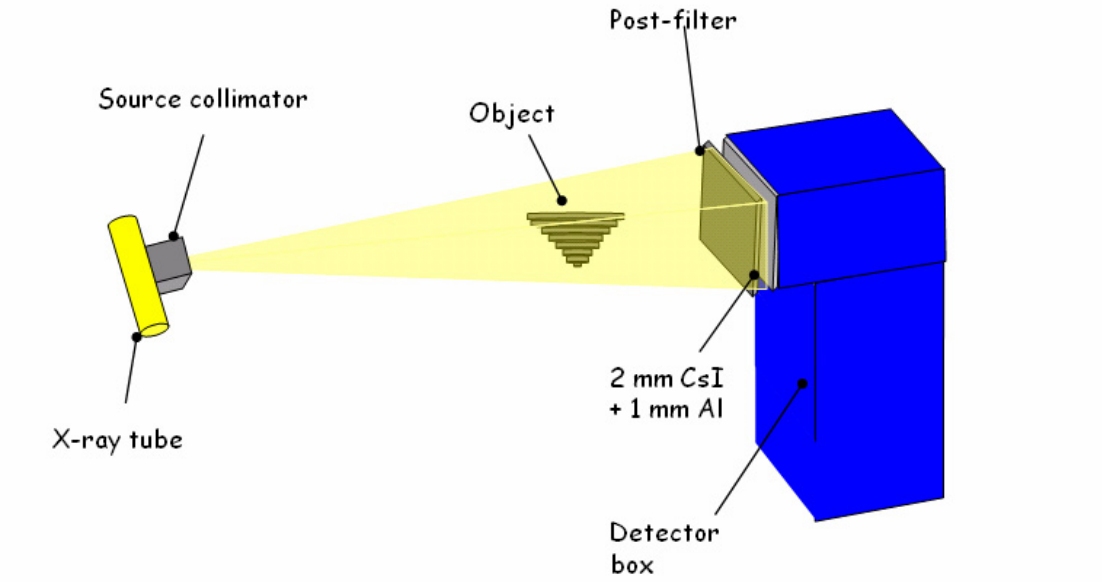

Figure 3.11 Simulation setup for the generation of the radiography. In the sketch the anti-scatter grid is not present.

Source collimator

The collimator n° 1 of table 3.3 was defined using the CSG representation. First we constructed a box of dimensions 90 x 90 x 100 mm^3 using G4Box, then we subtracted a trapezoid constructed by G4Trd using the Boolean operators. An image of the simulated collimator and its dimensions is shown in figure 3.12. The image was obtained with the Java WIRED software [35, 36]. An extract from the code can be found in appendix A.3.9.

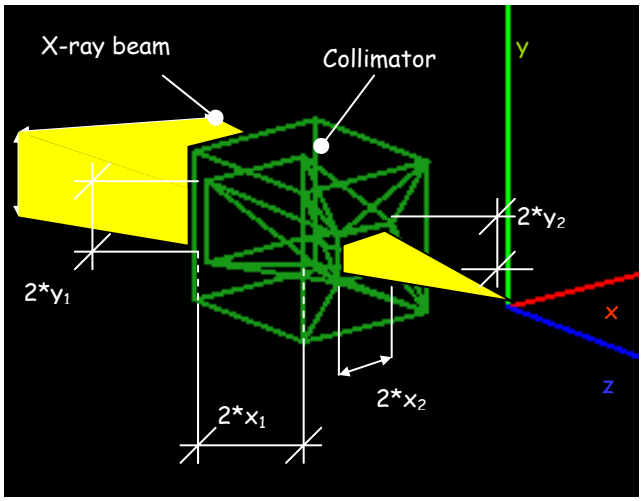

Figure 3.12 Collimator n° 1 simulated with GEANT4. The thickness was 100 mm. The values of x_1, x_2, y_1, y_2 were 35.9 mm, 20.3 mm, 24.6 mm, and 13.9 mm, respectively.

Object

We defined the objects using the CSG representation. Some objects were created as intersection, union, and/or subtraction of CSG solids. To simulate complex objects (§ 3.8) we used a code able to read STL-files developed at EMPA by J. Hofmann based on *Tessellated Solids*. An image of an object defined by STL file is shown in figure 3.13.

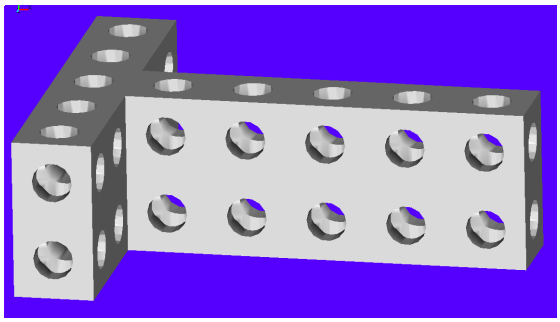

Figure 3.13 Image of the object obtained from a STL file.

Anti-scatter grids

2D anti-scatter grids

The 2D anti-scatter grid was created as a series of trapezoids using the class *G4Traps*. The creation of the grid was performed in eight steps as shown in figure 3.14. The first step was the creation of the vertical strips. The second step was the reflection of the strips with respect to the y axis. The third step was the creation of the horizontal septa in the region x>0 and y>0. The fourth step was the reflection of the created septa in the region of the space x<0 and y>0. The fifth step was the creation of the horizontal septa in the region of the space x>0 and y<0. The sixth step was the reflection of the septa created in the region x>0 and y<0 with respect to the y axis. The seventh and eighth steps were the creation of the central septa and the reflection of the septa with respect to the x axis.

Each trapezoid, whose center must be in the origin of the reference system, was defined by eight points. We calculated the coordinates that define the trapezoid by considering thickness of the interspace, thickness of the strips, height of the strips, number of strips, length L of the strips, and magnification of the grid (figure 3.15) and we centered the trapezoid in the origin of the reference system. After the creation we placed the trapezoid in the right position using *G4PVPlacement*. Implementation of the code can be found in appendix 3.10.

1D anti-scatter grids

The 1D anti-scatter grid was created as a series of trapezoids using the class *G4Trap*. We calculated the points that define the trapezoid considering the thickness of the interspace, thickness of the strips, height of the strips, number of strips, length L of the strips, and magnification of the grid (figure 3.16) as the strip was in the center of the reference system. Then we translate the trapezoid to the right position along the y and z axis using *G4PVPlacement*. To avoid unnecessary calculations we created the part of the grid placed in the region of the space y> 0 and we reflected it with respect to the y axis. Figures 3.16-3.17 show the simulated anti-scatter grid and the setup of a simulation with the anti-scatter grid visualized using the WIRED software [35]. The implementation of the code can be found in appendix 3.11.

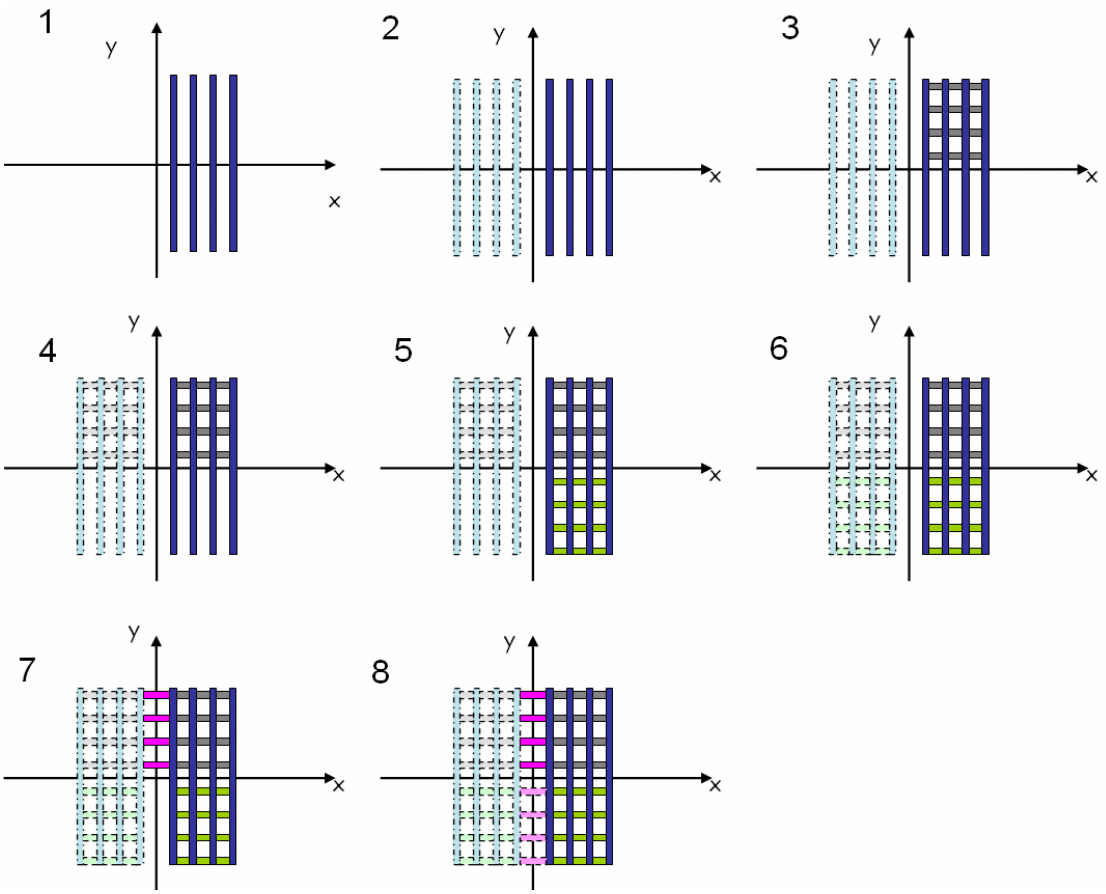

Figure 3.14 Steps to create the 2D anti-scatter grid.

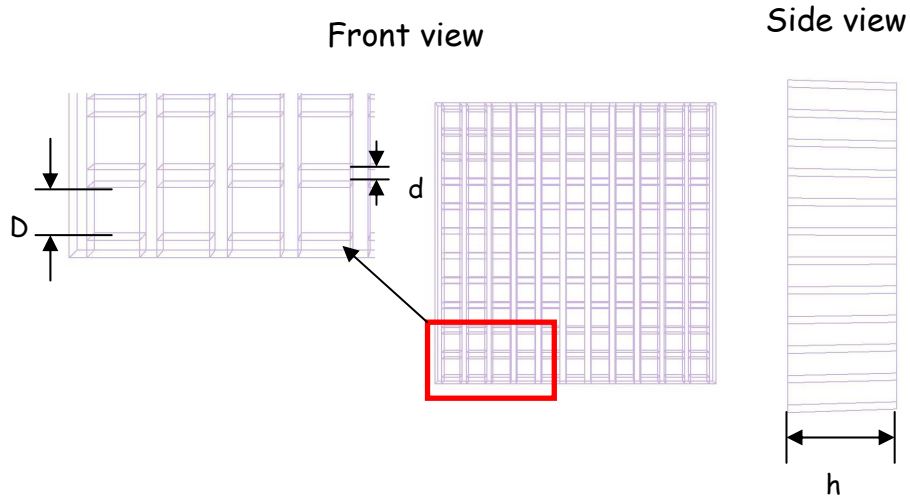

Figure 3.15 2D focused anti-scatter grid simulated with GEANT4. The visualization was obtained using the WIRED software.

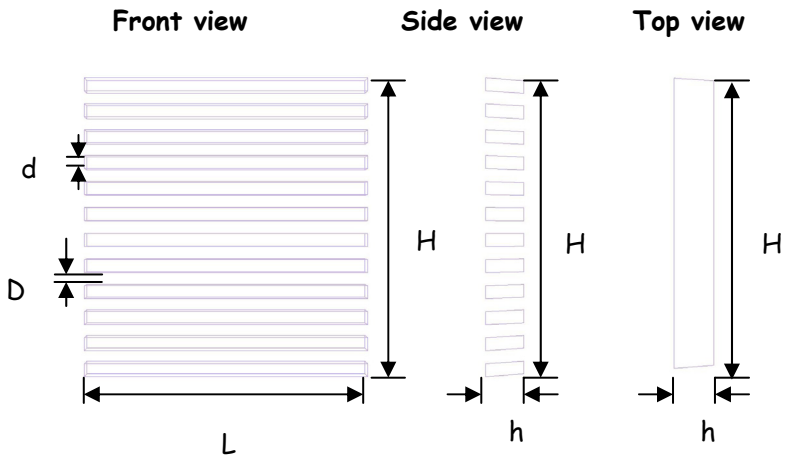

Figure 3.16 (a) 1D focused anti-scatter grid simulated with GEANT4. The visualization was obtained using the WIRED software.

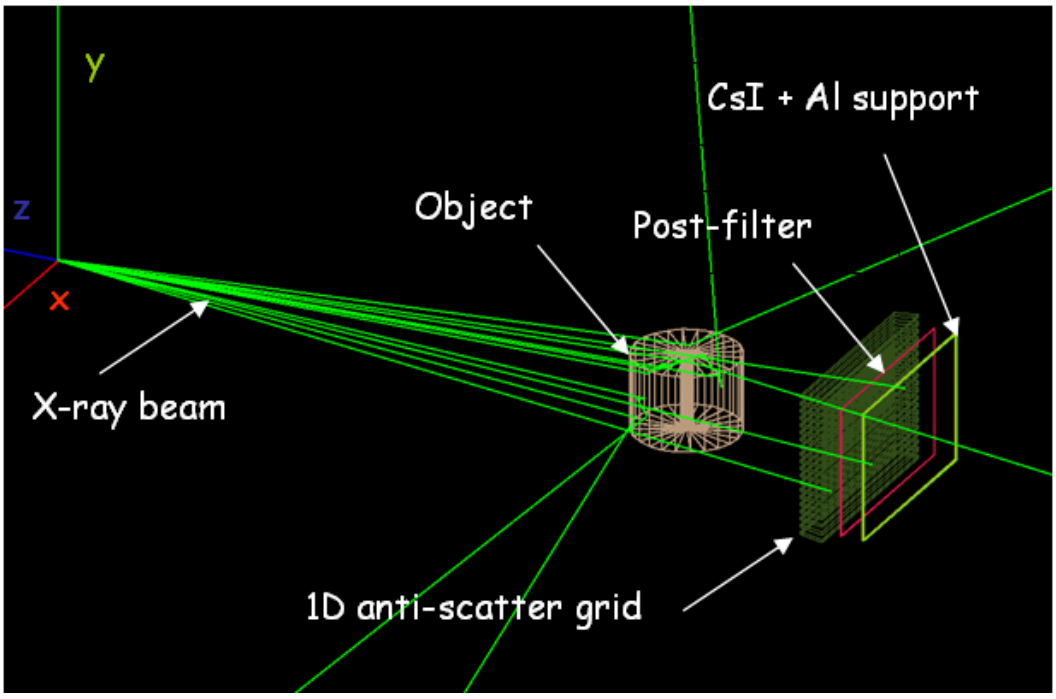

Figure 3.17 Simulation setup obtained with the WIRED software.

Post-filter

The post-filter was simulated as a box of silver 1.0 mm thick with the same front size as the detector using the class G4Box. The source post-filter distance was set to 1461 mm.

Scintillator screen

The scintillator screen was simulated as a bulk material, CsI, with density 4.52 g/cm^3 (table 3.8) using G4Box. The dimensions were 463.7 x 316.8 x 2 mm^3 and the pixel size was 0.96 x 0.96 mm^2, if not otherwise specified. The distance scintillator – source was set to 1500 mm. The support of the scintillator of 1.0 mm of aluminum was created using the class G4Box. The dimensions of the front size were the same as the scintillator screen. The support of the scintillator was placed before the scintillator screen.

Detector box

The detector box was created using *G4Box* in accordance with the dimensions provided by the manufacturer. The back side, lateral sides, top side, and bottom side were created using a 5 mm thick layer of steel, a 3 mm thick layer of lead, and a 3 mm thick layer of steel. Moreover, a detector box where the 3 mm thick layer of steel was absent was also simulated. Implementation of the code can be found in appendix 3.12.

Mirror

The mirror was simulated using the G4Box as a layer of SiO_2 (table 3.8) of dimension 420 x 420 x 3.0 mm^3. It was rotated of 45 degrees with respect to the normal of the CsI. The source-mirror distance was 1788 mm.

3.3 Validation of the MC simulations

This section is based on the papers [30, 33] by the author. Both the validation of the simulation to generate the energy spectrum of the X-ray tube and the simulation of the full CT system against measured data are presented. Moreover, the verification of the hypothesis of the isotropy of the angular distribution of the X-ray spectrum, which was used in the simulation of the full CT system, is described.

The validation of the simulation of the energy spectrum of the X-ray source was performed comparing the shape of the X-ray spectrum measured with the CdTe detector (§ 3.3.1) with the simulated X-ray spectrum. In addition, measured and simulated attenuation curves and first (1^{st} HVL) and second half-value layers (2^{nd} HVL) were compared. Besides, the energy and efficiency calibration of the CdTe detector, the analysis of the spurious detector effects performed with the MC method, and the procedure adopted to correct the *pulse height distribution* are illustrated.

To validate the simulation of the CT system, simulated projections were compared with projections measured with the CT system (§ 3.1.2) for several test objects. The projections of the test objects were acquired with a restrictive source collimator, limiting the beam to approximately 150 x 140 mm^2 at the detector (collimator n° 4 of table 3.3). The whole test object was irradiated by the direct X-ray beam. The intent was to reduce the environmental scatter to a negligible value to compare the measured data with the simulated data. The verification of environmental scatter being negligible using this configuration is also shown.

3.3.1 MC simulations of the X-ray tube spectra

3.3.1.1 Spectral shape

The output of the X-and γ-rays detector "*the pulse height distribution*" needs to be corrected for the different spurious detection effects, such as K-photon escape, Compton photon escape, electron escape, for detector efficiency, dead layers, and geometrical acceptance in order to obtain the incident photon spectrum. The spurious detector effects increase with the incident photon energy and decrease with increasing detector size [37]. Under certain experimental conditions, the detector can be exposed to scattered radiation due to leakage through the X-ray tube housing and to primary beam scattering in the irradiation room. This unwanted radiation is not negligible with respect to the direct beam output when heavy filtration and high energy are used. The contribution of the scattered radiation has to be subtracted from the pulse height

distribution before applying the correction procedure "*stripping procedure*" to obtain the incident photon spectrum.

Stripping procedure

Figure 3.18 illustrates the spectrum of ^{137}Cs obtained with the CdTe detector. The presence of spurious effects below the full energy peak is clearly visible. The spurious effects are due to radiation escaping from the detector or backscattered into it. The amount of spurious effects depends on the detector active volume and its atomic number [38]. To obtain the true spectra a careful analysis to determine the influence of spurious effects on the X-ray detector response is necessary. This analysis is based on the calculation of the radiation transport through the detector and becomes very complex when dealing with radiation that has a continuous energy spectrum. In this case, the only way to perform the analysis is to use a Monte Carlo procedure.

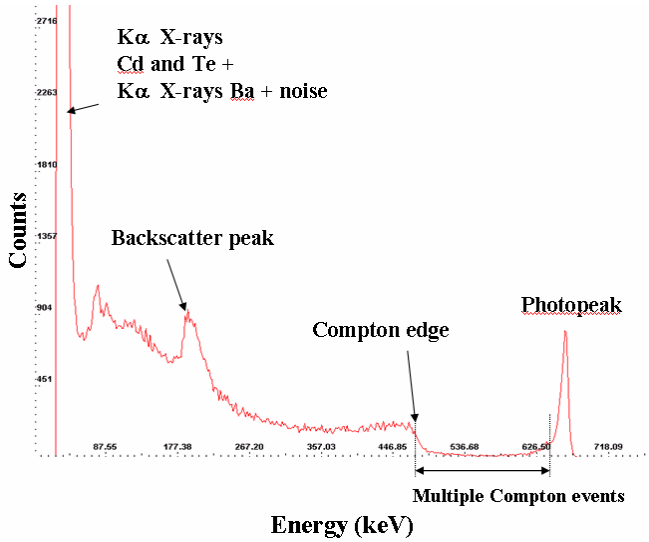

Figure 3.18 Spectrum of ^{137}Cs. The components of the spectrum are highlighted.

The stripping procedure adopted in this thesis work to correct the pulse height distribution consists of two steps. The first step is the subtraction of events due to Compton photon escape (single and multiple), K escape, photoelectron escape, and Compton electron escape. The spurious effects were evaluated by a GEANT4-based simulation. The second step is the correction for photopeak efficiency. The efficiency curve was measured using radioisotopes. The procedure was applied after the subtraction of the contribution of backscattered radiation from the pulse height distribution. The stripping procedure can be expressed by the following equation [39]:

$$N_t(E) = \frac{N_d(E) - N_{spur}(E)}{\varepsilon(E)} \qquad \text{Eq. 3.3}$$

where $N_t(E)$ is the true number of photons of energy E, $N_d(E)$ the number of detected photons with energy E, ε(E) the full energy peak efficiency and $N_{spur}(E)$ the number of spurious effects given by:

$$\begin{aligned} N_{spur}(E) = {} & r_{kCd}(E + k_{Cd}) N_t(E + k_{Cd}) \varepsilon(E + k_{Cd}) \\ & + r_{kTe}(E + k_{Te}) N_t(E + k_{Te}) \varepsilon(E + k_{Te}) \\ & + \sum_{E_o = E_{co}}^{E\max} h_1(E, E_o) N_t(E_o) \varepsilon(E_o) \\ & + \sum_{E_0 = E}^{Eco} h_2(E, E_o) N_t(E_o) \varepsilon(E_o) \end{aligned} \qquad \text{Eq. 3.4}$$

where E_o is the incident energy, $r_k(E_o)$ the ratio between the area of the escape peak and the area of the full energy peak, k_{Cd} the mean energy of the Cd characteristic radiation, k_{Te} the mean energy of the Te characteristic radiation, $h_1(E, E_o)$ the fraction of events at energy E due to single and multiple scattered photon and electron escape with respect to the photopeak events at energy E_o, E_{max} the maximum energy of the spectrum and $h_2(E, E_o)$ the fraction of events at energy E due to photoelectron and multiple scattered photon escape with respect to the photopeak events at energy E_o.

E_{co} is defined by the following equation:

$$E_{co} = \frac{E + \sqrt{E^2 + 2mc^2 E}}{2} \qquad \text{Eq. 3.5}$$

The stripping correction is applied step-by-step, starting from the highest energy of the spectrum.

Spurious effects evaluated by MC simulations

We developed a MC model based on the GEANT4 code to simulate the response of a CdTe detector, whose dimensions were corresponding to those of the detector used for the acquisition of the X-ray spectra of the tube, to incident monochromatic photon beams. Aim of the simulation was the evaluation of Compton photon escape, K escape, photoelectron escape, and Compton electron escape.

Simulation setup

A monochromatic pencil photon beam was sent towards a CdTe detector of dimensions of 5 x 5 x 2.25 mm^3 simulated as a bulk material. The beam was filtered by a 0.25 mm layer of beryllium (figure 3.19). The energy spectrum of the electrons generated by the interaction of the photon beam with the CdTe was retrieved. The

simulation was performed for incident monochromatic photon energies in the energy range [50, 450] keV, with a step size of 50 keV.

Quantities retrieved from the simulation

From each simulated spectrum we calculated the quantities defined in Eq. 3.4 given by the Eq. 3.6-3.9:

$$h_1(E,E_0)\big|_{E_0=350keV} = \frac{N_1(E)}{N_{ph}(E_0)} \qquad \text{Eq. 3.6}$$

$$h_2(E,E_0)\big|_{E_0=350keV} = \frac{N_2(E)}{N_{ph}(E_0)} \qquad \text{Eq. 3.7}$$

$$r_{kCd}(E_0)\big|_{E_0=350keV} = \frac{N_{kCd}}{N_{ph}(E_0)} \qquad \text{Eq. 3.8}$$

$$r_{kTe}(E_0)\big|_{E_0=350keV} = \frac{N_{kTe}}{N_{ph}(E_0)} \qquad \text{Eq. 3.9}$$

where $N_1(E)$ are the events at energy E due to single and multiple scattered photon and electron escape, $N_{ph}(E_o)$ are the photopeak events at energy E_o, $N_2(E)$ are the events at energy E due to photoelectron and multiple scattered photon escape, N_{kCd} are the events under the Cd escape peak, and N_{kTe} are the events under the Te escape peak.

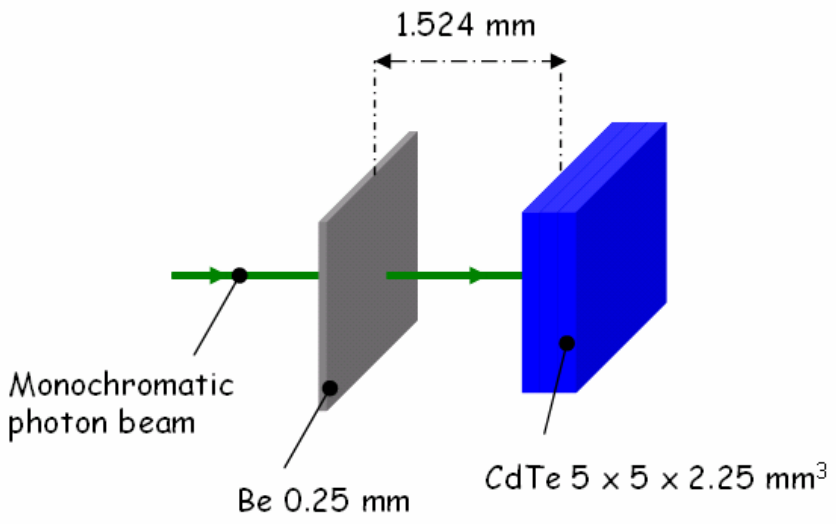

Figure 3.19 Simulation setup for the evaluation of the radiation escaping the CdTe detector. The dimensions and the distances were taken from the manual of the CdTe detector.

Energy and efficiency calibration of the CdTe detector using radioisotopes

The CdTe detector has to be calibrated in energy so that we have a relation between the channels of the MCA and the energy of the photons. To correct the pulse height distribution it is necessary to measure the efficiency curve, which relates the number of pulses counted to the number of photons incident on the detector. The energy and efficiency calibrations involve the acquisition of spectra of radioactive sources emitting X- and γ-rays of known energies and intensities. The sources should emit γ-rays at energies in the range of the unknown spectrum to be measured.

For the calibration we used the γ-rays emitted by ^{57}Co, ^{133}Ba, ^{137}Cs, and ^{241}Am (the decay tables of the radioisotopes can be found in appendix A.2). The gamma sources were provided by the Paul Scherrer Institute (Villigen, Switzerland). The radioisotopes were placed at 82 mm from the front face of the CdTe detector to minimize the geometric errors and the effect of coincidence summing. The peaking time was set to 2.4 μs, the flat top width to 0.2 μs, and the gain to 4.95. The number of channels was set to 1024 and the voltage to 1000 V. The measuring time was adjusted to the intensities of the different sources in a way to get statistical errors of less than 4% for the relevant peaks. The energies and relative intensities of all the suitable γ-rays (relative intensity higher than 3%) emitted from the radioisotopes are listed in table 3.9 [40]. The spectra were acquired with the ADMCA software. The setup of the experiment is shown in figure 3.20.

Table 3.9 Characteristics of the applied radioactive sources and of the suitable gamma-ray lines.

γ-ray source	Half life	γ -ray energy (keV)	Relative intensity
^{57}Co	271.79 d	14.41300	9.16
		122.0614	85.60
		136.4743	10.68
^{133}Ba	10.5 y	80.9971	34.06
		276.398	7.164
		302.853	18.33
		356.017	62.05
		383.851	8.94
^{137}Cs	30.1 y	661.657	85.1
^{241}Am	432.2 y	59.5412	35.9

(a)

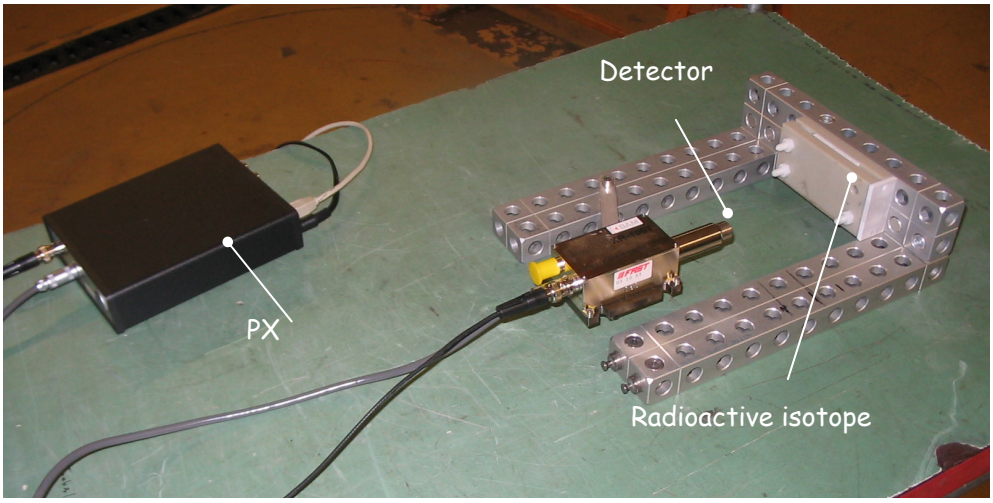

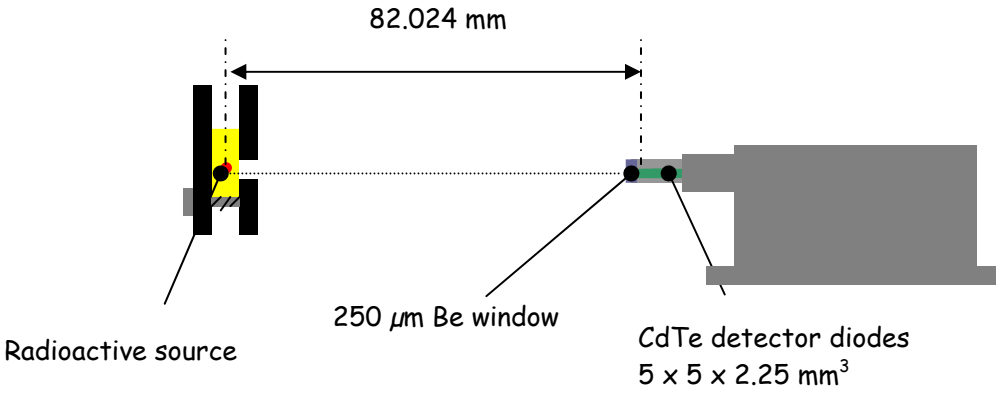

(b)

Figure 3.20 Photo (a) and schematic view (b) of the experimental setup for the energy and efficiency calibration of the CdTe detector.

The peaks listed in table 3.9 were used for the energy calibration, except the peak at 136 keV of the ^{57}Co and the peaks at 81 keV and 384 keV of ^{133}Ba. For each peak we retrieved the peak centroid using the software and assigned it to the known energy of the peak, H_0. The measured data were fitted by a straight line. For each peak we retrieved also the full width at half maximum (*FWHM*) and calculated the relative energy resolution (R) using the formula:

$$R = \frac{FWHM}{H_0} \qquad \text{Eq. 3.10}$$

Figure 3.21 shows the spectrum of ^{137}Cs, where the peak is highlighted in blue. The FWHM and the H_0 of the peak are also illustrated.

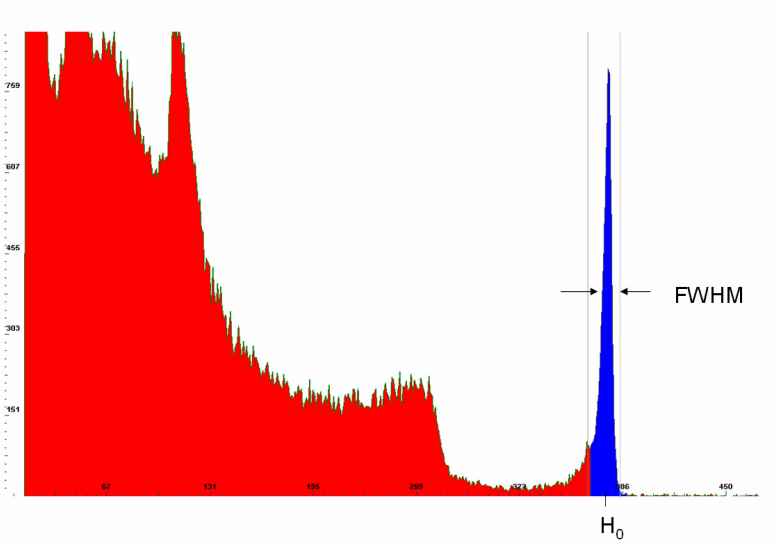

Figure 3.21 Spectrum of ^{137}Cs. The peak is highlighted in blue. FWHM and H_0 of the peak are also illustrated.

To verify the energy calibration we used the peak at 136 keV, the backscatter peak (182 keV) and the Compton edge (480 keV) of ^{57}Co and the peaks at 81 keV and 384 keV of ^{133}Ba.

Once the energy calibration was performed, we retrieved the number of counts in the photopeak (net area), $N_{fullPeak}$, using the ADMCA software for each peak listed in table 3.9. From the relative intensity of the peak (I_γ) and from the activity of the source, the source-detector distance (d) the detector area (a) and the acquisition time (t_{acq}) we calculated the intrinsic peak efficiency ε_{ip} using the formula:

$$\varepsilon_{ip} = \frac{N_{fullPeak}}{\frac{A(t)}{4\pi d^2} a I_\gamma t_{acq}} \qquad \text{Eq. 3.11}$$

Since only those interactions that deposit the full energy of the incident radiation are counted, the ε_{ip} is not sensitive to some perturbing effects like scattering from surrounding objects or spurious noise.

The curve of the intrinsic peak efficiency in function of the incident energy has been used in the stripping procedure to correct the pulse height distribution.

Correction for backscattered radiation

In order to correct for the backscattered radiation we subtracted the net area under the backscattering peak, $I_{backscat}$, from the total sum of counts under the peak in the pulse height distribution (figure 3.22).

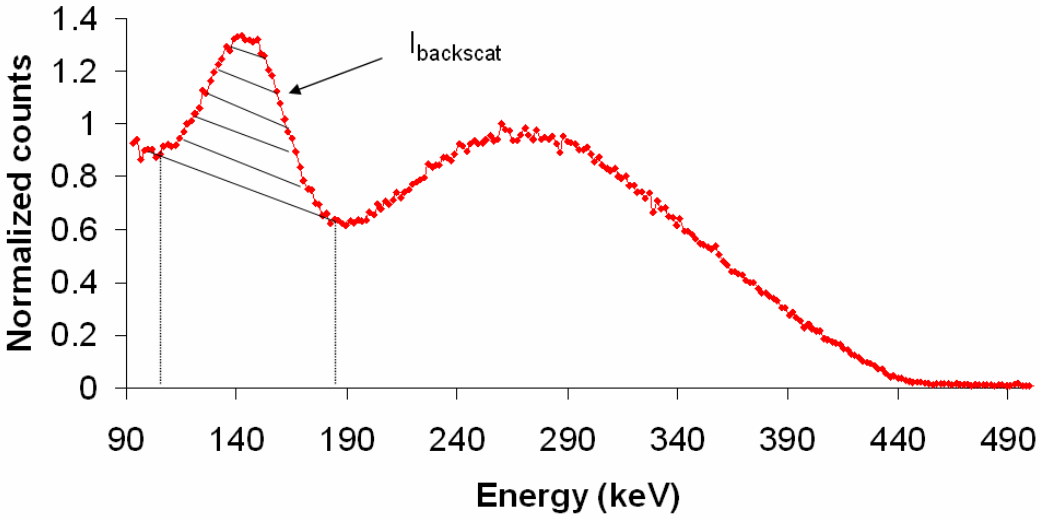

Figure 3.22 Pulse height distribution. The backscatter peak is highlighted.

Setup of the measurements and simulations of the X-ray spectrum

Measurements

X-ray spectra at 350, 400, and 450 kV were acquired with the calibrated CdTe detector. The X-ray source was the MXR-451 tube and the source-detector distance was 1.09 m. The flux of the X-ray tube was reduced using a heavy filtration (4.0 mm W) and the tube current was to set to 0.5 mA to keep the detector pile-up effects at a negligible level. To minimize radiation scattering from various devices and walls around the detector we set the collimator aperture to 6 x 2 mm^2. The photon penetration through the collimator was negligible. A laser point was used to align the detector axis to the X-ray beam. Figure 3.23 shows the experimental setup. The acquired pulse height distributions were corrected for backscattered radiation, spurious detector effects, and detector efficiency to obtain the true X-ray spectra, as explained above.

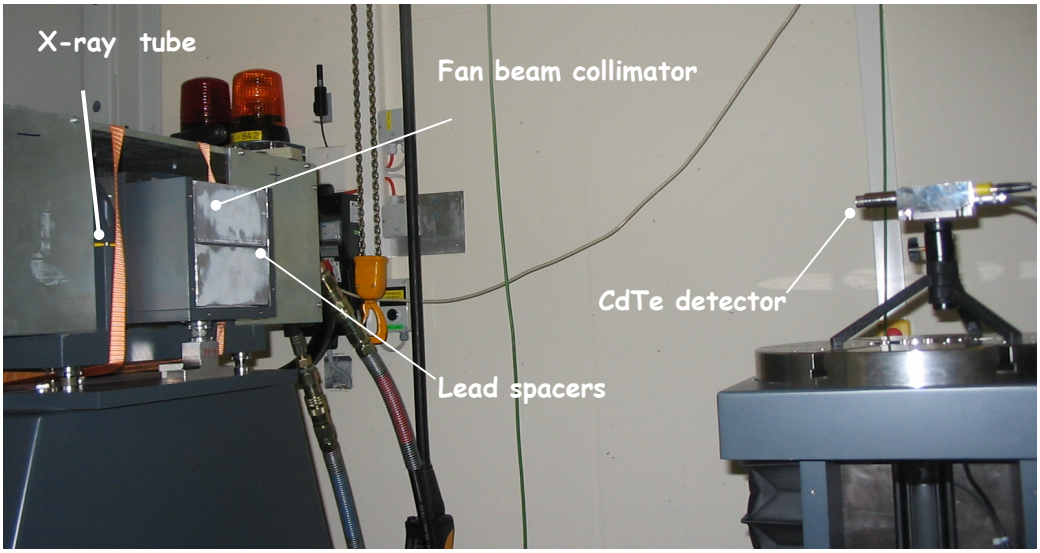

Figure 3.23 Experimental setup for the measurement of the X-ray spectrum.

Simulation

The spectrum of the X-ray tube was simulated as explained in § 3.3.1 with the parameters corresponding to those used in the experiment (inherent filtration: 2.3 mm Fe and 1.0 mm Cu, target angle: 30°, external filtration: 4.0 mm W, electron beam energies: 350, 400, and 450 keV).

The measured and simulated X-ray spectra were normalized by their maximum value.

3.3.1.2 Transmission curves

Measurements

The attenuation curves at 450 kV were measured using a $CdWO_4$ scintillator (dimensions 0.5 x 0.5 x 6 mm^3) coupled to fiber optics. A step wedge made of aluminum of overall dimensions 200 x 200 x 15 mm^3 having forty steps of thickness [5-200] mm (figure 3.24a) and a step wedge made of copper of overall dimensions 50 x 100 x 15 mm^3 having twenty steps of thickness [2.5-50] mm (figure 3.24b) were used. The experiment was carried out in narrow geometry that means that (i) the scattered radiation was prevented from reaching the detector by means of collimators placed in front of the X-ray source and the detector and that (ii) the incident beam could be assumed parallel because of the small angular aperture considered (figure 3.24c). Particular care was paid to minimize radiation scattering from various devices and walls around the detector. The data were fitted using a spline.

(a) 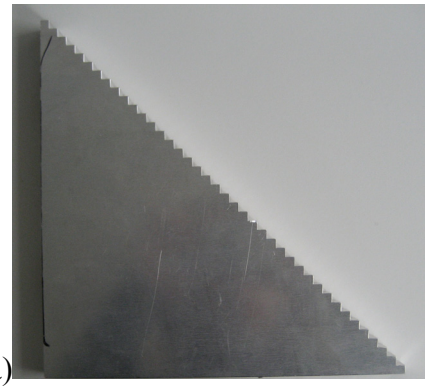 (b) 

(c) 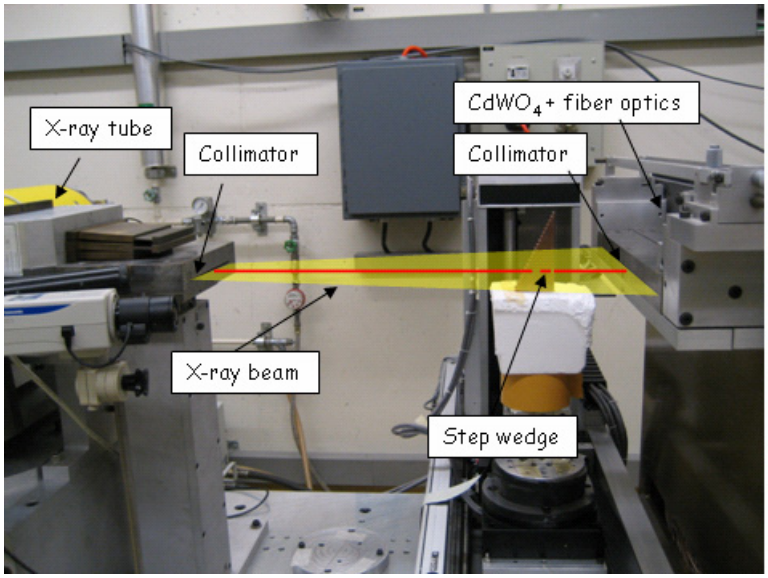

Figure 3.24 (a) Aluminum step wedge. (b) Copper step wedge. (c) Experimental setup. Only the detector along the central line of the beam (red line) was considered. The source-object distance was 945 mm. The object-detector distance was 362 mm.

Simulation

A pencil beam having an energy distribution given by the simulated X-ray spectrum at 450 keV was sent towards a filter. The energy deposited within the detector (CdWO4 of dimensions 0.5 x 0.5 x 6 mm^3) was retrieved. The simulation was run for several thicknesses of the aluminum and copper filters. The assumption of a pencil beam can be made because the experiment was carried out in the narrow geometry.

The 1^{st} and 2^{nd} HVLs were calculated from the measured and simulated attenuation curves.

3.3.1.3 Isotropic angular distribution of the X-ray beam

To verify the hypothesis of isotropic angular distribution, which was used in the simulation of the full CT system, we performed a simulation where we retrieved the X-ray spectrum generated by an electron beam of 450 keV incident on a tungsten target in five regions of the detector (figure 3.25) defined as follows:

- Region 1: $-a < z < a$ and $-d < x < d$
- Region 2: $b < z < c$ and $-d < x < d$
- Region 3: $z > -c$ and $z > -b$ and $-d < x < d$
- Region 4: $\sqrt{z^2 + x^2} < a$
- Region 5: $-d < z < d$ and $-d < x < d$

where a = l* tg (2.5°), b = l* tg (6.5°), c = l* tg (9°), d= l* tg (20°), and l is the distance between the position where the electron beam hits the target and the detector. The parameters of the simulation corresponded to those of the MXR-451 X-ray tube (inherent filtration: 2.3 mm Fe and 1.0 mm Cu, anode angle: 30°).

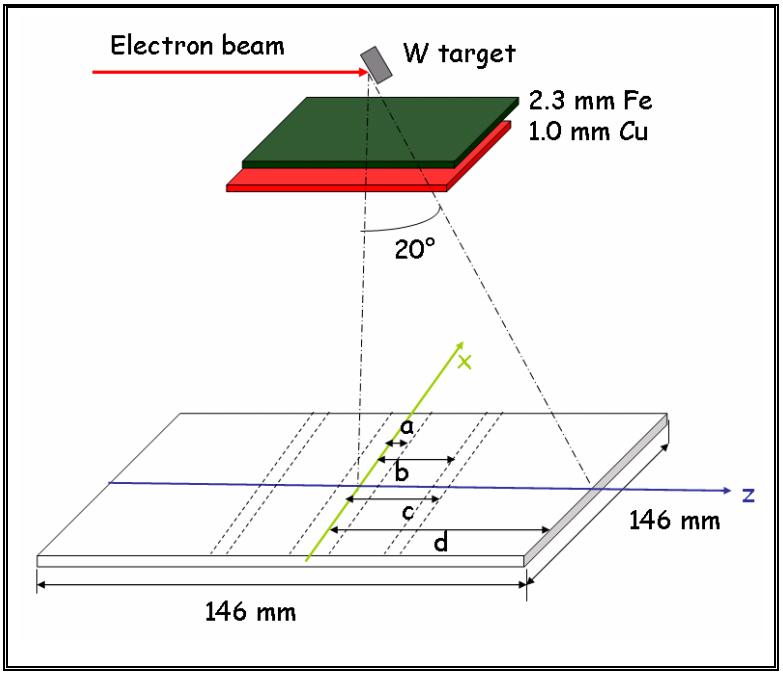

Figure 3.25 Setup of the simulation for the verification of the isotropy of the angular distribution of the X-ray beam. The considered regions of the detector are shown.

3.3.2 MC simulations of the X-ray CT system

To validate the simulation of the CT system we compared the simulated projections with projections measured with the CT system for several test objects. As mentioned in chapter 2 in some experimental conditions scattered radiation generated by the CT system structure and by the walls of the room (environmental scatter) reaches the detector leading to an underestimation of the attenuation. To reduce the environmental scatter to a negligible value we acquired the projections with a source collimator (collimator n° 4 of table 3.3) limiting the beam to 150 x 140 mm^2 at the detector.

Verification of negligible environmental scatter

In order to verify the hypothesis of a negligible environmental scatter for the considered configuration, radiographies with the collimator n° 4 and with a fan collimator (negligible environmental scatter) that limits the vertical aperture of the beam to 33 mm at the detector (n° 7 of table 3.3) were acquired. The X-ray tube was the MXR-451 HP/11/Y. The voltage was set to 450 kV and the current to 3.2 mA. The exposition time was set to 3 sec. A filter of 1.0 mm tungsten was employed. The dynamic range of the CCD camera was set to 12 bits. The projections were acquired without the object being present. The difference of intensity was calculated using the following formula:

$$Diff(x,y) = \frac{I_4(x,y) - I_7(x,y)}{I_7(x,y)} \qquad \text{Eq. 3.12}$$

where $I_4(x,y)$ and $I_7(x,y)$ are the intensities of the radiographic images corresponding to the pixel (x,y) on the detector with the collimator n° 4 and n° 7, respectively.

Setup of the measurements and simulations for the validation

Measurements. The X-ray tube was the MXR-451. The voltage was set to 450 kV and the current to 2 mA. The low energy X-rays were stopped by a filter of 1.0 mm of tungsten. The dynamic range of the CCD camera was set to 12 bits. The post-filter made of silver of 1.0 mm thickness was placed at a distance of 40 mm from the detector. The distance from the rotation axis to the detector plane was 226 mm (figure 3.26).

Test objects. Four test objects were manufactured: (i) an aluminum box of size 50 x 65 x 50 mm^3 with two holes of size 10 x 10 x 50 mm^3 and 8 x 10 x 50 mm^3 along the axial direction with equal distance from the object centre (figure 3.27a), (ii) the aluminum box containing two copper rods (figure 3.27b), (iii) a cylinder made of aluminum with an outer diameter of 66 mm and an inner diameter of 25 mm (small

cylinder) (figure 3.27c), and (iv) a step wedge made of aluminum of overall dimensions 100 x 100 x 20 mm^3 having 5 steps of thicknesses [20 - 100] mm (figure 3.27d).

Simulation. Simulations with parameters corresponding to those used in the experiments were performed. X-ray source, pre-filter, test objects, post-filter, and scintillator were simulated as described in § 3.2.4. The spectrum was simulated with 2 x 10^9 primary electron histories. The projections were obtained with 10^9 primary photon histories.

Evaluation and validation

All the acquired images, $I_{acq}(u, v)$, were normalized to remove some geometric effects and scanner non-uniformity, such as the spatial irregularity of the source radiation and the non-uniformity of the detector response, using the formula:

$$I_{norm}(u,v) = \frac{I_{acq}(u,v) - I_{dark}(u,v)}{I_{air}(u,v) - I_{dark}(u,v)} \qquad \text{Eq. 3.13}$$

where u and v are the detector coordinates, $I_{norm}(u, v)$ is the normalized image, $I_{air}(u, v)$ is the image in absence of the object and $I_{dark}(u, v)$ is the image without X-rays. A 4 x 4 binning was performed on the acquired images.

To quantitatively evaluate the accuracy of the MC simulations we calculated the absolute normalized error (ANE) given by the formula [34]:

$$ANE(x,y) = \left| \frac{I_m(x,y) - I_s(x,y)}{I_m(x,y)} \right| \qquad \text{Eq. 3.14}$$

where x and y are the detector coordinates, $I_m(x, y)$ is the experimental normalized image, and $I_s(x,y)$ is the simulated image.

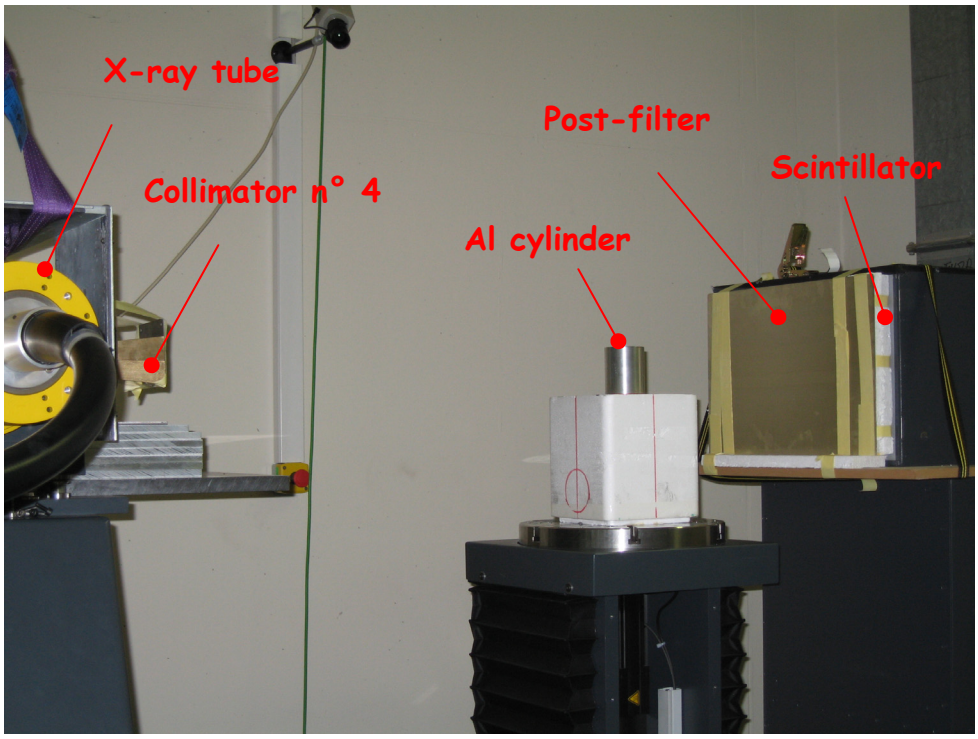

Figure 3.26 Acquisition setup for the validation of the MC simulation of the X-ray imaging system.

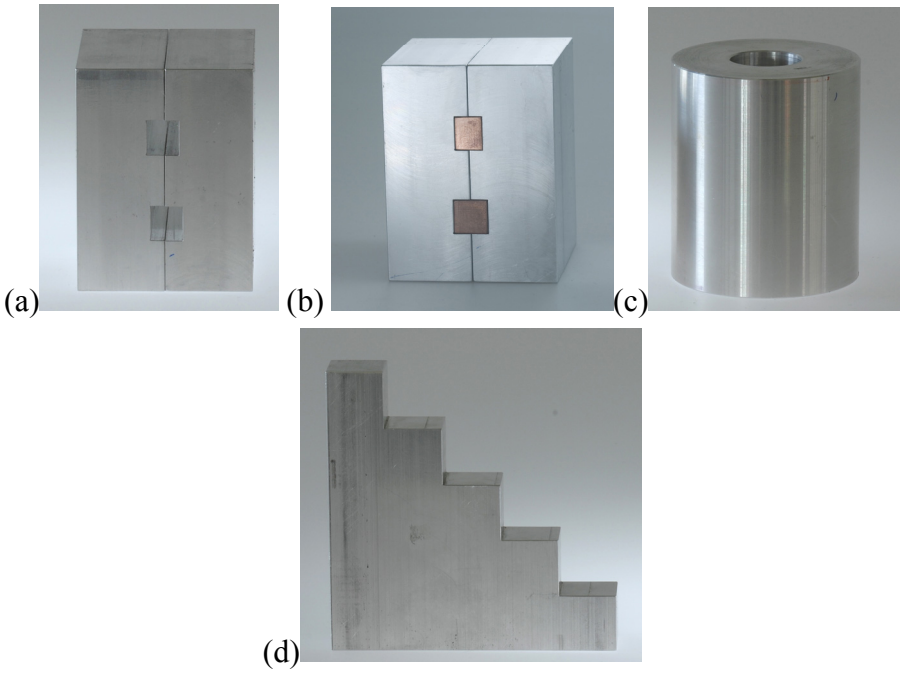

Figure 3.27 Test objects used for the validation of the MC simulatios. (a) Aluminum box. (b) Aluminum box with copper rods. (c) Aluminum cylinder. (d) Aluminum step wedge.

3.4 Optimization and performance of the CT system

In this section, based on the papers and reports [30, 41-43] by the author, we present the optimization of the hardware components of the CT system using MC simulations and the optimization of the scanning settings by means of experimental measurements.

Moreover, the performance of the CT system, optimized using the MC simulations, is shown for several objects (simulating cracks and holes, and real castings) and various configurations.

3.4.1 Optimization of the hardware components of the CT system

As already mentioned, the MC simulation is an excellent tool to optimize the components of a CT system. The evaluation of the response of different scintillator screens and the study of the scattered radiation generated separately by the different components of the CT system are some examples.

Here we studied the response of a scintillator screen of different thicknesses using the validated GEANT4-based MC simulation. In addition, we analyzed the scattering produced by detector box and mirror. The results were used to optimize the hardware of the CT system.

Thickness of the scintillator

The thickness of the scintillator is an important parameter in a CT system, since it is related to the time needed for an acquisition. The acquisition time is a key factor for industrial CT systems, where a series of objects has to be investigated. A thicker screen will produced more light photons because the probability of a photon interacting with it will be higher, hence the exposition time for each projection will be shorter. Here, we analyzed the performance in terms of energy absorbed, hence light photons emitted, of two scintillator screens made of CsI(Tl) having the same area and 1.0 mm and 2.0 mm thickness, respectively, using the validated MC simulation. The contribution of the primary photons and the first, second, and higher order scattering has been retrieved and compared.

Simulation setup

We simulated the MXR-451 X-ray tube with external filtration of 0.7 mm W and an energy of 450 keV, as explained in § 3.2.4.1. The half angle of the X-ray beam was 2.5°. The number of simulated events was $5*10^8$. The object was a hollow cylinder 80 mm high with an outer diameter of 66 mm and inner diameter of 25 mm. The source-object distance was 1250 mm. The post filter was simulated. The detector was CsI

with a thickness of 1.0 and 2.0 mm and a front size of 120 x 120 mm^2. The pixel size was 1 x 1 mm^2.

Scatter radiation from the detector box

The walls of the structure housing the mirror and the CCD camera (detector box) designed by Hans Wälischmiller GmbH were composed of a layer of steel of 3 mm (inner layer), a layer of lead of 3mm, and a layer of steel of 5 mm thickness. Our aim was to optimize the detector box, so that the amount of scattered radiation generated by it was almost negligible. To reach this aim, we performed a simulation with the validated MC code where the detector box was simulated in accordance with the parameters provided by the manufacturer and another simulation where the inner layer of steel of the detector box, which we thought was responsible for the creation of a non negligible amount of scattering, was removed. We compared the projections of the simulations described above with the projection simulated with the same configuration but without detector box.

Simulation setup

The spectrum of the MXR-451 X-ray tube with external filtration of 1.0 mm W and an energy of 450 keV was simulated. The half angle of the X-ray beam was chosen so that the scintillator screen was fully illuminated by the primary beam (11°). The number of simulated events was $2*10^9$.

The collimator n° 1 of table 3.3 corresponding to the configuration where the scintillator is completely irradiated by the X-ray beam was simulated as described in § 3.2.4.3. The object was a step cylinder made of eight aluminum hollow cylinders 20 mm high with inner diameter of 20 mm and outer diameters of 40, 60, 80, 100, 120, 160, 200, and 220 mm, respectively. The source-object distance was 1000 mm. The CsI screen was 463.7 x 316.8 x 2 mm^3 and the pixel size 0.96 x 0.96 mm^2.

Evaluation

Radiographies without the detector box, with the detector box with inner layer, and without inner layer were compared. The radiographic contrast for the different diameters of the object was calculated using the following equation:

$$C^i = \frac{\left\langle I_{SimNorm}(x,y)\right\rangle_{(x,y)\in ROIflat} - \left\langle I_{SimNorm}(x,y)\right\rangle_{(x,y)\in ROIObj}}{\left\langle I_{SimNorm}(x,y)\right\rangle_{(x,y)\in ROIObj}} \qquad \text{Eq. 3.15}$$

where *Obj* is a ROI in the image where the X-ray flux is attenuated by the object and *flat* where is not attenuated.

Scattered radiation from the mirror

We analyzed the contribution of the scattering generated by the mirror placed inside the detector box (simulated without the inner layer) to evaluate whether the contribution of the scattering generated by the mirror was negligible. To this aim, we performed a simulation with the mirror and one without the mirror and we compared the resulting projections. The simulation setup was the same as for the evaluation of the scattered radiation from the detector box except for the source-object distance that in this case was 1107 mm.

3.4.2 Optimization of the CT system settings

The setting of the CT system, which was optimized using the results of the MC simulations described above, was optimized by means of experiments. The figure of merit was the contrast of the reconstructed images. The parameters of the settings investigated were:

- X-ray energy
- Lens aperture and number of projections
- Dynamic range
- Number of averaged frames
- Filtration
- X-ray source collimators
- Lead glass in front of the CCD camera

In addition, we studied the contrast of the reconstructed images in function of the object diameter for a configuration corresponding to a fan beam geometry (only a thin slice of the object is irradiated and the environmental scatter is negligible).

Measurements

The X-ray tube was the MXR-451 HP/11/Y and the voltage was set to 450 kV except for the acquisition of the influence of X-ray energy on contrast where the energy 300 kV was also considered. Due to the higher penetration capability the large focal spot was selected for all scans. The source object distance was 1107 mm. The suitable current (2 mA - 3.3 mA) and integration time (0.5 s – 10 s) were chosen for each studied configuration. The parameters common to all the measurements are

summarized in table 3.10. Table 3.11 illustrates the parameters used for each investigation.

Test object

Aluminum step cylinder 160 mm high with an inner diameter of 20 mm and outer diameters of 40, 60, 80, 100, 120, 160, 200, 220 mm, respectively. Figure 3.28 shows a picture of the test object.

Figure 3.28 Aluminum step cylinder.

Reconstruction

The CT data were reconstructed with the HWM reconstruction software using the standard resolution and a shepp-logan filter.

Evaluation

We considered two positions of the object corresponding to an outer diameter of 160 mm and 120 mm, respectively (figure 3.29a). The contrast of the reconstructed slices was calculated using the following formula:

$$C_{slice} = \frac{\sum_{i=1}^{4} < I(x,y) >_{(x,y)\in ROI_m i} - < I(x,y) >_{(x,y)\in ROI_{air}}}{\sum_{i=1}^{4} < I(x,y) >_{(x,y)\in ROI_m i}} \qquad \text{Eq. 3.16}$$

where $I\ (x, y)$ represents the attenuation of the pixel (x, y) of the reconstructed slice, $ROI_m i$ and ROI_{air} denote a region of interest (ROI) in the reconstructed slice corresponding to material and air, respectively (figure 3.29b).

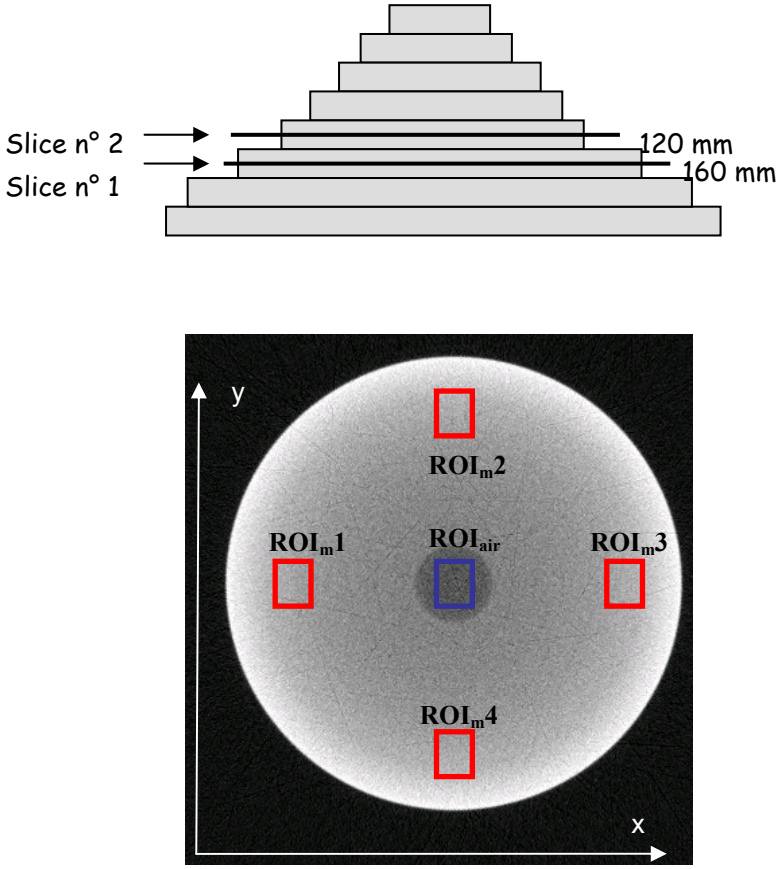

Figure 3.29 (a) Sketch of the aluminum step cylinder where the slice n° 1(outer diameter of 160 mm) and n° 2 (outer diameter of 120 mm) are highlighted. (b) Region of interests of the reconstructed slice used to calculate the contrast.

Table 3.10 Parameters common to all the measurements of the optimization of the CT system setting.

X-ray tube	MXR-451 HP/11/Y
Focal spot size	1.0 mm
Scintillator	2.0 mm CsI
Detector pixels	2184 x 1472
Pixel size projected onto detector plane	0.24 mm
Source-detector distance (mm)	1500
Camera type	Apogee Alta U32
Lens	Linos 25 mm
Binning	1
Source-object distance (mm)	1107
Resolution	standard

Table 3.11 Parameters used for the different investigations.

Influence of	Pre-filter	X-ray source collimator n°	Av. frames	Projections	Lens aperture	Dynamic range (bits)
X-ray energy	none	1	1	720	f/2.8	12
lens aperture and number of projections	none	1	1	360, 720	f/1.6, f/2.8, f/5.6	12
Dynamic range	none	1	1	720	f/2.8	12, 16
Number of averaged frames	none	1	1, 8	720	f/2.8	12
Filtration	W 0.5 mm, W 1.0 mm, Cu 2.0 mm, brass 2.0 mm, none	1	1	720	f/2.8	12
X-ray source collimator	0.5 mm W	1, 2, 5, 6	1	720	f/2.8	12
Lead glass	0.5 mm W	1	1	720	f/2.8	12
Object diameter	1.0 mm W	5	1	720	f/1.6	12

3.4.3 Performance of the CT system

The ability to detect cracks and holes (detector sensitivity) is of primary importance for non destructive testing (NDT) systems. The detection sensitivity of CT systems to a feature of an object depends on several factors: difference in the X-ray attenuation coefficients between the feature and the object, size of the feature, size of the object, dynamic range of the detector, system resolution, and amount of scattering [44]. We qualitatively studied the performance of the X-ray CT system in terms of detection limits when used to determine cracks and holes in steel, aluminum, and iron for different objects and configuration parameters, namely, focal spot size, collimation, resolution, source-object distance, and number of projections. Phantoms simulating cracks and holes as well as real casting parts were used.

Measurements

The X-ray tube was the MXR-451 HP/11/Y and the voltage was set to 450 kV. The large focal spot size (1.0 mm) and the small focal spot size (0.4 mm) were both considered. A filter of 1.0 mm W was employed. A suitable current (1.3 mA - 3.3 mA) and integration time (3 s – 10 s) were chosen for each studied configuration. The lens aperture was f/1.6. The dynamics of the CCD camera was set to 12 bits. The parameters common to all the measurements are summarized in table 3.12. Table 3.13 illustrates the configurations studied for each test object.

Test objects

To study the detection sensitivity of the CT system we investigated phantoms simulating cracks and holes, as well as real castings.

a. Objects manufactured on purpose to simulate:

- Cracks
  - slabs made of steel (St.37-2) of dimension 50 x 25 x 25 mm^3 simulating cracks of 20, 50, 100, and 200 μm (figure 3.30)
  - slabs made of aluminum (Al99.5) of dimension 50 x 25 x 25 mm^3 simulating cracks of 20, 50, 100, and 200 μm
- Holes
  - aluminum ring of diameter 100 mm with holes of several sizes ranging from 0.2 mm to 1.0 mm (figure 3.31)

- aluminum cylinder with a height of 20 mm and a diameter of 80 mm, simulating holes with diameters of 1, 2, 4, and 8 mm (figure 3.32)
- aluminum cylinder with a height of 20 mm and a diameter of 120 mm, simulating holes with diameters of 1 mm, 2 mm, 4 mm and 8 mm (figure 3.33)

b. Real castings:

- Cylinder of a motorcycle made of aluminum with a maximum diameter of 210 mm (figure 3.34a). In order to investigate the detection limits of the CT system for aluminum casts we compared the X-ray images of the object using two different configurations (table 3.13) with a reference image (acquired with a fan beam CT system).
- Automotive part (air suction duct of a turbocharged diesel engine) made of cast iron with a maximum diameter of 140 mm (figure 3.34b). To investigate the detection limits in iron castings we compared the X-ray images of the object using three different source collimators (table 3.13) with a reference image (acquired with a fan beam CT system).

Reconstruction

The CT data were reconstructed with the HWM reconstruction software using a shepp-logan filter. Both the standard and premium resolutions were considered.

Table 3.12 Parameters common to all the measurements of the performance of the CT system.

X-ray tube	MXR-451 HP/11/Y
Pre-filter	1.0 mm W
Energy	450 kV
Scintillator	2.0 mm CsI
Detector pixels	2184 x 1472
Pixel size projected onto detector plane	0.24 mm
Source-Detector distance	1500 mm
Lead glass	No
Camera type	Apogee Alta U32
Lens	Linos 25 mm
Lens aperture	1.6
Dynamic (bit)	12
Number of averaged frame	1
Binning	1

Table 3.13 Parameters used for the acquisitions.

Object	Influence	Setup	Number of proj.	F. spot (mm)	SOD (mm)	Source collimator	Resolution of the reconstruction
Objects simulating cracks	Focal spot size	A	720	0.4, 1.0	1107	4	standard
		B			567	5	premium
		C			567	4	standard
	X-ray source collimator	D	720	1.0	567	4, 5	premium
		E		0.4	567		premium
		F		0.4	1107		standard
		G		0.4	567		premium
	Reconstruction resolution		720	1.0	567	4	standard, premium
	Source-object distance		720	0.4	567, 1107	5	premium
	Number of projections		360, 720, 1440	0.4	567	5	premium
Objects simulating holes	Aluminum ring	A	720	0.4	1107	5	standard
		B	1440		567		premium
	Aluminum cylinder D=80 mm	A	720	0.4	1107	5	premium
		B		0.4	1107	7	
		C		1.0	747	7	
	Aluminum cylinder D=120 mm		720, 1440	1.0	1107	7	premium
Real castings	Cylinder of a motorcycle	A		1.0	1107	5	standard
		B		0.4		7	premium
	Automotive part		720	1.0	1107	2, 5, 8	premium

(a)

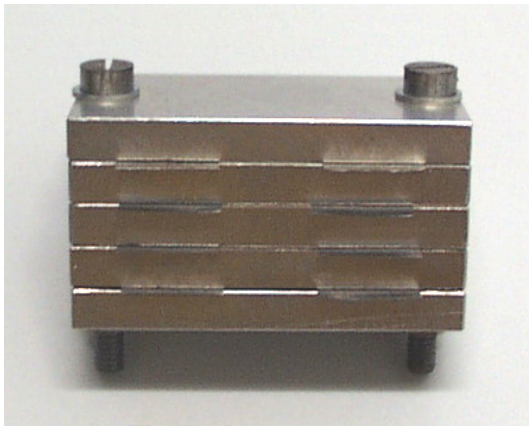

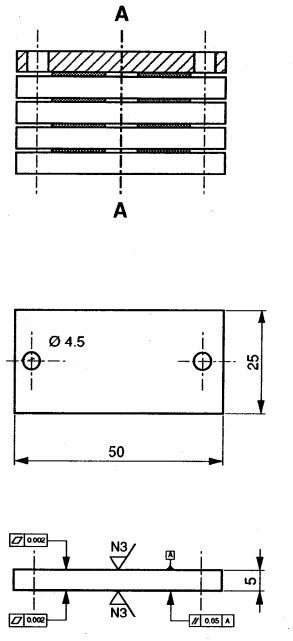

(b)

Figure 3.30 Object simulating cracks (a) and its drawing (b).

(a)

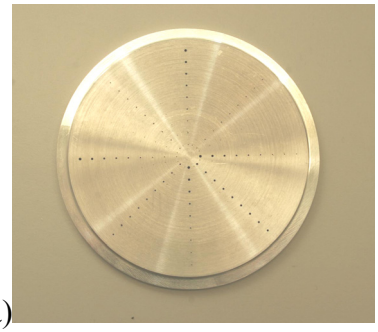

(b)

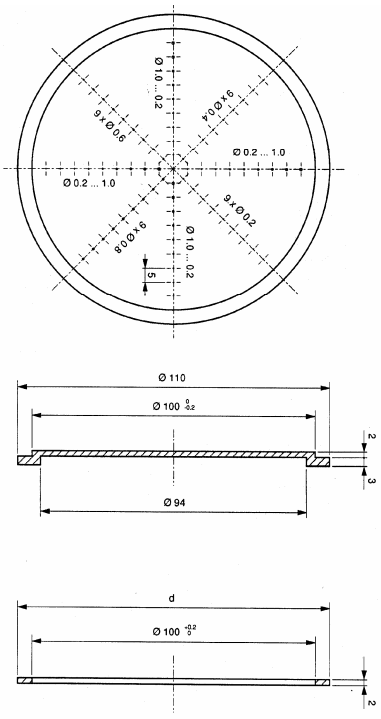

Figure 3.31 Aluminum ring simulating holes (a) and its drawing (b).

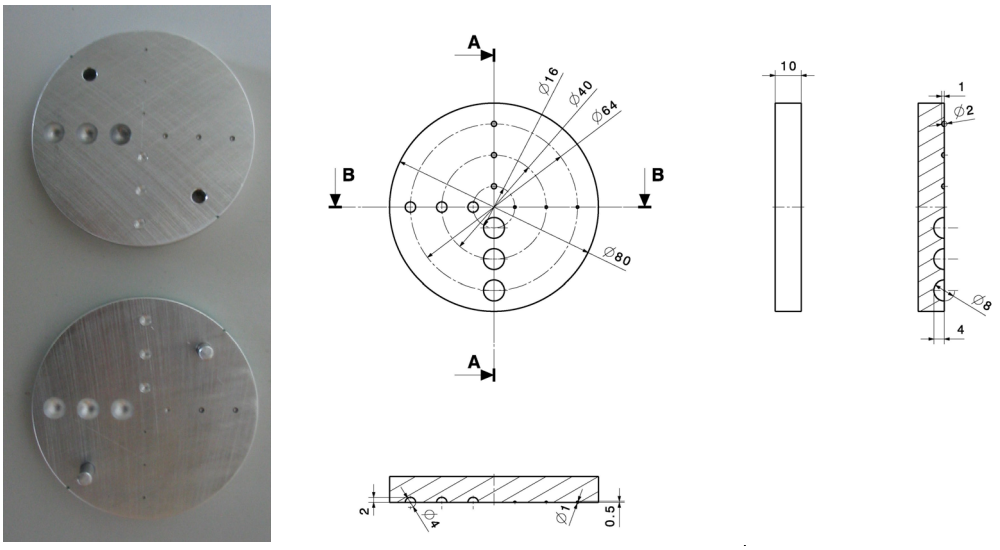

(a) (b)

Figure 3.32 Aluminum cylinder with outer diameter 80 mm simulating holes (a) and its drawing (b).

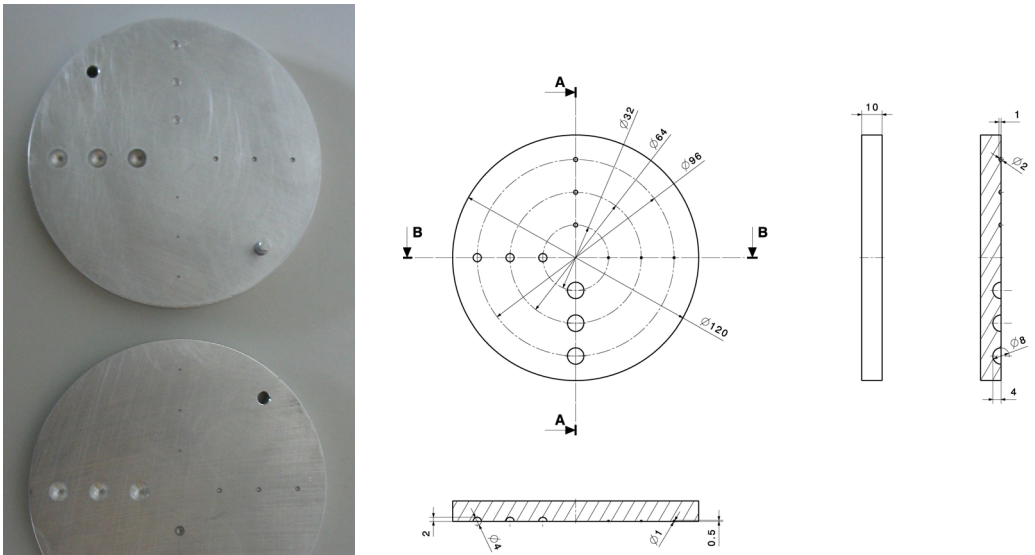

(a) (b)

Figure 3.33 Aluminum cylinder with outer diameter 120 mm simulating holes (a) and its drawing (b).

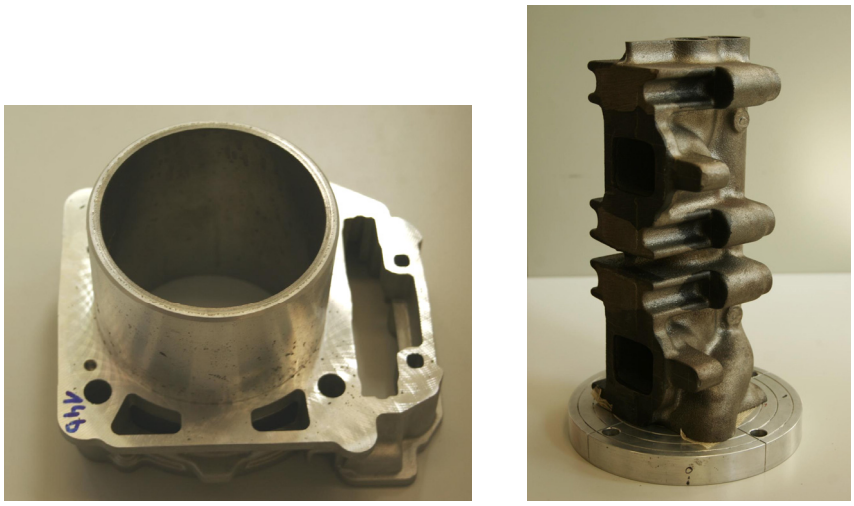

(a) (b)

Figure 3.34 Real castings: (a) Cylinder of a motorcycle, (b) Air suction duct of a turbocharged diesel engine.

3.5 Evaluation of scattered radiation

The evaluation of the scattered radiation generated by the object, the CT system structure, and the walls of the room is a key factor when one wants to correct the reconstructed images for the scattering, as explained in chapter 2.

Here we used the validated MC simulation to study how the different components of the scattered radiation generated by the object contribute to the image formation in function of the object size, shape, and material. Moreover, we studied the environmental scatter in function of beam aperture and object thickness using MC simulations and experimental measurements.

3.5.1 Scattering created by the object

The objects investigated were: (i) hollow aluminum cylinders with a height of 75, 100, 150, and 200 mm, an inner radius of 25 mm, and an outer radius of half of the height placed at a distance of 1000 mm from the source, (ii) aluminum boxes with a front size of 70 x 70 mm^2 and thicknesses ranging from 10 mm to 210 mm in steps of 20 mm placed at a distance of 1107 mm from the source, and (iii) aluminum and copper hollow cylinder with a height of 80 mm, an outer diameter of 66 mm, and an inner diameter of 25 mm placed at a distance of 1274 mm from the source. As X-ray source for the hollow aluminum cylinders the simulated spectrum of the MXR-451 X-ray tube with external filtration of 1.0 mm W and energy of 450 keV was used. The half angle of the X-ray beam was 9°. The detector was 501.1 x 501.1 x 2 mm^3 and the pixel size 1.92 x 1.92 mm^2. The number of simulated events was $2*10^9$. For the Al boxes and for the Al and Cu hollow cylinders with a height of 80 mm we simulated the MXR-451 HP/11/Y X-ray tube with an external filtration of 1.0 mm W and a voltage of 450 kV. The half angle of the X-ray beam was set to 4.3° and to 9°, respectively. The post filter was simulated too. The detector was a CsI screen of dimensions 463.7 x 316.8 x 2 mm^3 and a pixel size of 0.96 x 0.96 mm^2. The number of simulated events was 10^9.

For all the simulations we retrieved the images of the total radiation, primary radiation, first, second, and higher order of scattering. The images were normalized using the following formula:

$$I^{i}_{SimNorm}(x,y) = \frac{I^{i}_{Sim}(x,y)}{\left\langle I^{P}_{Sim}(x,y)\right\rangle_{(x,y)\in flat}}, i = T, P, S1, S2, SH2 \qquad \text{Eq. 3.17}$$

where $I^{i}_{SimNorm}(x,y)$ is the value of the energy deposited within the scintillator corresponding to the detector coordinates (x,y) for the image *i*, where *i* is the total (T), primary (P), first (S1), second (S2) and higher (SH2) order scattering, and *flat* is an ROI in the image where the X-ray flux is not attenuated by the object. The projections of the scattered images were de-noised using the Richardson-Lucy fit.

The corruption of projection data by scattered photons was investigated by calculating the scatter-to-primary ratio for each order of scatter, $SPR_n(x,y)$, defined by:

$$SPR_n(x,y) = \frac{S_n(x,y)}{P(x,y)} \qquad \text{Eq. 3.18}$$

and the total scatter-to-primary ratio, *SPR(x,y)*:

$$SPR(x,y) = \frac{\sum_n S_n(x,y)}{P(x,y)} = \sum_n SPR_n(x,y) \qquad \text{Eq. 3.19}$$

where $S_n(x,y)$ is the value of the scatter radiation of order n at the detector coordinates (x,y) and P(x,y) is the value of primary radiation at the detector coordinates (x,y).

For the hollow Al cylinders we also calculated the degradation of the radiographic contrast *CD* due to the scattered radiation using the equation:

$$CD = \frac{C^P}{C^T} \qquad \text{Eq. 3.20}$$

where C^P and C^T are the radiographic contrasts calculated from the image generated by primary radiation and total radiation, respectively. The radiographic contrast was calculated from the formula:

$$C^i = \frac{\left\langle I^i_{SimNorm}(x,y)\right\rangle_{(x,y)\in flat} - \left\langle I^i_{SimNorm}(x,y)\right\rangle_{(x,y)\in Obj}}{\left\langle I^i_{SimNorm}(x,y)\right\rangle_{(x,y)\in Obj}} \qquad \text{Eq. 3.21}$$

where I^i represents both the image generated by primary and total radiation, *Obj* is a ROI in the image where the X-ray flux is attenuated by the object, and *flat* is an ROI in the image where the X-ray flux is not attenuated by the object. In case of the hollow cylinder with an outer diameter of 200 mm we calculated also the radiographic contrast considering primary radiation plus 1st order of scattering and primary radiation plus 1st and 2nd order of scattering.

3.5.2 Environmental scatter

3.5.2.1 Influence of X-ray beam aperture

In order to investigate the influence of the X-ray beam aperture on the environmental scatter we acquired radiographies of a test object with the CT system using different X-ray source collimators and the X-ray beam not collimated.

Measurements

The X-ray tube was the MXR-451. The tube was set to 450 kV and 2 mA. The low energy of the X-ray tube was cut by a 1 mm thick tungsten filter. The dynamic range of the CCD camera was 12 bits. The post-filter of silver was used. The test object was the aluminum box of size 50 x 65 x 50 mm^3 with two holes of size 10 x 10 x 50 mm^3 and 8 x 10 x 50 mm^3 along the axial direction with equal distance from the object centre (figure 3.27a). The distance from the rotation axis to the detector plane was 226 mm. Radiographies of the test objects with the source collimators n° 1, 2, and 4 of table 3.3 were acquired. In addition, an acquisition without source-collimator was performed.

Evaluation

All the acquired images, $I_{acq}(u, v)$, were normalized using Eq. 3.13. To evaluate the degradation of the image caused by the environmental scatter we calculated the contrast degradation factor, *DFC(n),* from the profiles for each configuration:

$$DFC(n) = \frac{C(4)}{C(n)} \qquad \text{Eq. 3.22}$$

where *n* is the collimator (1, 2, or none) and *C(i)* is the radiographic contrast calculated from Eq. 3.15 where we used the measured projection instead of the normalized simulated projection. The ROI considered was 7 x 7 pixels.

The value of environmental scatter $I_{EnvScatt}$ given by Eq. 3.23, the fraction of environmental scatter on the measured data, and the underestimation of the attenuation due to the environmental scatter given by Eq. 3.24 were calculated.

$$I_{EnvScatt} = \left\langle I / I_o(x,y) \right\rangle_{(x,y)\in ROIObj}\Big|_{Coll.n} - \left\langle I / I_o(x,y) \right\rangle_{(x,y)\in ROIObj}\Big|_{Coll.4} \qquad \text{Eq. 3.23}$$

where I/I_o is the attenuation calculated for the *ROIObj* previously defined.

$$EnvScatt_{Error} = \frac{I_{meas}\big|_{Coll.n} - I_{meas}\big|_{Coll.4}}{I_{meas}\big|_{Coll.4}} \qquad \text{Eq. 3.24}$$

3.5.2.2 Influence of object thickness

In order to study the influence of the object thickness on the environmental scatter, we assumed the amount of environmental scatter for test objects of different thicknesses to be the difference between measured and simulated projections. Here, we present the study for aluminum boxes of thicknesses ranging from 10 to 210 mm for two source collimators (n° 2 and n° 3 of table 3.3) with a CT setting commonly used to investigate industrial samples. The simulated data were retrieved from the simulation of the Al boxes already performed (§ 3.5.1).

Measurements

The X-ray tube was the MXR-451 HP/11/Y and the high voltage was set to 450 kV. The large focal spot (1.0 mm) was used. A suitable current and integration time were chosen for each studied test object. The low energy of the X-ray tube was cut by a filter of 1.0 mm of tungsten. The test objects were aluminum boxes with a front size of 70 x 70 mm^2 and thicknesses ranging from 10 mm to 210 mm in steps of 20 mm. The radiographies of each test object were acquired using the source collimators n° 2, 3, and 4 of table 3.3. The dynamic range of the CCD camera was set to 12 bits. The post-filter of silver was used. The distance from the rotation axis to the detector plane was 393 mm.

Evaluation

To quantitatively evaluate the accuracy of the MC simulations we calculated the root mean square (RMS) of the difference between the experimental projections acquired using the collimator n° 4 and the simulated projections, defined by Eq. 3.25, and we compared the result to the uncertainty σ defined by Eq. 3.26:

$$RMS_A = \sqrt{< \left(I_{Exp}(x,y) - I_{Sim}(x,y)\right)^2 >_{(x,y)\in A}} \qquad \text{Eq. 3.25}$$

$$\sigma_A = \sqrt{< (I_{Exp}(x,y) - < I_{Exp}(x,y) >_{(x,y)\in A})^2 >_{(x,y)\in A}} + \\ + \sqrt{< (I_{Sim}(x,y) - < I_{Sim}(x,y) >_{(x,y)\in A})^2 >_{(x,y)\in A}} \qquad \text{Eq. 3.26}$$

where x and y are the detector coordinates, $I_{Exp}(x, y)$ is the experimental normalized image, $I_{Sim}(x, y)$ is the simulated image, and A is a region of interest.

The value of the environmental scatter was calculated using the formula:

$$I_{EnvScatt} = \left\langle I / I_o(x,y) \right\rangle_{(x,y)\in ROIObj}\Big|_{Meas} - \left\langle I / I_o(x,y) \right\rangle_{(x,y)\in ROIObj}\Big|_{Sim} \qquad \text{Eq. 3.27}$$

where *ROIObj* was the central ROI of 70 x 70 pixels in the shadow of the object. The uncertainty was calculated as the sum of the standard deviations of the ROIs in the experimental and simulated projections. The values of the environmental scatter in function of the object thickness were fitted by a polynomial curve of 5th order:

$$y = ax^5 + bx^4 + cx^3 + dx^2 + ex + f \qquad \text{Eq. 3.28}$$

In case of the configuration with collimator n° 2 the quantity $I_{EnvScatt}/I_{meas}$, representing the fraction of energy deposited by the environmental scatter over the total energy deposited within the detector, was calculated in function of the object thickness. Moreover, to show the contribution of the different components of the measured projection (Eq. 2.15) and their relative importance, we calculated the fraction of primary radiation (signal), environmental scatter, and scatter from the object over the total energy deposited within the detector. The underestimation of the attenuation due to the scattering generated by the object $Error_{ObjScatt}$ and due to the total scattering, object plus environmental scatter, $Error_{ObjScatt+EnvScatt}$ given by Eq. 3.29 and Eq. 3.30, respectively, are also illustrated.

$$Error_{ObjScatt} = \frac{I_{Sim} - I^P_{Sim}}{I^P_{Sim}} \qquad \text{Eq. 3.29}$$

$$Error_{ObjScatt+EnvScatt} = \frac{I_{Meas} - I^P_{Sim}}{I^P_{Sim}} \qquad \text{Eq. 3.30}$$

A comparison of the curves of the environmental scatter in function of the object thickness obtained with collimators n °2 and n° 3 is presented.

3.6 Correction of the scattering in the reconstructed images

As explained previously, the MC simulation enables the evaluation of the scattering in the CT system. Here we evaluated the scattering (from the object and from the CT structure and walls of the room) for a test object and a given configuration and used the information to correct the reconstructed images. The results were compared with the uncorrected CT images of the object.

Setup of the measurements and simulations

Measurements. The X-ray tube was the MXR-451 HP/11/Y. The voltage was set to 450 kV and the current to 2.9 mA. The exposition time was set to 4 sec. The dynamic range of the CCD camera was set to 12 bits. The data were acquired with 720 single-frame projections. The large focal spot (1.0 mm) was used. The low energy of the X-ray tube was cut by a filter of 1.0 mm of tungsten. The collimator n° 1 of table 3.3 was employed. The test object was a hollow aluminum cylinder with a height of 130 mm, an outer diameter of 180 mm, and an inner diameter of 20 mm. The source-object distance was 1107 mm. The post-filter was used.

Simulation. Simulations with parameters corresponding to those used in the experiments were performed. X-ray source, pre-filter, test object, post-filter, and scintillator were simulated as described in § 3.2.4. The half angle of the X-ray beam was set to 9°. The dimensions of the detector were 463.7 x 316.8 x 2 mm^3 and the pixel size was 0.96 x 0.96 mm^2. Because of the invariance of the object with respect to rotation, it was sufficient to simulate one projection. The projection was obtained with 2 x 10^9 primary photon histories.

Reconstruction and correction

The CT data were reconstructed with the statistical algorithm patented by Empa. The voxel size was 0.37 x 0.37 x 0.37 mm^3. The CT data were corrected for the scattering using the projections of 1^{st}, 2^{nd}, and higher than 2^{nd} order of scattering generated by the object (Eq. 3.17) and the scattering from the CT system structure and the walls of the room (Eq. 3.27) obtained with the developed MC simulation. The beam hardening was corrected using the algorithm developed by Dr. R. Thierry, Empa [9] using the simulated X-ray spectrum of the source.

3.7 Anti-scatter grids

3.7.1 Optimization of anti-scatter grids

The GEANT4-based MC simulation was used to study and optimize 2D and 1D anti-scatter grids for industrial CT systems working at 450 kV. The performance of the anti-scatter grids was evaluated for an object that resembles the objects commonly investigated with industrial CT systems, namely, a hollow aluminum cylinder of outer diameter 200 mm, inner diameter 50 mm and height 200 mm.

Associated with the design of an anti-scatter grid there are three geometrical parameters, namely, the height, *h*, of the strips made of absorbing material, the thickness, *d*, of the strips, and the thickness, *D*, of the interspace (figures 4.15 and 4.16). An additional parameter, the grid ratio, defined as the ratio between h and D is also commonly used [45].

The quantities retrieved by the MC simulation were the energy deposited within the scintillator by primary photons and the energy deposited by scattered photons. With primary photons we refer to the photons whose energy at the surface of the scintillator was equal to their initial energy.

2D anti-scatter grids

We simulated the MXR-451 X-ray tube with an external filtration of 0.7 mm W and an energy of 450 keV. The half angle of the X-ray beam was 5°. The number of simulated events was 10^7. The source-object distance was set to 1250 mm. The post-filter was simulated.

2D parallel anti-scatter grid

2D parallel anti-scatter grids made of gold with thicknesses of the interspace *D* equal to 0.3, 0.45, 0.6, and 1.2 mm, thickness of the strips d equal to 1/3 of D, and heights of the strips h equal to 1, 3, 5 mm were studied. A grid with D 0.6 mm, d 0.2 mm, and h 10 mm was also studied. In addition, grids made of lead with D 1.2 mm, h 1, 3, and 5 mm, and d 1/3 of D were evaluated.

2D focused anti-scatter grid

2D focused anti-scatter grids made of gold with D equal to 0.45, 0.6, 1.2, and 2.4 mm, d equal to 1/3 of D, and h equal to 15 mm were considered. A grid with D equal to 0.6 mm and h ranging from 1 to 10 mm was also studied. In addition, a grid with D 0.45 mm, d 0.15 mm, and height 5 mm was evaluated.

Grids made of LaserFormST-100 (table 3.8) with D 2.4 mm, h 15 mm, and d 1/3 of D were considered. Anti-scatter grids made of LaserFormST-100 were considered because of the characteristics of the material that enables the manufacturing of grids of large dimensions (+20 cm) with small D and d.

1D focused anti-scatter grid

We simulated the MXR-451 HP/11/Y X-ray tube with an external filtration of 1.0 mm W and an energy of 450 keV. The half angle of the X-ray beam was 9°. The number of simulated events was 10^6. The source-object distance was set to 1000 mm. The thicknesses of the tungsten strips were ranging from 1 to 10 mm, the grid ratio from 4/3 to 32, and heights of the strips from 5 to 50 mm. The anti-scatter grids were assumed to be composed of bare absorbing material strips without supporting material. This approximation is valid because the material and parameters of the studied grids allow the construction of a grid composed of strips fixed at the extremities on a metallic frame out of the primary beam.

Evaluation and validation

The influence of the grid parameters on the transmittance of primary radiation T_p and the transmittance of scattered radiation T_s defined by Eq. 3.31 and Eq. 3.32 was studied [46].

$$T_p = \frac{E_G^P}{E^P} \qquad \text{Eq. 3.31}$$

where E^P_G and E^P are the energies absorbed within the detector due to primary radiation with and without the grid, respectively, when the incident radiation is kept constant.

$$T_s = \frac{E_G^S}{E^S} \qquad \text{Eq. 3.32}$$

where E^S_G and E^S are the energies absorbed in the detector due to scattered radiation with the grid and without the grid, respectively.

For 2D anti-scatter grids the performance was evaluated in terms of selectivity defined as [46]:

$$\Sigma = \frac{T_p}{T_s} \qquad \text{Eq. 3.33}$$

The performance of 1D anti-scatter grids was evaluated in terms of scatter-to-primary ratio (SPR) and acquisition time factor. The SPR represents the amount of energy

deposited by the scattered radiation (noise) with respect to the one deposited by the primary radiation (signal). The acquisition time factor is defined as the factor by which the acquisition time is increased so that the amount of the energy deposited by the primary radiation remains the same as the one without the grid. The acquisition time is a key factor for industrial CT. We have to find a compromise between the SPR and the acquisition time factor. Moreover, we have to take into account that the strips will bend if their thickness is too low.

In case of 1D anti-scatter grids, we evaluated the amount of energy deposited within the scintillator by the photons scattered by the grid or passing through it without interacting.

3.7.2 Efficiency of the anti-scatter grid

A focused 1D grid made of tungsten with parameters optimized by the MC simulation was manufactured. Here we illustrate the improvement due to the use of the anti-scatter grid in the reduction of the scattering on reconstructed images of a test object.

Measurements

The X-ray tube was the MXR-451 HP/11/Y and the voltage was set to 450 kV. The large focal spot (1.0 mm) was used. The low energy of the X-ray tube was cut by a filter of 1.0 mm of tungsten. Tomographic data of a hollow aluminum cylinder of height 130 mm, inner diameter of 20 mm, and outer diameter of 180 mm were acquired using 720 single-frame projections. The data were acquired using the collimators n° 3 of table 3.3. The dynamic range of the CCD camera was set to 12 bits. The post-filter of silver was used. The distance between the backside of the anti-scatter grid and the source was 1390 mm. The distance from the rotation axis to the detector plane was 393 mm.

Reconstruction

For the reconstruction we used the statistical algorithm developed at Empa without beam hardening correction. The voxel size of the reconstructed volume was 0.742 x 0.742 x 0.742 mm^3.

Evaluation

The reconstructed images acquired with and without the anti-scatter grid were compared. In addition the contrast of the CT images was calculated using Eq. 3.16.

3.8 Complex objects

An important feature of the developed MC code is the possibility of simulating real objects (i.e. cylinder heads) described by STL-files.

Here, we show the images of the energy deposited by the primary radiation and by the primary plus scattered radiation for a test case. The code for reading, writing and converting STL-files that we used has been developed at Empa by J. Hofmann. The code is based on the class *G4TessellatedSolid* (§ 3.2.4) [28].

Simulation setup

The spectrum of the MXR-451 X-ray tube with an external filtration of 1.0 mm W and a voltage of 450 kV was simulated. The half angle of the X-ray beam was set to 5°. The object, described by an STL-file, was a T-shaped object with several holes with a diameter of 13 mm made of aluminum (figure 3.35). The distance source-object was 1107 mm. The post filter was simulated. The detector size was 463.7 x 316.8 x 2 mm^3 and the pixel size was 0.96 x 0.96 mm^2. The number of simulated events was $7*10^8$.

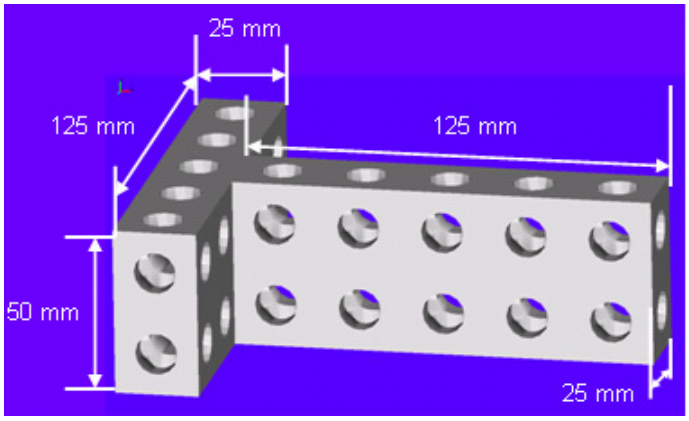

Figure 3.35 Image of the object obtained from the STL file.

3.9 References

1. Knoll, G.F., *Radiation detection and measurement*, ed. Second. 1989: John Wiley & Sons, Inc.
2. Redus, R.H., A. Huber, and T. Pantazis, *Multielement CdTe Stack Detectors for Gamma-Ray Spectroscopy.* IEEE Trans. Nucl. Sci., 2004. **51**(5): p. 2386.
3. *www.amptek.com.*
4. *www.osha.gov.*
5. Feldkamp, L.A., L.C. Davis, and J.W. Kress, *Practical Cone-Beam Algorithm.* Journal of the Optical Society of America a-Optics Image Science and Vision, 1984. **1**(6): p. 612-619.
6. www.hwm.com.
7. Thierry, R., *A Statistical Beam Hardening Correction for polychromatic X-ray CT device, PATENT 246/06, 2006*.
8. Hudson, H.M. and R.S. Larkin, *Accelerated Image-Reconstruction Using Ordered Subsets of Projection Data.* Ieee Transactions on Medical Imaging, 1994. **13**(4): p. 601-609.
9. Thierry, R., et al., *Statistical Beam-Hardening Correction for Industrial X-ray Computed Tomography.* Conference Proceedings We.3.7.2, ECNDT, Berlin (D), 2006.
10. Thierry, R., *Simulation of first-order scattering in X-ray Imaging: application to cone-beam CT".* Conference Proceedings, 8th XTOP, Baden-Baden (D), 2006.
11. Thierry, R., et al., *Hybrid simulation of projections in Industrial X-ray Cone Beam Computed Tomography.* Conference Proceedings, DIR2007, Lyon (F), 2007.
12. Thierry, R. and A. Miceli, *A rapid estimation of photon scattering in X-ray Images*. 2007.
13. Thierry, R., Miceli, A., Hofmann, J., Flisch, A., Sennhauser, U., *Hybrid Simulation of Scatter Intensity in Industrial Cone Beam Computed Tomography.* Nuclear Instruments & Methods in Physics Research Section A, 2007(Submitted).
14. Boone, J.M. and J.A. Seibert, *An Analytical Model of the Scattered Radiation Distribution in Diagnostic-Radiology.* Medical Physics, 1988. **15**(5): p. 721-725.
15. Honda, M., K. Kikuchi, and K.I. Komatsu, *Method for Estimating the Intensity of Scattered Radiation Using a Scatter Generation Model.* Medical Physics, 1991. **18**(2): p. 219-226.
16. Kyriakou, Y., T. Riedel, and W.A. Kalender, *Combining deterministic and Monte Carlo calculations for fast estimation of scatter intensities in CT.* Physics in Medicine and Biology, 2006. **51**(18): p. 4567-4586.
17. Agostinelli, S., et al., *GEANT4-a simulation toolkit.* Nuclear Instruments & Methods in Physics Research Section a-Accelerators Spectrometers Detectors and Associated Equipment, 2003. **506**(3): p. 250-303.
18. Allison, J., et al., *Geant4 developments and applications.* Ieee Transactions on Nuclear Science, 2006. **53**(1): p. 270-278.

19. Apostolakis, J., et al., *GEANT4 Low energy electromagnetic models for electrons and photons.* INFN/AE-99/18, 1999.
20. *http://www.ge.infn.it/geant4/events/nss2004/geant4course.html.*
21. Giani, S., *Physics simulation software and applications to detectors.* Troisieme cycle de la physique en suisse romande, 2005.
22. James, F., *A Review of Pseudorandom Number Generators.* Computer Physics Communications, 1990. **60**(3): p. 329-344.
23. *Physics Reference Manual.* Geant4 Users' Documents Version: Geant4 8.2 December 2006 2006
24. Geant4-Collaboration, *Geant4 User's Guide for Application Developers.*
25. *http://reat.space.qinetiq.com/gps/gps_sum_files/gps_sum.htm.*
26. *http://www.esa.int/esaCP/index.html.*
27. *http://www.nist.gov/srd/online.htm.*
28. Geant4-Collaboration, *Geant4 User's Guide for Application Developers, Version: geant4 8.3.* 2007.
29. *http://www.ge.infn.it/geant4/training/portland/basicStructure.pdf.*
30. Miceli, A., et al., *Monte Carlo simulations of a high-resolution X-ray CT system for industrial applications.* Nuclear Instruments & Methods in Physics Research Section A, 2007. **583**(2/3): p. 313-323.
31. Thierry, R., Miceli, A., Sennhauser, U., Flisch, A., *A rapid estimation of photon scattering in X-ray Images, PATENT EP 07 012 409.4, 2007.*
32. *http://www-unix.mcs.anl.gov/mpi/.*
33. Miceli, A., et al., *Comparison of simulated and measured spectra of an industrial 450 kV X-ray tube.* Nuclear Instruments & Methods in Physics Research Section a-Accelerators Spectrometers Detectors and Associated Equipment, 2007. **580**(1): p. 123-126.
34. Colijn, A.P., et al., *Experimental validation of a rapid Monte Carlo based micro-CT simulator.* Physics in Medicine and Biology, 2004. **49**(18): p. 4321-4333.
35. *http://geant4.slac.stanford.edu/g4cd/March2004/Documentation/.*
36. *http://www.slac.stanford.edu/BFROOT/www/Computing/Graphics/Wired/.*
37. Seelentag, W.W. and W. Panzer, *Stripping of X-Ray Bremsstrahlung Spectra up to 300-Kvp on a Desk Type Computer.* Physics in Medicine and Biology, 1979. **24**(4): p. 767-780.
38. Pani, R., R.F. Laitano, and R. Pellegrini, *Diagnostic-X-Ray Spectra Measurements Using a Silicon Surface-Barrier Detector.* Physics in Medicine and Biology, 1987. **32**(9): p. 1135-1149.
39. Laitano, R.F., R. Pani, and R. Pellegrini, *Determination of X-Ray-Spectra and of the Scattered Component up to 300 Kv.* Medical Physics, 1991. **18**(5): p. 934-938.
40. Ekström, L.P. and R.B. Firestone, *WWW Table of Radioactive Isotopes* 1999.
41. Miceli, A. and A. Flisch, *Study on how the scan parameters influence the detection limits of 3D-CT scans* DETECT project - Deliverable report D4.3 2007.

42. Miceli, A., et al., *Study on how the scan parameters influence the accuracy of 3D-CT scans* DETECT project - Deliverable report D4.2 2007.

43. Miceli, A., et al., *MC simulation for estimation of scatter intensities in a cone-beam CT system employing a 450 kV X-ray tube.* 4th International Workshop NDT in Progress, November 05-09, Prague, Czech Republic, 2007.

44. Gopalsami, N., P. Rizo, and W.A. Ellingson, *Detection sensitivity of X-ray CT imaging for NDE of green-state ceramics.* Argonne National Laboratory report ANL/CP-72955, 1991.

45. Chan, H.P. and K. Doi, *Investigation of the performance of antiscatter grids: Monte Carlo simulation studies.* Phys.Med.Biol., 1982. **27**(6): p. 785-803.

46. Kalender, W., *Calculation of x-ray grid characteristics by Monte Carlo methods.* Physics in Medicine and Biology, 1982. **27**(3): p. 353-361.

4 Results and Discussion

4.1 Validation of the MC simulations

4.1.1 MC simulations of the X-ray tube spectra

4.1.1.1 Spectral shape

Spurious effects of the detector evaluated by MC simulations

Figure 4.1 shows the simulated pulse height distribution of the CdTe detector (see § 3.3.1.1) for a monoenergetic incident photon energy of 350 keV. The Compton edge at 202 keV, the multiple scattering region, the escape peak of the Te at 323 keV, the escape peak of the Cd at 327 keV, and the photopeak at 350 keV are highlighted.

Figures 4.2-4.4 show the quantities $h_1 (E, E_0)$, $h_2 (E, E_0)$, r_{kCd} and r_{kTe}, respectively, defined in § 3.3.1. They are calculated from the simulated pulse height distributions of the incident monoenergetic photons. The data were interpolated with splines. Those quantities were used to calculate the number of spurious effects given by Eq. 3.4.

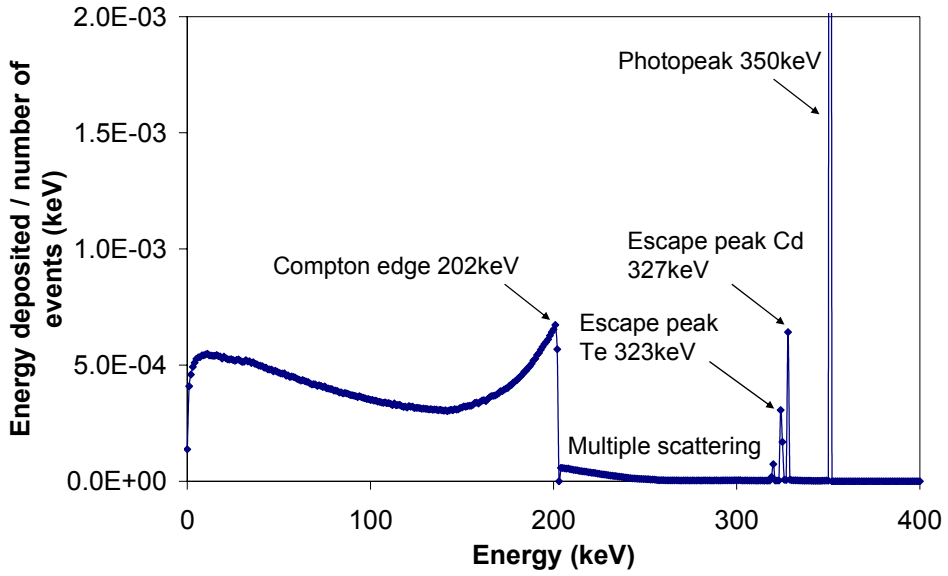

Figure 4.1 Simulated spectrum of a monochromatic photon beam of 350 keV interacting with the CdTe detector. The energy bin is 1 keV.

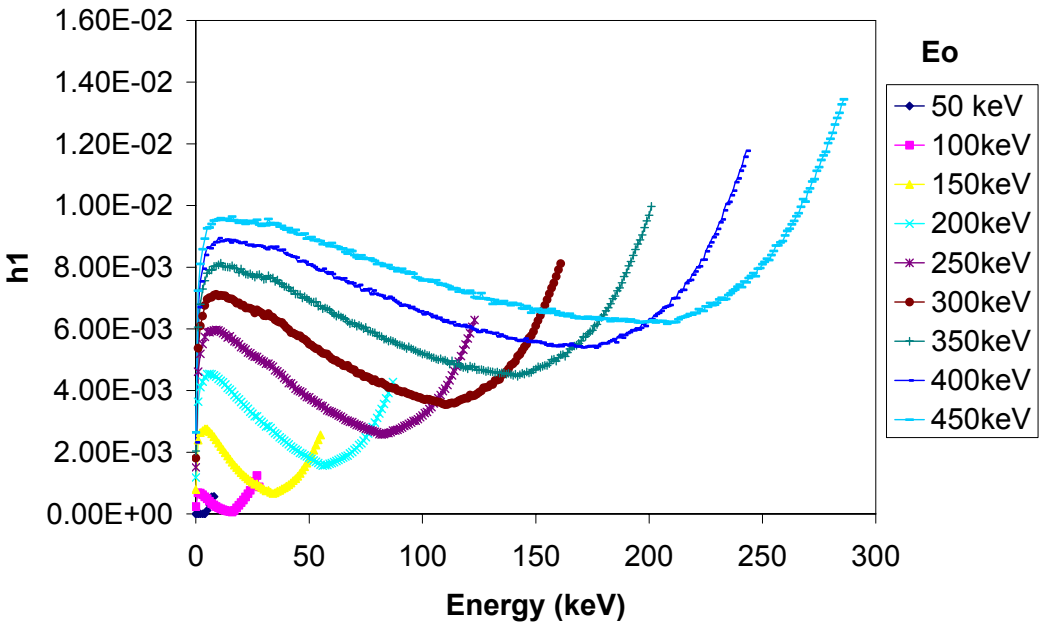

Figure 4.2 Fraction of events at energy E due to single and multiple scattered photon and electron escape with respect to the photopeak events at energy Eo calculated from the simulation of the CdTe detector. This quantity is defined in the region [0, Compton edge].

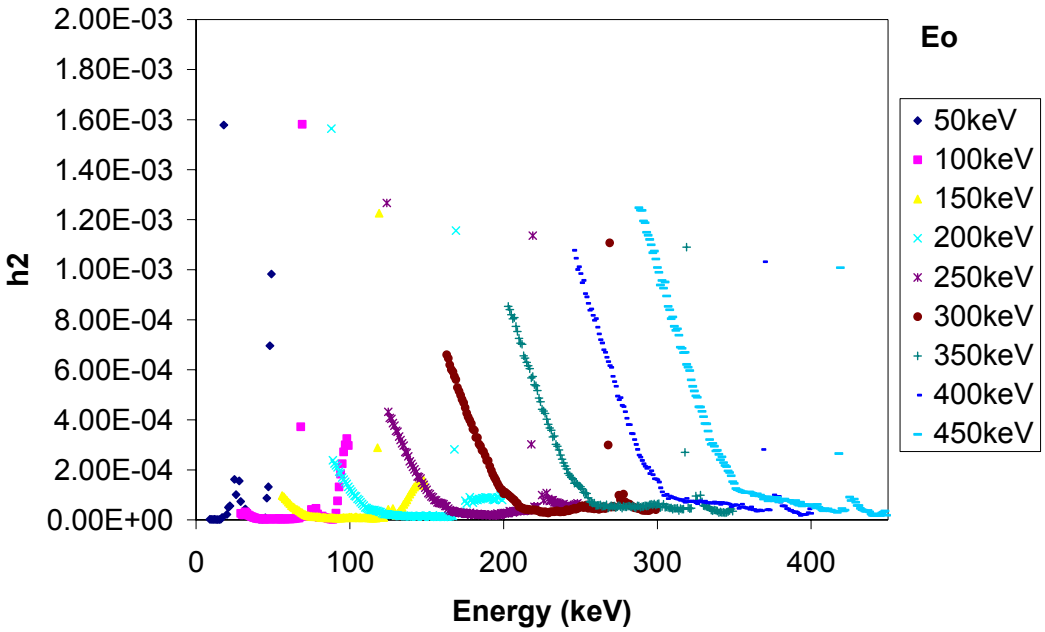

Figure 4.3 Fraction of events at energy E due to photoelectron and multiple scattered photon escape with respect to the photopeak events at energy Eo calculated from the simulation of the CdTe detector. This quantity is defined in the region [Compton edge, E_0]

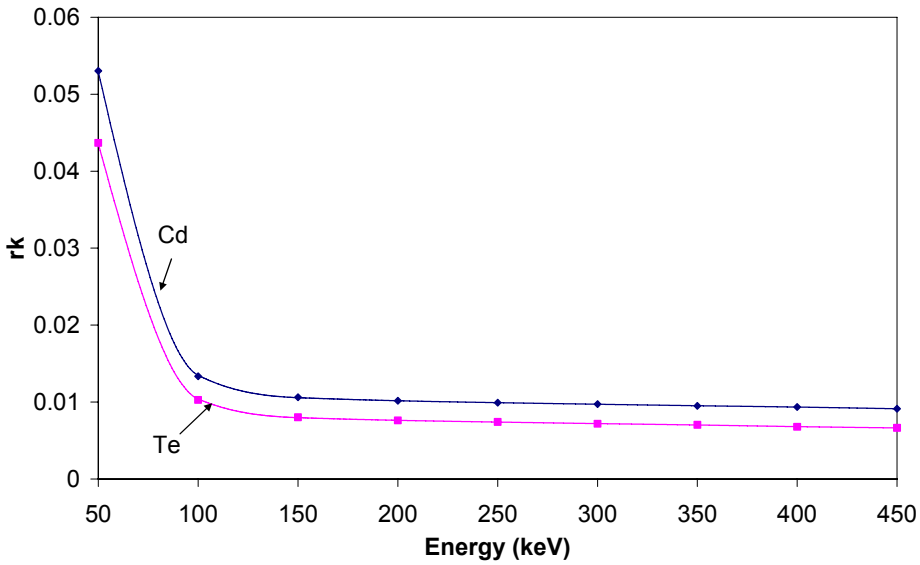

Figure 4.4 Ratio between the area of the escape peak to the area of the full energy peak for the Cd and Te calculated from the simulation of the CdTe detector. This quantity is defined in the region [0, 450] keV.

Energy and efficiency calibration of the CdTe detector

The energy calibration curve obtained using the gamma-rays emitted in the decays of ^{57}Co, ^{133}Ba, ^{137}Cs, and ^{241}Am is shown in figure 4.5. The measured points were fitted by a linear polynomial curve. The energy resolution of the CdTe detector calculated from Eq. 3.10 is displayed in figure 4.6; its value ranges from 5 to 7 keV depending on the energy. Figure 4.7 illustrates the experimental measurements of the full-energy peak efficiency of the CdTe detector calculated from Eq. 3.11. The measured points were fitted by a spline. From the figure it can be seen that the full-energy peak efficiency decreases dramatically with the energy: at 60 keV it is 75%, at 140 keV 40%, at 360 keV 3.4 % and at 660 keV 0.6 %, respectively.

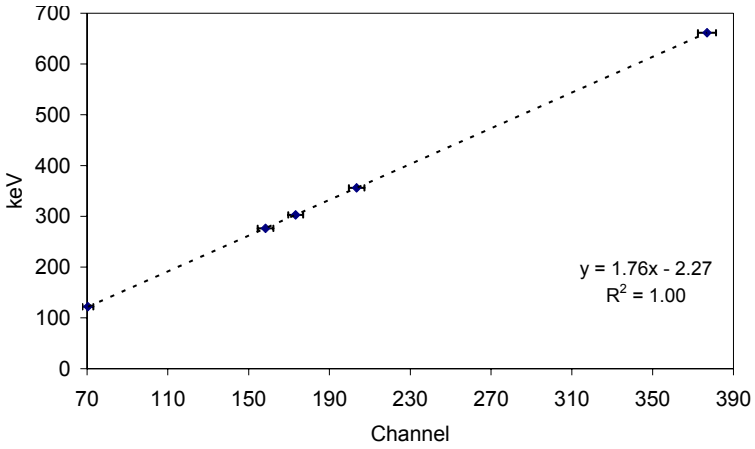

Figure 4.5 Curve relating the channel of the multi channel analyzer (MCA) to the energy of the incident photon for the XR-100T-CdTe-Stack detector in the energy range [0, 660] keV.

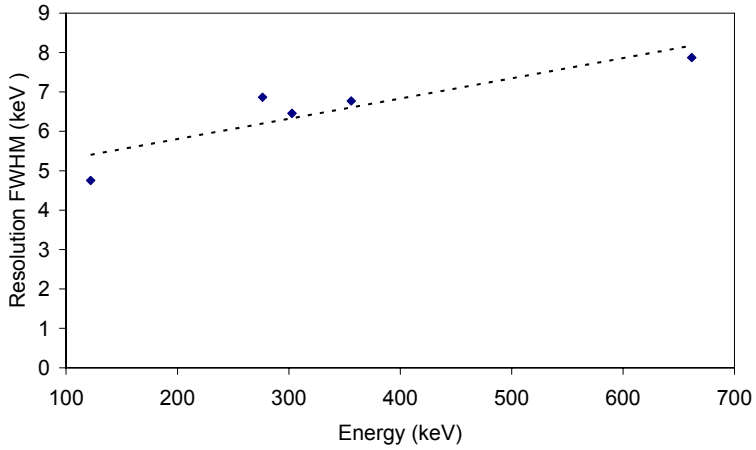

Figure 4.6 Energy resolution of the XR-100T-CdTe-Stack detector in the energy range [0, 660] keV.

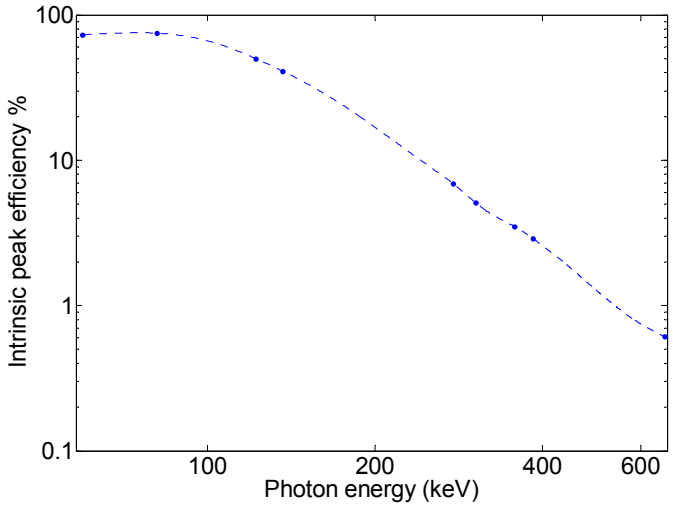

Figure 4.7 Intrinsic peak efficiency of the XR-100T-CdTe-Stack detector in the energy range 0 – 660 keV measured using radioisotopes.

Correction of the pulse height distribution

Figure 4.8 shows the pulse height distribution acquired with the CdTe detector and the spectrum obtained applying the correction for spurious effects, detector efficiency (figure 4.7) and for backscattered radiation described in § 3.3.1. The voltage of the X-ray tube was set to 450 kV. The external filtration was 4 mm of W.

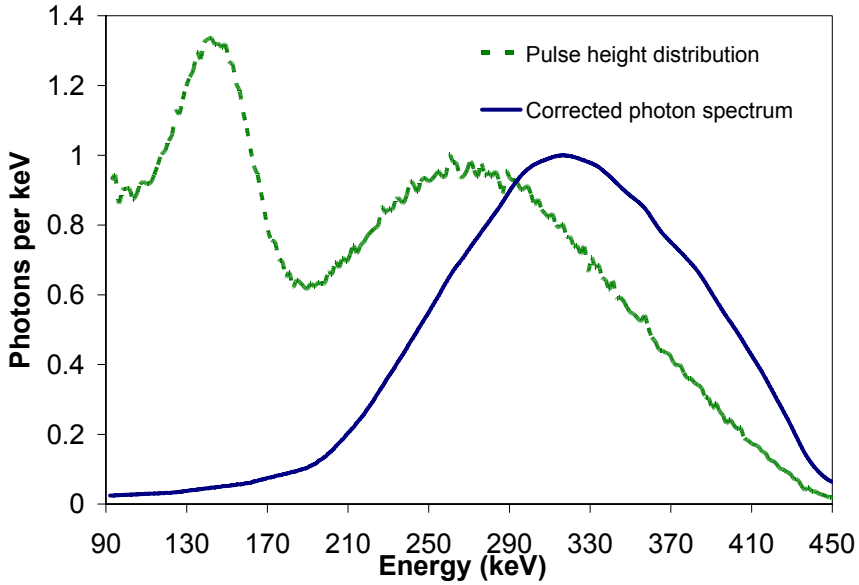

Figure 4.8 The pulse height distribution acquired using the CdTe detector and the photon energy spectrum corrected for spurious effects and detector efficiency when a voltage of 450 kV is applied are shown. The inherent filtration of the tube was 2.3 mm Fe + 1.0 mm Cu, the external filtration was 4.0 mm W.

Comparison of measured and simulated X-ray spectra

Figure 4.9 shows simulated X-ray spectra for different tube voltages (350 kV, 400 kV and 450 kV) and their comparison with the measured spectra corrected for detector escapes, efficiency and backscattered radiation. The inherent filtration was equivalent to 2.3 mm Fe plus 1.0 mm Cu, the external filtration was 4.0 mm W. Both the measured and simulated spectra were normalized by their maximum value. There is a good agreement between simulated and measured spectra. The slight differences are mainly due to the backscattered and scattered radiation that hits the CdTe detector.

4.1.1.2 Transmission curves

The difference in the quality of the X-ray spectrum for the simulated and measured spectrum at 450kV is illustrated in figure 4.10. It shows the transmission through aluminum and copper filters in function of thickness. The slight discrepancy observed when the transmission is lower than 0.01 is due to the fact that the detector used to acquire the data does not respond linearly when the transmission is below a certain threshold due to the limited dynamic range. Table 4.1 shows the values of the simulated and measured first and second half value layers (HVLs). The average difference is below 4.2% both for Al and Cu filters.

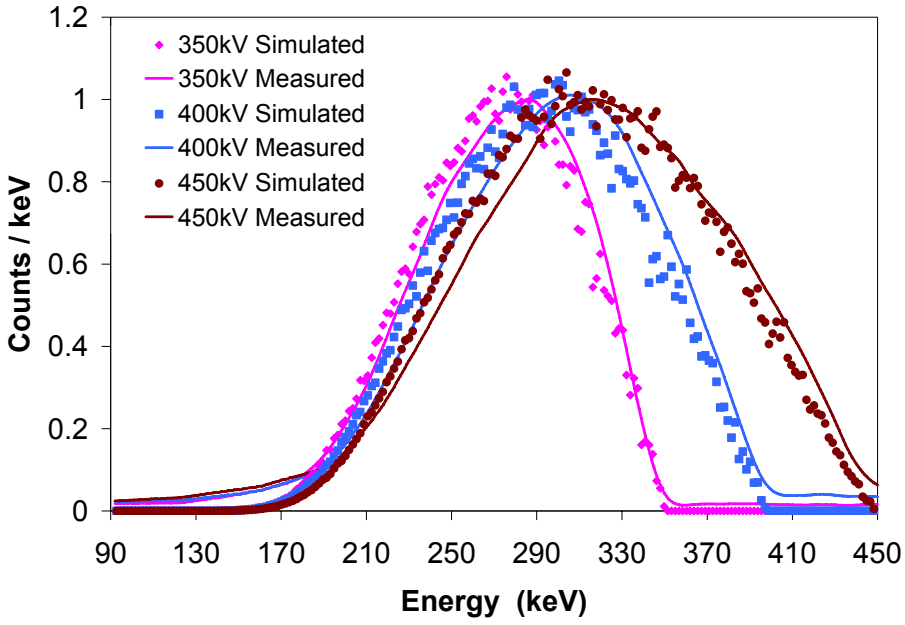

Figure 4.9 Simulated X-ray spectra at 350, 400 and 450 kV and their comparison with the measured spectra corrected for spurious detector effects, detector efficiency and stray radiation. The external filtration was W 4 mm thick.

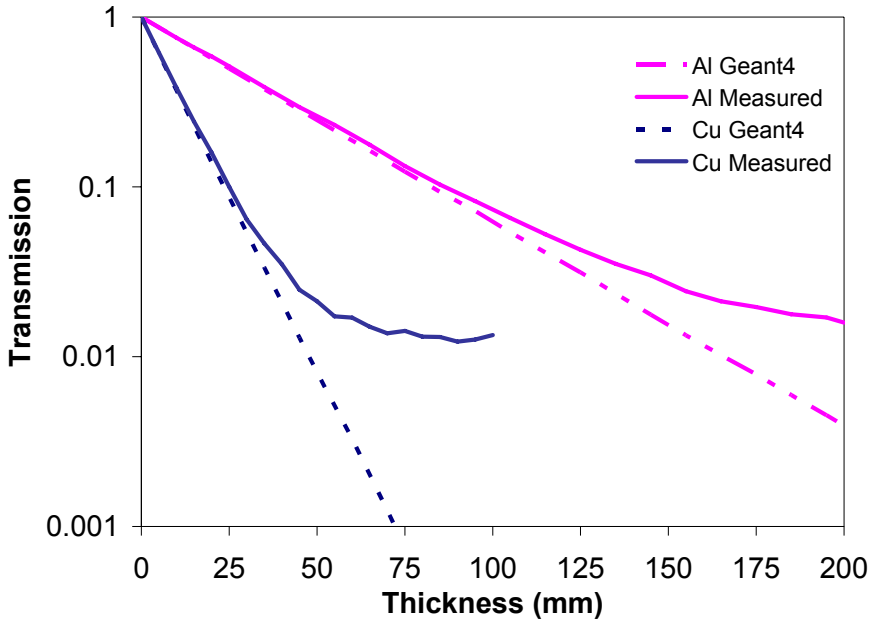

Figure 4.10 Comparison of transmission curves simulated by GEANT4 and measured data for aluminum and copper.

Table 4.1 Measured and simulated first and second half-value layers (HVLs).

Material	Measured 1st HVL	Simulated 1st HVL	Measured 2nd HVL	Simulated 2nd HVL	Average Difference %
Al	25. 89	24.83	51.84	49.61	4.19
Cu	7.19	6.97	14.66	14.04	3.63

4.1.1.3 Isotropic angular distribution of the X-ray beam

The comparison of simulated X-ray spectra (450 kV, filtered by 2.3 mm Fe and 1.0 mm Cu) retrieved in different regions of the detector is shown in figure 4.11. The spectra have been normalized by their maximum value of the bremsstrahlung part. The regions of the detector considered are defined in § 3.3.1.3. From the figure it can be seen that the shape of the spectrum does not depend on the region where we retrieve the data; therefore we can assume that the spectrum does not vary significantly with the angle. The hypothesis of isotropic angular distribution of the X-ray spectrum that was used in the simulation of the full CT system is therefore valid. The spectra were simulated with 4* 10^9 electron histories. The simulation was run in parallel on 10 CPUs and it had taken 14 hours.

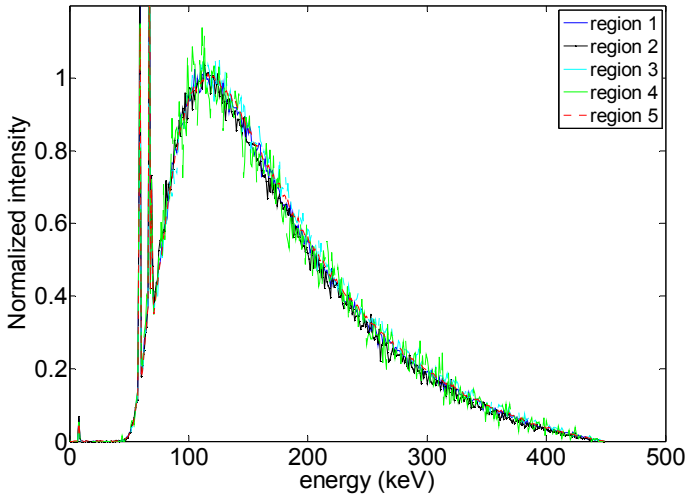

Figure 4.11 Comparison of simulated X-ray spectra retrieved in different regions of the detector.

4.1.2 MC simulations of the X-ray CT system

Verification of negligible environmental scatter

Figure 4.12 shows radiographic images without the object being present when the X-ray source collimator n° 4 and n° 7 of table 3.3 are employed together with a comparison of the profiles along the central horizontal line taken from the images. The maximum value of the difference of intensity calculated using Eq. 3.12 is 2.5 %. Therefore, we can assume that for the configuration with collimator n° 4 the hypothesis of negligible environmental scatter is valid.

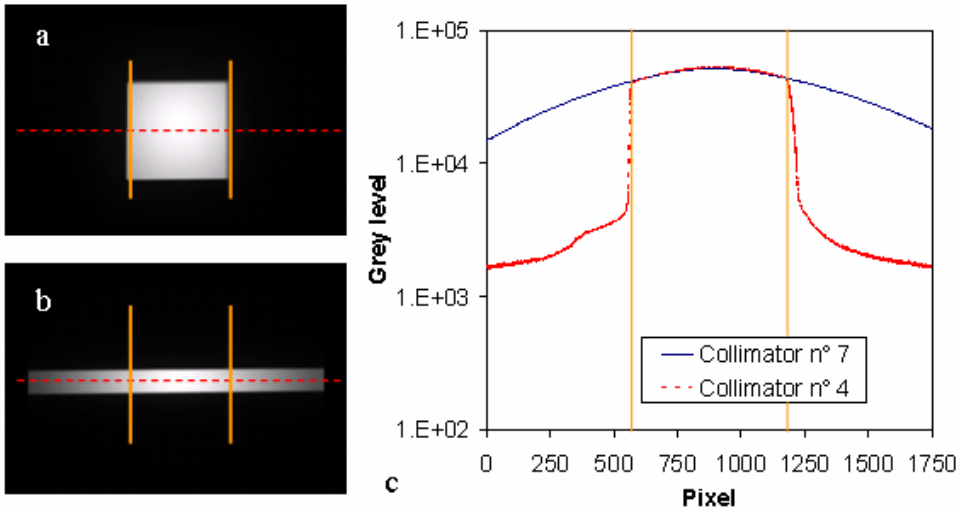

Figure 4.12 Radiographic images without the object being present acquired using the collimator n° 4 (a) and n° 7 (b). Profiles of the images along the horizontal central line of the detector (c).

Comparison of simulated and measured projections

Figure 4.13 shows the energy spectrum of the X-ray tube used in the simulation of the projections of the test objects. The spectrum was simulated as described in § 3.2.4 using the parameters of the X-ray tube provided by the manufacturer. The external filtration was 1.0 mm of tungsten (alloy HPM1750) and the energy of the electron beam was 450 keV.

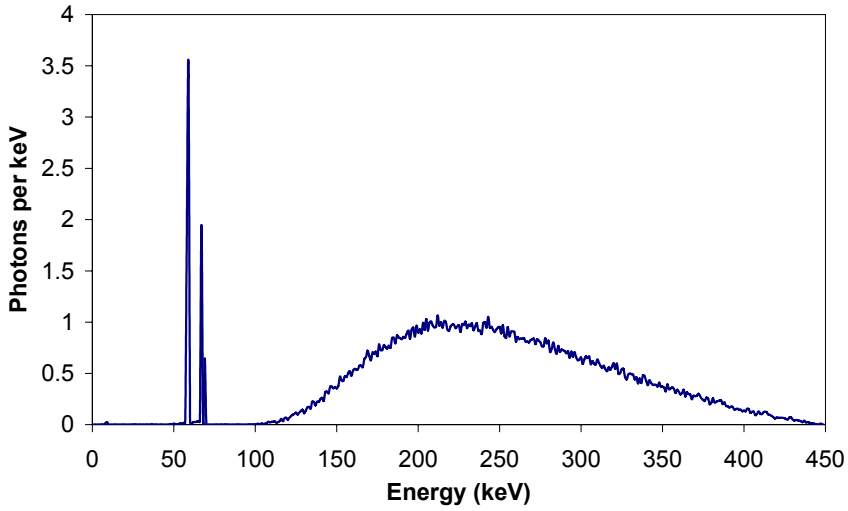

Figure 4.13 Simulated X-ray spectrum of the tube MXR-451 at 450 kV. 1.0 mm W was used for filtration.

Figures 4.14-4.17 show the simulated and measured images of the test objects together with the comparison of measured and simulated profiles presented in log-linear scale to magnify the differences between simulated and measured results. Although the profiles calculated from the simulated images are noisy it appears clearly that the simulated and measured profiles are in agreement. The absolute normalized errors (Eq. 3.14) are displayed in figures 4.14d-4.17d and their mean values, which are always lower than 0.05, are listed in table 4.2. From the figure it can be seen that the absolute normalized error peaks for the pixels of the detector corresponding to the borders of the object. This is probably due to slight geometric misalignment between the simulation and the measurement. In figure 4.17c the simulated profile appears to be slightly higher than the measured profile for x E [40, 60] mm. This is due to the fact that the flux is highly attenuated by the object and the signal-to-noise ratio (SNR) is low. For an accurate convergence of the result, it is necessary to simulate a larger number of photon histories.

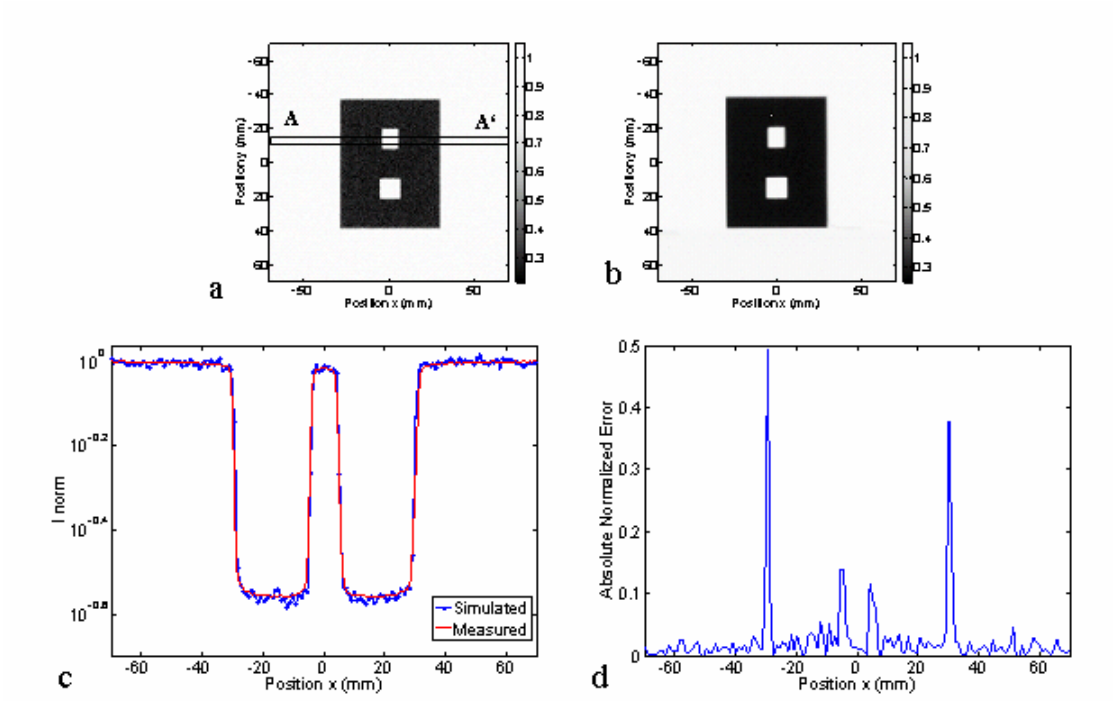

Figure 4.14 Comparison between simulated and experimental radiographies of the Al box. (a) Simulated image. (b) Measured image. (c) Profiles corresponding to the ROI AA' of the simulated and measured images. (d) Absolute normalized error of the profile.

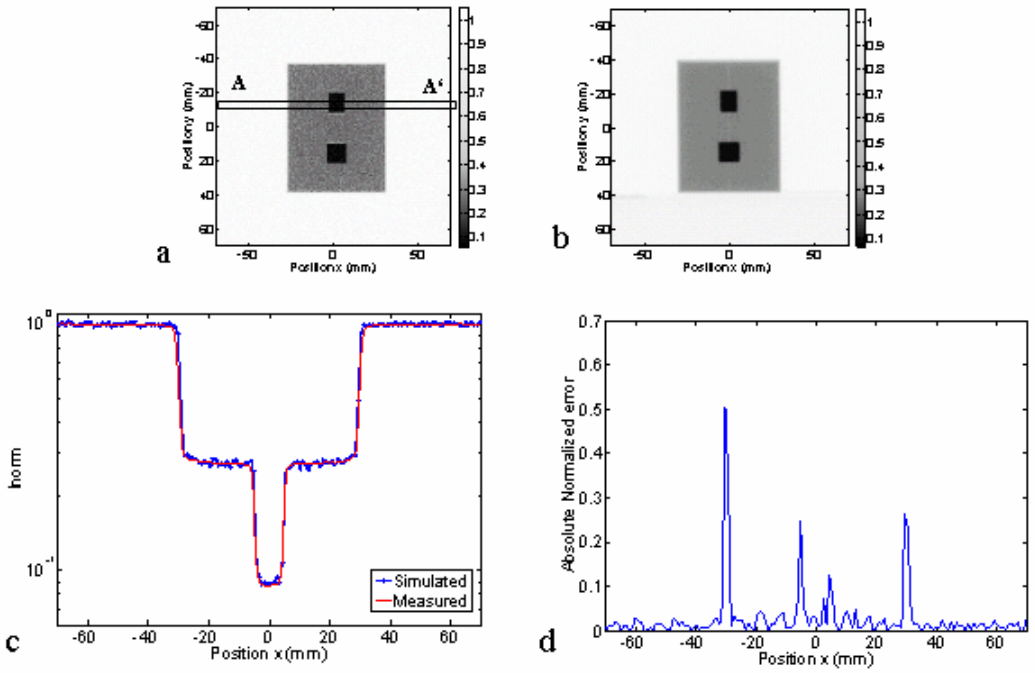

Figure 4.15 Same as figure 4.14 but for the Al box containing copper rods.

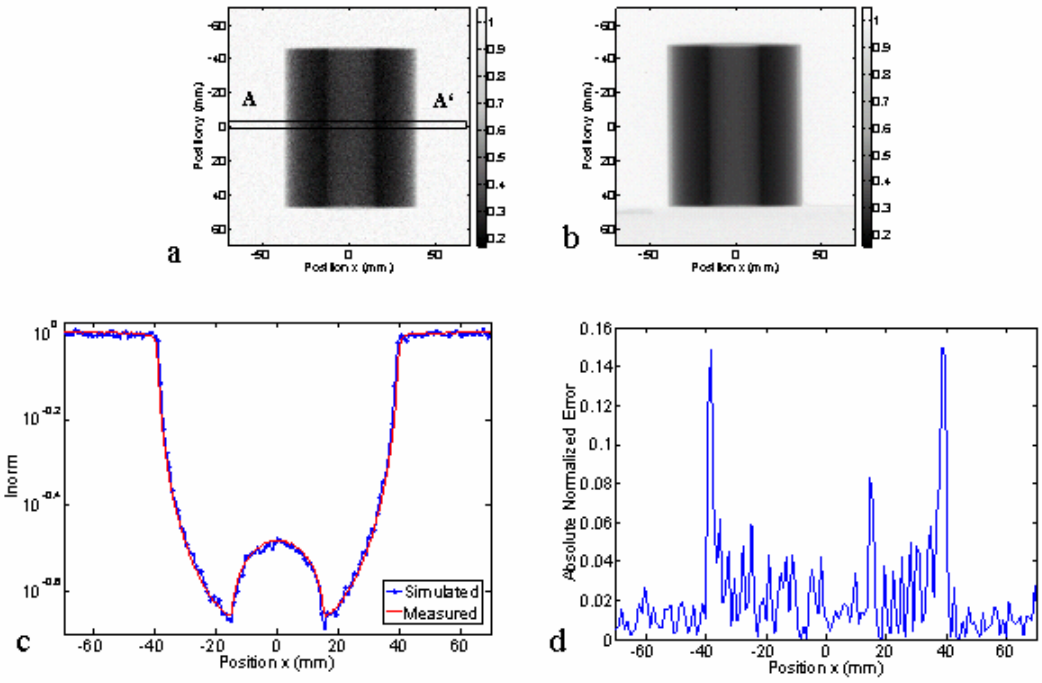

Figure 4.16 Same as figure 4.14 but for the Al cylinder.

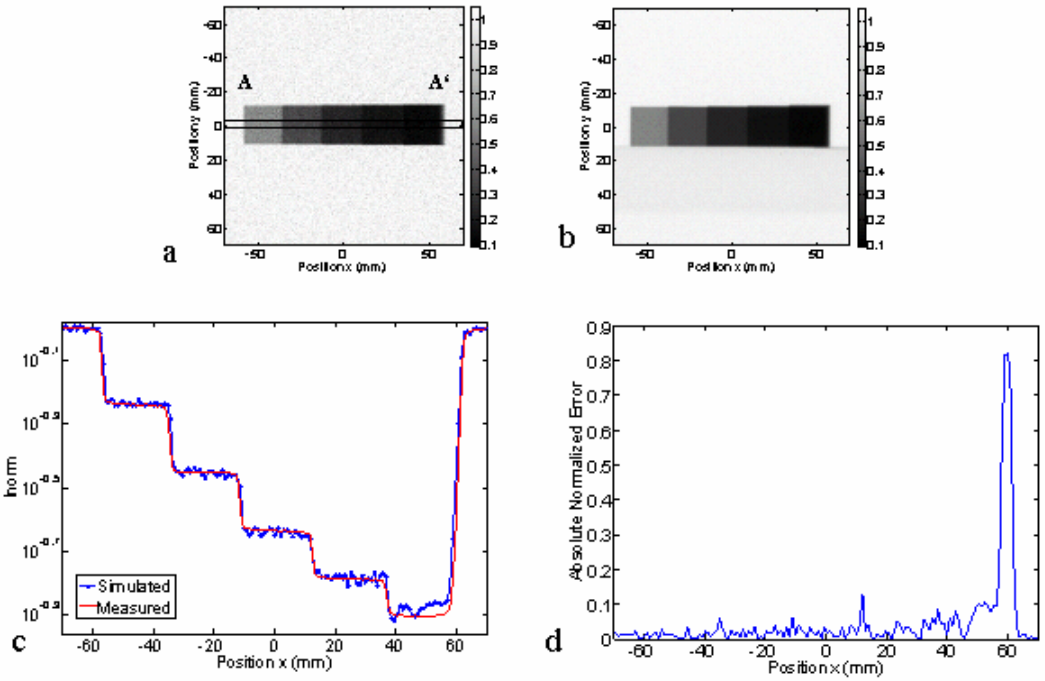

Figure 4.17 Same as figure 4.14 but for the Al step wedge.

Table 4.2 Mean values of the absolute normalized error calculated from the figures 4.14-4.17d.

Test object	Absolute NE
Al box	0.0253
Al box with copper rods	0.0273
Al cylinder	0.0216
Al step wedge	0.0477

4.2 Optimization and performance of the CT system

4.2.1 Optimization of the hardware components of the CT system

Thickness of the scintillator

Figure 4.18 shows the simulated X-ray spectrum used for the simulation of the full CT system and the profiles of the primary radiation, first, second, and higher order of scattering obtained with the scintillator screens of 1 mm and 2 mm thick CsI. The number of initially simulated photons was constant in both simulations. The results show that the energy deposited within the scintillator by the primary radiation and the scattering in case of a 2 mm thick screen is two times higher than the energy deposited when the screen of 1 mm is simulated. Therefore, the 2 mm scintillator produces the double of light photons compared to the 1 mm screen. This means that the acquisition time, which is an important factor for industrial CT where a series of objects have to be investigated, is reduced by 50 % when the screen of 2 mm is employed. For that reason, it was used in the X-ray imaging system.

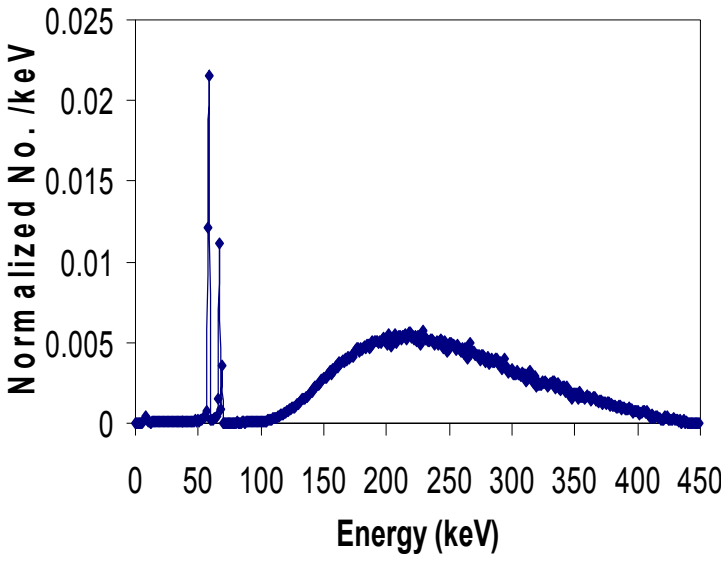

(a)

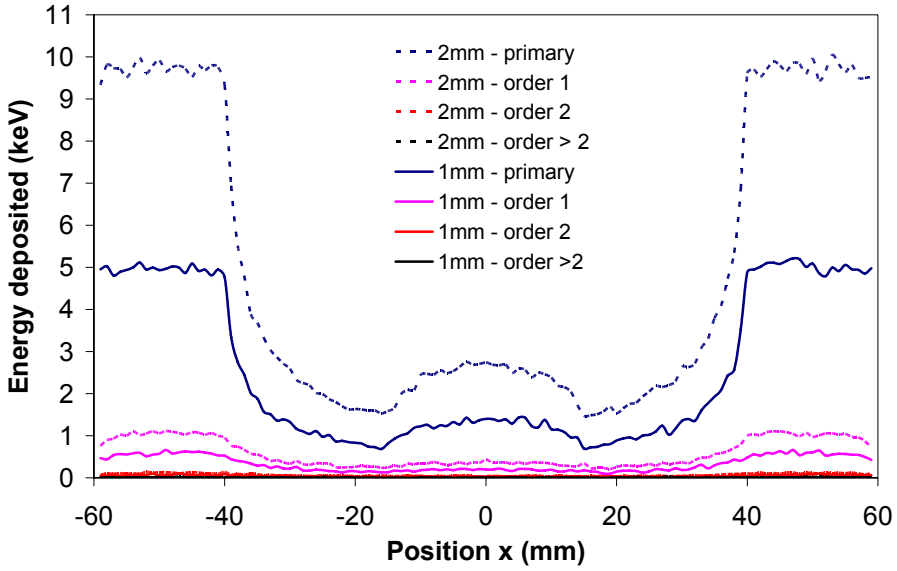

(b)

Figure 4.18 (a) Simulated spectrum of the X-ray tube. (b) Profiles of the hollow cylinder (height: 80 mm, outer diameter: 66 mm, inner diameter: 25 mm) of the primary radiation and the first, second, and higher order scattering obtained when simulating the 1 and 2 mm thick screens. The values of the energy deposited were divided by 10^5.

Scattered radiation from the detector box

The image of the step cylinder obtained when the detector box is simulated is displayed in figure 4.19a. Figure 4.19b and 4.19c show the comparison of the profile extracted from the image in figure 4.19a with the profiles obtained when the detector box is not simulated. The profile obtained in the same conditions but considering the walls of the box composed of two layers (3 mm lead and 5 mm steel) is also shown. The value of the attenuated intensity in the region corresponding to the maximum path length is 0.02 % with the detector box, 0.01 % without the detector box and 0.01 % with the detector box without the inner layer. We conclude that the inner layer of steel is the major source of scattering. Table 4.3 shows the contrast calculated from the central vertical profile (Figure 4.19b) for each step. The degradation of the contrast due to the detector box with walls composed of three layers is 68 % in correspondence to the ring of diameter 220 mm. Due to the high attenuation, it was not possible to distinguish between the ring of diameter 200 mm and 220 mm. As a consequence of the simulation, we removed the inner layer of 3 mm of steel from the detector box.

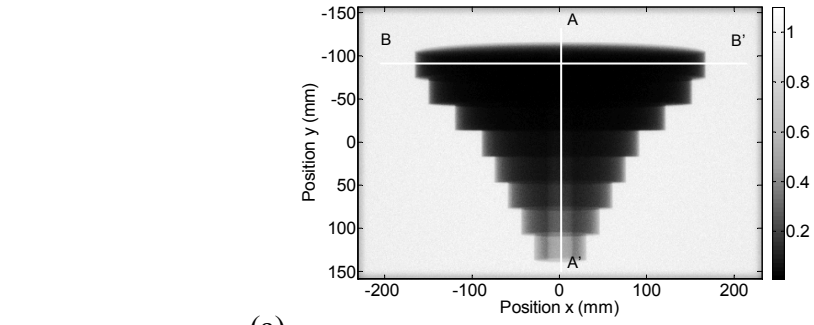

(a)

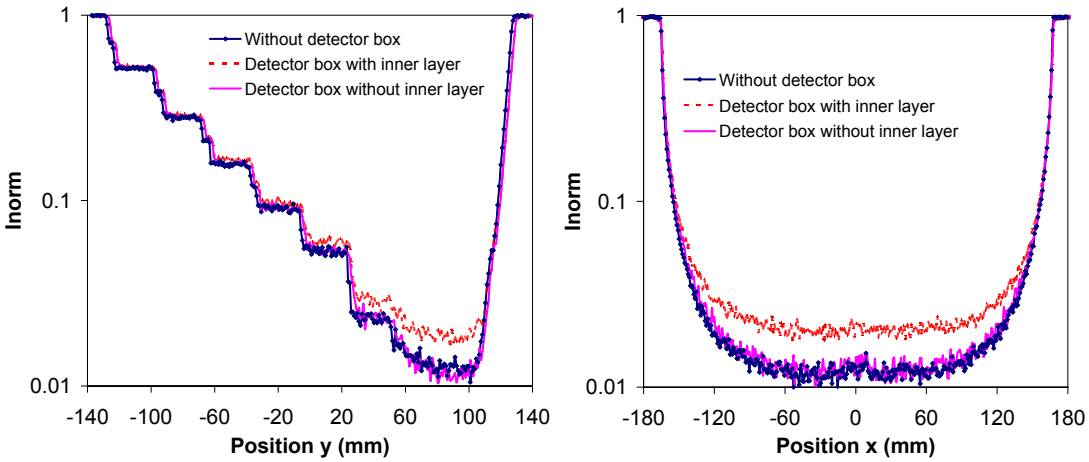

(b) (c)

Figure 4.19 (a) Image of the simulated step cylinder with the detector box with the steel layer. (b) Profile along the line AA'. (c) Profile along the line BB'.

Table 4.3 Contrast calculated from the profiles in figure 4.19b.

Diameter ring (mm)	$C_{\text{Detector box}}$	$C_{\text{Detector box without inner layer}}$	$C_{\text{Without detector box}}$
40	0.89 ± 0.04	0.90 ± 0.05	0.92 ± 0.04
60	2.46 ± 0.09	2.5 ± 0.1	2.54 ± 0.09
80	5.0 ± 0.2	5.3 ± 0.2	5.3 ± 0.2
100	9.3 ± 0.4	9.9 ± 0.4	9.9 ± 0.4
120	15.5 ± 0.9	17.2 ± 0.9	17.6 ± 0.9
160	34 ± 2	41 ± 3	42 ± 2
220	53 ± 3	85 ± 6	78 ± 5

Scattered radiation from the mirror

Figure 4.20 shows the profiles of the simulated normalized energy deposited within the CsI obtained in presence and in absence of the mirror. From the figure it can be seen that the amount of scattering generated by the mirror is negligible. We conclude that efforts to optimize the mirror do not improve the image quality and therefore are not necessary.

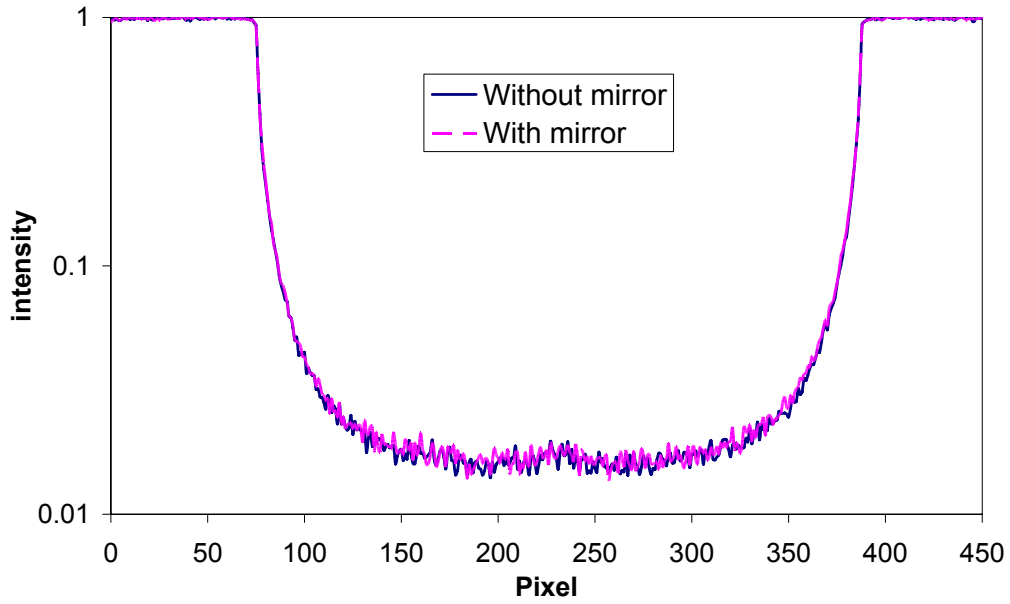

Figure 4.20 Profiles of the step cylinder corresponding to the step of outer diameter 220 mm simulated with and without mirror.

4.2.2 Optimization of the CT system settings

X-ray energy

The contrasts of the slices n° 1 and n° 2 defined in figure 3.29 acquired using high voltages of 300 and 450 kV are listed in table 4.4. The contrast was calculated from Eq. 3.16. From the table it can be seen that the contrast of the reconstructed images is higher when the voltage of 450 kV is applied. The reason is that the voltage of 300 kV has an insufficient penetration capability for path lengths that are encountered in the object (approx. 140 mm for the slice n° 1). The X-ray voltage suitable to investigate the test object is therefore 450 kV.

Table 4.4 Contrast of the slices n° 1 and n° 2.

X- ray voltage	Contrast	
	Slice n° 1	Slice n° 2
300 kV	0.31	0.71
450 kV	0.37	0.78

Lens aperture and number of projections

The results of the calculations of the contrast of the slices n° 1 and n° 2 show that the contrast is slightly higher when the object is acquired and reconstructed with 720 projections (figure 4.21). In fact, a rule of thumb says that the number of projections required for a tomographic reconstruction is approximately the number of pixels covered by the shadow of the object in the projection. Therefore, 360 projections are not sufficient for the investigated object. For this reason, the subsequent measurements are acquired using 720 projections. Regarding the lens aperture, we see that the apertures f/2.8 and f/5.6 are better in terms of contrast compared to the aperture f/1.6. To choose the suitable lens aperture, it is necessary to take into account also the exposition time needed for each projection. If we select the aperture f/2.8 the exposition time is 2 times the exposition time needed for the aperture f/1.6. For the aperture f/5.6 the exposition time is 8 times the exposition time for the aperture f/1.6. For that reason, we considered only the apertures f/1.6 and f/2.8 in the subsequent acquisitions.

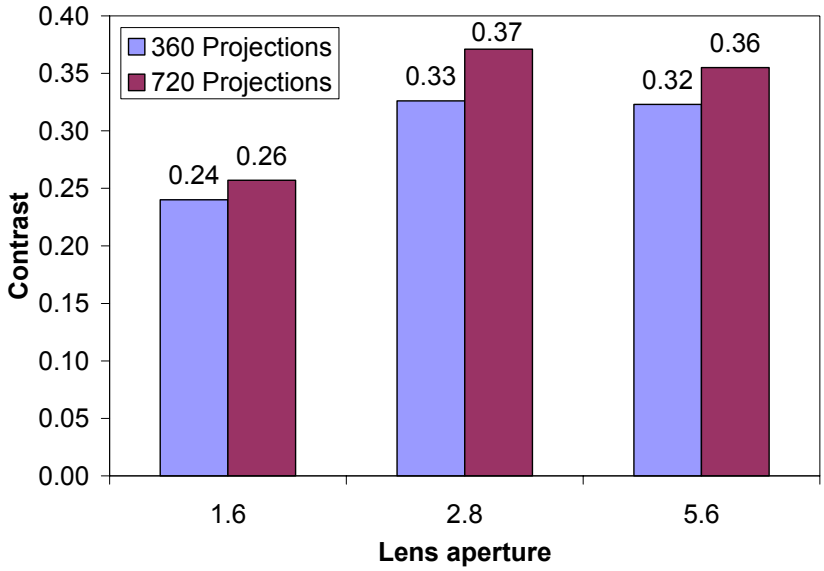

(a)

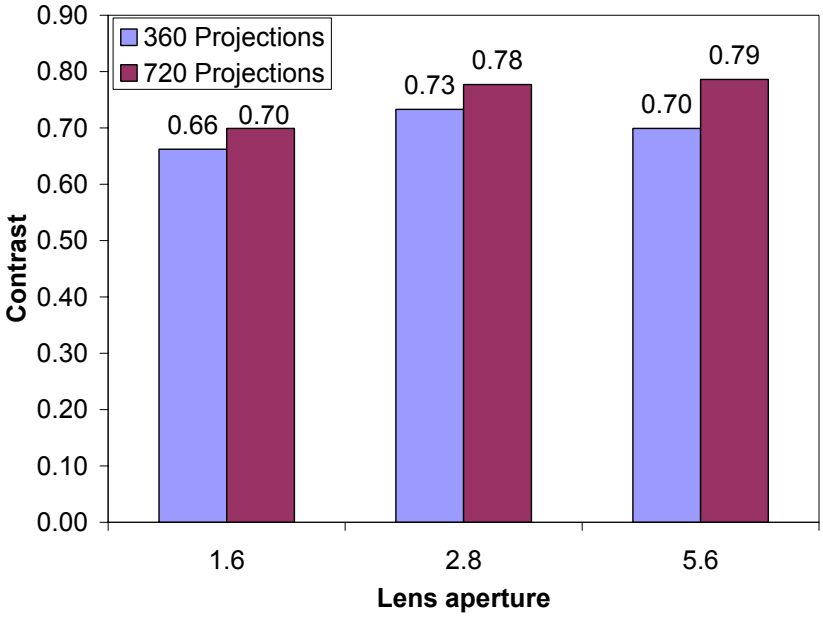

(b)

Figure 4.21 Influence of the lens aperture and number of projections on the image contrast of slices n° 1 (a) and n° 2 (b).

Dynamic range of the CCD camera

The brightness levels measured by the CCD are converted by the analog-digital converter to integers. The dynamic range represents the sensitiveness of the sensor to the variation of the brightness levels. A higher value of the dynamic range should result in an improvement of the contrast of the image. On the other hand it results in a larger amount of data. In our case, the contrast of the slice n° 1 is 0.35 with 16 bits and 0.37 with 12 bits for the slice n° 1 and 0.75 with 16 bits and 0.78 with 12 bits for the slice n° 2. Therefore, since there is no improvement in setting the dynamic range to 16 bits, we selected 12 bits to reduce the amount of data.

Number of averaged frames

Since the noise of the image is distributed randomly, we expect that the signal-to-noise ratio, consequently the image contrast, improves when increasing the number of averaged frames. Unexpectedly, the results show that the values of the contrast calculated on the slice n° 2 acquired with single-frame projections and with multiple-frames (eight) projections are the same. Together with the fact that the acquisition time for the 3D data was in both cases the same, we concluded that the function of the

HWM software, that sets the number of averaged frames, does not work properly. We reported the bug to the developer of the software.

Filtration

The filtration, which consists in removing the soft component of the X-ray spectrum placing a layer of absorbing material in front of the X-ray tube window, is an important parameter of the CT settings. In fact, removing the soft component of the X-ray spectrum, which does not contribute to the generation of the image on the detector because it is fully absorbed by the object, it is possible to reduce the cupping artifact in the CT images. From figure 4.22, which shows the contrast of the slices n° 1 and n° 2 for different filters (none, 0.5 mm W, 1.0 mm W, 2.0 mm Cu, and 2.0 mm brass), it can be seen that the 1.0 mm thick filter of tungsten is more efficient compared to the other filters. If it is compared to the configuration without filtration, the contrast with the 1.0 mm thick filter of tungsten is 1.5 times higher. Figure 4.23 shows the reconstructed slices.

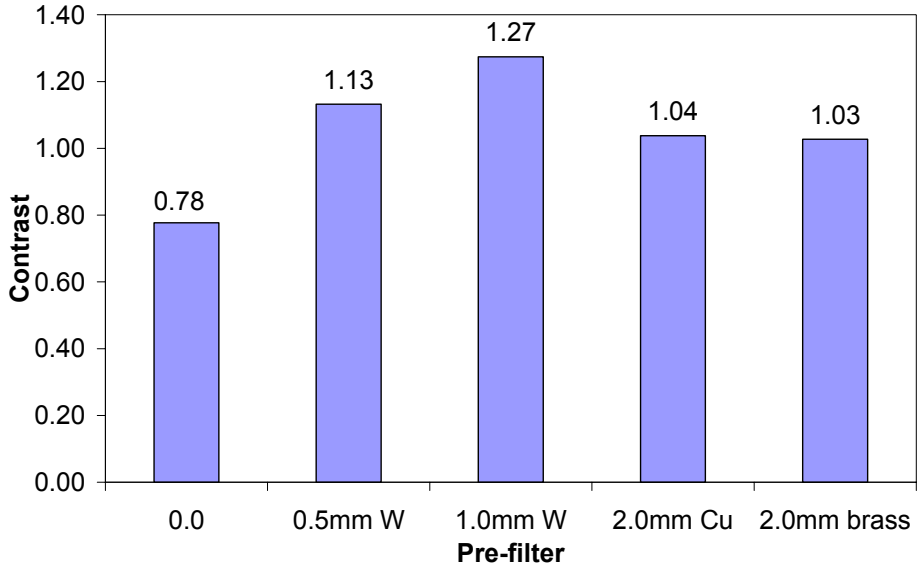

(a)

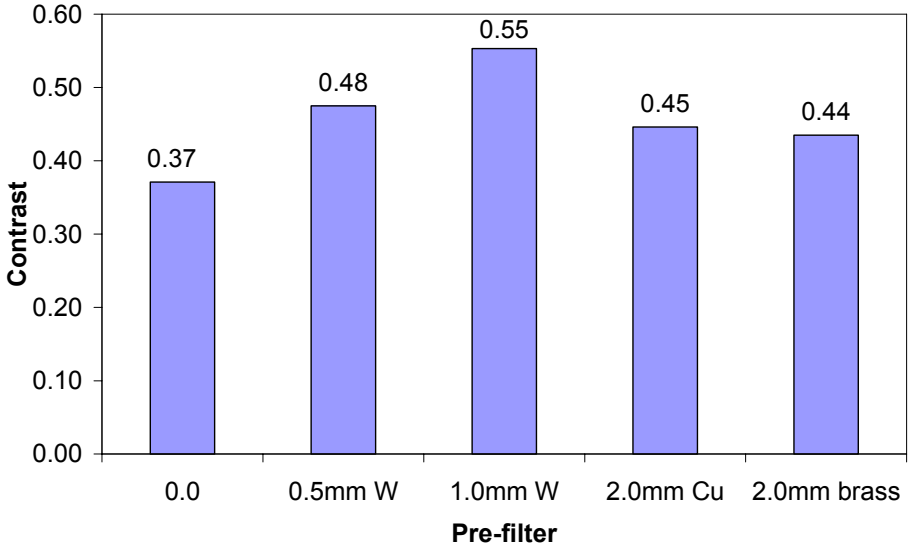

(b)

Figure 4.22 (a) Influence of the filtration on the image contrast of slices n° 1 (a) and n° 2 (b).

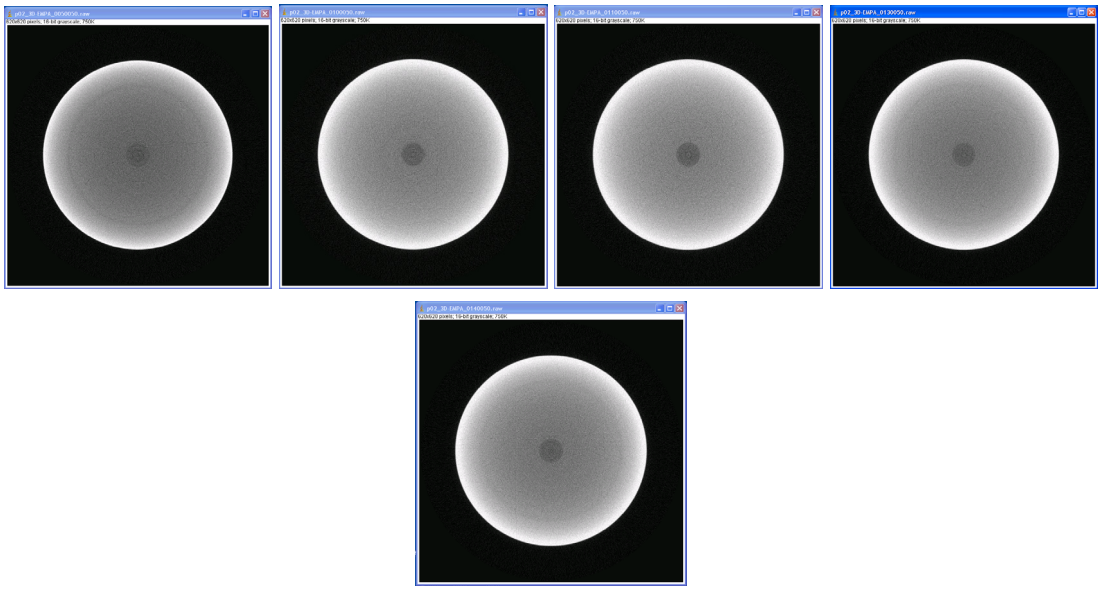

(a)

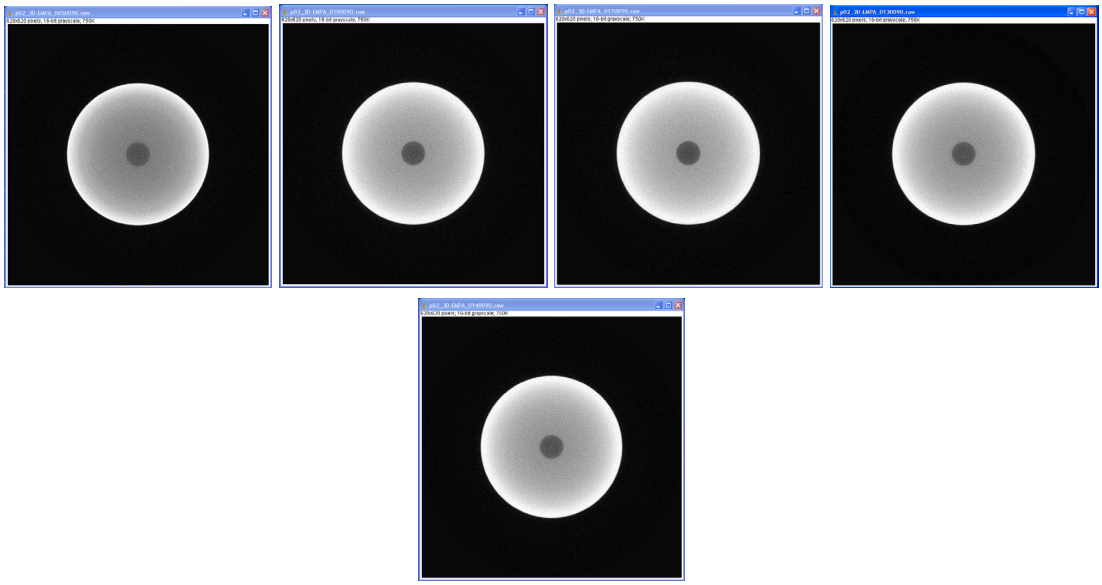

(b)

Figure 4.23 (a) From left to right: slice n° 1 acquired without filter, with 0.5 mm W, 1.0 mm W, 2.0 mm Cu, and 2.0 mm brass. (b) Same as above for the slice n° 2.

X-ray source collimator

The source collimator is an essential component in a CT system because it limits the emission cone of the X-ray beam. Figure 4.24 shows the contrast of the reconstructed images acquired with cone-beam and fan-beam X-ray source collimators. The results show that the contrast increases with a decreasing aperture of the X-ray beam. That is due to the fact that by narrowing the X-ray beam we reduce the environmental scatter and also the scattering from the object, in the case of the collimator n° 6 of table 3.3 (fan-beam collimator). From figure 4.25 showing the reconstructed images of the test object, it can be seen that the cupping effect is strongly reduced when the collimator n° 6 is used.

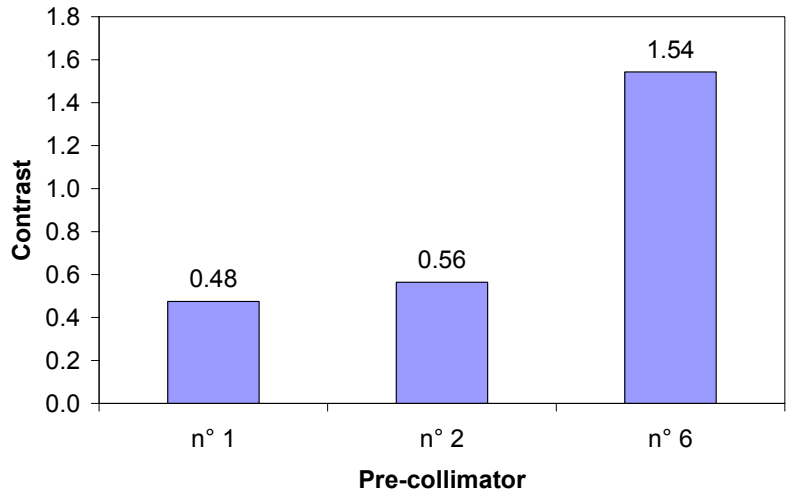

(a)

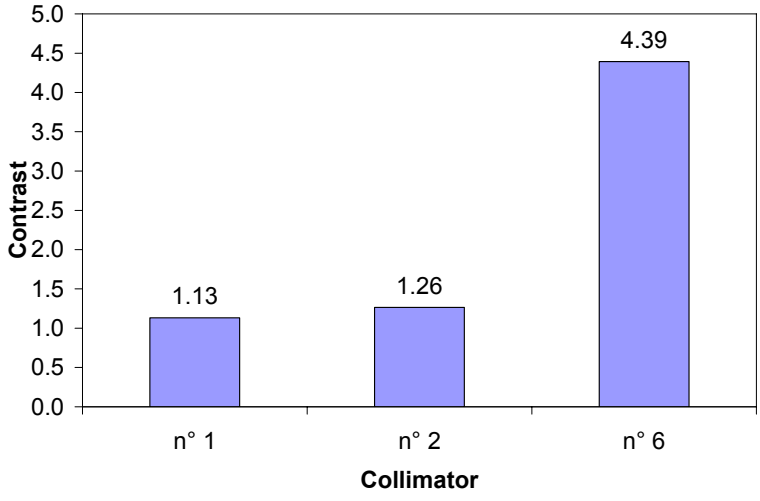

(b)

Figure 4.24 Influence of several source collimators on image contrast of slices n° 1 (a) and n° 2 (b).

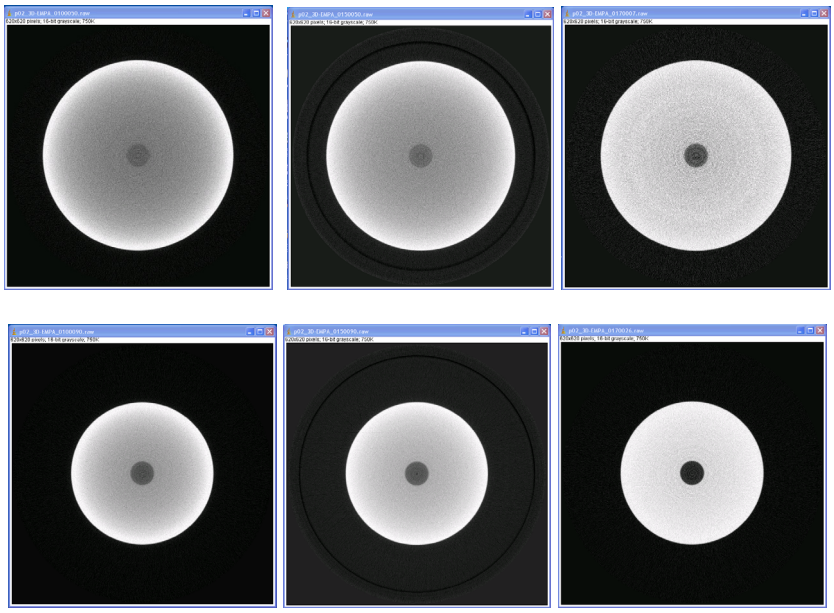

Figure 4.25 Top: Slice n° 1. From left to right: collimator n° 1, n° 2, and n° 6. Bottom: Slice n° 2. From left to right: collimator n° 1, n° 2, and n° 6.

Lead glass

The CCD camera is placed inside a lead box that shields the CCD camera from the X-ray photons. Nevertheless some X-ray photons enter the shielding box through the aperture on the top of the box from where the visible photons enter. The experiment shows that placing a lead glass in front of the aperture does not substantially improve the contrast (the value of the contrast with lead glass is 0.50, without it is 0.48). On the other hand, the exposition time needed for the acquisition of a projection is higher when the lead glass is used compared to the acquisition without it. Therefore, the subsequent experiments were performed without the lead glass.

Contrast and object diameter

Figure 4.26 displays the value of the contrast in function of the diameter for a fan-beam configuration (collimator n° 6 of table 3.3). The contrast slowly decreases in function of the diameter size. The hole is visible for each diameter, but for diameters larger than 160 mm the value of the contrast is about 1. Figure 4.27 shows the reconstructed images of the test object corresponding to the different diameters.

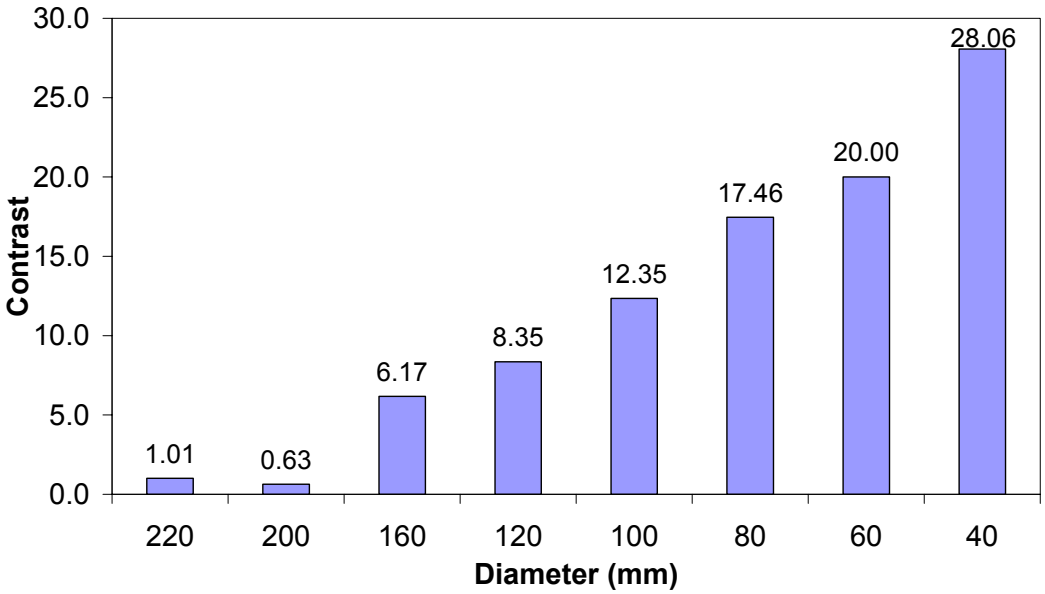

Figure 4.26 Influence of the object diameter on the contrast.

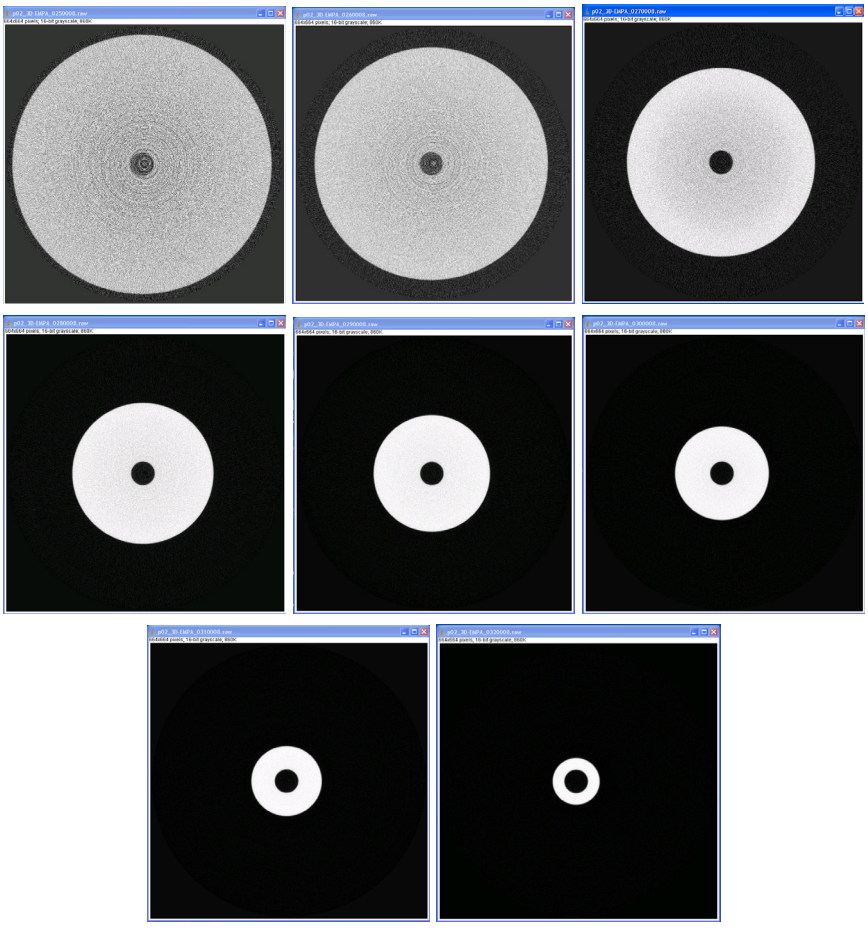

Figure 4.27 Slices of the steps of the test objects in decreasing order (outer diameter: 220 – 40 mm).

4.2.3 Performance of the CT system

Objects simulating cracks

Figures 4.28-4.29 show a series of CT images of the test objects made of steel and aluminum simulating cracks, acquired with focal spot 0.4 mm and 1.0 mm and using the configurations described in table 3.13. Cracks down to 100 μm are clearly visible for each configuration, whereas cracks of 50 and 20 μm are visible only when the focal spot of 0.4 mm is employed and with the configurations B and C. The unsharpness due to the larger focal spot is clearly visible for the configurations B and C, whereas for the configuration A it is not possible to appreciate the improvement of the sharpness due to the smaller focal spot. Figure 4.30 shows that when the geometrical unsharpness is greater in size than the crack (setup B, focal spot 1.0 mm) there is a loss of image contrast.

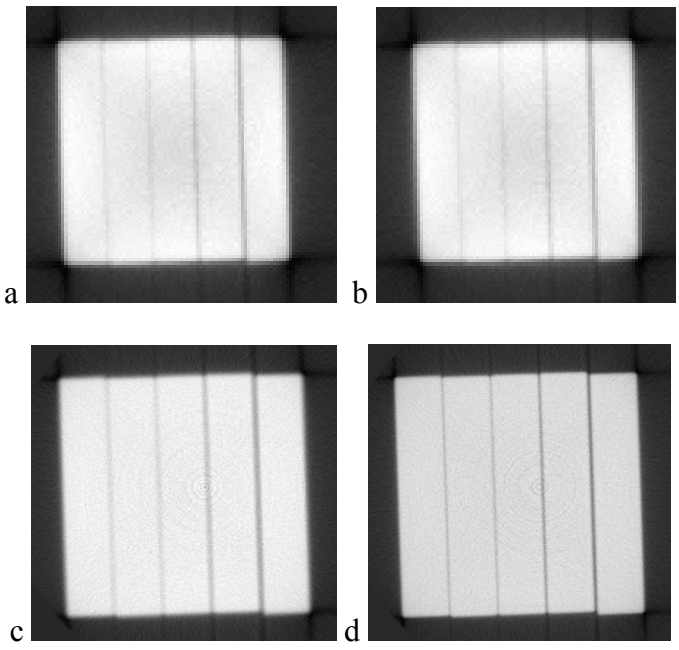

Figure 4.28 Reconstructed slices of the steel test object. Setup A with focal spot 1.0 mm (a) and 0.4 mm (b). Setup B with focal spot 1.0 mm (c) and 0.4 mm (d).

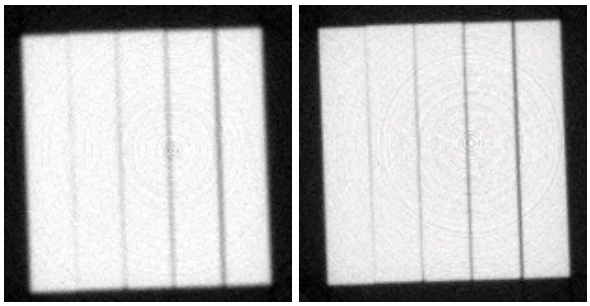

a b

Figure 4.29 Reconstructed slices of the aluminum test object. Setup C with focal spot 1.0 mm (a) and 0.4 mm (b).

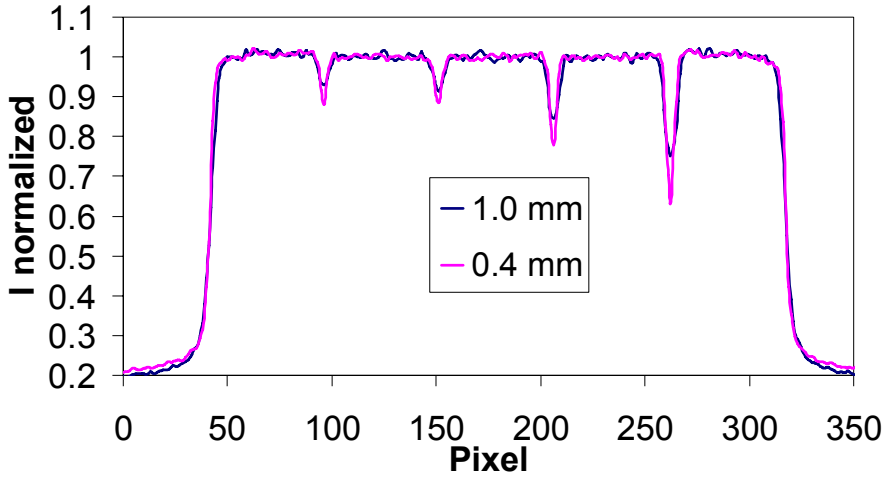

Figure 4.30 Profiles of X-ray images acquired using the setup B with focal spots of 1.0 mm and 0.4 mm.

Figure 4.31 shows the reconstructed images of the steel and aluminum test objects acquired with different source collimators. From the figure it can be seen that the image quality is not affected by the tested source collimators. In fact, since the environmental scatter is negligible for both collimators, the scattering from the object is the only component responsible for a difference in image quality. In this case, because of the small thickness and front size, the object produces a negligible amount of scattered radiation, hence it is not possible to see the difference between the image acquired when the object is fully illuminated (collimator n° 4) and when just a slice of the object of approximately 13 mm is illuminated (collimator n° 5).

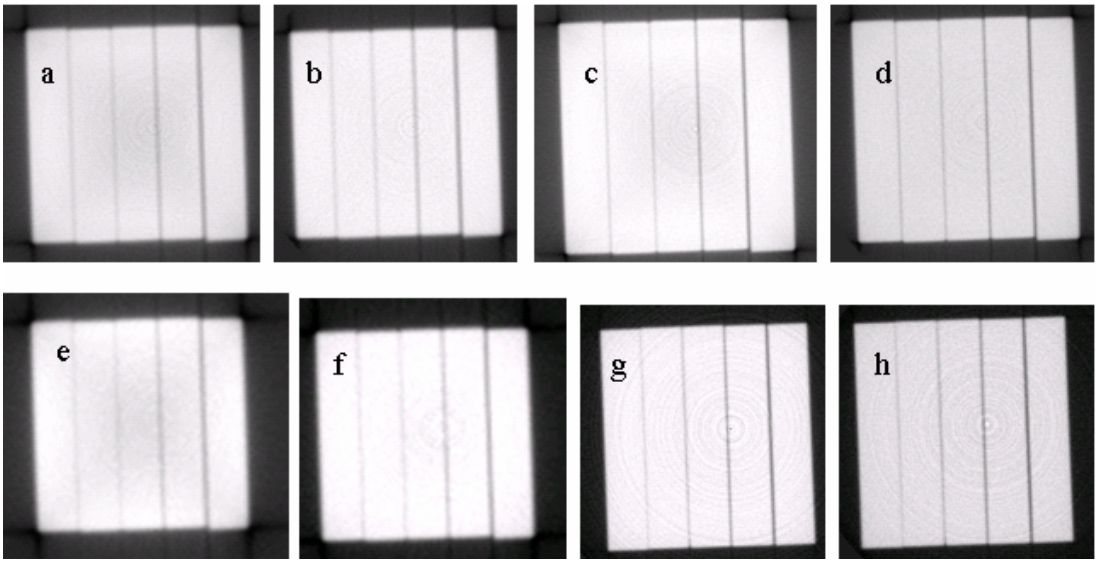

Figure 4.31 Reconstructed slices of the steel test object. Setup D with collimators n° 4 (a) and n° 5 (b). Setup E with collimators n° 4 (c) and n° 5 (d). Setup F with collimators n° 4 (e) and n° 5 (f). Reconstructed slices of the Al test object. Setup G with collimators n° 4 (g) and n° 5 (h).

Figure 4.32 shows the images of the steel test object reconstructed with the standard and premium resolution of the HWM reconstruction software. From the figure it can be seen that there is no difference in the quality of both reconstructed images.

Figure 4.33 shows the reconstructed images of the steel test object placed at different distances from the source. Cracks down to 20 μm can be clearly seen in the case of a source-distance of 567 mm, whereas at a distance of 1107 mm the cracks of 20 and 50 μm are hardly visible.

Figure 4.34 shows the X-ray images of the object made of steel acquired with 360, 720, and 1440 projections. We can clearly see that the cracks are visible in all the images and that there is not a significant improvement of the image quality by increasing the number of projections. In fact, due to the small size of the object already 360 projections are sufficient to reconstruct the image correctly.

Figure 4.35 shows the reconstructed image of the steel test object and the image of the aluminum test object. The cracks of 20 μm are visible in both images.

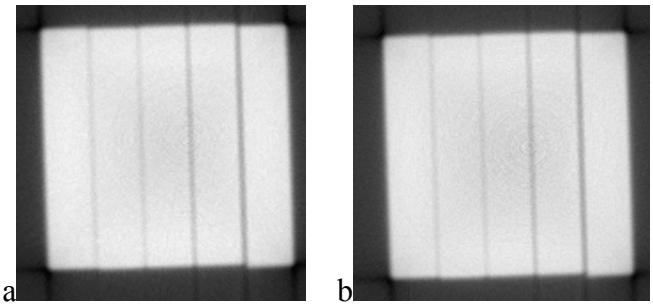

Figure 4.32 X-ray images of the test object reconstructed with standard (a) and premium (b) resolution.

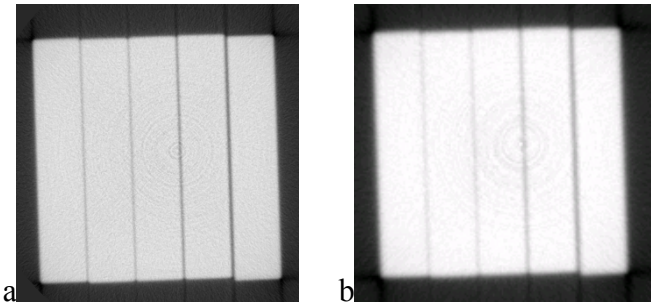

Figure 4.33 X-ray images of the test object placed at a distance of 567 mm (a) and of 1107 mm (b).

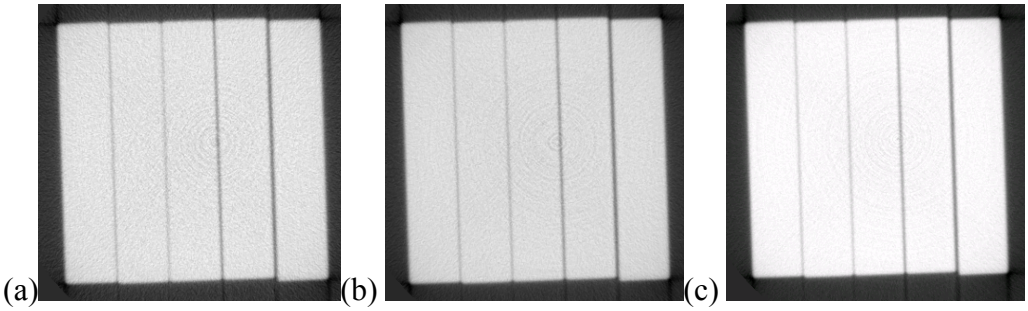

Figure 4.34 X-ray images acquired with 360 (a), 720 (b), and 1440 (c) projections.

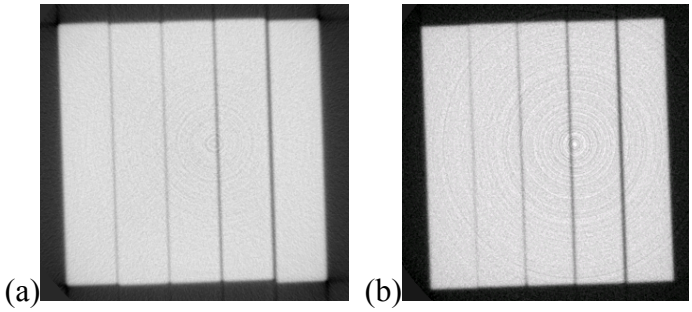

Figure 4.35 X-ray images of (a) the test object made of steel (setup B, focal spot 0.4 mm) and the test object made of aluminum (setup G, collimator n° 5).

Object simulating holes

From figure 4.36 showing the reconstructed images of the aluminum ring it can be seen that using the configuration A we can detect holes down to 0.5 mm, whereas using the configuration B (object closer to the source, higher number of projections, and premium resolution) holes of diameters down to 0.3 mm can be easily detected. The figure also shows a reference image (obtained with a fan beam CT system, Empa). Holes down to 0.3 mm can be detected.

Figure 4.37 shows the reconstructed images of the cylinder made of aluminum with a diameter of 80 mm acquired with three different configurations (table 3.13) where we varied the focal spot, the source object distance and the source collimator. From the figure it can be seen that the holes of diameters down to 1.0 mm are clearly visible in each studied configuration.

Figure 4.38 shows the reconstructed images of the cylinder made of aluminum with a diameter of 120 mm acquired using a different number of projections. The holes with diameters down to 1.0 mm are easily detected in both cases.

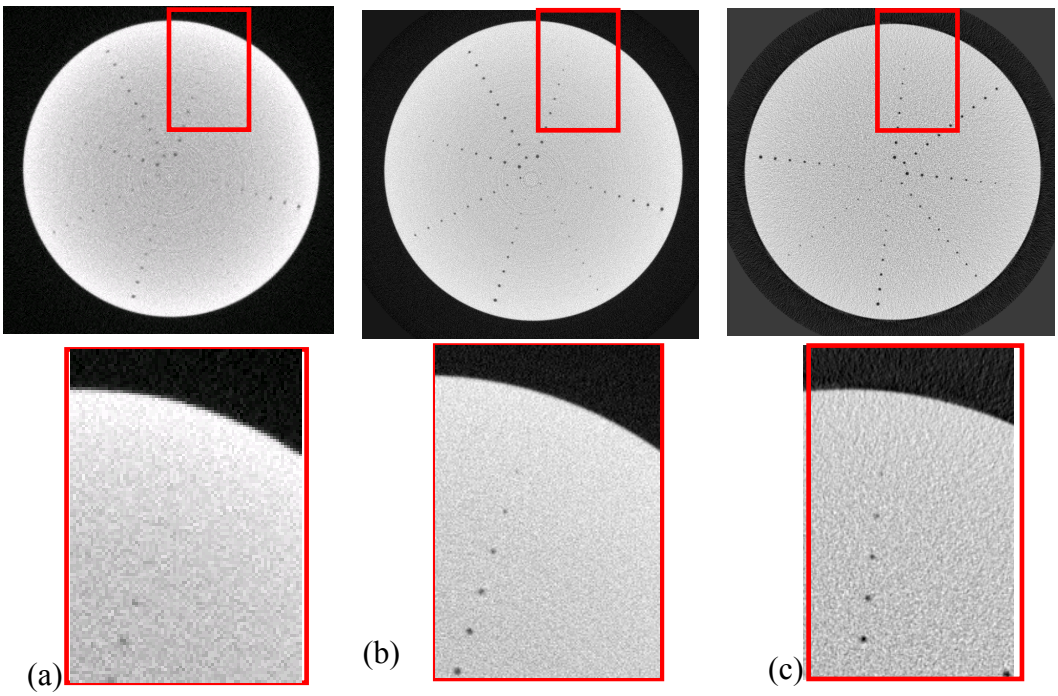

Figure 4.36 X-ray images of the aluminum ring acquired with the setup A (a), setup B (b), and reference image (c).

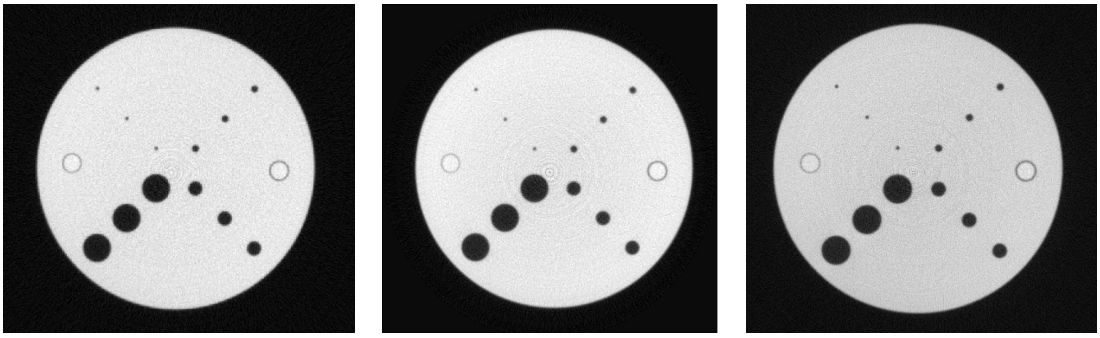

a b c

Figure 4.37 X-ray images of the test object acquired with setup A (a), setup B (b), and setup C (c).

(a) 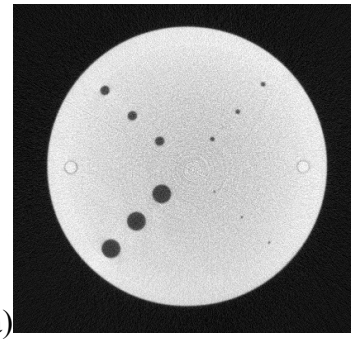 (b) 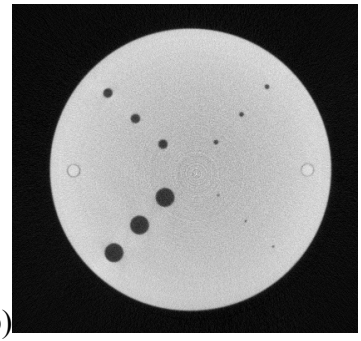

Figure 4.38 X-ray images of the test object with a diameter of 120 mm acquired and reconstructed with 720 (a) and 1440 (b) projections.

Real castings

Figure 4.39 shows the reconstructed images of a cylinder of a motorcycle acquired with two different configurations were the focal spot, source collimator, and resolution of the reconstruction varied. A reference image acquired using the fan-beam CT system of Empa [1] is also shown. From the figure it can be seen that for both configurations the image quality is higher than the image quality of the reference image. The quality of the image acquired with the setup B is better than with the setup A because of the smaller focal spot, smaller area of the scintillator illuminated by the X-ray beam, and the reconstruction resolution. The figure shows an important characteristic of the cone beam CT that is the isotropy of the spatial resolution. In the reference image we see clearly the non-uniformity of the data in the axial direction, due to the fact that in a fan beam CT the spatial resolution in the plane of the slice is different from the vertical resolution.

Figure 4.40 shows the reconstructed images of an air suction duct of a turbocharged engine containing a flaw. The images were acquired with different source collimators. A reference image (acquired by Tomo Adour, France using a fan beam CT system; project DETECT) is also shown. The flaw is visible for each configuration. In the case of the collimator n° 2 the quality of the image is not comparable to the reference image due to the scatter artifacts, whereas in case of collimators n° 5 and n° 8 the scatter artifacts, even if present, are strongly reduced and the image quality is comparable with the reference image.

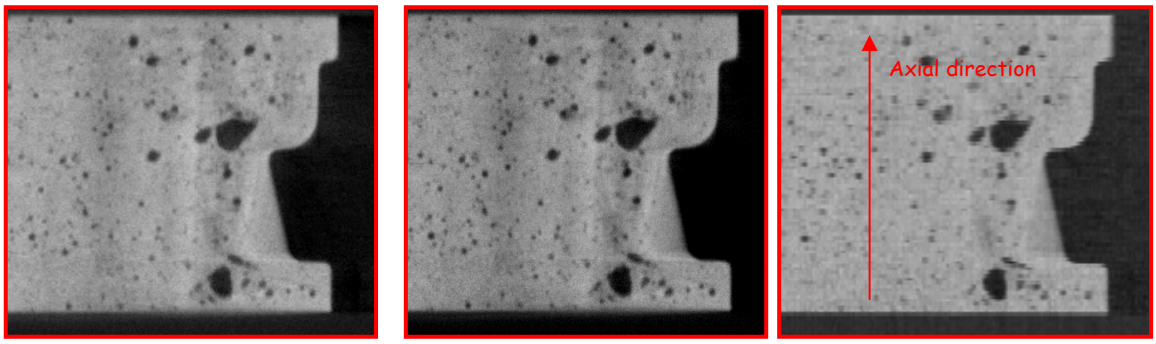

Figure 4.39 Region of interest in the X-ray images of the aluminum cast acquired with the setup A (a) and B (b) and in the reference image (c).

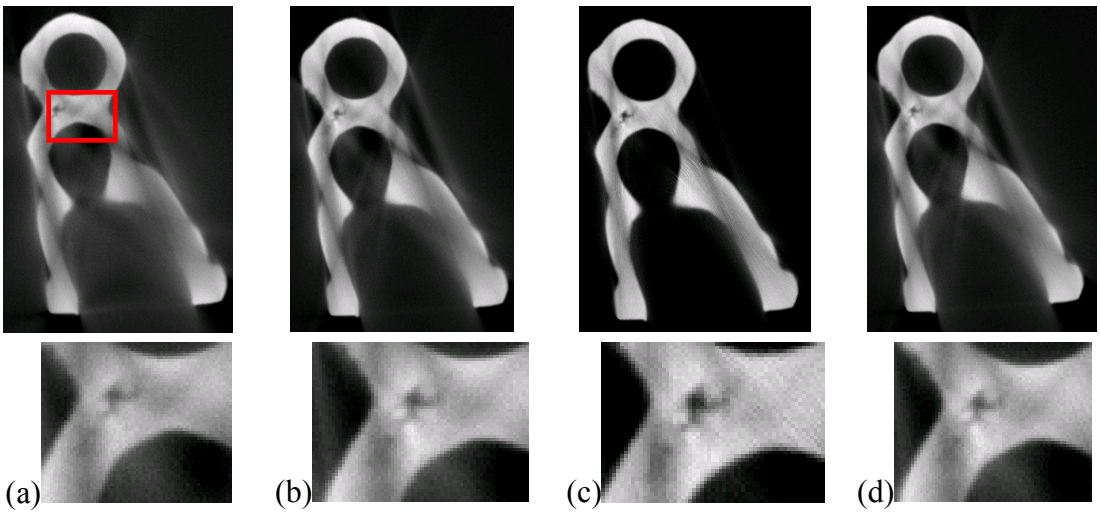

Figure 4.40 X-ray images of the air suction duct acquired with collimators n° 2 (a), n° 8 (b), and n° 5 (c) and the reference image (d).

4.3 Evaluation of the scattered radiation

4.3.1 Scattering created by the object

Figure 4.41 shows the simulated projections of an aluminum hollow cylinder generated by the energy deposited within the scintillator by the primary plus scattered (total) radiation, primary radiation, first, second, and higher order of scattering obtained using the developed MC code. This information allows the study of the different components of the energy deposited within the detector and the investigation of their relative influence. The images of the scattered radiation were de-noised with the Richardson-Lucy fit.

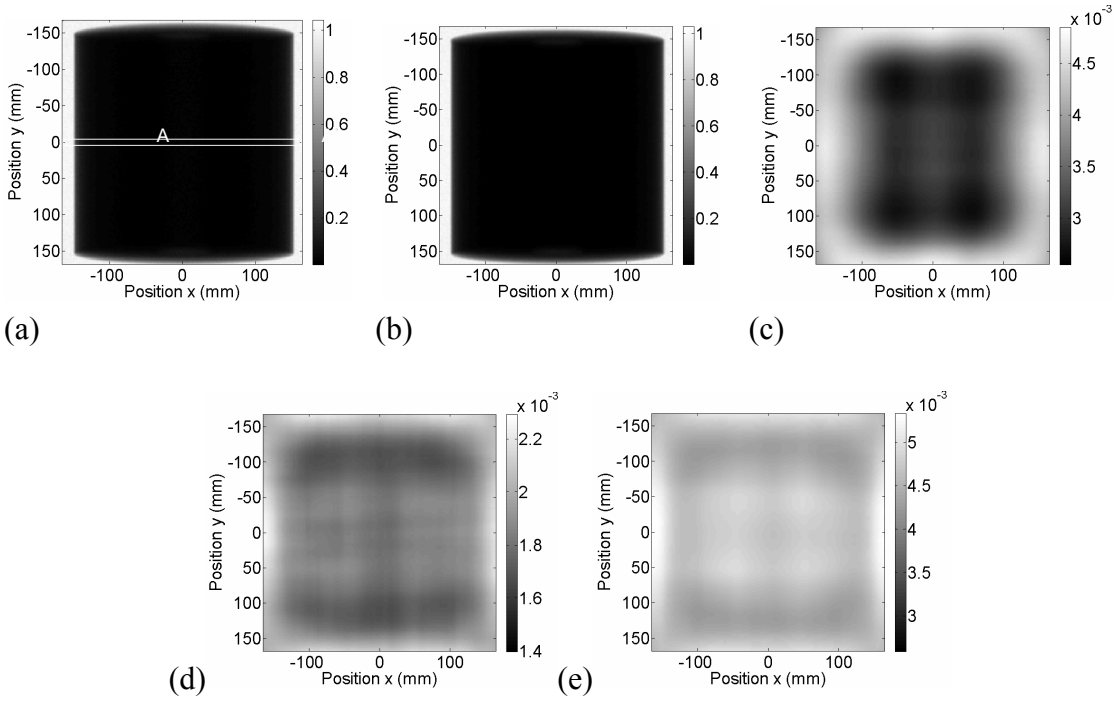

Figure 4.41 Al cylinder with external diameter of 200 mm and inner diameter of 50 mm. Simulated images of the energy deposited by (a) total radiation, (b) primary radiation, (c) first-order scattering, (d) second-order scattering, and (e) higher-order scattering.

De-noising procedure

Figure 4.42 shows the simulated image of the energy deposited by the higher than second order scattering before and after the application of the de-noising procedure and their profiles. In the de-noised image the shape of the object, an aluminum box of dimension 70 x 70 x 190 mm^3, can be clearly seen. Using this method, smooth estimates of scattered projections can be obtained with a low number of photons, reducing the time needed for the simulations.

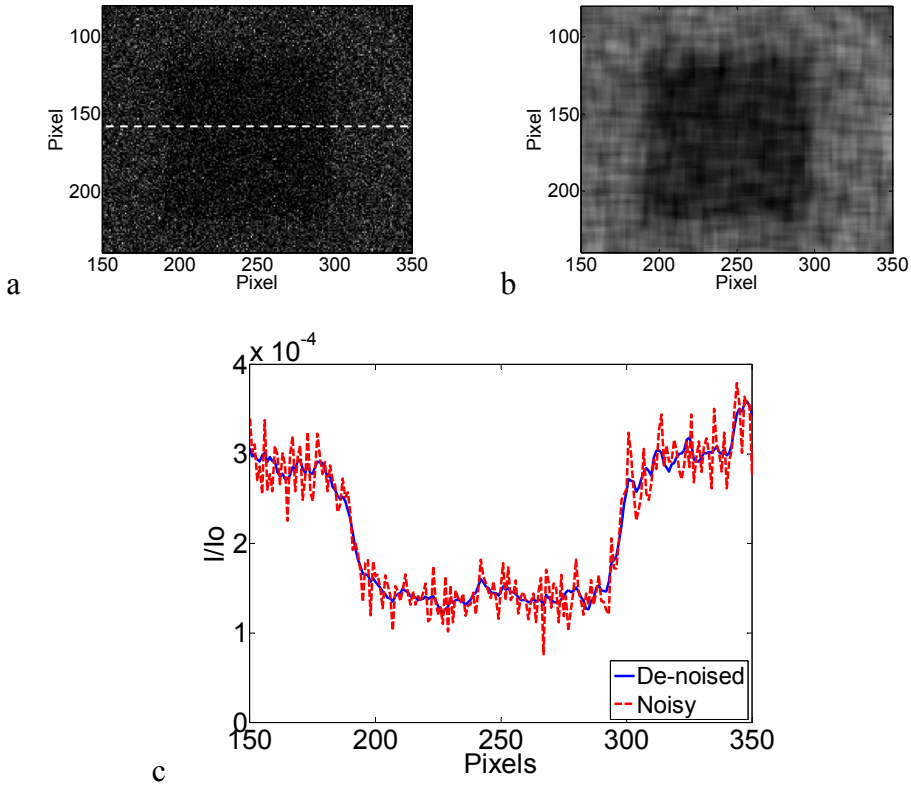

Figure 4.42 Image of higher than second order scattering (a) before the de-noising procedure, (b) after the procedure, (c) comparison of the profiles.

Figures 4.43-4.44 show the profiles of the simulated energy deposited by total radiation, primary radiation, and first, second, and higher order scattering for the hollow aluminum cylinders and the SPR_1, SPR_2, and $SPR_{>2}$ calculated from the profiles. The images of the scattered radiation were de-noised using 10 iterations of the Richardson-Lucy fit and a standard deviation of 30 detector pixels.

From figure 4.43 it can be seen that for the cylinder with an outer diameter of 200 mm the energy deposited within the scintillator by higher than 2nd order scattering is higher than the energy deposited by 1st order scattering and, in the region of maximum

path length (see figure 4.43a), it is even higher than the energy deposited by the primary radiation (signal).

From figure 4.44 it can be seen how the SPR for each order of scattering varies in function of the object size. For the hollow cylinder with a diameter of 75 mm the maximum value of the SPR_1 was estimated to be below 4 %, and the SPR_2 and $SPR_{>2}$ below 1 %. In the hollow cylinder with a 100 mm diameter the maximum value of SPR_1 rises to 10 %, and SPR_2 and $SPR_{>2}$ are below 3 %. For the hollow cylinder with a 150 mm diameter the SPR_1 becomes 40 %, the SPR_2 is about 20 %, and the $SPR_{>2}$ is about 30 %. In the hollow cylinder with a diameter of 200 mm the SPR_1 reaches a maximum value of about 70 %, the SPR_2 is slightly below 50 %, and the $SPR_{>2}$ is about 120 %.

For the cylinders with a diameter larger than 100 mm, the contribution of 2nd and higher order scattering should therefore be taken into account to increase the accuracy of the simulated image and to correct for the scatter in the scatter correction algorithms. Table 4.5 presents the values of the contrast calculated from the profiles of the primary C^P and total radiation C^T for the ROI *Center* defined in figure 4.43a. The values of the degradation of the radiographic contrast CD due to the scattered radiation defined in Eq. 3.20 are also listed. From the table it can be seen that the degradation of the contrast for cylinders with an outer diameter up to 100 mm is around 1.0, whereas for the cylinder with an outer diameter of 200 mm, CD is about 2.0.

For the hollow cylinder with an outer diameter of 200 mm we calculated also the contrast considering the 1st order of scattering and the 1st plus 2nd order of scattering for the ROIs *Center* and *Max. path length* (figure 4.45). The degradation of the radiographic contrast calculated from the figure is 3.4, 1.92, and 1.55 for C^T, C^{P+1+2}, and C^{P+1}, respectively, considering the ROI *Max. path length*.

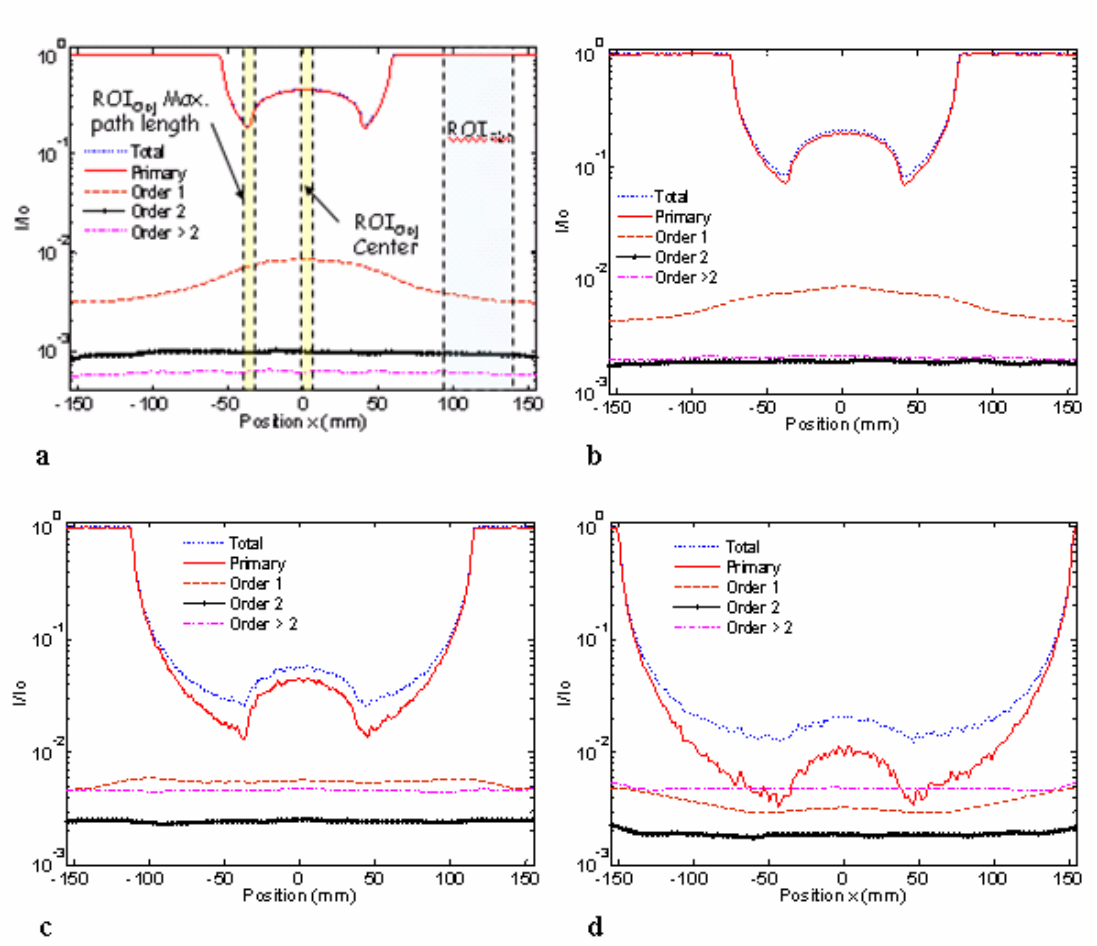

Figure 4.43 Profiles of the energy deposited by total radiation, primary radiation, and 1st, 2nd, and higher order scattering for the hollow cylinder with an outer diameter of (a) 75 mm, (b) 100 mm, (c) 150 mm, and (d) 200 mm. The ROI considered was the 10 x 400 pixels in the center of the detector.

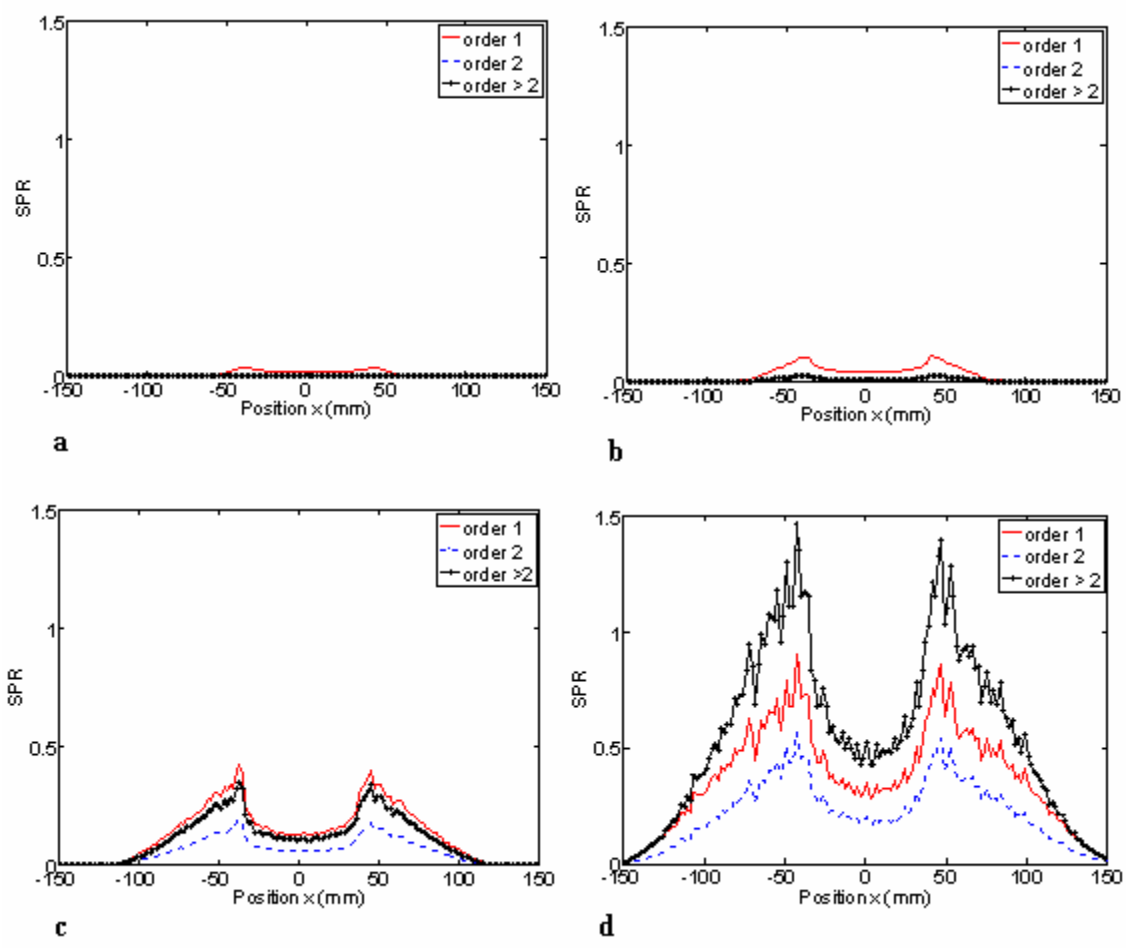

Figure 4.44 Scatter-to-primary ratio for each order of scattering calculated from the profiles of figure 4.43. Hollow cylinder with an outer diameter of (a) 75 mm, (b) 100 mm, (c) 150 mm, and (d) 200 mm.

Table 4.5 Values of contrast calculated in the center using the primary radiation and the total radiation together with the degradation of the radiographic contrast for the hollow aluminum cylinders.

Diameter (mm)	C^P	C^T	CD
75	1.24 ± 0.04	1.20 ± 0.04	1.03
100	3.9 ± 0.1	3.7 ± 0.1	1.05
150	21.3 ± 0.7	16.5 ± 0.5	1.30
200	94 ± 9	48 ± 2	1.96

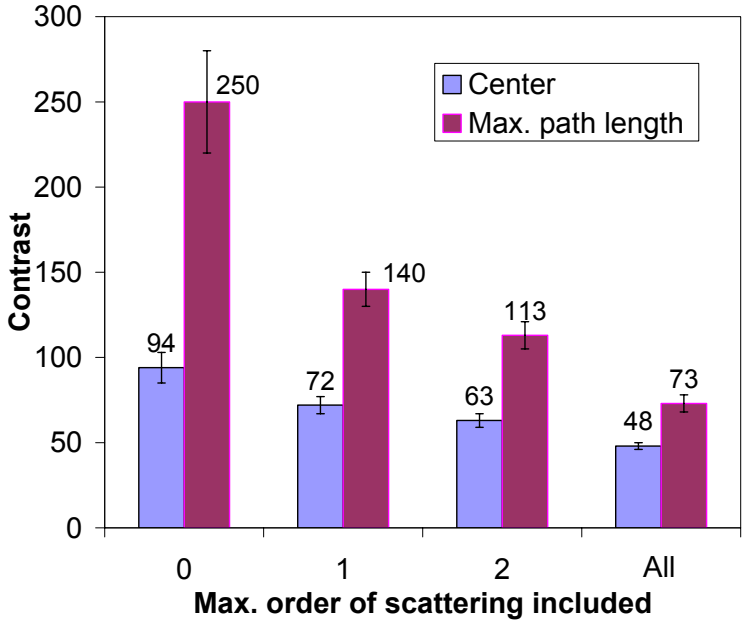

Figure 4.45 Contrast calculated for the hollow cylinder with an outer diameter of 200 mm.

Figure 4.46 shows the simulated radiographies of the boxes of thicknesses 10 and 170 mm and the profiles of the energy deposited by total radiation, first, second, and higher order of scattering together with the scatter-to-primary ratio calculated using Eq. 3.18. The images of the scattered radiation were de-noised using 10 iterations of the Richardson-Lucy fit and a standard deviation of 30 detector pixels. From the figures of the SPR it can be seen that for a thickness of 10 mm the energy deposited by 1st order scattering is lower than 1% of the signal (primary), the 2nd and higher than 2nd order scattering are lower than 0.1%. For the thickness of 170 mm the energy deposited by the 1st order of scattering is lower than 2.5%, the 2nd and higher than 2nd order of scattering are lower than 1%.

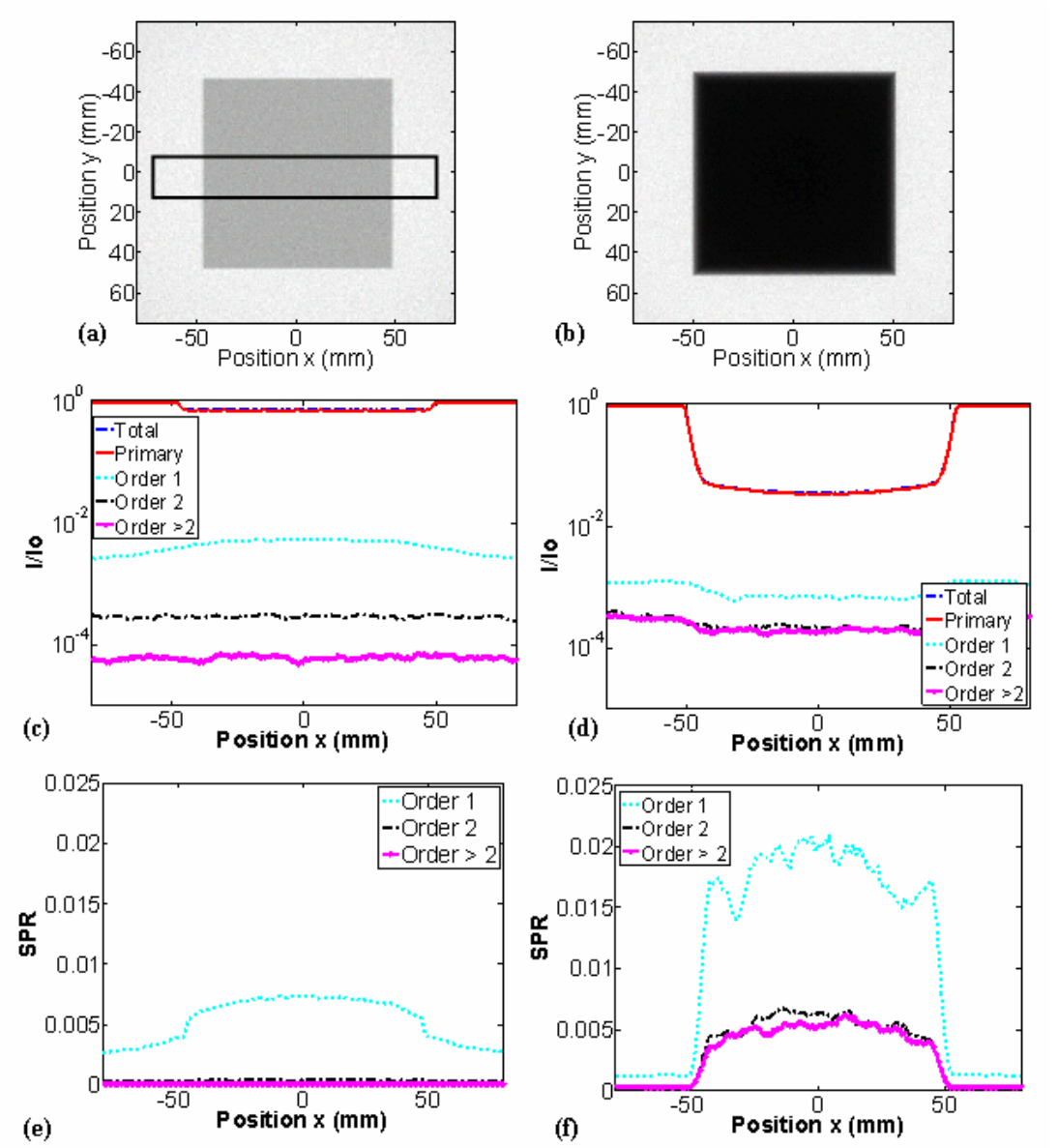

Figure 4.46 Simulated radiographies of the Al box with a thickness of (a) 10 mm and (b) 170 mm. Profiles of the energy deposited by total and primary radiation, and by first, second, and higher order scattering for (c) 10 mm and (d) 170 mm. SPR for (e) 10 mm and (f) 170 mm.

Figure 4.47a shows the normalized energy deposited by total and primary radiation, and first, second, and higher order scattering in function of object thickness. The ROI considered was the central ROI of 70 x 70 pixels. The dependence of the SPR of 1st (SPR_1), 2nd (SPR_2), and higher than 2nd ($SPR_{>2}$) order scattering on object thickness calculated from the data of figure 4.47a is shown in figure 4.47b. As it can be seen from the figure, the ratio between the energy deposited by first order scattering and the energy deposited by primary radiation (SPR_1) is 0.7 for 10 mm, reaches a maximum at a thickness of 90 mm with a value of 4.0 and decreases down to a value of 1.0 for a thickness of 210 mm. The ratio between the energy deposited by second order scattering and the energy deposited by primary radiation (SPR_2) has its maximum at 110 mm; it starts at 0.04 for 10 mm, at its maximum it is 1.0, and slowly decreases down to 0.3 for a thickness of 210 mm. The $SPR_{>2}$ reaches its maximum of 0.7 at 120 mm; it starts at 0.008, and at 210 mm its value is the same as the SPR_2. In fact, increasing the thickness of the object increases the amount of photons that scatter more than once within the object, but after a certain thickness the photons are absorbed within the object itself and the ones that escape the detector have very low energy and are most likely absorbed by the post-filter of 1.0 mm silver or by the support of the scintillator screen of 1.0 mm Al.

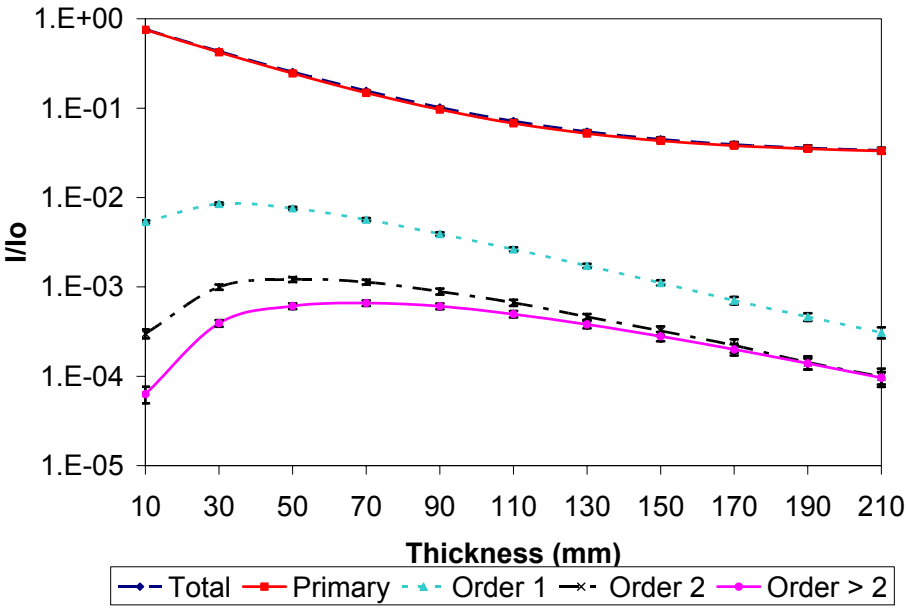

(a)

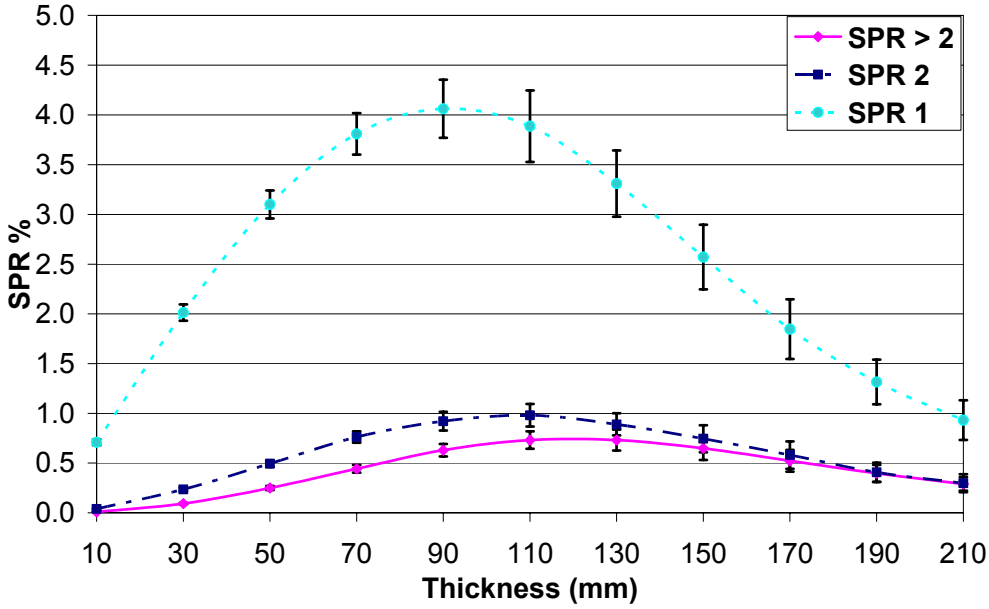

(b)

Figure 4.47 (a) Normalized energy deposited by total, primary radiation, first, second, and higher order of scattering in function of object thickness. (b) SPR calculated from the energy deposited in function of object thickness.

Figure 4.48 shows the simulated radiographies of the Al and Cu hollow cylinders, the profiles of the energy deposited by total radiation, and first, second, and higher order of scattering together with the scatter-to-primary ratio calculated using Eq. 3.18. The value of SPR_1 is 0.07 in the region of maximum path length for aluminum and 0.04 for copper. SPR_2 and $SPR_{>2}$ are around or lower than 0.01 for both cylinders. SPR_1 is higher for the Al than for the Cu cylinder because the probability of Compton scattering is slightly higher for Al than for Cu and because the probability of Compton scattering is higher than the probability of the photoelectric effect for Cu at energies above 140 keV, whereas for Al this point is reached at 52 keV (figure 4.49).

The projections of the Cu hollow cylinder generated by the scattered radiation were de-noised using 20 iterations of the Richardson-Lucy fit and the standard deviation of the Gaussian kernel was set to 40 detector pixels. The projections of the Al hollow cylinder generated by the scattered radiation were de-noised using 10 iterations of the algorithm and a Gaussian kernel of 16 detector pixels.

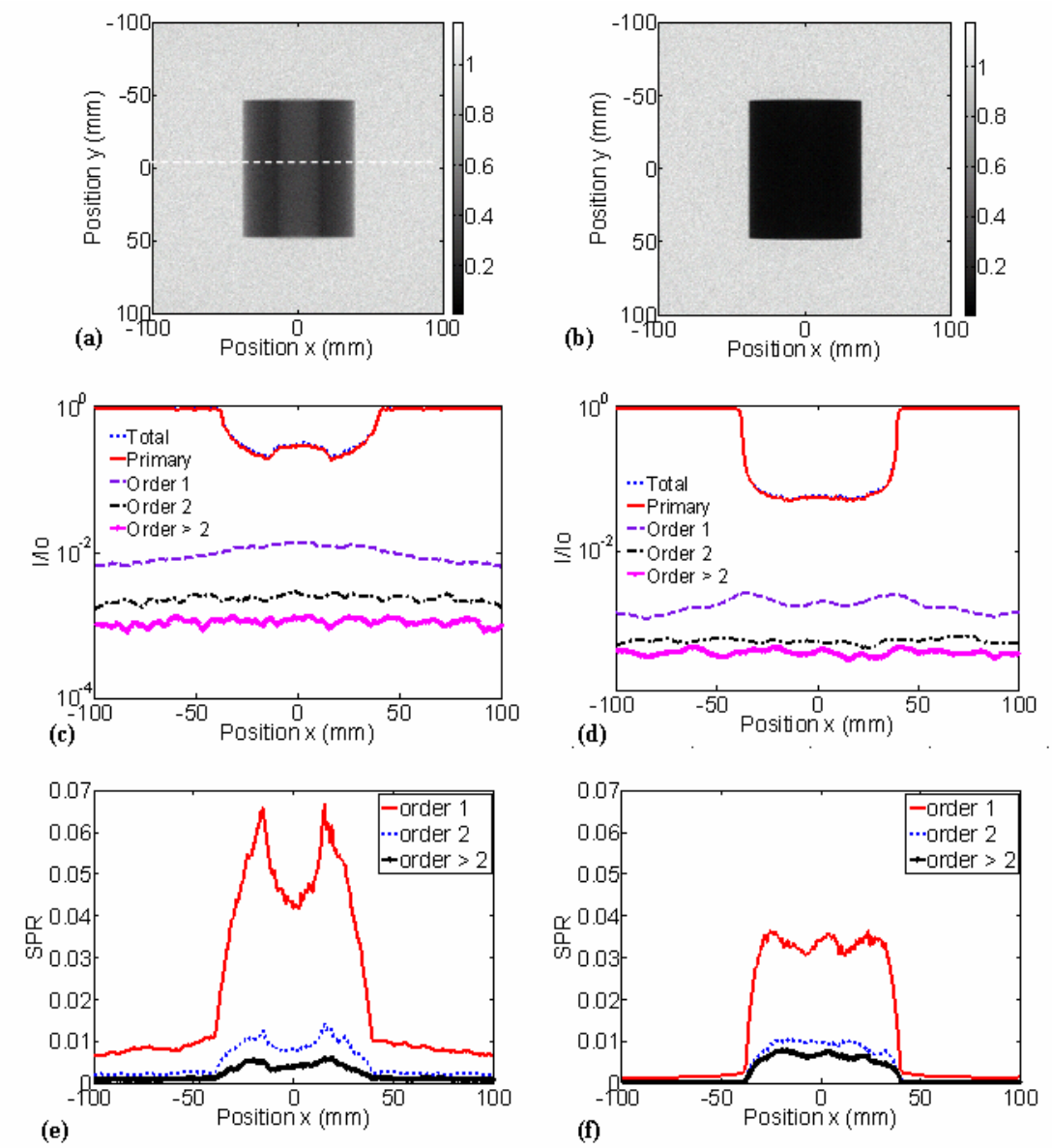

Figure 4.48 Simulated radiographies of the Al (a) and Cu cylinder (b). Profiles of the total and primary radiation, 1st, 2nd, and higher order scattering for the aluminum hollow cylinder (c) and for the hollow copper cylinder (d). SPR calculated from the profiles for the aluminum hollow cylinder (e) and the copper hollow cylinder (f).

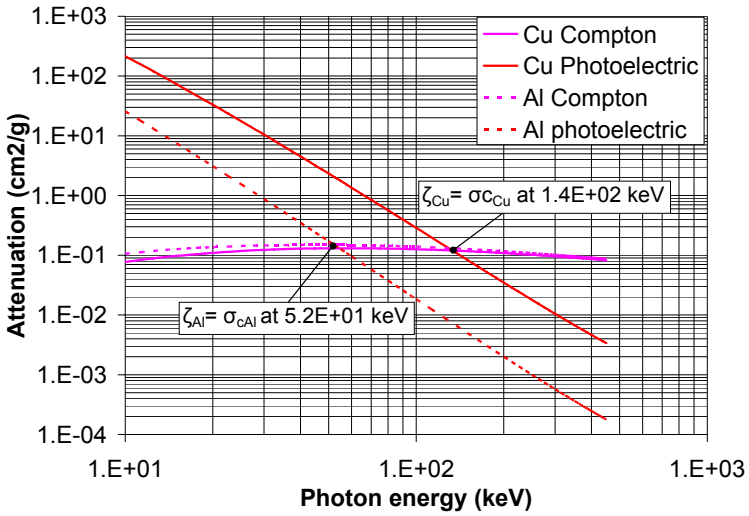

Figure 4.49 Photoelectric and Compton cross section for aluminum and copper. The points where the photoelectric and Compton cross sections have the same value are highlighted.

4.3.2 Environmental scatter

4.3.2.1 Influence of X-ray beam aperture

The profiles of the radiographies acquired using different X-ray source collimators (figure 4.50) show how the environmental scatter contributes to the degradation of the contrast of the radiography. We see clearly that the underestimation of the attenuation increases as the aperture of the X-ray beam (i.e. the background scatter) increases. The value of the degradation of the radiographic contrast defined by Eq. 3.22 calculated from the data of figure 4.50 is 1.22, 1.43, and 1.59 when the collimator n° 2, n° 1, and none are used, respectively. The environmental scatter defined by Eq. 3.23 is 13 %, 22%, and 28% of the measured value when the collimator n° 2, n° 1, and none are used, respectively. The attenuation of the object can be underestimated by 15%, 28%, and 38%, with the collimator n° 2, n° 1, and without collimator, respectively, if the component of the scattering due to the environmental scatter is neglected. The scatter background decreases significantly the contrast and therefore should be reduced using source collimators or evaluated and subtracted from the data. Table 4.6 lists the values of transmission, environmental scatter, fraction of environmental scatter over the measured data $I_{ScattEnv}/I_{Meas}$, and underestimation of the attenuation of the object.

The small dimensions of the room, the material of the walls, the high energy of the X-ray beam, and the CT system structure are the cause of this considerable amount of environmental scatter. The environmental scatter can be reduced placing the CT system in a larger room and optimizing the composition of the walls to reduce the scattering and optimizing the structure of the detector housing. If the system is not modifiable and already installed in a shielding room, the environmental scatter can be evaluated by acquiring a radiograph of the investigated object and performing a simulation with the parameters of the experiment. The difference between the results represents the environmental scatter.

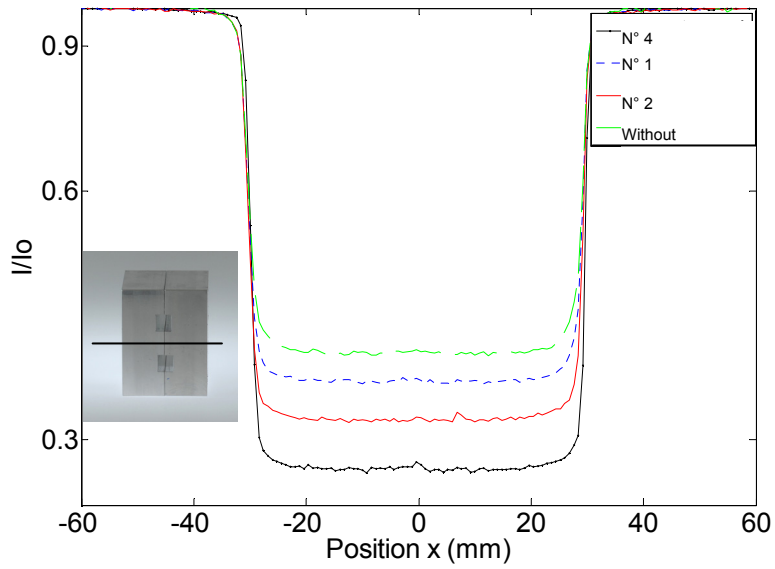

Figure 4.50 Profiles of the aluminum box obtained with the collimators n° 1, 2, and 4 and without a collimator along the central horizontal line.

Table 4.6 Transmission, environmental scatter, percentage of environmental scatter compared to the total for the collimators n° 1, 2, and 4. The result without collimator is also included.

Collimator	$\langle I / I_o(x,y) \rangle_{(x,y)\in ROIObj}$	$I_{EnvScatt}$	$I_{ScattEnv}/I_{Meas}$ %	$EnvScatt_{Error}$
none	0.3828	0.106	28 %	38 %
n° 1	0.3534	0.077	22 %	28 %
n° 2	0.3175	0.041	13 %	15 %
n° 4	0.2768	-	-	-

4.3.2.2 Influence of object thickness

Comparison of simulated and measured projections

Figure 4.51 shows the comparison of simulated and measured reference values (obtained using collimator n° 4 for which the environmental scatter is negligible § 4.1.2) for thicknesses of 10 mm and 190 mm. The slight discrepancy at 190 mm is probably due to the response of the detector, which is not perfectly linear, whereas the response of the simulated detector is linear. In table 4.7 the RMS and the uncertainties calculated using Eq. 3.25 and Eq. 3.26 are listed. The RMS is smaller than the uncertainty for all the thicknesses studied.

Environmental scatter using the collimator n° 2

Figure 4.52 shows the projection acquired with the X-ray source collimator n° 2 and the simulated projection of the aluminum box with a thickness of 210 mm together with the comparison of the central horizontal profiles. The normalized value calculated in the central ROI 70 x 70 pixels of the measured radiograph is 0.088, whereas the value calculated from the simulated radiograph is 0.030. The discrepancy between the simulated and measured data is due to the environmental scatter.

Figure 4.53 shows the environmental scatter defined by Eq. 3.27 in function of the object thickness. The data were interpolated with Eq. 3.28, where $a= -3*10^{-13}$, $b=1*10^{-10}$, $c=1*10^{-8}$, $d=-9*10^{-6}$, e= 0.0013, and f=-0.0047. The value of R-square is 0.9996. From the figure it can be seen that the amount of energy deposited by the environmental scatter increases with increasing object thickness, for thicknesses below 130 mm; above this value the environmental scatter reaches a plateau. That is due to the fact that the probability that a photon is absorbed within the object increases slowly above a certain object thickness.

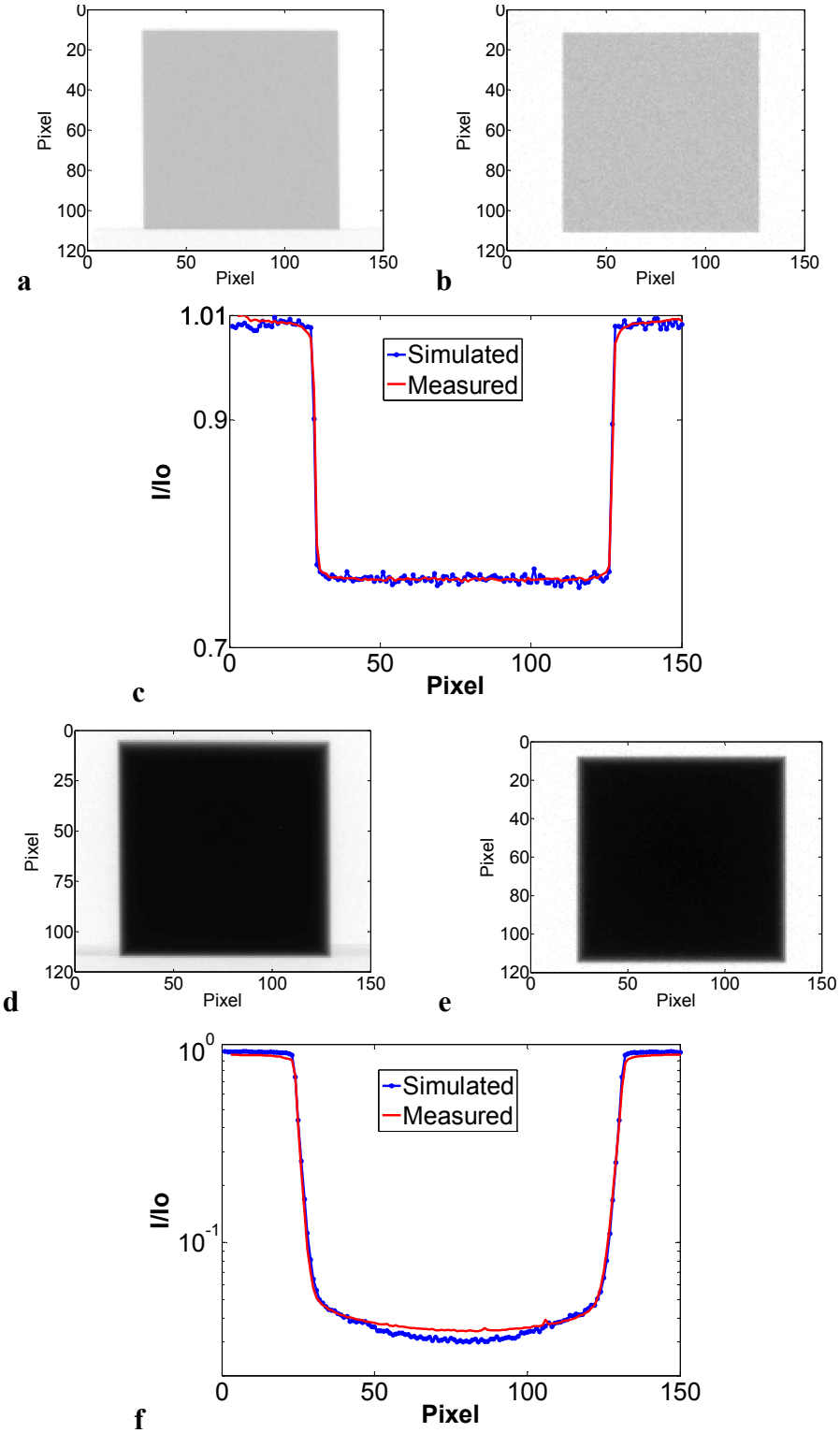

Figure 4.51 The projections of the measured aluminum box of thickness 10 mm (a) and the simulated aluminum box with a thickness of 10 mm (b) together with the comparison of the central horizontal profiles between measured and simulated image are shown (c). Same as above but for the aluminum box with a thickness of 190 mm, illustrating the measured (d) and the simulated (e) projections and the horizontal profiles (f).

Table 4.7 RMS calculated from the simulated and the measured reference profiles.

Thickness (mm)	RMS [10^{-2}]	Uncertainty [10^{-2}]
10	0.25	0.36
30	0.29	0.41
50	0.18	0.54
70	0.17	0.64
90	0.12	0.66
110	0.14	0.71
130	0.18	0.70
150	0.12	0.68
170	0.30	0.68
190	0.16	0.68
210	0.32	0.66

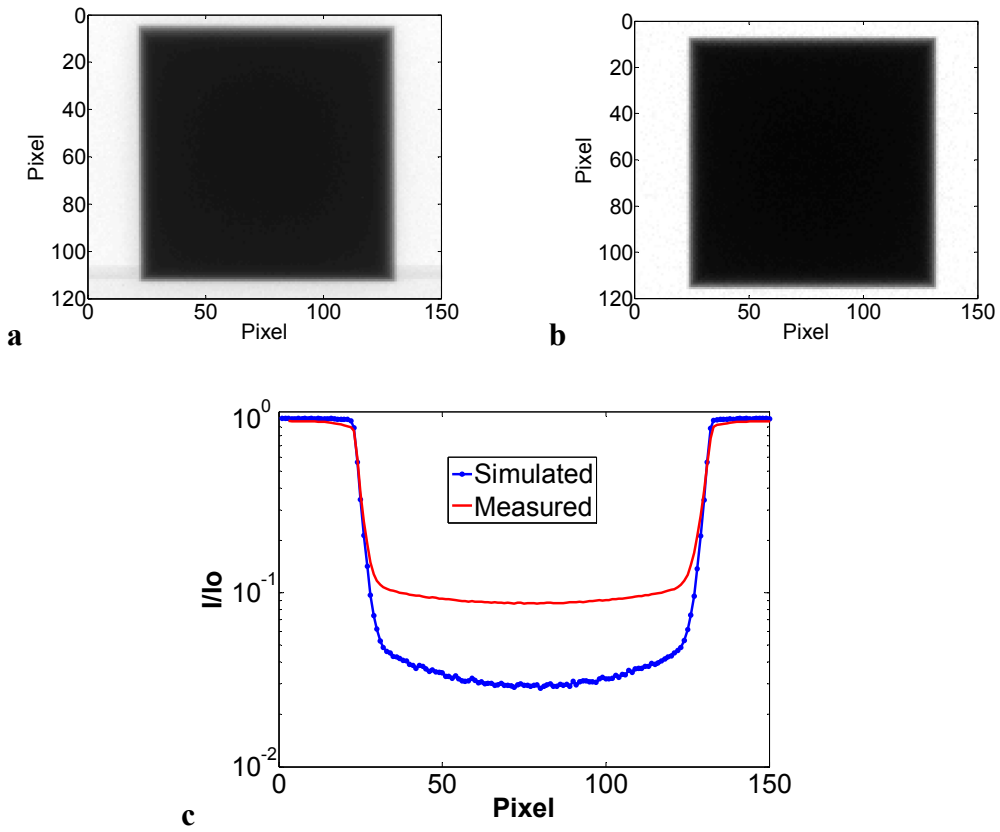

Figure 4.52 Projections of the measured aluminum box of thickness 210 mm (a) and simulated aluminum box of thickness 210 mm (b) together with the comparison of central horizontal profiles between measured and simulated image are shown (c).

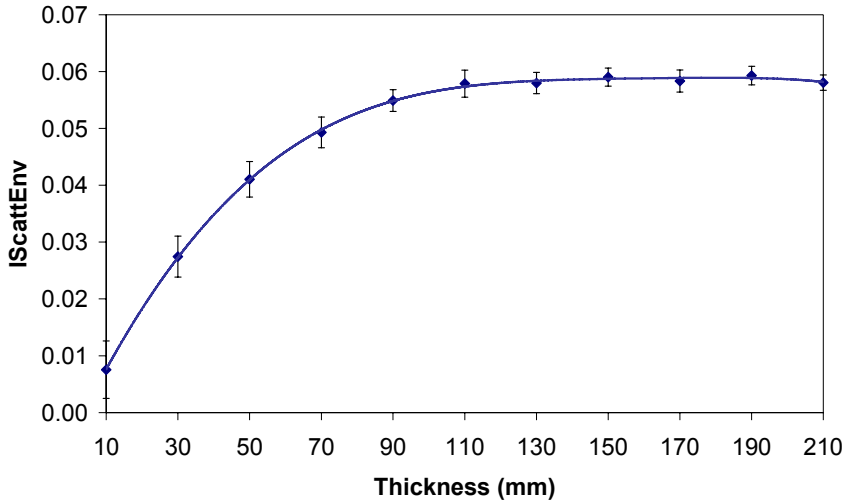

Figure 4.53 Environmental scatter in function of the object thickness for the collimator n° 2.

Figure 4.54 shows the fraction of energy deposited by the environmental scattered radiation over the total energy deposited within the detector. The fraction of environmental scatter increases with the thickness of the object dramatically up to a thickness of 130 mm. For the thickness of 210 mm the fraction of the environmental scatter is 62%. This result means that 62% of the quantity measured by the CT system is due to the environmental scatter and only the 38% of it is due to the primary radiation (signal) plus the scattering generated by the object.

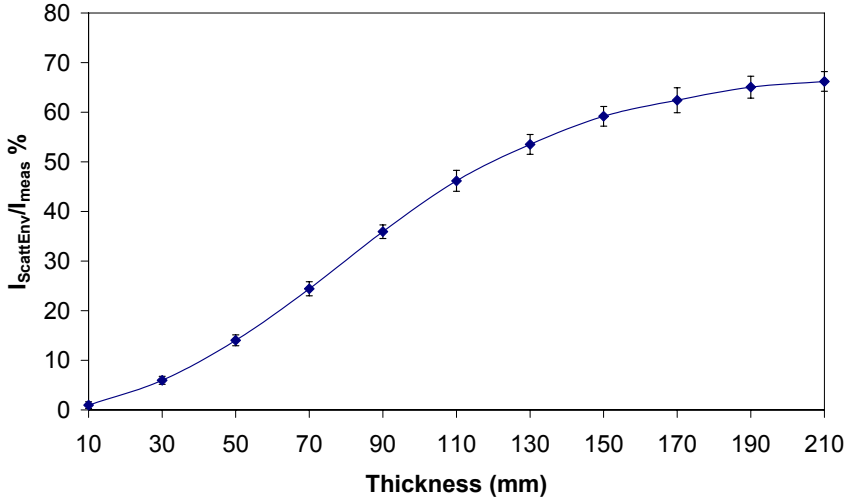

Figure 4.54 Fraction of energy deposited by the environmental scatter over the total energy deposited within the detector.

Figure 4.55 shows the percentage of primary radiation (signal) $I_{primary,}$ scattering generated by the investigated object $I_{ScattObj}$ and scattering created by the walls and CT system structure $I_{EnvScatt}$ in function of the object thickness. The fraction of $I_{EnvScatt}$ is higher than 50% for thicknesses above 130 mm. The amount of $I_{EnvScatt}$ is higher than the primary radiation for thicknesses equal or higher than 130 mm. The scatter from the object is much lower than the scatter from the environment. At 130 mm $I_{ScattObj}$ is less than 3%, whereas the fraction of environmental scatter is 51 % and at 210 mm $I_{ScattObj}$ is less than 1%, whereas the fraction of environmental scatter is 63 %.

Table 4.8 shows the underestimation of the attenuation when the scatter from the object and the scatter from the object plus the environmental scatter, respectively, are not removed from the data. When we consider the 10 mm thick object the attenuation can be underestimated by 0.8%, if the component of the scattered radiation from the object is neglected and by 1.4%, if also the component of the scattered radiation from the environment is neglected. In case of 210 mm thick object, the attenuation can be underestimated by 1.5%, if the component of the scattered radiation from the object is neglected and by 160%, if also the component of the scattered radiation from the environment is neglected. Therefore, to reduce the artifacts in the CT images due to the scattered radiation it is necessary to take into account also the environmental scatter, which was found to be the major source of scattering in the CT system studied.

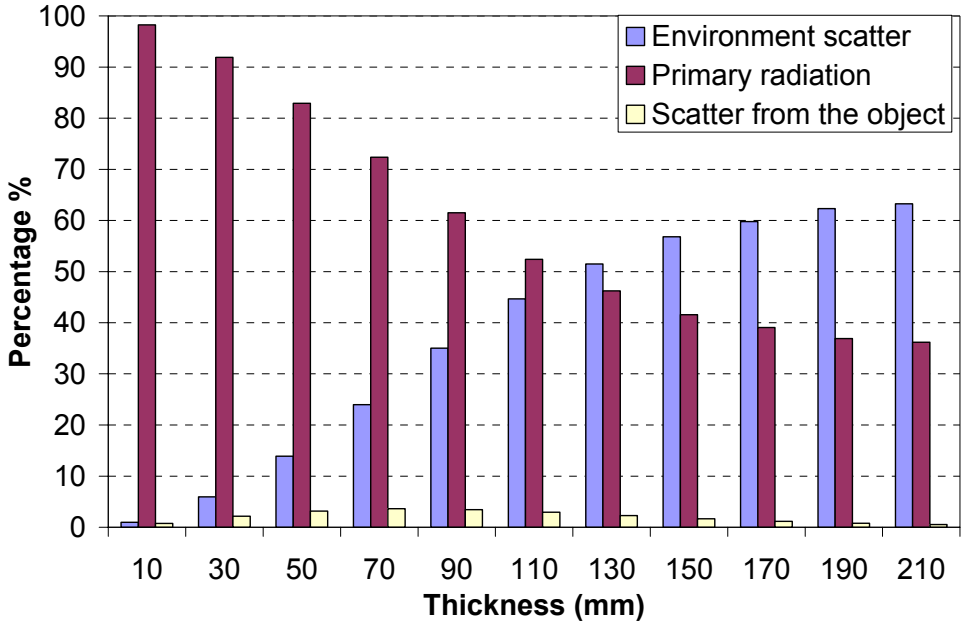

Figure 4.55 Percentage of the different components of the measured signal $I_{measured}$ for the collimator n° 2.

Table 4.8 Error in the calculation of the attenuation due to the scattered radiation.

Thickness (mm)	$Error_{ObjScatt}$ %	$Error_{ObjScatt+EnvScatt}$ %
10	0.8	1.4
30	2.3	8.2
50	3.8	18.7
70	5.0	34.1
90	5.6	54.0
110	5.6	77.8
130	4.9	100.0
150	4.0	120.5
170	3.0	139.8
190	2.1	146.2
210	1.5	156.6

Environmental scatter using the collimator n° 3

Figure 4.56 shows the environmental scatter in function of object thickness for the configuration with the collimator n°3. The data in the figure were interpolated using Eq. 3.28, where $a=4*10^{-13}$, $b=-3*10^{-10}$, $c=1*10^{-7}$, $d=2*10^{-5}$, e= 0.0016, and f=-0.0089. The value of R-square is 0.9991. As expected, the curve has the same behavior as the curve obtained with the collimator n° 2.

Figure 4.57 shows the comparison of environmental scatter for the collimators n° 3 and n° 2. With the collimator n° 3 we have a lower amount of environmental scatter despite the fact that the area irradiated on the detector is slightly larger (the area illuminated by the collimator n° 3 is 741 cm^2 and the area illuminated by the collimator n°2 is 737 cm^2). That is due to the fact that with the collimator n° 3 the lateral walls of the detector box are not illuminated by the direct X-ray beam, whereas with the collimator n° 2 they area illuminated (figure 4.58). Therefore, we conclude that the lateral walls of the detector box have a small influence on the environmental scatter.

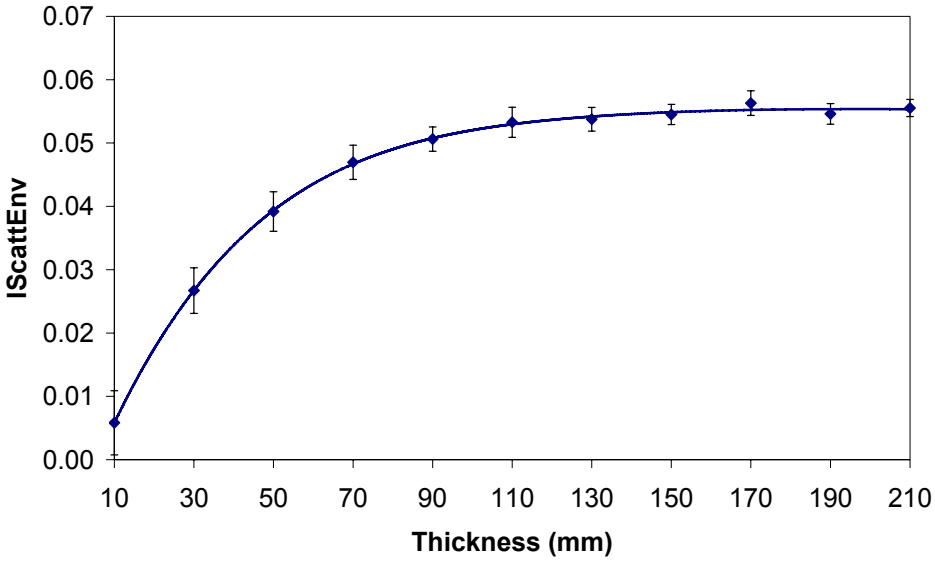

Figure 4.56 Environmental scatter in function of the object thickness for the collimator n° 3.

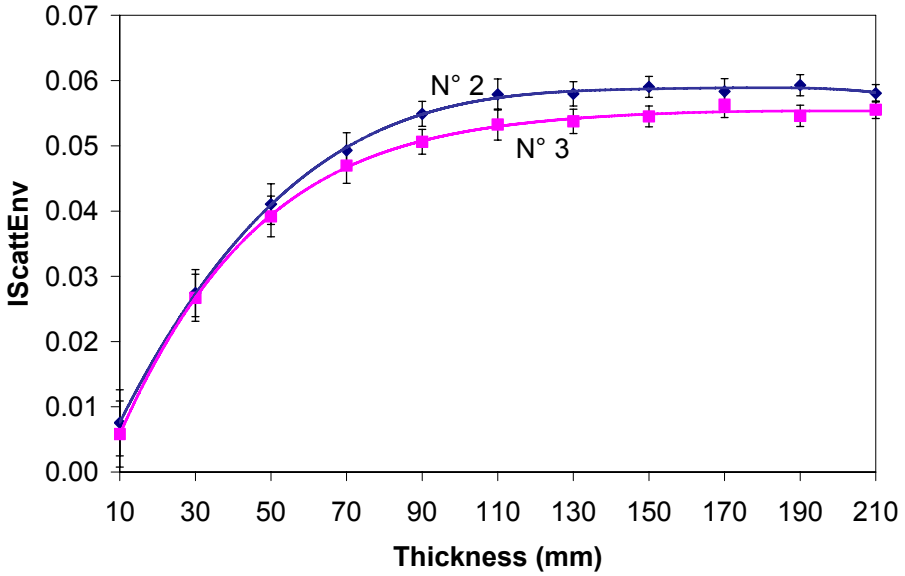

Figure 4.57 Comparison of the environmental scatter in function of the object thickness for the collimators n° 2 and n° 3.

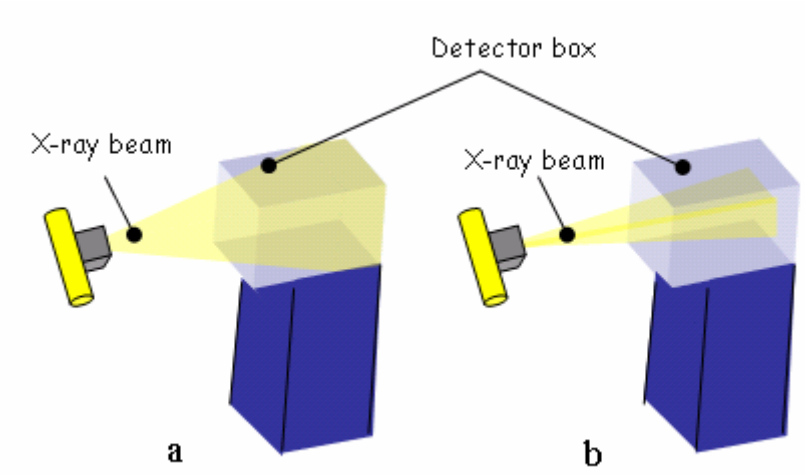

Figure 4.58 Sketch of the region of the detector box irradiated when the collimator n° 2 (a) and n° 3 (b) is employed.

4.4 Correction of the scattering in the reconstructed images

Figure 4.59a shows the uncorrected reconstructed image of the hollow aluminum cylinder with an outer diameter of 180 mm. Figure 4.59b shows the image reconstructed using the scatter correction algorithm developed by Dr. R. Thierry at Empa [2]. The projections generated by the 1st, 2nd, and higher than 2nd order scattering simulated with the validated MC code and the value of the environmental scatter defined by Eq. 3.27 evaluated with the results of the MC simulations are the input for the scatter correction algorithm. Figure 4.59c shows the profiles of the uncorrected and corrected reconstructed images. As we can see, thanks to the correction of the scattering, the cupping effect in the image is strongly reduced. Nevertheless, part of the cupping effect is still present. That may be due to the implementation of the scatter correction algorithm.

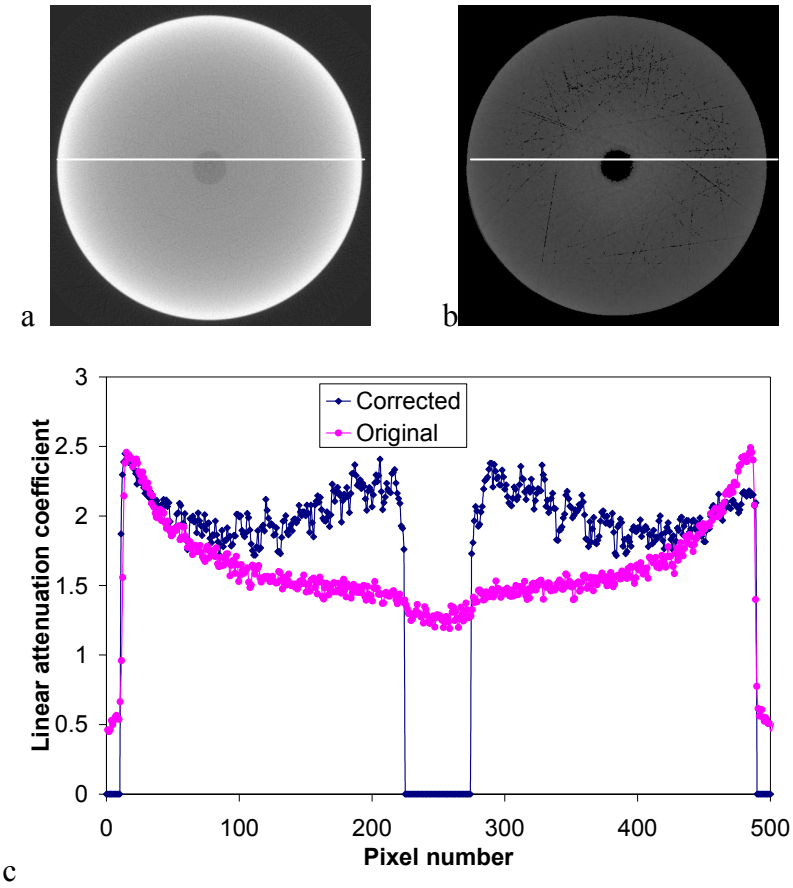

Figure 4.59 Images of the measured hollow aluminum cylinder reconstructed with the statistical reconstruction software developed at Empa before (a) and after (b) the correction together with the comparison of central horizontal profiles between corrected and non corrected images (c).

4.5 Anti-scatter grids

4.5.1 Optimization of anti-scatter grids

4.5.1.1 2D anti-scatter grids

Parallel grids

Figure 4.60 shows the dependence of the transmittance of primary and scattered radiation on height of the strips h, if the thickness of the interspace D is constant (see figure 3.15). From the figure it can be seen that T_p and T_s decrease with increasing h. Figure 4.61 shows the dependence of the transmittance of primary and scattered radiation on D, if h is constant. We see that T_p and T_s increase with increasing D.

Table 4.9 shows the selectivity for the parallel 2D anti-scatter grids studied. If D is constant, the selectivity increases with increasing h for h smaller or equal to 5 mm, then it decreases. For constant h, the selectivity increases with increasing D for D smaller or equal to 0.6 mm, then it decreases. That is due to the fact that the grid is not focused in the direction of primary X-ray photons. When we compare grids having the same parameters but different materials (gold and lead) we see that the grid of gold has better performance in terms of selectivity. In conclusion, the best parameters for the 2D parallel anti-scatter grids studied are h 5 mm, D 0.6 mm, and d 0.2 mm. However, the selectivity is not higher than 2.2.

In a cone-beam CT system where the area irradiated on the detector is quite large (approx. 40 x 30 cm^2) it is necessary to employ an anti-scatter grid that takes into account the direction of the primary X-ray photons, so that they are not attenuated by the grid in the interspaces.

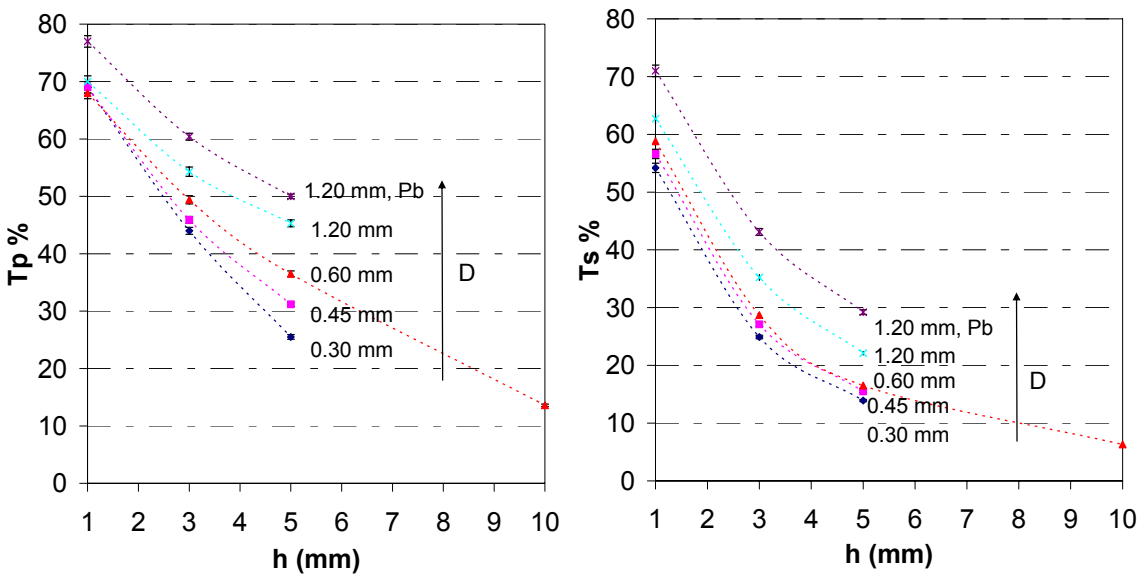

(a) (b)

Figure 4.60 Dependence of the transmittance of primary (a) and scattered (b) radiation on height of the gold strips for grids with thickness of the interspace ranging from 0.30 and 1.20 mm and material-to-interspace ratio 1/3. The results for the lead grid are also illustrated.

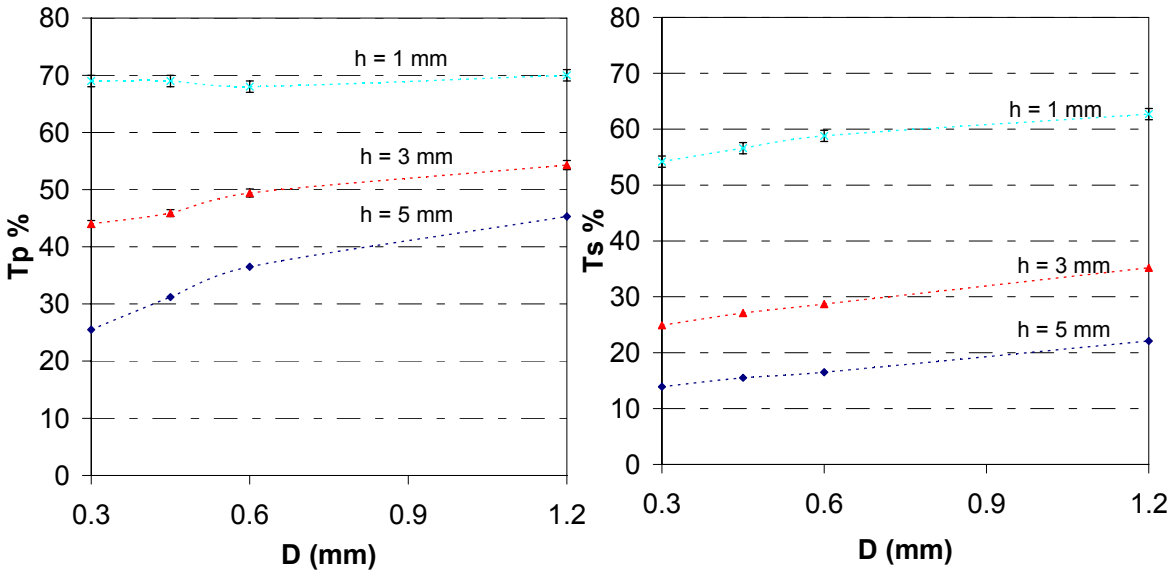

(a) (b)

Figure 4.61 Dependence of the transmittance of primary (a) and scattered (b) radiation on the thickness of the interspace for gold grids with height of the strips ranging from 1 and 5 mm and material-to-interspace ratio 1/3.

Table 4.9 Selectivity for the 2D parallel anti-scatter grids.

Material	D (mm)	d (mm)	h (mm)	Σ
Au	0.3	0.1	1	1.27 ± 0.04
	0.3	0.1	3	1.77 ± 0.05
	0.3	0.1	5	1.84 ± 0.05
	0.45	0.15	1	1.22 ± 0.03
	0.45	0.15	3	1.69 ± 0.05
	0.45	0.15	5	2.01 ± 0.06
	0.6	0.2	1	1.16 ± 0.03
	0.6	0.2	3	1.72 ± 0.05
	0.6	0.2	5	2.21 ± 0.06
	0.6	0.2	10	2.16 ± 0.06
	1.2	0.4	1	1.11 ± 0.03
	1.2	0.4	3	1.54 ± 0.04
	1.2	0.4	5	2.06 ± 0.06
Pb	1.2	0.4	1	1.07 ± 0.03
	1.2	0.4	3	1.40 ± 0.04
	1.2	0.4	5	1.71 ± 0.05

Focused grids

Table 4.10 shows the Tp, Ts, and selectivity of the 2D focused anti-scatter grids made of gold for several heights of the strips h, thicknesses of the strips d, and thicknesses of the interspace D. Moreover, the results for a grid made of LaserFormST-100 are shown. The results show that the material is inappropriate for the construction of a grid because of the low selectivity compared to gold with the same height and thickness of the strips. From the table it can be seen that when D is constant the selectivity increases with increasing h. That is due to the fact that the grid is focused in the direction of the X-rays. When h is constant the selectivity increases as D decreases.

If we compare a parallel grid and a focused grid with the same parameters we see that the selectivity of the focused grid is higher than the selectivity of the parallel grid, because, as explained above, the focused grid takes into account the direction of the primary X-ray photons that are therefore not attenuated in the interspaces.

In conclusion, among the studied configurations the best parameters of a 2D focused anti-scatter grid for a CT system working at 450 kV are D 0.45 mm, h 15 mm, and d 0.15 mm. Unfortunately, up to now, it is not possible to manufacturer large grids (40 cm) with these parameters. For that reason, we focused our attention on 1D anti-scatter grids.

Table 4.10 Transmission of primary and scattered radiation and selectivity of the 2D focused anti-scatter grids.

Material	D (mm)	d (mm)	h (mm)	Tp	Ts	Σ
Au	0.45	0.15	5	0.560±0.008	0.193 ±0.003	2.90±0.08
	0.45	0.15	15	0.522±0.007	0.103±0.001	5.0±0.1
	0.6	0.2	1	0.71±0.01	0.588±0.008	1.20±0.03
	0.6	0.2	3	0.592±0.008	0.303±0.004	1.96±0.05
	0.6	0.2	5	0.580±0.008	0.205±0.003	2.83±0.08
	0.6	0.2	10	0.532±0.007	0.122±0.002	4.4±0.1
	0.6	0.2	15	0.539±0.008	0.109±0.002	4.9±0.1
	1.2	0.4	15	0.517±0.007	0.113±0.002	4.6±0.1
	2.4	0.8	15	0.548±0.008	0.141±0.002	3.9±0.1
LaserForm ST-100	2.4	0.8	15	0.670±0.009	0.69±0.01	0.97±0.03

4.5.1.2 1D anti-scatter grids

Figure 4.62 shows the dependence of the transmission of primary and scattered radiation, selectivity, and scatter-to-primary ratio on the height of the strips h for 1D focused anti-scatter grids made of tungsten with 5 mm interspace and 5 mm strips (see figure 3.16). From the figure it can be seen that the selectivity and the SPR improve drastically with increasing h, for values of h smaller than 40 mm; above this value the SPR increases slowly. We concluded that the suitable height of the strips for the studied configuration (450 keV) is 40 mm.

Figure 4.63 shows the dependence of T_p and T_s on the grid ratio for grids with a thickness of the strips ranging from 1 to 10 mm and a height of the strips of 40 mm. T_p

and T_s decrease with increasing grid ratio due to the decrease of the solid angle defined by the space between the strips. T_p and Ts decrease with increasing d.

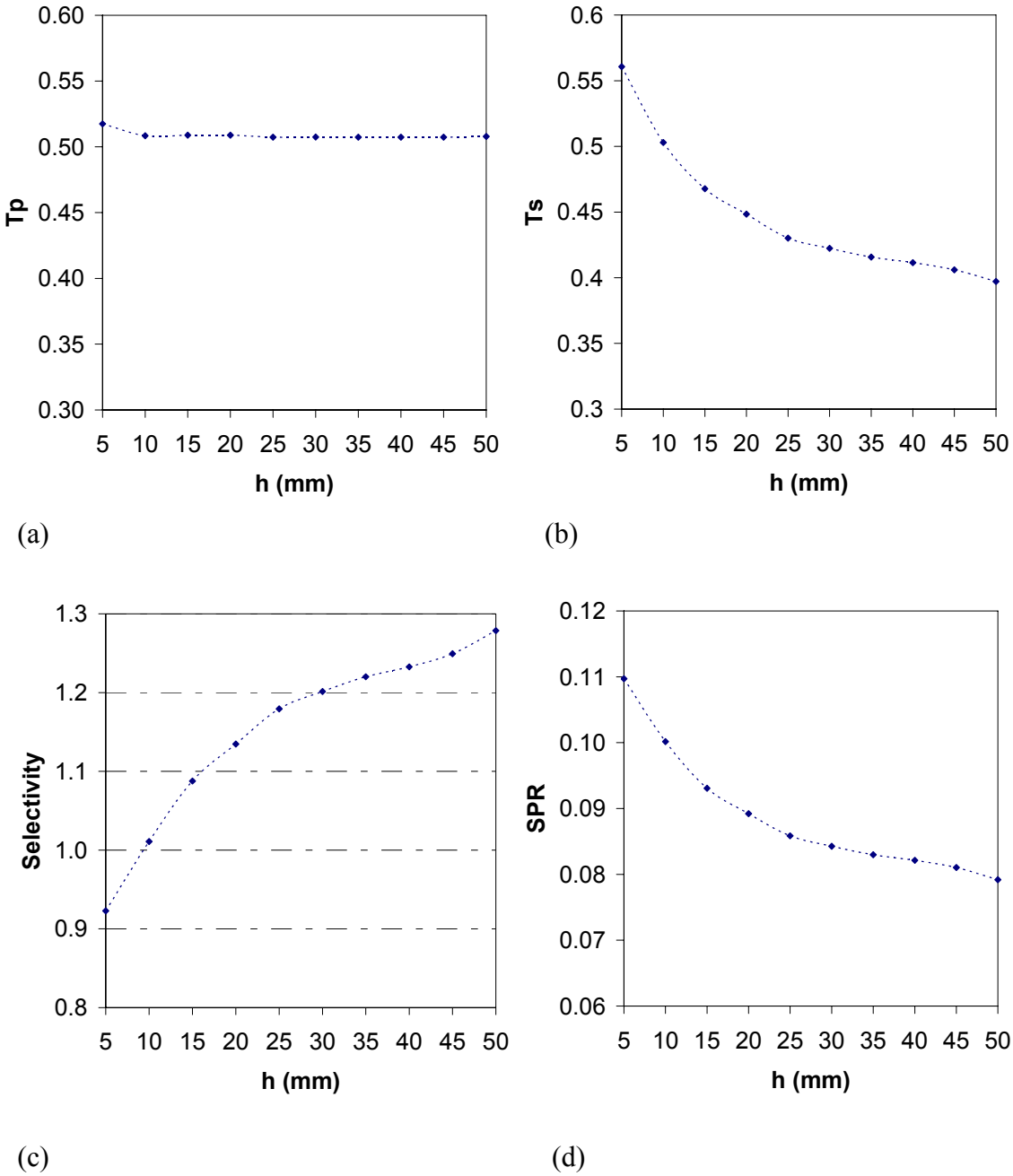

Figure 4.62 Dependence of the transmission of primary and scattered radiation, selectivity and scatter-to-primary ratio on the height of the strips h for grids with a thickness of the interspace of 5 mm and of the strips of 5 mm.

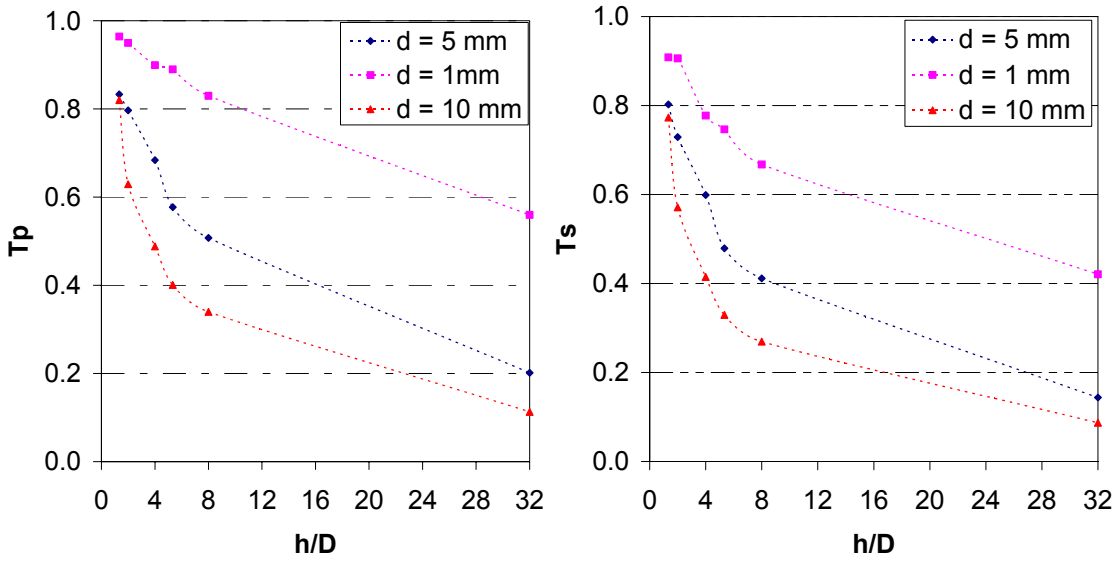

(a) (b)

Figure 4.63 (a) Dependence of the transmittance of the primary radiation on the grid ratio for grids with a thickness of the strips ranging from 1 to 10 mm and a height of 40 mm. (b) Dependence of the transmittance of scattered radiation on the grid ratio for grids with a thickness of the strips ranging from 1 to 10 mm and a height of 40 mm.

Figure 4.64 compares the performance of the anti-scatter grids evaluated in terms of scatter-to-primary ratio (SPR) and acquisition time factor, for grids with a height of the tungsten strips of 40 mm, d ranging from 1 to 10 mm constant along each curve, and a grid ratio ranging from 4/3 to 32. From the figure and taking into account that a focused anti-scatter grid with *d* too low will bend, we found that the parameters for an anti-scatter grid suitable for the studied CT system working at 450 kV are: *d* 5mm, grid ratio 16/3, and height 40 mm. This grid is a good compromise in terms of SPR (0.084) and acquisition time factor (1.73). The amount of energy deposited by the photons leaving the grid (passing through without interacting or scattered by the grid) is less than 5 % of the total energy deposited.

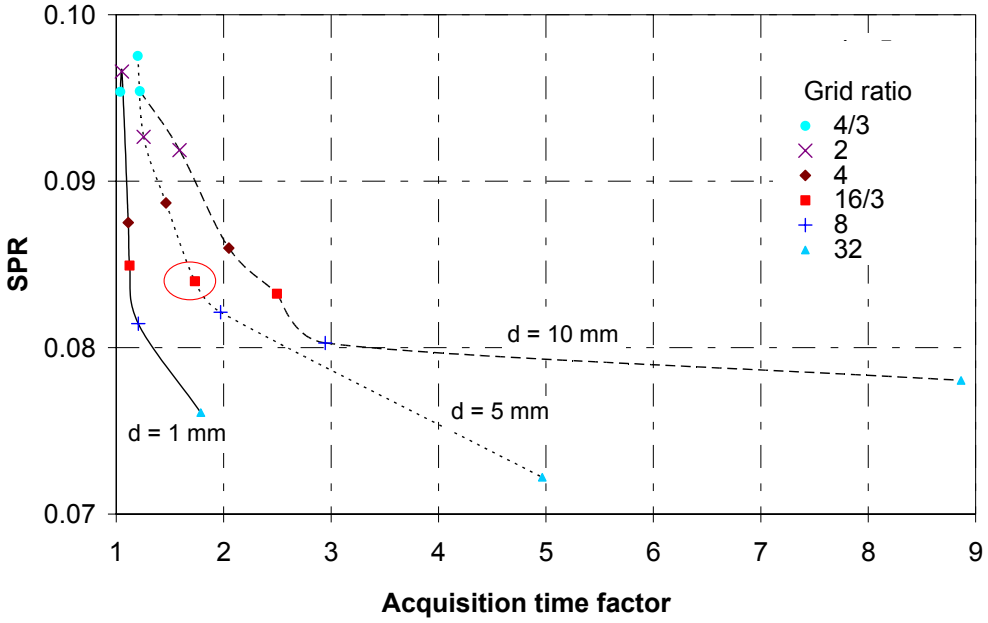

Figure 4.64 Relationships between the scatter-to-primary ratio and the acquisition time for grids with an interspace ranging from 4/3 to 32 mm and a thickness of the strips ranging from 1 to 10 mm. The grid chosen is highlighted.

4.5.2 Efficiency of the anti-scatter grid

An example of the efficiency of the anti-scatter grid, which was optimized using the MC simulation, is shown in figure 4.65. The figure shows the reconstructed image of a hollow aluminum cylinder with an outer diameter of 180 mm acquired using the CT system with the 1D focused anti-scatter grid and the reconstructed image of the object acquired in absence of the grid. From the figure it can be seen that the cupping artifact is reduced by the anti-scatter grid. The remaining cupping is due to the beam hardening that here was not corrected and to the scattering generated by the CT system structure, the walls and the investigated object that was not stopped by the grid. The value of the contrast of the reconstructed images calculated from Eq. 3.16 with and without the grid is 0.45 and 0.35, respectively. The improvement due to the use of the anti-scatter grid depends on the investigated object as well as on the settings of the acquisition (source object distance, source collimator, etc.).

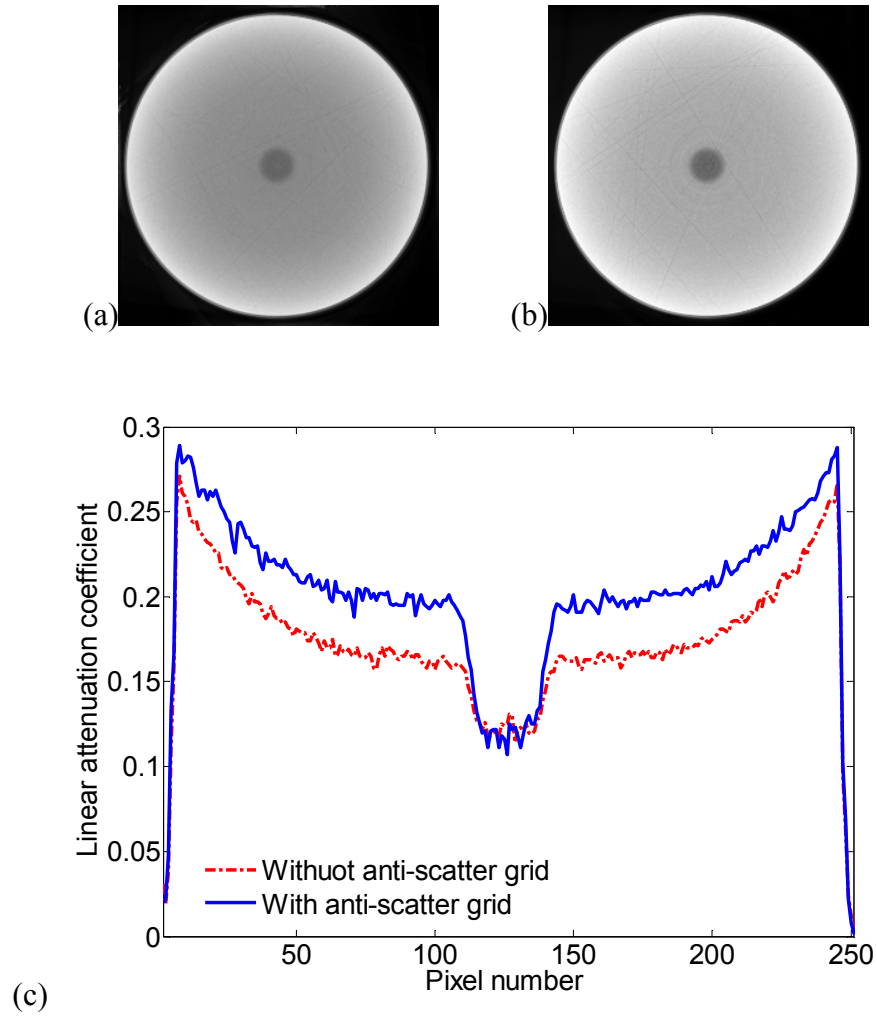

Figure 4.65 Images of the measured hollow aluminum cylinder reconstructed using the statistical reconstruction developed at Empa without (a) and with anti-scatter grid (b) together with the comparison of central horizontal profiles (c) are shown. The images were reconstructed without beam hardening correction.

4.6 Complex objects

Figure 4.66 shows a simulated projection of the T-shape test object described in § 3.8 together with the simulated image generated by the scattered radiation, which represents the information necessary to correct the reconstructed images. The first-order, second-order, and higher-order scattering were considered. The image of the scattered radiation was de-noised using 10 iterations of the Richardson-Lucy fit and a standard deviation of the Gaussian kernel of 30 detector pixels. The images were normalized to the mean value of a ROI located outside the shadow of the object, in the image generated by the primary radiation.

The possibility of simulating objects defined by STL-files is an important feature of the developed MC simulation, since the objects investigated by CT systems are often too complex to be described by simply adding, subtracting, or intersecting standard forms (tubes, cones, boxes, etc.). The drawback of simulating objects using STL-files is the simulation time that, in the case of very complex geometries, increases considerably compared to the simulation time needed to simulate standard forms. High performance computers, grid technology, and parallelization can be a solution.

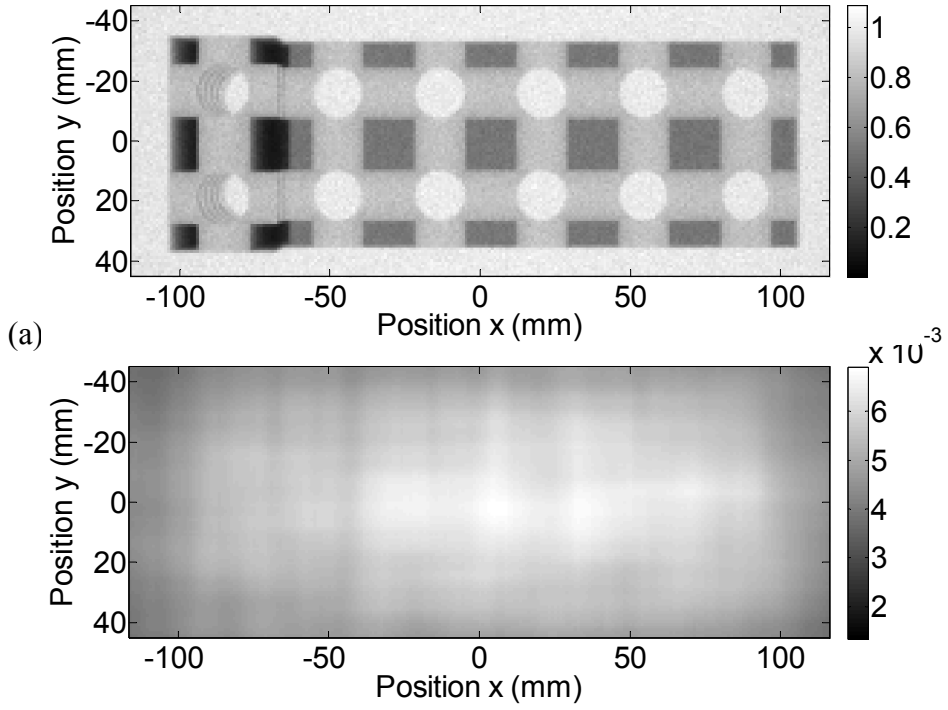

Figure 4.66 (a) Simulated radiography of the T-shape test object with holes of 13 mm diameter. (b) Image of the test object generated by the scattered radiation de-noised using the Richardson-Lucy fit.

4.7 References

1. Flisch, A. and J. Wirth, *Industrial computed tomography in reverse engineering applcations.* Int. symposium on computerized tomography for industrial applications and image processing in radiology, Berlin, 1999.
2. Thierry, R., Miceli, A., Hofmann, J., Flisch, A., Sennhauser, U., *Hybrid Simulation of Scatter Intensity in Industrial Cone Beam Computed Tomography.* Nuclear Instruments & Methods in Physics Research Section A, 2007(Submitted).

5 Conclusions and future work

The Department of Physics of the University of Bologna has developed an industrial cone-beam tomography system equipped with a 450 kV X-ray tube. This work has been carried out in the framework of the European project DETECT. The performance of the CT system has been tested for several objects. For small objects (50 x 50 x 50 mm^3) the system provides excellent results, whereas for larger objects, as for instance cylinder heads or turbine blades, the scattered radiation leads to a degradation of the image quality. Aim of this thesis work was the investigation and the reduction of the scattering in the CT system and its optimization. Simulations and experimental measurements were carried out. A GEANT4-based Monte Carlo model of the CT system has been developed and experimentally validated using CT scans of several test objects. The simulated projections were in excellent agreement with the measured data. The model was used to optimize the hardware components of the CT system as well as to investigate and to reduce the scattering created by the object and by the CT system structure and X-ray room (environmental scatter). The images of the energy deposited within the scintillator by first, second, and higher order scattering were calculated for objects of different sizes, shapes, and materials. In the case of objects resembling the ones commonly investigated in industrial CT, the results show that the multiple scattering is 2.3 times the primary radiation. This result leads us to conclude that the evaluation of multiple scattering is of primary importance for the optimization of industrial cone-beam CT systems. Studies of environmental scatter on aluminum boxes of front size 70 x 70 mm^2 have shown that the environmental scatter is the major component of the scattered radiation and that its value varies in function of the size of the investigated object. We conclude that the environmental scatter represents a key factor in the achievement of high image quality and that it should be evaluated for each projection. For that reason, in the future, further studies on the reduction of the environmental scatter have to be carried out.

The quality of the CT images that were reconstructed using the scatter correction algorithm, where the object and environmental scatter were taken into account, is considerably improved compare to the quality of the uncorrected images, even if the cupping effect, although reduced, is still present. The investigation of the parameters of an anti-scatter grid by means of the developed MC code has resulted in the construction of a 1D focused anti-scatter grid optimized for the CT system. The reconstructed images of a test object acquired with and without the optimized anti-scatter grid show a clear improvement of the image quality due to the presence of the grid, even if a post acquisition correction of the scattering is still necessary to obtain a high image quality.

The developed model enables the simulation of objects of any complexity. That is fundamental for industrial applications, where often the investigated objects are too complex to be expressed as a combination of simple forms. However, in case of very complex object geometries, the simulation becomes computationally too intensive to be used for simulating sets of projections; future work is needed to decrease the simulation time.

This work demonstrates that the developed MC code of the industrial X-ray CT system is an accurate, powerful, and useful tool to investigate and reduce the object and environmental scattering and to optimize the components of the CT system. In addition, this approach may be used to aid the design of X-ray rooms. The developed MC model for the simulation of the X-ray spectrum, which has been validated by comparison with measured data, is itself a useful tool to generate X-ray spectra of industrial X-ray tubes. Some examples of applications of the MC model of the energy spectrum are the algorithms for the correction of beam hardening and deterministic simulations. The developed MC simulation together with the improved reconstruction algorithm have allowed cone-beam CT with the same 3D-spatial resolution as state-of-the-art well collimated 2D-CT bringing the advantage of a reduction of the acquisition time of a factor 10. The results open new interesting applications in non-destructive testing and evaluation, *first article inspection*, and *reverse engineering* with a high economic impact.

Appendix

A.1 Tutorial CT software

Double-click on the “RayScan” icon.

The following window will appear containing the window for the initialization of the manipulator, X-ray tube and detector. Click **Start**.

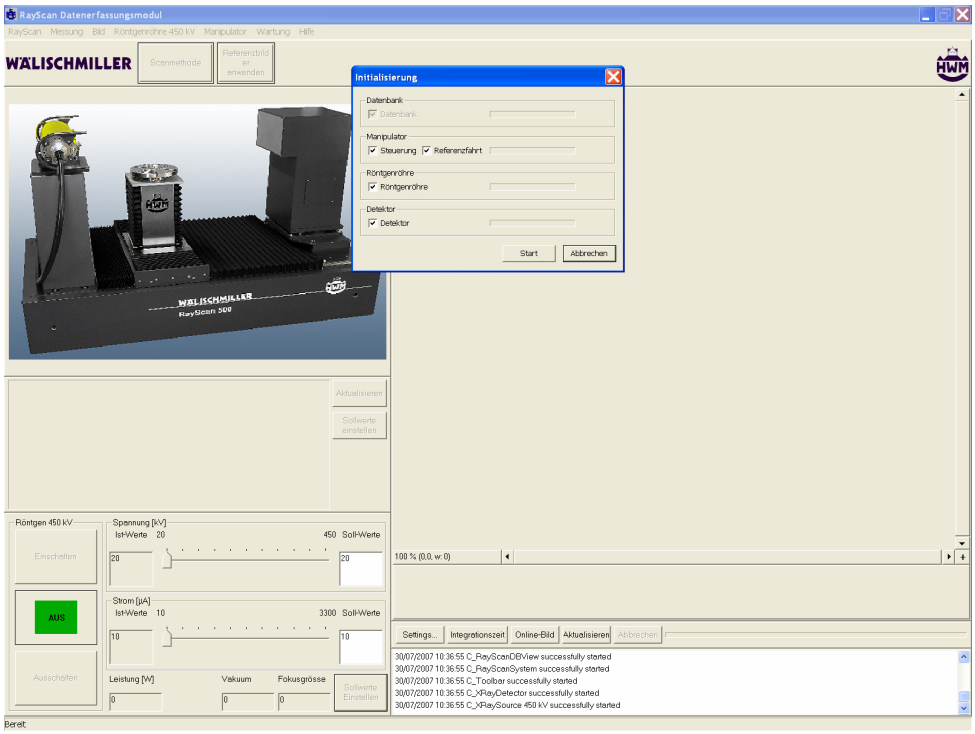

When the initialization is completed the following window will appear. Click **OK**.

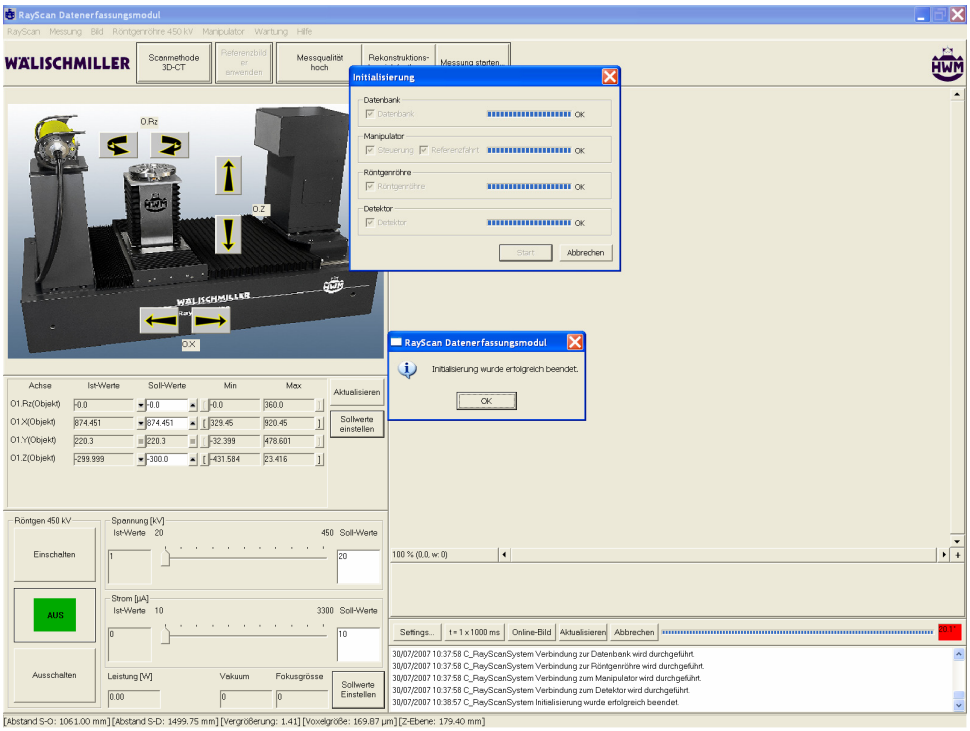

From the **Messung** menu, select **Laden Einstellungen.**

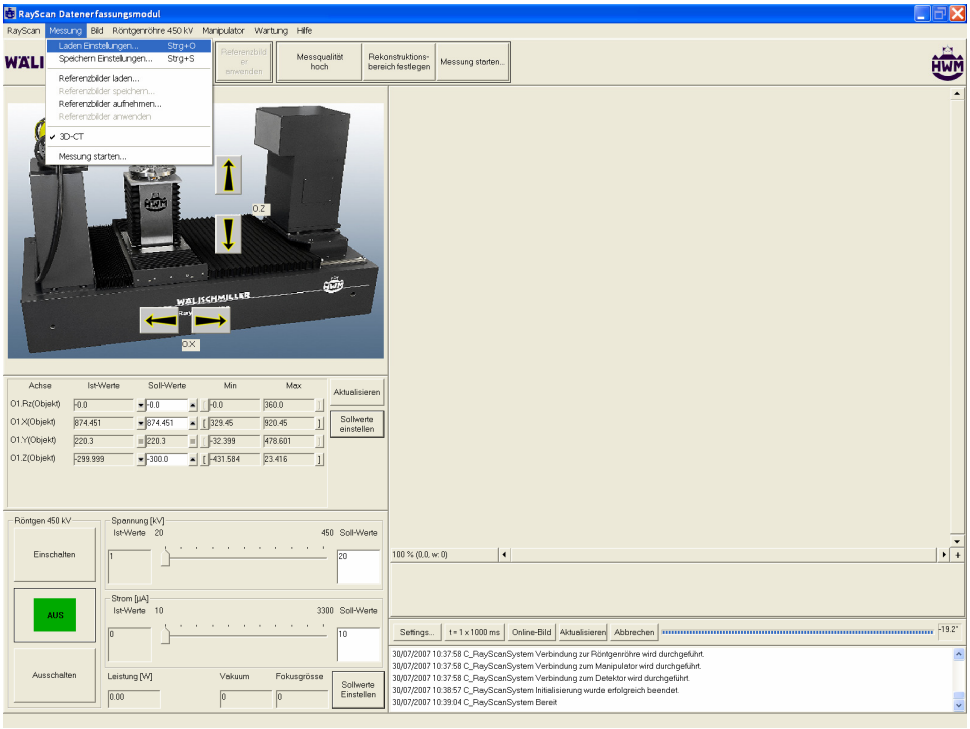

You will see a dialog box showing the folders containing the parameters of the previous acquisitions.

Now select any one of the set of parameters, and click **OK**.

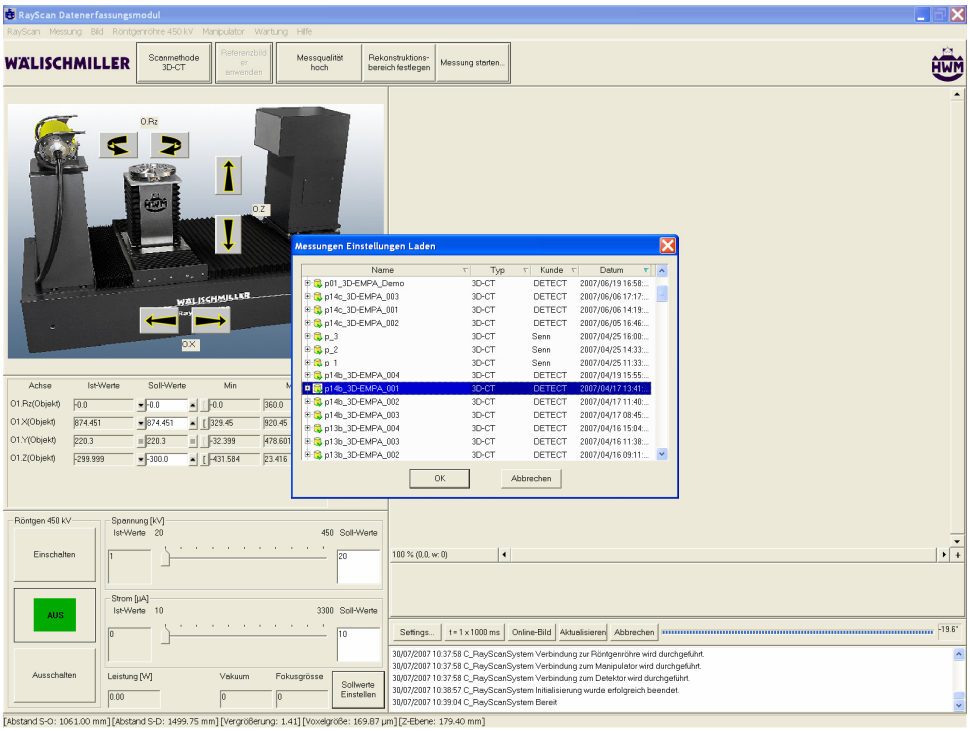

Now the chosen set of parameters is uploaded.

To modify the X-position or Z-position of the manipulator move the mouse cursor on the section Manipulator and enter the new values. Click **Sollwerte Einstellen**.

To rotate the sample, move the mouse cursor on the section Manipulator and enter the value of the angular rotation. Click **Sollwerte Einstellen**.

To modify the settings of the camera move the mouse cursor on the section Detector.

Select **Settings** to change the dynamic of the camera (12 bits or 16 bits) or to change the binning of the image.

Select **t = 1 x 3000 ms** to change the number of averaged frames or the exposition time.

To modify the voltage or the energy of the X-ray tube, move the mouse cursor on the section Source.

Enter the new values of the voltage or current. Click **Sollwerte Einstellen**.

Click on the section Röntgen 450 kV **Einschalten** to switch on the X-ray source.

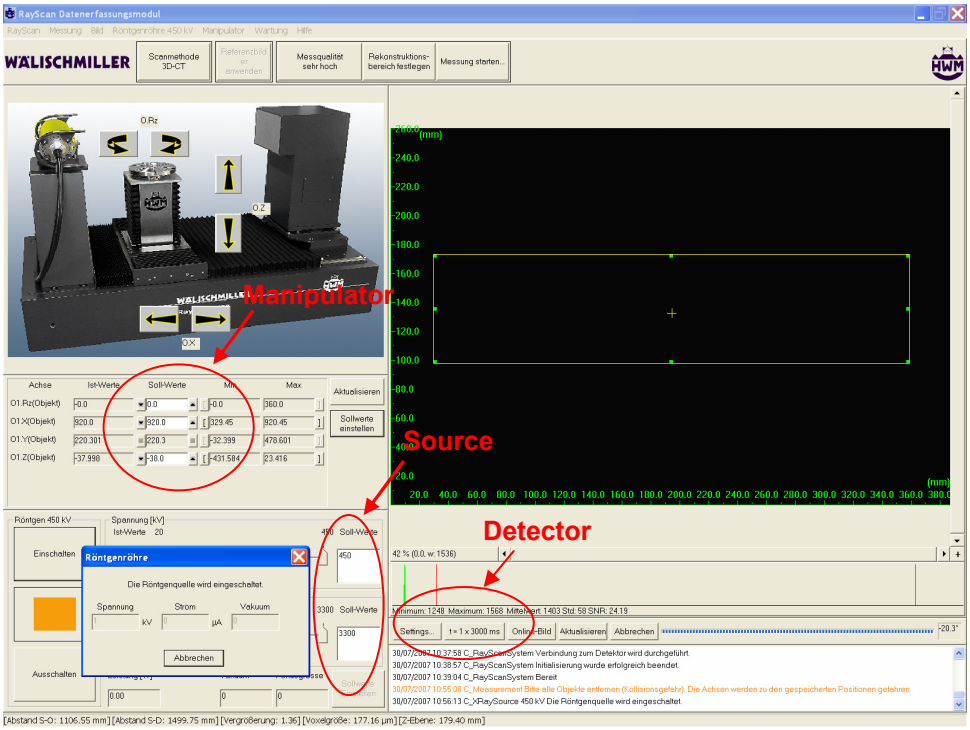

The radiography of the object appears on the upper right corner of the screen. The histogram of the selected ROI (yellow) is shown on the center right corner of the screen.

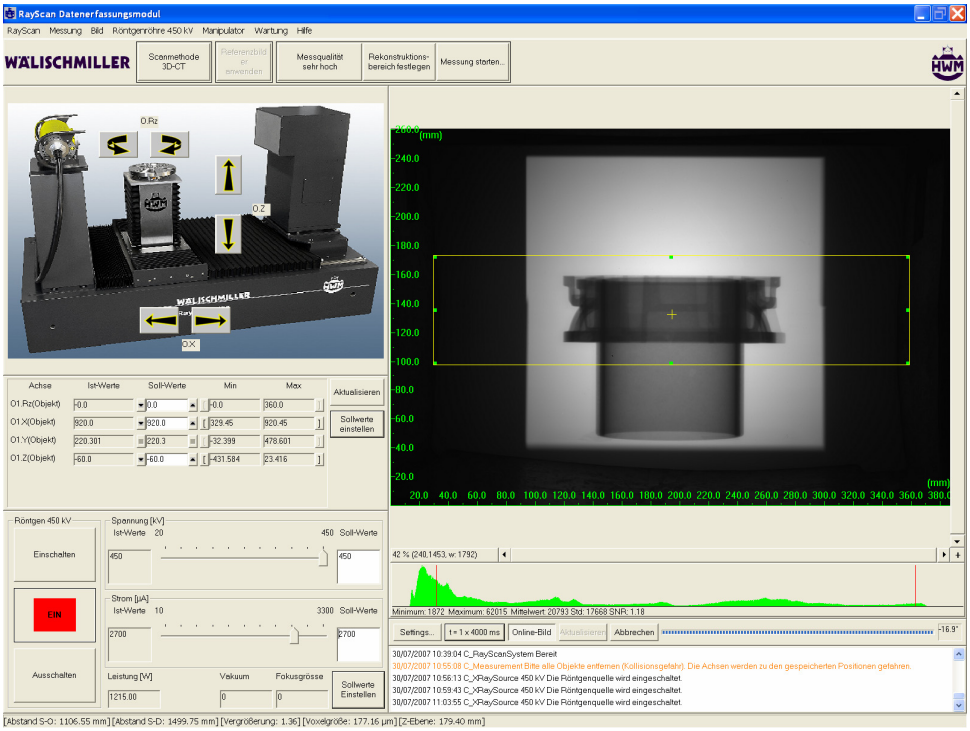

Right-click to select a different ROI. The new ROI will appear in green.

Click on **Rekonstruktionsbereich festlegen** to set the new ROI.

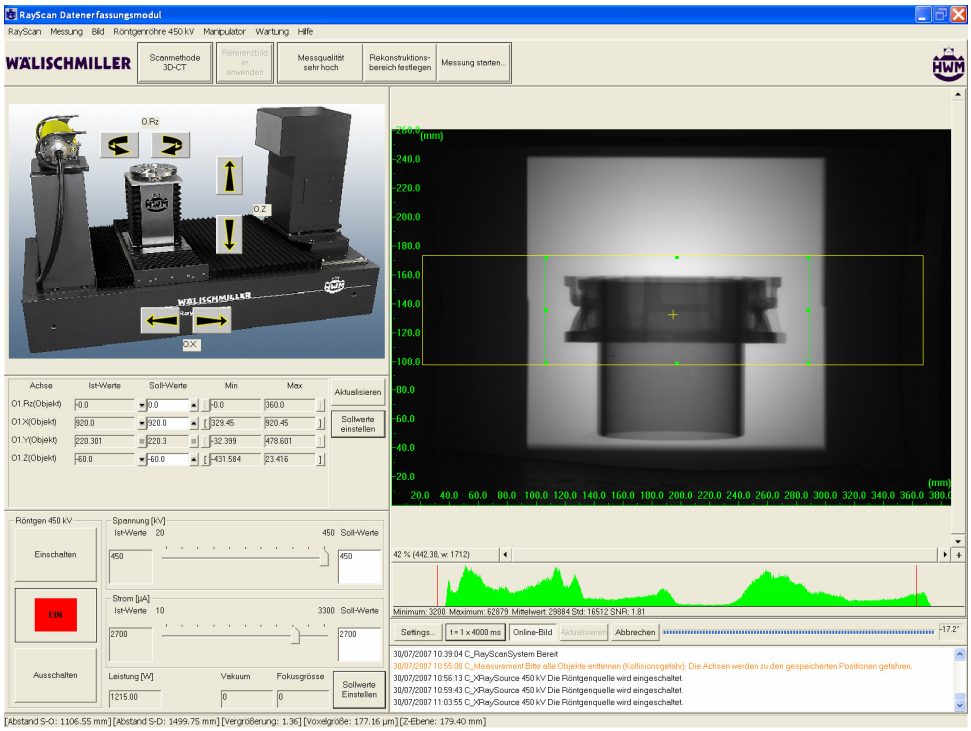

Click on **Messung Starten** to start the acquisition.

The following window will appear.

Enter the information about the object, the name of the file and the parameters of the reconstruction.

Click **Start**.

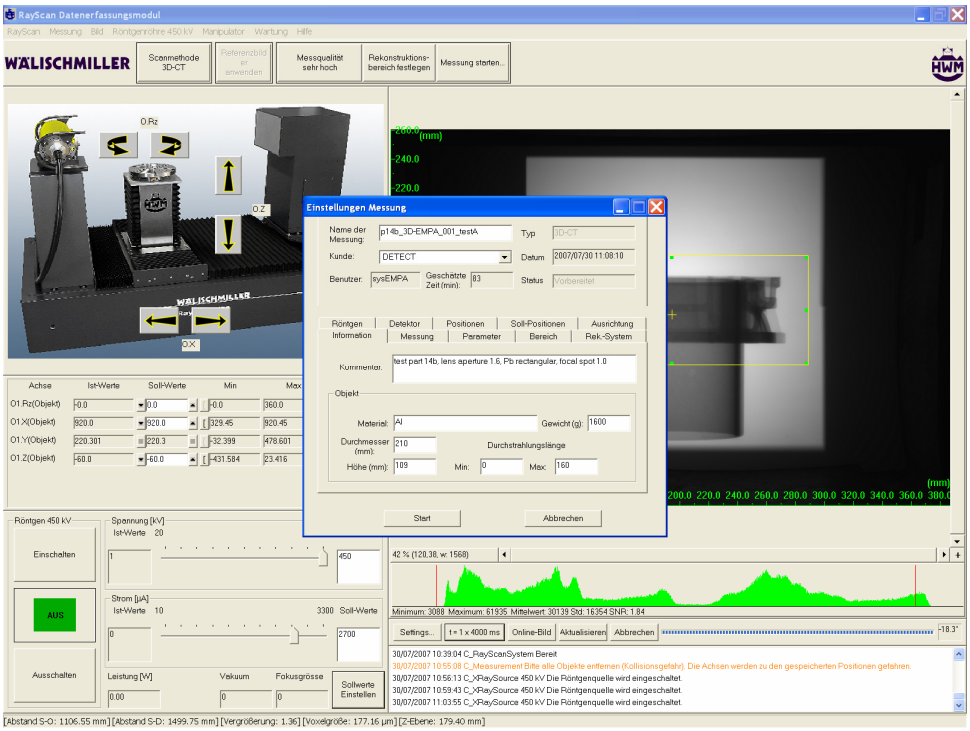

The following window showing the progress of the scan and the remaining time will appear.

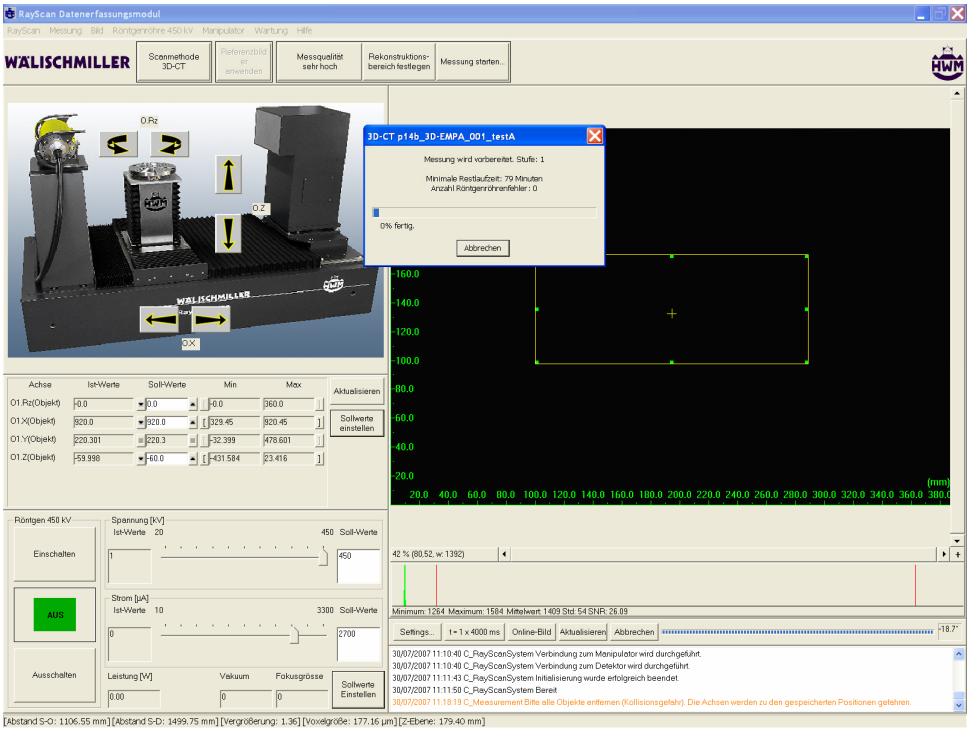

A.2 Decay tables

A.2.1 Cobalt-57

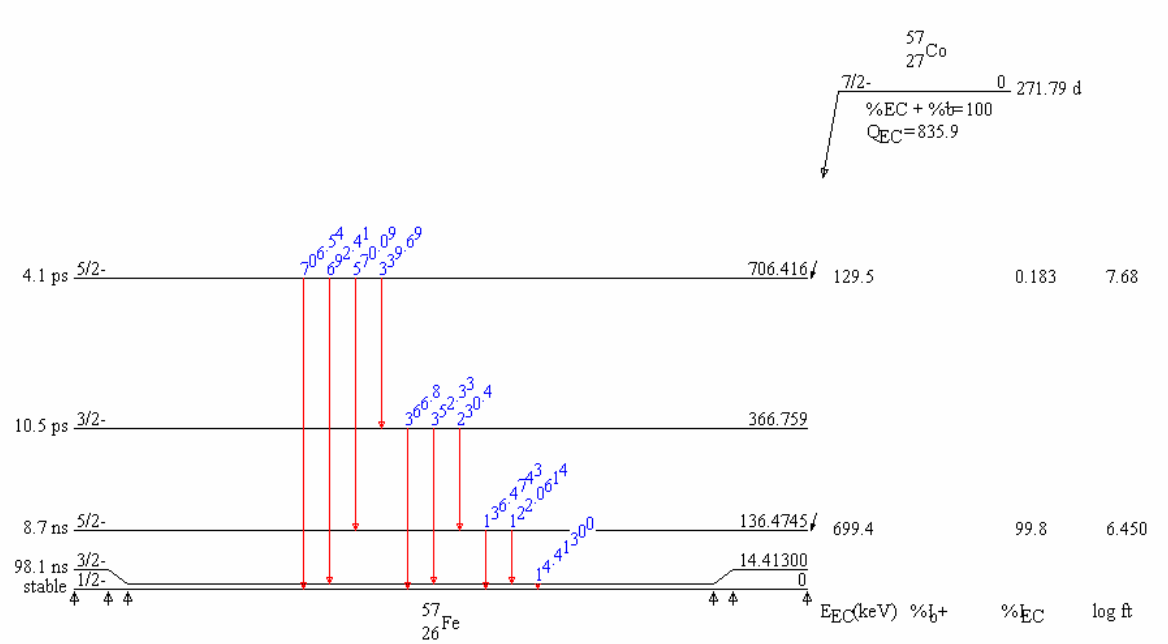

A.2.2 Barium – 133

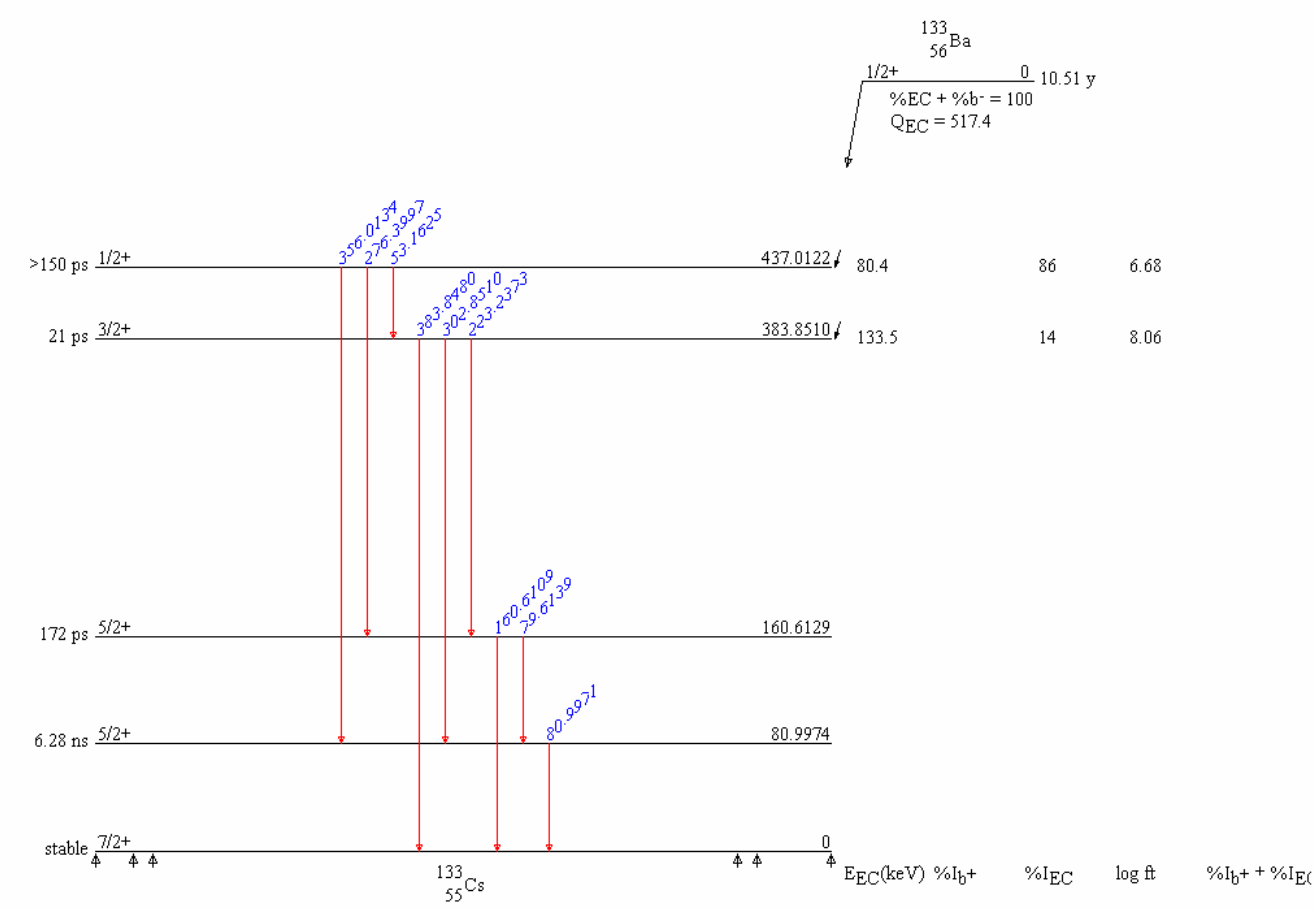

A.2.3 Cesium-137

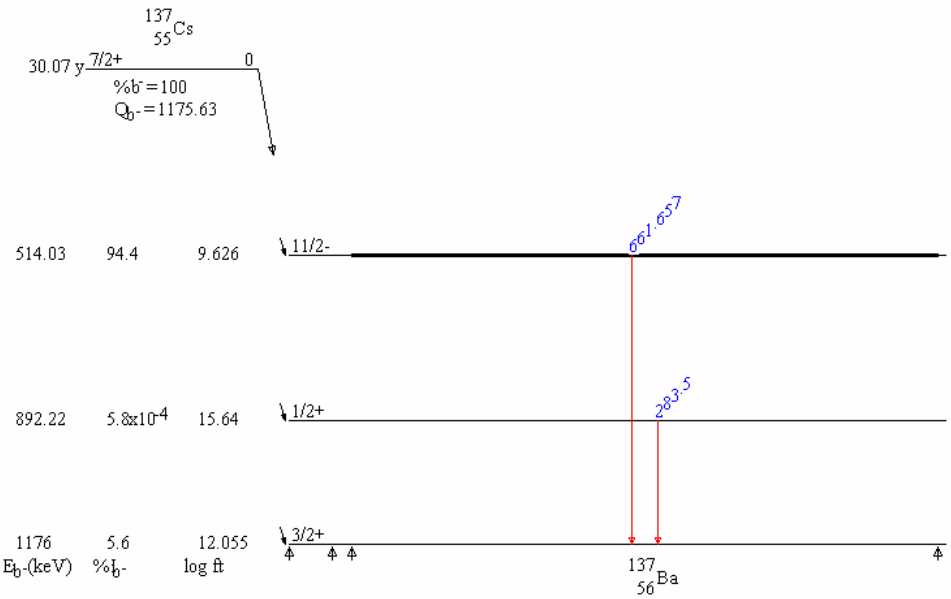

A.2.4 Americium-241

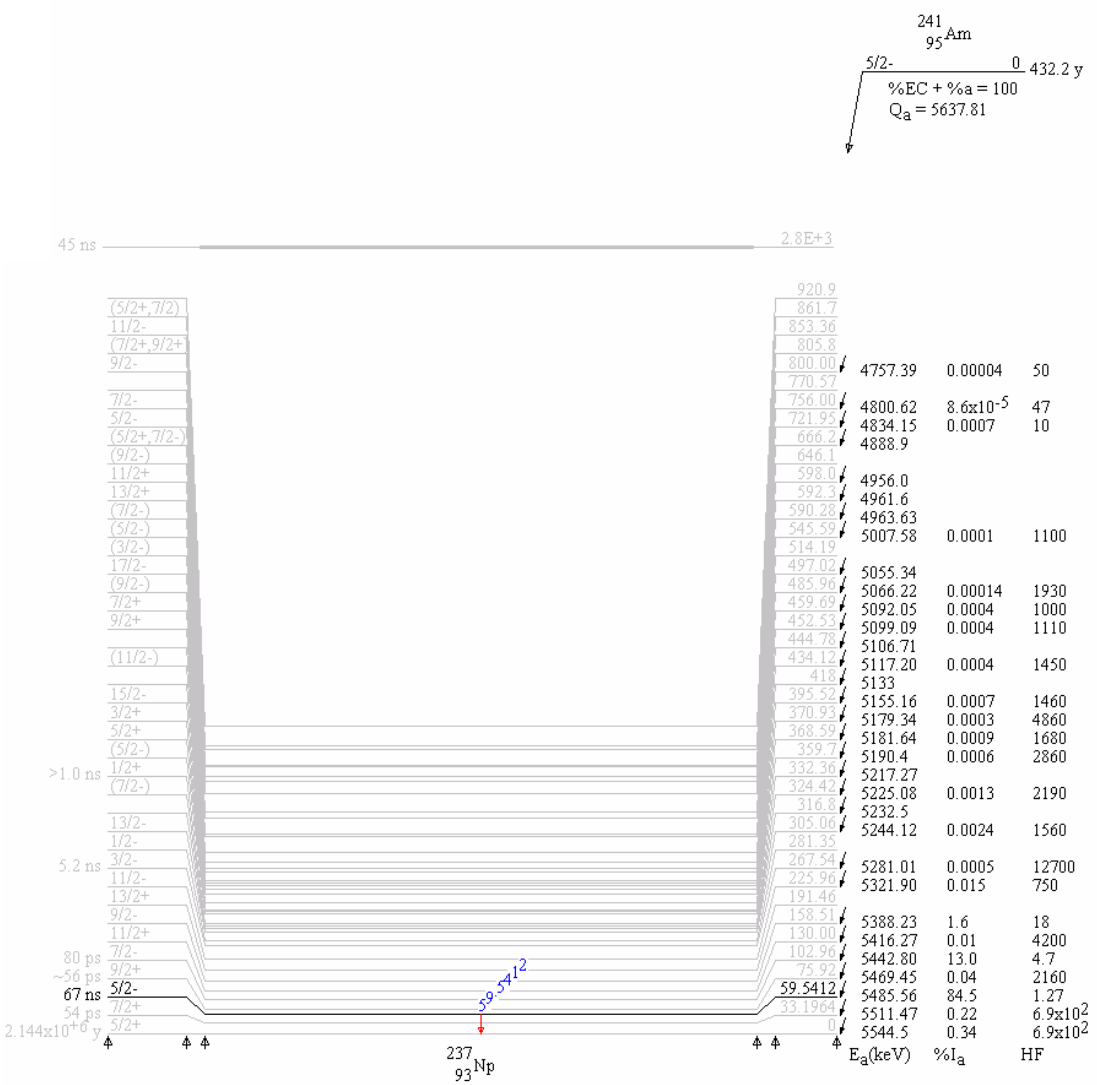

A.3 Extracts from the MC simulation code

A.3.1 Random engine

```
// RadiographyAndProfile.cpp
#include "G4RunManager.hpp"
#include "G4UImanager.hpp"
#include "SzinDetectorConstruction.hpp"
#include "SzinPhysicsList.hpp"
#include "SzinPrimaryGeneratorAction.hpp"
#include "SzinUserTrackingAction.hpp"
#include "SzinSteppingAction.hpp"
#include "SzinRunAction.hpp"
#include "SzinEventAction.hpp"
#include "SzinPrintAndAnalysis.hpp"
#include "G4UImanager.hpp"
#include "G4UIterminal.hpp"
#include "G4UItcsh.hpp"
#include <Windows.h>
BOOL WINAPI CtrlHandler (DWORD dwEvent);
//#define MPICH_IGNORE_CXX_SEEK (turn around MPI bug)
// --> done in property page compilers command line options: -DMPICH_IGNORE_CXX_SEEK
#include <mpi.h>
#include <cstdlib>
#ifdef _WIN32
#define putenv _putenv
#endif
class DetectorSpecifications Detect_spec;
class ObjectSpecifications Object_spec;
unsigned int g_numberOfProcesses;
unsigned int g_processNumber;
unsigned int g_numEventsPerProcess;
char g_computerName[MPI_MAX_PROCESSOR_NAME+1];
int main(int argc,char** argv)
{
        putenv("G4LEDATA=c:\\geant4_7_0\\data\\G4EMLOW2.3");
   int len;
        MPI::Init(argc, argv);
        g_numberOfProcesses = MPI::COMM_WORLD.Get_size();
        g_processNumber = MPI::COMM_WORLD.Get_rank();
        MPI::Get_processor_name(g_computerName, len);

        G4RunManager* runManager = new G4RunManager;// Construct the default run manager
   unsigned int totalNumberOfEvents;
   unsigned int rest;
   if(g_processNumber == 0)
   {
      std::cout << "\n** Specify tolal of events: ";
      std::cin >> totalNumberOfEvents;
   }
   MPI::COMM_WORLD.Bcast(&totalNumberOfEvents, 1, MPI::INT, 0);
   rest = totalNumberOfEvents % g_numberOfProcesses;
   int eventsPerProcess = totalNumberOfEvents/g_numberOfProcesses;
   if(g_processNumber == g_numberOfProcesses-1)
```

```
   {
      eventsPerProcess +=  rest;
   }
   g_numEventsPerProcess = eventsPerProcess;
//RANDOM ENGINE: HepJames
          HepRandom ::setTheSeed(g_processNumber);
```

A.3.2 Particles and physical processes

```
//PhysicsList.cpp
#include "SzinPhysicsList.hpp"
#include "G4ParticleTypes.hpp"
#include "G4RegionStore.hpp"
#include "G4ProcessManager.hpp"
#include "G4ParticleDefinition.hpp"
#include "G4LowEnergyGammaConversion.hpp"
#include "G4LowEnergyCompton.hpp"
#include "G4LowEnergyRayleigh.hpp"
#include "G4LowEnergyPhotoElectric.hpp"
#include "G4LowEnergyBremsstrahlung.hpp"
#include "G4LowEnergyIonisation.hpp"
#include "G4hLowEnergyIonisation.hpp"
#include "G4hIonisation.hpp"
#include "G4MultipleScattering.hpp"
#include "G4ionIonisation.hpp"
#include "G4ios.hpp"
#include "G4StepLimiter.hpp"
#include "G4RegionStore.hpp"
SzinPhysicsList::SzinPhysicsList()
{
SetVerboseLevel(3);
defaultCutValue=0.1*mm;
}
SzinPhysicsList::~SzinPhysicsList()
{;}
void SzinPhysicsList::ConstructParticle()
{
G4Gamma::GammaDefinition();
G4Electron::ElectronDefinition();
G4Positron::PositronDefinition();
}
void SzinPhysicsList::ConstructProcess()
{
AddTransportation();
ConstructEM();
}
#include "G4LowEnergyGammaConversion.hpp"
#include "G4LowEnergyCompton.hpp"
#include "G4LowEnergyRayleigh.hpp"
#include "G4LowEnergyPhotoElectric.hpp"
#include "G4LowEnergyBremsstrahlung.hpp"
#include "G4LowEnergyIonisation.hpp"
#include "G4MultipleScattering.hpp"
void SzinPhysicsList::ConstructEM()
{
```

```
theParticleIterator->reset();
while((*theParticleIterator)()){
G4ParticleDefinition *particle = theParticleIterator->value();
G4ProcessManager *pManager = particle->GetProcessManager();
G4String particleName=particle->GetParticleName();
if (particleName=="gamma") {
        G4LowEnergyPhotoElectric* lowePhot;
        lowePhot=new G4LowEnergyPhotoElectric("LowEnPhotoElec");
        pManager->AddDiscreteProcess(new G4LowEnergyRayleigh);
        pManager->AddDiscreteProcess(lowePhot);
        pManager->AddDiscreteProcess(new G4LowEnergyCompton);
        pManager->AddDiscreteProcess(new G4LowEnergyGammaConversion);
}
else if (particleName=="e-") {
        G4LowEnergyBremsstrahlung* loweBrem;
        G4LowEnergyIonisation* loweIon;
        loweBrem = new G4LowEnergyBremsstrahlung("LowEnergyBrem");
        loweIon = new G4LowEnergyIonisation("LowEnergyIon");
        pManager->AddProcess(new G4MultipleScattering, -1,1,1);
        pManager->AddProcess(loweIon, -1,2,2);
        pManager->AddProcess(loweBrem, -1,-1,3);
}
}
}
void SzinPhysicsList::SetCuts()
{
SetCutsWithDefault();
}
```

A.3.3 Initial beam

```
// PrimaryGeneratorAction.ccp
#include "SzinPrimaryGeneratorAction.hpp"
#include "G4Event.hpp"
#include "G4GeneralParticleSource.hpp"
#include "G4ParticleTable.hpp"
#include "G4ParticleDefinition.hpp"
#include "globals.hpp"
#include "Randomize.hpp"
//#include "SzinAnalysisManager.hpp"
SzinPrimaryGeneratorAction::SzinPrimaryGeneratorAction()
{
/*the SOURCE  is set in the macro file  */
particleSource= new G4GeneralParticleSource();
#ifdef G4ANALYSIS_USE
   //SzinAnalysisManager* analysis = SzinAnalysisManager::getInstance();
#endif
/*set the particle species  */
G4ParticleTable* particleTable = G4ParticleTable::GetParticleTable();
G4String particleName;
particleSource->SetParticleDefinition(particleTable->FindParticle(particleName="gamma"));
/*set the number of particle */
particleSource->SetNumberOfParticles(1);
/*set the level of verbosity */
particleSource->SetVerbosity(0);
}
```

```
SzinPrimaryGeneratorAction::~SzinPrimaryGeneratorAction()
{
delete particleSource;
}
```

Macro file

```
/gps/ene/type Mono
/gps/energy 50 keV
/gps/pos/type Plane
/gps/pos/shape Rectangle
/gps/pos/centre 0.0 0.0 0.0 mm
/gps/pos/halfx 0.265 mm
/gps/pos/halfy 0.66 mm
/gps/direction 0 0 -1
/run/beamOn 2000000
```

A.3.4 Elements and materials

```
//DetectorConstruction.cpp
#include "SzinDetectorConstruction.hpp"
#include "G4BooleanSolid.hpp"
#include "G4SubtractionSolid.hpp"
#include "G4Material.hpp"
#include "G4Element.hpp"
#include "G4Box.hpp"
#include "G4Tubs.hpp"
#include "G4Cons.hpp"
#include "G4LogicalVolume.hpp"
#include "G4ThreeVector.hpp"
#include "G4PVPlacement.hpp"
#include "G4PVReplica.hpp"
#include "globals.hpp"
#include "G4UserLimits.hpp"
#include "SzinSD.hpp"
#include "G4SDManager.hpp"
#include "G4RotationMatrix.hpp"
#include "SzinRunAction.hpp"
#include "G4VisAttributes.hpp"
#include "G4AssemblyVolume.hpp"
#include "G4ReflectionFactory.hpp"
#include "G4BREPSolidBox.hpp"
#include <CLHEP/Geometry/Point3D.h>
#include "G4Trap.hpp"
#include "G4Trd.hpp"
#include <math.h>
#include "SzinPrintAndAnalysis.hpp"
#include "StackingAction.hpp"
#include "geometry.hpp"

SzinDetectorConstruction::SzinDetectorConstruction()
 :  experimentalHall_phys(0),  detector_phys(0)
{;}
SzinDetectorConstruction::~SzinDetectorConstruction()
{
}
```

```
G4VPhysicalVolume* SzinDetectorConstruction::Construct()
{
/*
                MATERIALS AND ELEMENTS
*/
G4Element* elementN = new G4Element( "Nitrogen", "N", 7. , 14.00674*g/mole );
                        G4Element* elementO = new G4Element( "Oxygen", "O", 8. ,
15.9994*g/mole );
        G4Element* elementAr = new G4Element( "Argon", "Ar", 18. , 39.948*g/mole );
                        G4Material* matAir =
                        new G4Material("Air",  1.205*mg/cm3, 3);
                        matAir->AddElement(elementN, 0.76);
                        matAir->AddElement(elementO, 0.23);
        matAir->AddElement(elementAr, 0.01);
                        G4Material* Cu =
                        new G4Material("Cooper", 29.0, 63.546*g/mole, 8.23*g/cm3);
                        G4Material* Pb =
                        new G4Material("Lead",82,207.2*g/mole, 11.34*g/cm3);
                        G4Material* Fe =
                        new G4Material ("Iron",26, 55.845*g/mole,7.86*g/cm3);
                        G4Material* Ag=
                                new G4Material("Silver",47,107.87*g/mole,10.5*g/cm3);
                        G4Material* W =
                        new G4Material ("Tungsten",74, 183.84*g/mole,19.3*g/cm3);
                        G4Material* Al=
                                new G4Material("Aluminium",13,26.982*g/mole,2.702*g/cm3);
                        G4Material* Vacuum=
                          new G4Material("vacuum",1.,1.008*g/mole,1.e-25*g/cm3,
                        kStateGas, 2.73*kelvin, 3.e-18*pascal);
                        G4Element* elementI = new G4Element( "Iodine", "I", 53. ,
126.90447*g/mole );
                        G4Element* elementCs = new G4Element( "Cesium", "Cs", 55. ,
132.90543*g/mole );
                        G4Material* matCsIDetector =
                        new G4Material("CsIDetector",  4.51*g/cm3, 2, kStateSolid, 273.15*kelvin,
1.0*atmosphere );//
                        matCsIDetector->AddElement( elementI, 1 );
                        matCsIDetector->AddElement( elementCs, 1 );
                        G4Element* elementNi=new G4Element ("Nickel","Ni", 28.,
58.693*g/mole);
                        G4Element* elementFe=new G4Element ("Iron","Fe", 26., 55.845*g/mole);
                        G4Element* elementW=new G4Element ("Tungsten","W", 74.,
183.84*g/mole);

                        G4Element* elementCu=new G4Element ("Copper","Cu", 29.,
63.546*g/mole);
                        G4Element* elementPb=new G4Element ("Lead","Pb", 82., 207.2*g/mole);
                        G4Element* elementZn=new G4Element ("Zinc","Zn", 30., 65.39*g/mole);
                        G4Material* matBrass_st= new G4Material("Brass_st", 8.47*g/cm3, 3 );
                        matBrass_st->AddElement(elementZn, 0.39);
                        matBrass_st->AddElement(elementPb, 0.03);
                    matBrass_st->AddElement(elementCu, 0.58);
                        G4Element* elementSi=new G4Element ("Silicon","Si", 14.,
28.086*g/mole);
                        G4Element* elementMn=new G4Element ("Manganese","Mn", 25.,
54.938*g/mole);
```

```
                        G4Element* elementMg=new G4Element ("Magnesium","Mg", 12.,
24.305*g/mole);
                        G4Element* elementCr=new G4Element ("Chromium","Cr", 24.,
51.996*g/mole);
                        G4Element* elementTi=new G4Element ("Titanium","Ti", 22.,
47.867*g/mole);
                        G4Element* elementAl=new G4Element ("Aluminium","Al", 13.,
26.982*g/mole);
                        G4Material* mat_AlMgSi1= new G4Material("AlMgSi1", 2.7*g/cm3,9);
                        mat_AlMgSi1->AddElement(elementSi ,0.01);
                        mat_AlMgSi1->AddElement(elementFe , 0.005);
                        mat_AlMgSi1->AddElement(elementCu , 0.001);
                        mat_AlMgSi1->AddElement(elementMn , 0.007);
                        mat_AlMgSi1->AddElement(elementMg , 0.009);
                        mat_AlMgSi1->AddElement(elementCr , 0.0025);
                        mat_AlMgSi1->AddElement(elementZn , 0.002);
                        mat_AlMgSi1->AddElement(elementTi , 0.001);
                        mat_AlMgSi1->AddElement(elementAl , 0.9625);
                        G4Element* elementS=new G4Element ("Sulphur","S", 16.,
32.065*g/mole);
                        G4Element* elementGd=new G4Element ("Gadolinium","Gd", 64.,
157.25*g/mole);
                        G4Element* elementC=new G4Element ("Carbon","C", 6., 12.011*g/mole)
                        G4Material* mat_Steel= new G4Material("Steel", 7.87*g/cm3, 2);
                        mat_Steel->AddElement(elementFe, 0.9982);
                        mat_Steel->AddElement(elementC, 0.0018);
                        G4Element* elementSb=new G4Element ("Anti-
mony","Sb",51.,121.76*g/mole);
                        G4Material* Au =
                        new G4Material("Gold", 79, 196.97*g/mole, 19.32*g/cm3);
```

A.3.5 Run Action

```
// RunAction.cpp
#include "SzinRunAction.hpp"
#include <stdlib.h>
#include <math.h>
#include "G4Run.hpp"
#include "G4UImanager.hpp"
#include "G4VVisManager.hpp"
#include "G4ios.hpp"
#include "G4ThreeVector.hpp"
#include "SzinDetectorConstruction.hpp"
#include "SzinPrintAndAnalysis.hpp"
#include "SzinEventAction.hpp"
#include <time.h>
#include <mpi.h>
unsigned extern int g_processNumber;
unsigned extern int g_numberOfProcesses;
extern unsigned int g_numEventsPerProcess;
extern class DetectorSpecifications Detect_spec;
extern class ObjectSpecifications Object_spec;
extern DetectorSpecifications Detect_spec;
extern G4String Prec_info;
```

```
extern G4String Object_info;
extern G4String PostFilter_info;
extern G4String Detector_info;
extern G4String Support_info;
extern G4double object_sourceDistance;
extern G4String Pb_Shielding_info;
extern const G4double theta;
G4double NPhotonReachWorldBoundary_object;
G4double NPhotonReachWorldBoundary_filter;
G4double NPhotonReachWorldBoundary_AlSupport;
G4double NPhotonReachWorldBoundary_Scintillator;
G4double Scatt_Object_Out;
G4double Scatt_Filter_Out;
G4double Scatt_AlSupport_Out;
G4double Scatt_Scintillator_Out;
std::ofstream outFile;
std::ofstream outFile_ScattEverywhere;
std::ofstream outFile_Matrix;
std::ofstream outFile_MatrixPrimary;
std::ofstream outFile_Matrix_Order1;
std::ofstream outFile_Matrix_Order2;
std::ofstream outFile_Matrix_Mult;
std::ofstream outFile_Spectrum;
InfoUser user_info;
G4double EnDepByScattEverywhere[number_of_pixels_x][number_of_pixels_y];
G4double EnergyDeposited[number_of_pixels_x][number_of_pixels_y];
G4double EnergyDepositedPrim[number_of_pixels_x][number_of_pixels_y];
G4double EnergyDeposited_Order1[number_of_pixels_x][number_of_pixels_y];
G4double EnergyDeposited_Order2[number_of_pixels_x][number_of_pixels_y];
G4double EnergyDeposited_Mult[number_of_pixels_x][number_of_pixels_y];
G4double EnDepByScattEverywhere_Sum[number_of_pixels_x][number_of_pixels_y];
G4double EnergyDeposited_Sum[number_of_pixels_x][number_of_pixels_y];
G4double EnergyDepositedPrim_Sum[number_of_pixels_x][number_of_pixels_y];
G4double EnergyDeposited_Order1_Sum[number_of_pixels_x][number_of_pixels_y];
G4double EnergyDeposited_Order2_Sum[number_of_pixels_x][number_of_pixels_y];
G4double EnergyDeposited_Mult_Sum[number_of_pixels_x][number_of_pixels_y];
G4double EnergySpectrum[array_energy];
SzinRunAction::SzinRunAction()
{
}
SzinRunAction::~SzinRunAction()
{
}
time_t start,end;
G4double dif_time;
void SzinRunAction::BeginOfRunAction(const G4Run* aRun)
{
            time (&start);
             NPhotonReachWorldBoundary_object = NPhotonReachWorldBoundary_filter = NPhoton-
ReachWorldBoundary_AlSupport =
             NPhotonReachWorldBoundary_Scintillator = Scatt_Object_Out = Scatt_Filter_Out =
    Scatt_AlSupport_Out =Scatt_Scintillator_Out = 0.;
             for (G4int j=0; j<number_of_pixels_y; j++) {
                      for (G4int i=0; i<number_of_pixels_x ; i++){
                          EnergyDeposited[i][j] = EnergyDepositedPrim[i][j] = EnergyDe-
posited_Order1[i][j]
```

```
                                = EnergyDeposited_Order2[i][j] = EnergyDeposited_Mult[i][j] =  EnDep-
ByScattEverywhere[i][j] = 0.;
                        }
            }
             for (G4int i_sp=0; i_sp<array_energy; i_sp++){  EnergySpectrum[i_sp]=0.; }
     if(g_processNumber == 0)
     {
              for (G4int j=0; j<number_of_pixels_y; j++)
      {
                        for (G4int i=0; i<number_of_pixels_x ; i++)
          {
                            EnergyDeposited_Sum[i][j] = EnergyDepositedPrim_Sum[i][j] = EnergyDe-
posited_Order1_Sum[i][j]
                                = EnergyDeposited_Order2_Sum[i][j] = EnergyDeposited_Mult_Sum[i][j]
= EnDepByScattEverywhere_Sum[i][j] = 0.;
                        }
      }
     }
          user_info.DayAndTime = "---";
          G4cout<<"  -.-.-.-.-.-.-.-.-.-.-.-.-.-.-.-.-.-.-.-.-.-.-.-.-."<<G4endl;
          G4cout<<"  -.-.-.-.-.-.-.-.-.-.-.-.-.-.-.-.-.-.-.-.-.-.-.-.-."<<G4endl;
          G4cout<<"!!!!!!!!!!!!!!!!!!!!!!!!!!!!!!!!!!!!!!!!!!!!!!!!!!!"<<G4endl;
          G4cout<<"!!!!!!!!!!!!!!!!!!!!!!!!!!!!!!!!!!!!!!!!!!!!!!!!!!!"<<G4endl;
          G4cout<<"!!!!!!!!!!!!!!RUN  "<< aRun->GetRunID()<<" START"<<G4endl;

}
void SzinRunAction::EndOfRunAction(const G4Run* aRun)
{
   G4cout << "Process #" << g_processNumber << " run status:  100.0% of " <<
g_numEventsPerProcess << " events done. \n";
   char cProcessum[10];
   sprintf(cProcessum, "_P%d", g_processNumber);
   G4String name_info_file="info";
   name_info_file += cProcessum;
   name_info_file += ".dat";
   G4String name_matrixFile="matrix";
   name_matrixFile += cProcessum;
   name_matrixFile += ".dat";
   G4String name_matrixScattEverywhere="ScattEverywhere";
   name_matrixScattEverywhere += cProcessum;
   name_matrixScattEverywhere += ".dat";
   G4String name_matrixPrimaryFile="primary";
   name_matrixPrimaryFile += cProcessum;
   name_matrixPrimaryFile += ".dat";
   G4String name_matrixOrder1File="order1";
   name_matrixOrder1File += cProcessum;
   name_matrixOrder1File += ".dat";
   G4String name_matrixOrder2File="order2";
   name_matrixOrder2File += cProcessum;
   name_matrixOrder2File += ".dat";
   G4String name_matrixMultFile="orderM";
   name_matrixMultFile += cProcessum;
   name_matrixMultFile += ".dat";
   G4String name_Spectrum="EnSpectrum";
   name_Spectrum += cProcessum;
   name_Spectrum += ".dat";
```

```
   MPI::COMM_WORLD.Reduce(EnDepByScattEverywhere, EnDepByScattEverywhere_Sum, num-
ber_of_pixels_x *number_of_pixels_y, MPI_DOUBLE, MPI::SUM, 0);
   MPI::COMM_WORLD.Reduce(EnergyDeposited, EnergyDeposited_Sum, number_of_pixels_x
*number_of_pixels_y, MPI_DOUBLE, MPI::SUM, 0);
   MPI::COMM_WORLD.Reduce(EnergyDepositedPrim, EnergyDepositedPrim_Sum, num-
ber_of_pixels_x *number_of_pixels_y, MPI_DOUBLE, MPI::SUM, 0);
   MPI::COMM_WORLD.Reduce(EnergyDeposited_Order1, EnergyDeposited_Order1_Sum, num-
ber_of_pixels_x *number_of_pixels_y, MPI_DOUBLE, MPI::SUM, 0);
   MPI::COMM_WORLD.Reduce(EnergyDeposited_Order2, EnergyDeposited_Order2_Sum, num-
ber_of_pixels_x *number_of_pixels_y, MPI_DOUBLE, MPI::SUM, 0);
   MPI::COMM_WORLD.Reduce(EnergyDeposited_Mult, EnergyDeposited_Mult_Sum, num-
ber_of_pixels_x *number_of_pixels_y, MPI_DOUBLE, MPI::SUM, 0);
                        outFile.open(name_info_file);
          if(!outFile) G4cerr<<" error opening  "<<name_info_file<<"  file"<<G4endl;
   outFile_ScattEverywhere.open(name_matrixScattEverywhere);
          if (!outFile_ScattEverywhere)G4cerr<<" error opening  "<<name_matrixScattEverywhere<<"
file"<<G4endl;
          outFile_Matrix.open(name_matrixFile);
          if(!outFile_Matrix) G4cerr<<" error opening "<< name_matrixFile<<" file"<<G4endl;
   outFile_MatrixPrimary.open(name_matrixPrimaryFile);
          if(!outFile_MatrixPrimary) G4cerr<<" error opening "<< name_matrixPrimaryFile<<"
file"<<G4endl;
   outFile_Matrix_Order1.open(name_matrixOrder1File);
          if(!outFile_Matrix_Order1) G4cerr<<" error opening "<< name_matrixOrder1File<<"
file"<<G4endl;
          outFile_Matrix_Order2.open(name_matrixOrder2File);
          if(!outFile_Matrix_Order2) G4cerr<<" error opening "<< name_matrixOrder2File<<"
file"<<G4endl;
          outFile_Matrix_Mult.open(name_matrixMultFile);
          if(!outFile_Matrix_Mult) G4cerr<<" error opening "<< name_matrixMultFile<<"
file"<<G4endl;
          outFile_Spectrum.open(name_Spectrum);
          if(!outFile_Spectrum) G4cerr<<" error opening "<< name_Spectrum<<" file"<<G4endl;
   std::cout << "\n\nStore data to files ...";
   std::flush(std::cout);
          Print_RunAction print_info;
   G4int NumberOfEvents= g_numberOfProcesses* g_numEventsPerProcess;
   outFile<<" -*-*-*-*-*- Information  File -*-*-*-*-*- "<<G4endl;
   outFile<<"*-                                *- "<<G4endl;
          outFile<<"Simulation started:  "<<user_info.DayAndTime<<G4endl;
   outFile<<"//                // "<<G4endl;
   outFile<<"/     Geometry     / "<<G4endl;
          outFile<<"//                // "<<G4endl;
          outFile<<"Total number of events: "<<NumberOfEvents<<G4endl;
          outFile<<"X-ray spectrum: "<<Detect_spec.Spectrum<<G4endl;
          outFile<<"Half angle of the X-ray beam (theta): "<<Detect_spec.theta<<G4endl;
          outFile<<"Precollimator: "<<Prec_info<<G4endl;
   outFile<<"Object: "<<Object_info<<G4endl;
          outFile<<"PostFilter: "<<PostFilter_info<<G4endl;
          outFile<<"Support: "<<Support_info<<G4endl;
          outFile<<"Detector: "<<Detector_info<<G4endl;
          outFile<<"Detector size: x= "<<Detect_spec.Detector_size_x<<"mm  y= "<<De-
tect_spec.Detector_size_y<<
                  "mm Thickness= "<<Detect_spec.Detector_size_z<<"mm"<<G4endl;
   outFile<<"Detector:Pixel size "<<De-
tect_spec.pixel_size_X<<"X"<<Detect_spec.pixel_size_Y<<"mm2"<<G4endl;
```

```
	outFile<<"Detector - source distance: "<<Detect_spec.detector_sourceDistance<<" mm   (if
material = vacuum this is the distance source front side of the vacuum detector)"<<G4endl;
	outFile<<"Object - source Distance: "<<Object_spec.object_sourceDistance<<"
mm"<<G4endl;
	outFile<<"Lead Shielding behind the CsI: "<<Pb_Shielding_info<<G4endl;
	outFile<<" "<<G4endl;
	outFile<<" "<<G4endl;
   outFile<<" ***************  Results ************************"<<G4endl;
   outFile<<"Number of photons leaving the object =  "<< Scatt_Object_Out*100/NumberOfEvents<<
" %"<<G4endl;
	outFile<<"Number of photons leaving the filter =  "<<
Scatt_Filter_Out*100/NumberOfEvents<<" %"<<G4endl;
	outFile<<"Number of photons leaving the Al Support =  "<<
Scatt_AlSupport_Out*100/NumberOfEvents<<" %"<<G4endl;
	outFile<<"Number of photons leaving the CsI =  "<<
Scatt_Scintillator_Out*100/NumberOfEvents<<" %"<<G4endl;
	outFile<<"Number of photons reaching the world boundary after interacting with the object =
" << NPhotonReachWorldBoundary_object*100/NumberOfEvents <<" %"<<G4endl;
	outFile<<"Number of photons reaching the world boundary after interacting with the filter = "
<< NPhotonReachWorldBoundary_filter*100/NumberOfEvents <<" %"<<G4endl;
   outFile<<"Number of photons reaching the world boundary after interacting with the Al support = "
<< NPhotonReachWorldBoundary_AlSupport*100/NumberOfEvents <<" %"<<G4endl;
   outFile<<"Number of photons reaching the world boundary after interacting with the CsI = " <<
NPhotonReachWorldBoundary_Scintillator*100/NumberOfEvents<<" %"<<G4endl;
   outFile<<" "<<G4endl;
   outFile<<" "<<G4endl;
   outFile<<" "<<G4endl;
	outFile<< "********** Files name (Values in MeV)*******************"<<G4endl;
   outFile<<"name of information file: "<<name_info_file<<G4endl;
	outFile<<"name of matrix file: "<<name_matrixFile<<G4endl;
	outFile<<"name of primary matrix file: "<<name_matrixPrimaryFile<<G4endl;
	outFile<<"name of order 1 scattering matrix file (scatter radiation by the object):
"<<name_matrixOrder1File<<G4endl;
   outFile<<"name of order 2 scattering matrix file (scatter radiation by the object):
"<<name_matrixOrder2File<<G4endl;
   outFile<<"name of order >2 scattering matrix file (scatter radiation by the object):
"<<name_matrixMultFile<<G4endl;
	outFile<<"name of Spectrum of Energy deposited file: "<<name_Spectrum<<G4endl;
	outFile<<"name of energy deposited by photons scattered within the precollim, object, postfil-
ter or/and CsI support: "<<name_matrixScattEverywhere <<G4endl;
   outFile<<"_._._.__._._.__._._.__._._.__._._.__._._.__._._.__._._.__._._._"<<G4endl;
	for (G4int j_e=0; j_e<number_of_pixels_y; j_e++) {
		for (G4int i_e=0; i_e<number_of_pixels_x ; i_e++){
			outFile_ScattEverywhere<<EnDepByScattEverywhere[i_e][j_e]<<" \t";
		}
		outFile_ScattEverywhere<<G4endl;
	}
	for (G4int j=0; j<number_of_pixels_y; j++) {
		for (G4int i=0; i<number_of_pixels_x ; i++){
			outFile_Matrix<<EnergyDeposited[i][j]<<" \t";
		}
		outFile_Matrix<<G4endl;
	}
	for (G4int j_order0=0; j_order0<number_of_pixels_y; j_order0++) {
		for (G4int i_order0=0; i_order0<number_of_pixels_x ; i_order0++){
		   outFile_MatrixPrimary<<EnergyDepositedPrim[i_order0][j_order0]<<" \t";
		}
```

```
                outFile_MatrixPrimary<<G4endl;
        }
        for (G4int j_order1=0; j_order1<number_of_pixels_y; j_order1++) {
                for (G4int i_order1=0; i_order1<number_of_pixels_x ; i_order1++){
                   outFile_Matrix_Order1<<EnergyDeposited_Order1[i_order1][j_order1]<<" \t";
                }
                outFile_Matrix_Order1<<G4endl;
        }
        for (G4int j_order2=0; j_order2<number_of_pixels_y; j_order2++) {
                for (G4int i_order2=0; i_order2<number_of_pixels_x ; i_order2++){
                   outFile_Matrix_Order2<<EnergyDeposited_Order2[i_order2][j_order2]<<" \t";
                }
                outFile_Matrix_Order2<<G4endl;
        }
        for (G4int j_order_mult=0; j_order_mult<number_of_pixels_y; j_order_mult++) {
                for (G4int i_order_mult=0; i_order_mult<number_of_pixels_x ; i_order_mult++){
                   outFile_Matrix_Mult<<EnergyDeposited_Mult[i_order_mult][j_order_mult]<<"
\t";
                }
                outFile_Matrix_Mult<<G4endl;
        }
   outFile_Spectrum<<"counts / keV"<<G4endl;
        for (G4int i_s=0; i_s<array_energy; i_s++) {
     outFile_Spectrum<<EnergySpectrum[i_s]<<G4endl;
        }
        time (&end);
   dif_time = difftime (end,start);
   outFile<<" "<<G4endl;
        outFile<<" "<<G4endl;
        outFile<<" "<<G4endl;
   outFile<<"The simulation has taken "<<dif_time/60.0<<" minutes"<<G4endl;
        outFile.close();
   outFile_Matrix.close();
        outFile_MatrixPrimary.close();
        outFile_Matrix_Order1.close();
        outFile_Matrix_Order2.close();
        outFile_Matrix_Mult.close();
        outFile_Spectrum.close();
   outFile_ScattEverywhere.close();
   G4cout<<" done.\n\n Files close"<<G4endl;
   G4cout<<"!!!!!!!!!!!!!!!! END OF RUN !!!!!!!!!!! "<<G4endl;
   if(g_processNumber == 0)
   {
      name_matrixScattEverywhere +=  ".sum";
      outFile_ScattEverywhere.open(name_matrixScattEverywhere);
            if (!outFile_ScattEverywhere)G4cerr<<" error opening
"<<name_matrixScattEverywhere<<"  file"<<G4endl;
      name_matrixFile +=  ".sum";
            outFile_Matrix.open(name_matrixFile);
            if(!outFile_Matrix) G4cerr<<" error opening "<< name_matrixFile<<" file"<<G4endl;
      name_matrixPrimaryFile +=  ".sum";
      outFile_MatrixPrimary.open(name_matrixPrimaryFile);
            if(!outFile_MatrixPrimary) G4cerr<<" error opening "<< name_matrixPrimaryFile<<"
file"<<G4endl;
      name_matrixOrder1File +=  ".sum";
      outFile_Matrix_Order1.open(name_matrixOrder1File);
```

```
        if(!outFile_Matrix_Order1) G4cerr<<" error opening "<< name_matrixOrder1File<<"
file"<<G4endl;
    name_matrixOrder2File +=  ".sum";
        outFile_Matrix_Order2.open(name_matrixOrder2File);
        if(!outFile_Matrix_Order2) G4cerr<<" error opening "<< name_matrixOrder2File<<"
file"<<G4endl;
    name_matrixMultFile +=  ".sum";
        outFile_Matrix_Mult.open(name_matrixMultFile);
        if(!outFile_Matrix_Mult) G4cerr<<" error opening "<< name_matrixMultFile<<"
file"<<G4endl;
        for (G4int j_e=0; j_e<number_of_pixels_y; j_e++) {
            for (G4int i_e=0; i_e<number_of_pixels_x ; i_e++){
                outFile_ScattEverywhere<<EnDepByScattEverywhere_Sum[i_e][j_e]<<"
\t";
            }
            outFile_ScattEverywhere<<G4endl;
        }
        for (G4int j=0; j<number_of_pixels_y; j++) {
            for (G4int i=0; i<number_of_pixels_x ; i++){
                outFile_Matrix<<EnergyDeposited_Sum[i][j]<<" \t";
            }
            outFile_Matrix<<G4endl;
        }
        for (G4int j_order0=0; j_order0<number_of_pixels_y; j_order0++) {
            for (G4int i_order0=0; i_order0<number_of_pixels_x ; i_order0++){
              outFile_MatrixPrimary<<EnergyDepositedPrim_Sum[i_order0][j_order0]<<"
\t";
            }
            outFile_MatrixPrimary<<G4endl;
        }
        for (G4int j_order1=0; j_order1<number_of_pixels_y; j_order1++) {
            for (G4int i_order1=0; i_order1<number_of_pixels_x ; i_order1++){
              out-
File_Matrix_Order1<<EnergyDeposited_Order1_Sum[i_order1][j_order1]<<" \t";
            }
            outFile_Matrix_Order1<<G4endl;
        }
        for (G4int j_order2=0; j_order2<number_of_pixels_y; j_order2++) {
            for (G4int i_order2=0; i_order2<number_of_pixels_x ; i_order2++){
              out-
File_Matrix_Order2<<EnergyDeposited_Order2_Sum[i_order2][j_order2]<<" \t";
            }
            outFile_Matrix_Order2<<G4endl;
        }
        for (G4int j_order_mult=0; j_order_mult<number_of_pixels_y; j_order_mult++) {
            for (G4int i_order_mult=0; i_order_mult<number_of_pixels_x ; i_order_mult++){
              out-
File_Matrix_Mult<<EnergyDeposited_Mult_Sum[i_order_mult][j_order_mult]<<" \t";
            }
            outFile_Matrix_Mult<<G4endl;
        }
    outFile_Matrix.close();
        outFile_MatrixPrimary.close();
        outFile_Matrix_Order1.close();
        outFile_Matrix_Order2.close();
        outFile_Matrix_Mult.close();
    outFile_ScattEverywhere.close();
```

```
    G4cout<<"!!!!!!!!!!!!!!!! Reduction done !!!!!!!!!!!! "<<G4endl;
  }
}
```

A.3.6 Event Action

```
//EventAction.cpp
#include "SzinEventAction.hpp"
#include "SzinRunAction.hpp"
#include "G4Event.hpp"
#include "G4EventManager.hpp"
#include "G4TrajectoryContainer.hpp"
#include "G4Trajectory.hpp"
#include "G4VVisManager.hpp"
#include "G4ios.hpp"
#include "SzinPrintAndAnalysis.hpp"
#include "SzinSteppingAction.hpp"
#include "SzinDetectorConstruction.hpp"
extern DetectorSpecifications Detect_spec;
extern G4double EnDepByScattEverywhere[number_of_pixels_x][number_of_pixels_y];
extern G4double EnergyDeposited[number_of_pixels_x][number_of_pixels_y];
extern G4double EnergyDepositedPrim[number_of_pixels_x][number_of_pixels_y];
extern G4double EnergyDeposited_Order1[number_of_pixels_x][number_of_pixels_y];
extern G4double EnergyDeposited_Order2[number_of_pixels_x][number_of_pixels_y];
extern G4double EnergyDeposited_Mult[number_of_pixels_x][number_of_pixels_y];
extern G4double EnergySpectrum[array_energy];
extern unsigned int g_numEventsPerProcess;
static unsigned int incr = 0;
extern unsigned int g_processNumber;
extern class DetectorSpecifications Detect_spec;
G4int order_scattering;
G4int ScattEverywhere;
G4int n_control;
G4int Step_int_obj;
G4int Step_int_filter;
G4int Step_int_AlSupport;
G4int Step_int_Scintillator;
//....oooOO0OOooo.....oooOO0OOooo.....oooOO0OOooo.....oooOO0OOooo.....
SzinEventAction::SzinEventAction()
{}
//....oooOO0OOooo.....oooOO0OOooo.....oooOO0OOooo.....oooOO0OOooo.....
SzinEventAction::~SzinEventAction()
{}
//....oooOO0OOooo.....oooOO0OOooo.....oooOO0OOooo.....oooOO0OOooo.....
void SzinEventAction::BeginOfEventAction(const G4Event*evt)
{
        G4int event_id = evt->GetEventID();
        EnergyAbs = PositionWeigh_X = PositionWeigh_Y =  0.;
        order_scattering = n_control = ScattEverywhere =  0;
        Step_int_obj = Step_int_filter = Step_int_AlSupport = Step_int_Scintillator = -2;
  float p = static_cast<float>(event_id)/static_cast<float>(g_numEventsPerProcess);
  p *= 1000.0f;
  unsigned int percent = static_cast<unsigned int>(p);
  if(incr < percent)
  {
    std::cout << "process #" << std::setw(3) << std::setfill('0')
              << g_processNumber << ": "
```

```
                << std::showpoint << std::setw(4) << std::fixed
                << std::setprecision(1) << std::setfill(' ')
                << std::right << p*0.1 << "%" << " done\r";
      if(percent%250 == 0) std::cout << "\n";
      std::flush(std::cout);
   }
   incr = percent;
}
void SzinEventAction::EndOfEventAction(const G4Event* evt)
{
   if (EnergyAbs > 0.)
          {
                  G4double ext_inf_X= Detect_spec.Detector_size_x *0.5;
                  G4double ext_inf_Y= Detect_spec.Detector_size_y *0.5;
      G4double PosWeigh_X=PositionWeigh_X/(EnergyAbs/keV);     // mm
                  G4double PosWeigh_Y=PositionWeigh_Y/(EnergyAbs/keV);            // mm
      G4double pos_i_double=(PosWeigh_X + ext_inf_X)/Detect_spec.pixel_size_X;
                  G4double a_x=ceil(pos_i_double);
            G4double b_x=floor(pos_i_double);
            G4int pos_i = ((a_x-pos_i_double)<=(pos_i_double-b_x)) ? a_x : b_x;
      //G4int pos_i =pos_i_double;
      G4double pos_j_double=(PosWeigh_Y + ext_inf_Y)/Detect_spec.pixel_size_Y;
                  G4double a_y=ceil(pos_j_double);
            G4double b_y=floor(pos_j_double);
            G4int pos_j = ((a_y-pos_j_double)<=(pos_j_double-b_y)) ? a_y : b_y;
                  //G4int pos_j =pos_j_double;
                  G4int energy_int = EnergyAbs/keV + 0.5;
            EnergySpectrum[energy_int]=EnergySpectrum[energy_int]+1;
      EnergyDeposited[pos_i][pos_j]=EnergyDeposited[pos_i][pos_j]+EnergyAbs/MeV;
           if (ScattEverywhere > 0){
                    EnDepByScattEveryw-
here[pos_i][pos_j]=EnDepByScattEverywhere[pos_i][pos_j]+EnergyAbs/MeV;
            }
                  switch(order_scattering){
                     case 0:
                                    EnergyDeposited-
Prim[pos_i][pos_j]=EnergyDepositedPrim[pos_i][pos_j]+EnergyAbs/MeV;
                                    break;
                              case 1:
           EnergyDe-
posited_Order1[pos_i][pos_j]=EnergyDeposited_Order1[pos_i][pos_j]+EnergyAbs/MeV;
                                    break;
                              case 2:
                                    EnergyDe-
posited_Order2[pos_i][pos_j]=EnergyDeposited_Order2[pos_i][pos_j]+EnergyAbs/MeV;
                                    break;
                              default:
                                    EnergyDe-
posited_Mult[pos_i][pos_j]=EnergyDeposited_Mult[pos_i][pos_j]+EnergyAbs/MeV;
                                    break;
                  }
   }
}
```

A.3.7 Stepping Action

```
// SteppingAction.cpp
#include "SzinSteppingAction.hpp"
#include "SzinDetectorConstruction.hpp"
#include "SzinEventAction.hpp"
#include "SzinTrackInformation.hpp"
#include "SzinPrintAndAnalysis.hpp"
#include "G4TrackStatus.hpp"
#include "G4Track.hpp"
#include "G4Step.hpp"
#include "G4SteppingManager.hpp"
#include "G4StepPoint.hpp"
#include "G4VPhysicalVolume.hpp"
#include "G4ParticleDefinition.hpp"
#define material_detector 1
extern DetectorSpecifications Detect_spec;
extern G4double EnergyOnTheInputWin;
extern G4int order_scattering;
extern G4int ScattEverywhere;
extern G4int Box_Counter;
extern G4int n_control;
extern G4double Scatt_Object_Out;
extern G4double Scatt_Filter_Out;
extern G4double Scatt_AlSupport_Out;
extern G4double Scatt_Scintillator_Out;
extern G4int Step_int_obj;
extern G4int Step_int_filter;
extern G4int Step_int_AlSupport;
extern G4int Step_int_Scintillator;
extern G4double NPhotonReachWorldBoundary_object;
extern G4double NPhotonReachWorldBoundary_filter;
extern G4double NPhotonReachWorldBoundary_AlSupport;
extern G4double NPhotonReachWorldBoundary_Scintillator;
SzinSteppingAction::SzinSteppingAction(SzinDetectorConstruction* det, SzinEventAction* evt)
:detector(det), eventAction(evt)
{ }
//....oooOO0OOooo.....oooOO0OOooo.....oooOO0OOooo.....oooOO0OOooo.....
void SzinSteppingAction::UserSteppingAction(const G4Step*bStep)
{
        const G4Track* ftrack = bStep->GetTrack();
                                G4String Name=ftrack->GetDefinition()->GetParticleName();
                                G4int parent_id=ftrack->GetParentID();
                                G4int Current_step_number=ftrack->GetCurrentStepNumber();
                                G4ThreeVector posTrack=ftrack->GetPosition();
                                //SzinTrackInformation* info=(SzinTrackInformation*) (ftrack-
>GetUserInformation());
        G4StepPoint* point1= bStep->GetPreStepPoint();
        G4StepPoint* point2= bStep->GetPostStepPoint();
                                G4ThreeVector pos1= point1->GetPosition();
        G4ThreeVector pos2= point2->GetPosition();
                                /*Volume where the step has just gone through */
                                G4String volume_name= "OutOfWorld";
                                if (point1->GetPhysicalVolume()!=0)  volume_name= point1-
>GetPhysicalVolume()->GetName();
                                G4Material* material = point1->GetMaterial();
```

```
                        G4String material_name= material->GetName();
                        G4String Track_Next_Volume= "OutOfTheWorld";
        if (ftrack->GetNextVolume() != 0)Track_Next_Volume=ftrack->GetNextVolume()-
>GetName();
                        /* process which has limited the step */
                        G4String process_name= "NULL";
                        if (point2->GetProcessDefinedStep() != NULL)process_name= point2-
>GetProcessDefinedStep()->GetProcessName();
                        if (volume_name == "Object_phys" && (process_name == "LowEnComp-
ton" || process_name == "LowEnRayleigh")){
                order_scattering=order_scattering+1;
                        }
                        if (point2->GetStepStatus() == fGeomBoundary && Name == "gamma"){
                                if (volume_name == "Object_phys"){
                                        Scatt_Object_Out= Scatt_Object_Out+1;
                                        Step_int_obj = Current_step_number;
                                }
                                if (volume_name == "PostfilterPhysVol"){
                                        Scatt_Filter_Out= Scatt_Filter_Out+1;
                                        Step_int_filter = Current_step_number;
                                }
          if (volume_name == "Al_DetectorPhys"){
                                        Scatt_AlSupport_Out= Scatt_AlSupport_Out+1;
                                        Step_int_AlSupport = Current_step_number;
                                }
                        if (volume_name == "ScintillatorPhys"){
                                        Scatt_Scintillator_Out= Scatt_Scintillator_Out+1;
                                        Step_int_Scintillator = Current_step_number;
                                }
                        }
                        if (point1->GetStepStatus() == fGeomBoundary && point2-
>GetStepStatus()== fGeomBoundary && Name == "gamma"&& volume_name == "expHall"
                                && process_name == "Transportation" && Track_Next_Volume
== "OutOfTheWorld"){
                                if (Current_step_number == Step_int_obj+1) NPhotonReach-
WorldBoundary_object=NPhotonReachWorldBoundary_object+1;
                                if (Current_step_number == Step_int_filter+1) NPhotonReach-
WorldBoundary_filter=NPhotonReachWorldBoundary_filter+1;
          if (Current_step_number == Step_int_AlSupport+1) NPhotonReachWorldBound-
ary_AlSupport=NPhotonReachWorldBoundary_AlSupport+1;
                                if (Current_step_number == Step_int_Scintillator+1) NPhoton-
ReachWorldBoundary_Scintillator=NPhotonReachWorldBoundary_Scintillator+1;
                        }
#if material_detector
                        G4double edep = bStep->GetTotalEnergyDeposit();
                        if (edep > 0. && point1->GetPhysicalVolume()!= detector->GetAbsorber())
return;
                        eventAction->AddAbs(edep);
                        eventAction->Position_weighted(edep,posTrack.x());
                        eventAction->Position_weighted_Y(edep,posTrack.y());
        if ((volume_name == "Object_phys"  || volume_name == "PostfilterPhysVol" || volume_name
== "PrecRect_phys"
                                || volume_name == "Al_DetectorPhys")&& (process_name ==
"LowEnCompton" || process_name == "LowEnRayleigh"))ScattEverywhere=ScattEverywhere+1;
#else // material_detector
                        G4double EnergyOnTheInputWin=ftrack->GetKineticEnergy();
```

```
                        G4double frontside_min=-
(Detect_spec.detector_sourceDistance+0.00001*mm);
                        G4double frontside_max=-(Detect_spec.detector_sourceDistance-
0.00001*mm);
                        if (Track_Next_Volume == "SurfaceVacuum" &&  -
posTrack.z()>frontside_min &&
                    -posTrack.z()<frontside_max  && Name== "gamma" && parent_id==0 &&
n_control == 0){
                                n_control=n_control+1;
                                eventAction->AddAbs(EnergyOnTheInputWin);
                                eventAction-
>Position_weighted(EnergyOnTheInputWin,posTrack.x());
                                eventAction-
>Position_weighted_Y(EnergyOnTheInputWin,posTrack.y());
          }
#endif // material_detector
}
```

A.3.8 Geometry - Generation of the X-ray spectrum

DetectorConstruction.cpp

```
/*tungsten tar-
get*****************************************************************************/

                        G4Box *target_box = new G4Box("target", 7.5*mm,7.5*mm,7.5*mm);
                        G4LogicalVolume* target_log = new G4LogicalVolume(target_box,W,
"TargetLogVol", 0,0,0);
                        G4VisAttributes* target_boxVisAtt= new
G4VisAttributes(G4Colour(0.,1.,1.)); //azzurro
                        target_boxVisAtt->SetForceWireframe(true);
                        target_log->SetVisAttributes(target_boxVisAtt);
                        /*  ruoto l'anodo*/
                        G4RotationMatrix* RotObj= new G4RotationMatrix();
                        RotObj->rotateX(79.*deg);  //Target angle: 60.*deg  -> 30°; 79.*deg -> 11°
                        target_phys = new G4PVPlacement(RotObj,

        G4ThreeVector(0.0,0.0,-7.5*mm),
                                                                target_log,
                                                                "targetPhys",
                                                        experimentalHall_log,
                                                        false,
                                                                0);




///* inherent filtration  2.3mm Fe
*********************************************************/
                        G4Box *inh_filter_box = new G4Box("inh_filter",
73*mm,1.15*mm,73*mm);
```

```
                        G4LogicalVolume* inh_filter_log = new
G4LogicalVolume(inh_filter_box,Fe,"inh_filterLogVol", 0,0,0);
                        G4VisAttributes* inh_filter_boxVisAtt= new
G4VisAttributes(G4Colour(0.,0.5,0.2));
                        inh_filter_boxVisAtt->SetForceWireframe(true);
                        inh_filter_log->SetVisAttributes(inh_filter_boxVisAtt);
                        G4VPhysicalVolume* inh_filter_phys = new G4PVPlacement(0,

        G4ThreeVector(0.,-40.0*mm,0.0),
                                                                    inh_filter_log,

        "inh_filterPhys",
                                                        experimentalHall_log,
                                                        false,
//                                                      0);
//
///* inherent filtration  1.0mm Cu
**********************************************************/
                        G4Box *inh_filter_Cu_box = new G4Box("inh_filter_Cu",
73*mm,0.5*mm,73*mm);
                        G4LogicalVolume* inh_filter_Cu_log = new
G4LogicalVolume(inh_filter_Cu_box,Cu,"inh_filterCuLogVol", 0,0,0);
                        G4VisAttributes* inh_filter_Cu_boxVisAtt= new
G4VisAttributes(G4Colour(0.2,0.8,0.));
                        inh_filter_Cu_boxVisAtt->SetForceWireframe(true);
                        inh_filter_Cu_log->SetVisAttributes(inh_filter_Cu_boxVisAtt);
                        G4VPhysicalVolume* inh_filter_Cu_phys = new G4PVPlacement(0,

        G4ThreeVector(0.,-43.0*mm,0.0),

        inh_filter_Cu_log,

        "inh_filterCuPhys",
                                                        experimentalHall_log,
                                                        false,
                                                        0);



///* extern filtration 4.5mm Brass
**********************************************************/
                        G4Box *ext_filter_box = new G4Box("ext_filter",
73*mm,2.25*mm,73*mm);
                        G4LogicalVolume* ext_filter_log = new
G4LogicalVolume(ext_filter_box,Brass,"ext_filterLogVol", 0,0,0);
                        G4VisAttributes* ext_filter_boxVisAtt= new
G4VisAttributes(G4Colour(0.,1.,1.));
                        ext_filter_boxVisAtt->SetForceWireframe(true);
                ext_filter_log->SetVisAttributes(ext_filter_boxVisAtt);
                        G4VPhysicalVolume* ext_filter_phys = new G4PVPlacement(0,

        G4ThreeVector(0.,-48.0*mm,0.0),
                                                        ext_filter_log,

        "ext_filterPhys",
                                                        experimentalHall_log,
                                                        0);
```

```
/*detector  ******************************************/


G4Box* detector_box=new G4Box ("detector",73*mm,1*mm,73*mm);
                        G4LogicalVolume* detector_log = new
G4LogicalVolume(detector_box,Vacuum, "DetectorLogVol", 0, 0, 0);
                        G4VisAttributes* det_boxVisAtt= new
G4VisAttributes(G4Colour(0.5,0.3,0.1));
                        det_boxVisAtt->SetForceWireframe(true);
                        detector_log->SetVisAttributes(det_boxVisAtt);
                        G4VPhysicalVolume* detector_phys =
                        new G4PVPlacement(0,
                                                        G4ThreeVector(0.,-
201.0*mm,0.0),
                                                detector_log,
                                                "DetectorPhys",
                                                experimentalHall_log,
                                                false,
                                                0);



                        G4SDManager* SDman = G4SDManager::GetSDMpointer();
                        G4String szinDetectorSDname = "/szin/detector";
                        SzinSD * szinDetectorSD = new SzinSD(szinDetectorSDname);
                        SDman->AddNewDetector(szinDetectorSD);
                        detector_log->SetSensitiveDetector(szinDetectorSD);
                        return experimentalHall_phys;
```

A.3.9 X-ray source collimator

```
void Geometry_Construction::Precollimator(G4LogicalVolume* experimentalHall_log_dum,
G4Material* material_dum)
{
                G4Box* PrecRect_Box=new G4Box("PrecRect_Box", 45*mm,45*mm,50*mm);
     G4double  In_hole_dx1=35.9*mm;
     G4double  In_hole_dx2=20.3*mm;
     G4double  In_hole_dy1=24.55*mm;
     G4double  In_hole_dy2=13.85*mm;
     G4double  In_hole_dz= 50*mm;
          G4Trd* In_hole= new
G4Trd("In_hole_trap",In_hole_dx1,In_hole_dx2,In_hole_dy1,In_hole_dy2,In_hole_dz);
     G4ThreeVector translation_prec(0,0,0);
     G4SubtractionSolid *PrecRect = new G4SubtractionSolid("PrecRect",PrecRect_Box,In_hole, 0,
translation_prec);
                G4LogicalVolume *PrecRect_log= new
G4LogicalVolume(PrecRect,material_dum,"PrecRect_log",0,0,0);
                G4VisAttributes* PrecRect_VisAtt=new G4VisAttributes(G4Colour(0.1,0.6,0.1));
                PrecRect_VisAtt->SetForceWireframe(true);
                PrecRect_log->SetVisAttributes(PrecRect_VisAtt);
                G4VPhysicalVolume* PrecRect_phy=new G4PVPlacement(0,G4ThreeVector(0,0,-
180*mm),
```

```
                PrecRect_log,"PrecRect_phys",experimentalHall_log_dum,false,0);
}
```

A.3.10 2D anti-scatter grid

```
// COLLIMATOR   -GRID CONE BEAM COLLIMATOR

void Geometry_Construction::Collimator_Grid(G4LogicalVolume* experimental-
Hall_log_dum,G4Material* material_dum,G4int CellsNumber, G4float grid_X, G4float grid_G,
G4float grid_Z )
{
                G4double GridFontSide_posZ=-1390.0;
                G4double GridCollim_positionZ = GridFontSide_posZ - grid_Z*0.5;
                        /* septi vertical */
                        G4double i_max=(CellsNumber*0.5+0.5);
                        for (G4int i_index=0; i_index<i_max; i_index++){
                                Vertex_Vertical vertexV;
                                ver-
texV.CenteredTrap(i_index,grid_X,grid_G,grid_Z,CellsNumber);
                                G4Trap* septum_i_box=new
G4Trap("trap",vertexV.pPoints);
                                G4LogicalVolume * sep_log= new
G4LogicalVolume(septum_i_box,material_dum, "septi log");
                                G4VisAttributes* sep_VisAtt=new
G4VisAttributes(G4Colour(0.2,0.3,0.1));
                                sep_VisAtt->SetForceWireframe(true);
                                sep_log->SetVisAttributes(sep_VisAtt);
                                G4VPhysicalVolume* sep_phy=new
G4PVPlacement(0,G4ThreeVector(vertexV.CenterTrapez.x()*mm,vertexV.CenterTrapez.y()*mm,Grid
Collim_positionZ*mm),sep_log,"sep_phys",experimentalHall_log_dum,false,0);
                                //reflection
                                G4Translate3D translation_v(-
vertexV.CenterTrapez.x()*mm,-vertexV.CenterTrapez.y()*mm,GridCollim_positionZ*mm);
                                G4ReflectX3D reflection_v;
                                G4Transform3D trans-
form_v=translation_v*reflection_v;
                                G4ReflectionFactory::Instance()-
>Place(transform_v,"sep_phys",sep_log,experimentalHall_log_dum,false,1);
                        }

                        /* septi orizontal  */
                        for (G4int m_index=0; m_index<i_max; m_index++){ //mi
sposto di una riga  //problema 3D
                        //for (G4int m_index=0; m_index<1; m_index++){
//Problema 2D: solo 1 cella lungo la y
                                G4float FactorA=(grid_X-grid_G)*0.5;
                                G4float y_oriz=FactorA+m_index*grid_X;
                                G4int a;
                                G4int b;
                                for (G4int index=0; index<2; index++){
                                        a=1-2*index;
                                        b=0-index;
                                        G4float y1_i=a*y_oriz+b*grid_G;
```

```
                                                    for (G4int m_c_index=-1;
m_c_index<i_max-1; m_c_index++){ // mi sposto sulla stessa riga di una colonna
                                                        Vertex_Orizontal vertexO;
                                                        vertexO.CenteredTrap_O(y1_i,
m_c_index,grid_X,grid_G,grid_Z,CellsNumber);
                                                        G4Trap* septum_i_box_o= new
G4Trap("septum oriz pos", vertexO.pPoints_o);
                                                        G4LogicalVolume * sep_log_o=
new G4LogicalVolume(septum_i_box_o,material_dum, "septi o log");
                                                        G4VisAttributes*
sep_o_VisAtt=new G4VisAttributes(G4Colour(0.2,0.3,0.1));
                                                        sep_o_VisAtt-
>SetForceWireframe(true);
                                                        sep_log_o-
>SetVisAttributes(sep_o_VisAtt);
                                                        G4VPhysicalVolume*
sep_phy_o=new
G4PVPlacement(0,G4ThreeVector(vertexO.CenterTrapez_o.x()*mm,vertexO.CenterTrapez_o.y()*mm,
GridCollim_positionZ*mm),sep_log_o,"sep_phys o",experimentalHall_log_dum,false,0);
                                                        //reflection
                                                        if (m_c_index > -1)
                                                        {
                                                            G4Translate3D transla-
tion(-vertexO.CenterTrapez_o.x()*mm,vertexO.CenterTrapez_o.y()*mm,GridCollim_positionZ*mm);
                                                        G4ReflectX3D reflec-
tion;
                                                        G4Transform3D trans-
form=translation*reflection;

          G4ReflectionFactory::Instance()->Place(transform,"sep_phys
o",sep_log_o,experimentalHall_log_dum,false,1);
                                                        }
                                                    }
                                                }
                                            }
}

/* methods to build the cone beam GRID collimator*/

                    void Vertex_Vertical::CenteredTrap(G4int i,G4float value_X,G4float
value_G,G4float value_Z,G4int value_CellsNumber)
                    {
                    // E' diverso ora //
              G4float Back_Side_z=1494.5;

                    G4float FactorA=(value_X-value_G)*0.5;
                    /*  if parallel grid Magn=1 */
                    //G4float Magn=1.0;
                    G4float Magn=-Back_Side_z/(-Back_Side_z+value_Z); // Magnification

                    G4float y1=(value_G+value_X*value_CellsNumber)*0.5;

                    //G4float y1=(value_G+value_X*1)*0.5; //per problema 2 D: costruisco in altezza
solo 1 cella //

                    G4float FactorA_prim=FactorA*Magn;
                    G4float X_prim=value_X*Magn;
```

```
G4float y1_prim=y1*Magn;
G4float G_prim=value_G*Magn;
G4float Fact_1=FactorA+i*value_X;
G4float Fact_2=Fact_1+value_G;
G4float Fact_1_prim=FactorA_prim+i*X_prim;
G4float Fact_2_prim=Fact_1_prim+G_prim;
/* 1) trap points*/
G4ThreeVector A= G4ThreeVector(Fact_1_prim*mm,-y1_prim*mm,0);
G4ThreeVector B= G4ThreeVector(Fact_2_prim*mm, -y1_prim*mm,0);
G4ThreeVector C= G4ThreeVector(Fact_1_prim*mm,y1_prim*mm,0);
G4ThreeVector D= G4ThreeVector(Fact_2_prim*mm,y1_prim*mm,0);
G4ThreeVector A_prim= G4ThreeVector(Fact_1*mm,-y1*mm,value_Z*mm);
G4ThreeVector B_prim= G4ThreeVector(Fact_2*mm,-y1*mm,value_Z*mm);
G4ThreeVector C_prim= G4ThreeVector(Fact_1*mm, y1*mm,value_Z*mm);
G4ThreeVector D_prim= G4ThreeVector(Fact_2*mm, y1*mm,value_Z*mm);
/* 2) trap centering in the center of the reference frame */
Center=(A+B+C+D)/4;
Center_prim=(A_prim+B_prim+C_prim+D_prim)/4;
CenterTrapez=(Center+Center_prim)/2;
A=A-CenterTrapez;
B=B-CenterTrapez;
C=C-CenterTrapez;
D=D-CenterTrapez;
A_prim=A_prim-CenterTrapez;
B_prim=B_prim-CenterTrapez;
C_prim=C_prim-CenterTrapez;
D_prim=D_prim-CenterTrapez;
Center_after=(A+B+C+D)/4;
Center_prim_after=(A_prim+B_prim+C_prim+D_prim)/4;
CenterTrapez_after=(Center_after+Center_prim_after)/2.0;
pPoints[0]=A;
pPoints[1]=B;
pPoints[2]=C;
pPoints[3]=D;
pPoints[4]=A_prim;
pPoints[5]=B_prim;
pPoints[6]=C_prim;
pPoints[7]=D_prim;
}

void Vertex_Orizontal::CenteredTrap_O(G4float y1, G4int m_c,G4float
value_X,G4float value_G,G4float value_Z,G4int value_CellsNumber)
{

G4float Back_Side_z=1494.5;

G4float FactorA=(value_X-value_G)*0.5;
/*  if parallel grid Magn=1 */
//G4float Magn=1.0;
G4float Magn=-Back_Side_z/(-Back_Side_z+value_Z); // Magnification
const G4float toler=0.0002*mm; //tolerance Geant4 0.1 micron
G4float  Fact_1_o=FactorA+value_G+toler;
G4float Fact_2_o=FactorA-toler;
G4float x_1=Fact_1_o+m_c*value_X;
G4float x_2=Fact_2_o+value_X*(m_c+1);
if (m_c==-1) { x_1=-FactorA+toler; x_2=FactorA-toler;} // central septum
G4float x_1_prim=x_1*Magn;
```

```
                    G4float x_2_prim=x_2*Magn;
                    G4float y1_prim=y1*Magn;
                    G4float y2_prim=(y1+value_G)*Magn;
                    G4ThreeVector A_o= G4ThreeVector(x_1_prim*mm,y1_prim*mm,0.);
                    G4ThreeVector B_o= G4ThreeVector(x_2_prim*mm,y1_prim*mm,0.);
                    G4ThreeVector C_o= G4ThreeVector(x_1_prim*mm,y2_prim*mm,0.);
                    G4ThreeVector D_o= G4ThreeVector(x_2_prim*mm,y2_prim*mm,0.);
                    G4ThreeVector A_prim_o= G4ThreeVector(x_1*mm,y1*mm,value_Z*mm);
                    G4ThreeVector B_prim_o= G4ThreeVector(x_2*mm,y1*mm,value_Z*mm);
                    G4ThreeVector C_prim_o=
G4ThreeVector(x_1*mm,(y1+value_G)*mm,value_Z*mm);
                    G4ThreeVector D_prim_o=
G4ThreeVector(x_2*mm,(y1+value_G)*mm,value_Z*mm);
                    /* 2) trap centering in the center of the reference frame */
                    Center_o=(A_o+B_o+C_o+D_o)/4;
                    Center_prim_o=(A_prim_o+B_prim_o+C_prim_o+D_prim_o)/4;
                    CenterTrapez_o=(Center_o+Center_prim_o)/2;
                    A_o=A_o-CenterTrapez_o;
                    B_o=B_o-CenterTrapez_o;
                    C_o=C_o-CenterTrapez_o;
                    D_o=D_o-CenterTrapez_o;
                    A_prim_o=A_prim_o-CenterTrapez_o;
                    B_prim_o=B_prim_o-CenterTrapez_o;
                    C_prim_o=C_prim_o-CenterTrapez_o;
                    D_prim_o=D_prim_o-CenterTrapez_o;
                    Center_after_o=(A_o+B_o+C_o+D_o)/4;
                    Center_prim_after_o=(A_prim_o+B_prim_o+C_prim_o+D_prim_o)/4;
                    CenterTrapez_after_o=(Center_after_o+Center_prim_after_o)/2.0;
                    pPoints_o[0]=A_o;
                    pPoints_o[1]=B_o;
                    pPoints_o[2]=C_o;
                    pPoints_o[3]=D_o;
                    pPoints_o[4]=A_prim_o;
                    pPoints_o[5]=B_prim_o;
                    pPoints_o[6]=C_prim_o;
                    pPoints_o[7]=D_prim_o;
                    }
```

A.3.11 1D anti-scatter grid

```
//SLITS CONE BEAM COLLIMATOR   ////**********
****************************************

void Geometry_Construction::Collimator_Slit(G4LogicalVolume* experimental-
Hall_log_dum,G4Material* material_dum,G4int CellsNumber,G4float slit_X,G4float slit_G,G4float
slit_Z, G4float x1)
{
        G4double GridFontSide_posZ=-1390.0;
        G4double SlitCollim_positionZ = GridFontSide_posZ - slit_Z*0.5;
        G4double i_max=CellsNumber*0.5+0.5;
            for (G4int negative=0; negative<2; negative++){
              for (G4int i_index=0; i_index<i_max; i_index++){
                        Slit_oriz vertexV;
```

```
                                        ver-
texV.CenteredTrap(i_index,slit_X,slit_G,slit_Z,CellsNumber,negative, x1);
                                        G4Trap* septum_i_box=new G4Trap("trap",vertexV.pPoints);
                                        G4LogicalVolume * sep_log= new
G4LogicalVolume(septum_i_box,material_dum, "septi log");
                                        G4VisAttributes* sep_VisAtt=new
G4VisAttributes(G4Colour(0.2,0.3,0.1));
                                        sep_VisAtt->SetForceSolid(true); // sep_VisAtt-
>SetForceWireframe(true);
                                        sep_log->SetVisAttributes(sep_VisAtt);
                                        G4VPhysicalVolume* sep_phy=new
G4PVPlacement(0,G4ThreeVector(vertexV.CenterTrapez.x()*mm,vertexV.CenterTrapez.y()*mm,Slit
Collim_positionZ*mm),sep_log,"sep_phys",experimentalHall_log_dum,false,0);
                                }
                        }
}


*method to build the SLIT cone beam collimator*/

void Slit_oriz::CenteredTrap(G4int i,G4float value_X,G4float value_G,G4float value_Z,
                                                                                G4int
value_CellsNumber,G4int neg, G4float x1)
                {
                        const G4float GridSideFront_posZ=1390.0;
                        G4float Magn=(GridSideFront_posZ+value_Z)/GridSideFront_posZ;
                        G4float FactorA=(value_X-value_G)*0.5;
                        G4float x1_prim=x1*Magn;
                        G4float FactorA_prim=FactorA*Magn;
                        G4float X_prim=value_X*Magn;
                        G4float G_prim=value_G*Magn;
                        G4float Fact_1=FactorA+i*value_X;
                        G4float Fact_2=Fact_1+value_G;
                        G4float Fact_1_prim=FactorA_prim+i*X_prim;
                        G4float Fact_2_prim=Fact_1_prim+G_prim;
                        /* 1) trap points*/
                        G4ThreeVector A= G4ThreeVector(-x1_prim*mm,Fact_1_prim*mm,0);
                        G4ThreeVector B= G4ThreeVector(x1_prim*mm,Fact_1_prim*mm,0);
                        G4ThreeVector C= G4ThreeVector(-x1_prim*mm,Fact_2_prim*mm,0);
                        G4ThreeVector D= G4ThreeVector( x1_prim*mm,Fact_2_prim*mm,0);
                        G4ThreeVector A_prim= G4ThreeVector(-x1*mm,Fact_1*mm,
value_Z*mm);
                        G4ThreeVector B_prim=  G4ThreeVector(x1*mm,Fact_1*mm,
value_Z*mm);
                        G4ThreeVector C_prim= G4ThreeVector(-
x1*mm,Fact_2*mm,value_Z*mm);
                        G4ThreeVector D_prim=
G4ThreeVector(x1*mm,Fact_2*mm,value_Z*mm);
                        if (neg==1){
                        /* 1) trap points*/
                        A= G4ThreeVector(-x1_prim*mm,-Fact_2_prim*mm,0);
                        B= G4ThreeVector(x1_prim*mm,-Fact_2_prim*mm,0);
                        C= G4ThreeVector(-x1_prim*mm,-Fact_1_prim*mm,0);
                        D= G4ThreeVector( x1_prim*mm,-Fact_1_prim*mm,0);
                        A_prim= G4ThreeVector(-x1*mm,-Fact_2*mm, value_Z*mm);
                        B_prim=  G4ThreeVector(x1*mm,-Fact_2*mm, value_Z*mm);
```

```
                C_prim= G4ThreeVector(-x1*mm,-Fact_1*mm,value_Z*mm);
                D_prim= G4ThreeVector(x1*mm,-Fact_1*mm,value_Z*mm);
                }
                /* 2) trap centering in the center of the reference frame */
                Center=(A+B+C+D)/4;
                Center_prim=(A_prim+B_prim+C_prim+D_prim)/4;
                CenterTrapez=(Center+Center_prim)/2;
                A=A-CenterTrapez;
                B=B-CenterTrapez;
                C=C-CenterTrapez;
                D=D-CenterTrapez;
                A_prim=A_prim-CenterTrapez;
                B_prim=B_prim-CenterTrapez;
                C_prim=C_prim-CenterTrapez;
                D_prim=D_prim-CenterTrapez;
                Center_after=(A+B+C+D)/4;
                Center_prim_after=(A_prim+B_prim+C_prim+D_prim)/4;
                CenterTrapez_after=(Center_after+Center_prim_after)/2.0;
                pPoints[0]=A;
                pPoints[1]=B;
                pPoints[2]=C;
                pPoints[3]=D;
                pPoints[4]=A_prim;
                pPoints[5]=B_prim;
                pPoints[6]=C_prim;
                pPoints[7]=D_prim;
        }
```

A.3.12 Detector box

```
 //File geometry.cpp

// BOX SHIELDING  SANDWICH 3 LAYERS

void Geometry_Construction::ShieldingBox(G4LogicalVolume* experimental-
Hall_log_dum,G4Material* material_dum, G4Material* material_Inner_dum)
{
//                                      ////   Layer 1 Extern Steel 5 mm
**************************************************************************
*****
//
                                        G4double ThickShield1=5*mm;
        G4double Layer1_x=451.0*mm;
        G4double Layer1_y=303.0*mm;
                                        G4double Layer1_z=507.0*mm;
                                        G4Box* Layer1_box=new G4Box("Layer1",Layer1_x*0.5,
Layer1_y*0.5, Layer1_z*0.5);
                                        G4double Remove1_x=451.0*mm-ThickShield1*2;
        G4double Remove1_y=303.0*mm + 7.0*mm;
                                        G4double Remove1_z=507.0*mm-ThickShield1*2;
        G4Box* Remove1_box=new G4Box("Remove1",Remove1_x*0.5, Remove1_y*0.5, Re-
move1_z*0.5);
                                        G4ThreeVector translationRemove1(0,-8.5*mm,0);
                                        G4SubtractionSolid *Shield1 = new
G4SubtractionSolid("Shield1",Layer1_box,Remove1_box, 0, translationRemove1);
```

```
                                    G4LogicalVolume * Shield1_log= new
G4LogicalVolume(Shield1,material_dum,"Shield1_log");
                                    G4VisAttributes* Shield1_VisAtt=new
G4VisAttributes(G4Colour(0.2,0.3,0.1));
                                    Shield1_VisAtt->SetForceWireframe(true);
                                    Shield1_log->SetVisAttributes(Shield1_VisAtt);
                                    G4double Shiled1SourceD=-1500*mm-Layer1_z/2-1.1;
                                    G4VPhysicalVolume* Shield1_phy=new
G4PVPlacement(0,G4ThreeVector(0,0,Shiled1SourceD),
                                    Shield1_log,"Shield1_phy",experimentalHall_log_dum,false,0);

        G4double ThickShield2=3*mm;
        G4double Layer2_x=Remove1_x-0.1*mm;
        G4double Layer2_y=Layer1_y-ThickShield1*2-0.1*mm;
                                    G4double Layer2_z=Remove1_z-0.1*mm;
                                    G4Box* Layer2_box=new G4Box("Layer2",Layer2_x*0.5,
Layer2_y*0.5, Layer2_z*0.5);
                                    G4double Remove2_x=Layer2_x-ThickShield2*2;
        G4double Remove2_y=Layer2_y + 7.0*mm;
                                    G4double Remove2_z=Layer2_z-ThickShield2*2;
        G4Box* Remove2_box=new G4Box("Remove2",Remove2_x*0.5, Remove2_y*0.5, Re-
move2_z*0.5);
                                    G4ThreeVector translationRemove2(0,-6.5*mm,0);
                                    G4SubtractionSolid *Shield2 = new
G4SubtractionSolid("Shield2",Layer2_box,Remove2_box, 0, translationRemove2);
                                    G4LogicalVolume * Shield2_log= new
G4LogicalVolume(Shield2,material_Inner_dum,"Shield2_log");
                                    G4VisAttributes* Shield2_VisAtt=new
G4VisAttributes(G4Colour(0.5,0.1,0.6));
                                    Shield2_VisAtt->SetForceWireframe(true);
                                    Shield2_log->SetVisAttributes(Shield2_VisAtt);

        //when it is used within the sandwich
                                    G4VPhysicalVolume* Shield2_phy=new
G4PVPlacement(0,G4ThreeVector(0,0,0),
                                    Shield2_log,"Shield2_phy",Shield1_log,false,0);

                                    //when it is used alone
                                    //G4VPhysicalVolume* Shield2_phy=new
G4PVPlacement(0,G4ThreeVector(0,0,Shiled1SourceD),
                                    //Shield2_log,"Shield2_phy",experimentalHall_log_dum,false,0);

//                                  //////  Layer Inner Steel 3 mm
**********************************************************************************
*****
//
        G4double ThickShield3=3*mm;
        G4double Layer3_x=Remove2_x-0.1*mm;
        G4double Layer3_y=Layer2_y-ThickShield2*2-0.1*mm;
                                    G4double Layer3_z=Remove2_z-0.1*mm;
                                    G4Box* Layer3_box=new G4Box("Layer3",Layer3_x*0.5,
Layer3_y*0.5, Layer3_z*0.5);
                                    G4double Remove3_x=Layer3_x-ThickShield3*2;
        G4double Remove3_y=Layer3_y + 7.0*mm;
                                    G4double Remove3_z=Layer3_z-ThickShield3*2;
        G4Box* Remove3_box=new G4Box("Remove3",Remove3_x*0.5, Remove3_y*0.5, Re-
move3_z*0.5);
```

```
                                    G4ThreeVector translationRemove3(0,-6.5*mm,0);
                                    G4SubtractionSolid *Shield3 = new
G4SubtractionSolid("Shield3",Layer3_box,Remove3_box, 0, translationRemove3);
                                    G4LogicalVolume * Shield3_log= new
G4LogicalVolume(Shield3,material_dum,"Shield3_log");
                                    G4VisAttributes* Shield3_VisAtt=new
G4VisAttributes(G4Colour(0.2,0.9,0.1));
                                    Shield3_VisAtt->SetForceWireframe(true);
                                    Shield3_log->SetVisAttributes(Shield3_VisAtt);
                                    G4VPhysicalVolume* Shield3_phy=new
G4PVPlacement(0,G4ThreeVector(0,0,0),
                                    Shield3_log,"Shield3_phy",Shield2_log,false,0);

//              ///Bottom part
**********************************************************************************
*********
//
          G4double bottom_pos_z=-1501*mm-0.1*mm-115*0.5*mm;
//
//
//                                  // bottom_3 3 mm mat Steel
                                    G4Box* Bottom_3_box=new
G4Box("Bottom_3_box",451*0.5*mm, ThickShield3*0.5*mm, 115*0.5*mm);
                                    G4LogicalVolume * Bottom_3_log= new
G4LogicalVolume(Bottom_3_box,material_dum,"Bottom_3_log");
                                    G4VisAttributes* Bottom_3_VisAtt=new
G4VisAttributes(G4Colour(0.2,0.3,0.6));
                                    Bottom_3_VisAtt->SetForceWireframe(true);
                                    Bottom_3_log->SetVisAttributes(Bottom_3_VisAtt);

                                    G4double bottom_3pos_y=-
(Layer1_y*0.5+0.1*mm+ThickShield3*0.5);
                                    G4VPhysicalVolume* Bottom_3_phy=new G4PVPlacement(
                                    0,G4ThreeVector(0.0,bottom_3pos_y,bottom_pos_z)

          ,Bottom_3_log,"Bottom_3_phys",experimentalHall_log_dum,false,0);

                                    // bottom_2 3 mm Pb
                                    G4Box* Bottom_2_box=new
G4Box("Bottom_2_box",451*0.5*mm, ThickShield2*0.5*mm, 115*0.5*mm);
                                    G4LogicalVolume * Bottom_2_log= new
G4LogicalVolume(Bottom_2_box,material_Inner_dum,"Bottom_2_log");
                                    G4VisAttributes* Bottom_2_VisAtt=new
G4VisAttributes(G4Colour(0.4,0.1,0.6));
                                    Bottom_2_VisAtt->SetForceWireframe(true);
                                    Bottom_2_log->SetVisAttributes(Bottom_2_VisAtt);
                                    G4double bottom_2pos_y=bottom_3pos_y-ThickShield3*0.5-
0.1*mm-ThickShield2*0.5;
                                    G4VPhysicalVolume* Bottom_2_phy=new G4PVPlacement(
                                    0,G4ThreeVector(0.0,bottom_2pos_y,bottom_pos_z)

          ,Bottom_2_log,"Bottom_2_phys",experimentalHall_log_dum,false,0);

//
//                                  // bottom_1 5 mm Steel
                                    G4Box* Bottom_1_box=new
G4Box("Bottom_1_box",451*0.5*mm, ThickShield1*0.5*mm, 115*0.5*mm);
```

```
                                        G4LogicalVolume * Bottom_1_log= new
G4LogicalVolume(Bottom_1_box,material_dum,"Bottom_1_log");
                                        G4VisAttributes* Bottom_1_VisAtt=new
G4VisAttributes(G4Colour(0.3,0.2,0.7));
                                        Bottom_1_VisAtt->SetForceWireframe(true);
                                        Bottom_1_log->SetVisAttributes(Bottom_1_VisAtt);
                                        G4double bottom_1pos_y= bottom_2pos_y - ThickShield2*0.5 -
0.1*mm - ThickShield1*0.5;
                                        G4VPhysicalVolume* Bottom_1_phy=new G4PVPlacement(
                                        0,G4ThreeVector(0.0,bottom_1pos_y,bottom_pos_z)

        ,Bottom_1_log,"Bottom_1_phys",experimentalHall_log_dum,false,0);
//
//          /// BackSide  ///////////////
//
                                G4double backside_pos_y=-(Layer1_y*0.5+0.1*mm+692*0.5*mm);
//
//                                      // backside_3 3 mm mat Steel
                                        G4Box* backside_3_box=new
G4Box("backside_3_box",451*0.5*mm,692*0.5*mm, ThickShield3*0.5*mm);
                                        G4LogicalVolume * backside_3_log= new
G4LogicalVolume(backside_3_box,material_dum,"backside_3_log");
                                        G4VisAttributes* backside_3_VisAtt=new
G4VisAttributes(G4Colour(0.2,0.3,0.6));
                                        backside_3_VisAtt->SetForceWireframe(true);
                                        backside_3_log->SetVisAttributes(backside_3_VisAtt);

                                        G4double backside_3pos_z=- 1501*mm - 507*mm + Thick-
Shield1*0.5 + ThickShield1*0.5 + 0.1*mm + ThickShield2*0.5 + 0.1*mm + ThickShield2*0.5 +
ThickShield3*0.5;
                                        G4VPhysicalVolume* backside_3_phy=new G4PVPlacement(
                                        0,G4ThreeVector(0.0,backside_pos_y,backside_3pos_z)

        ,backside_3_log,"backside_3_phys",experimentalHall_log_dum,false,0);
//
//
                                        // backside_2 3 mm PbSb4
                                        G4Box* backside_2_box=new
G4Box("backside_2_box",451*0.5*mm,692*0.5*mm, ThickShield2*0.5*mm);
                                        G4LogicalVolume * backside_2_log= new
G4LogicalVolume(backside_2_box,material_Inner_dum,"backside_2_log");
                                        G4VisAttributes* backside_2_VisAtt=new
G4VisAttributes(G4Colour(0.1,0.5,0.6));
                                        backside_2_VisAtt->SetForceWireframe(true);
                                        backside_2_log->SetVisAttributes(backside_2_VisAtt);

                                        G4double backside_2pos_z= - 1501*mm - 507*mm + Thick-
Shield1*0.5 + ThickShield1*0.5 + 0.1*mm + ThickShield2*0.5;
                                        G4VPhysicalVolume* backside_2_phy=new G4PVPlacement(
                                        0,G4ThreeVector(0.0,backside_pos_y,backside_2pos_z)

        ,backside_2_log,"backside_2_phys",experimentalHall_log_dum,false,0);

//
//                                      // backside_1 5 mm Steel
                                        G4Box* backside_1_box=new
G4Box("backside_1_box",451*0.5*mm,692*0.5*mm, ThickShield1*0.5*mm);
```

```
                                    G4LogicalVolume * backside_1_log= new
G4LogicalVolume(backside_1_box,material_dum,"backside_1_log");
                                    G4VisAttributes* backside_1_VisAtt=new
G4VisAttributes(G4Colour(0.1,0.5,0.6));
                                    backside_1_VisAtt->SetForceWireframe(true);
                                    backside_1_log->SetVisAttributes(backside_1_VisAtt);

                                    G4double backside_1pos_z= -1501*mm-
507*mm+ThickShield1*0.5;
                                    G4VPhysicalVolume* backside_1_phy=new G4PVPlacement(
                                    0,G4ThreeVector(0.0,backside_pos_y,backside_1pos_z)

        ,backside_1_log,"backside_1_phys",experimentalHall_log_dum,false,0);

//
//                                  //Front Side ////////////////////////
//
                                    G4double frontSide_pos_y=-
(Layer1_y*0.5+11.4*mm+680*0.5*mm);
//
//                                  //frontSide_3 3 mm mat Steel
                                    G4Box* frontSide_3_box=new
G4Box("frontSide_3_box",451*0.5*mm,680*0.5*mm, ThickShield3*0.5*mm);
                                    G4LogicalVolume * frontSide_3_log= new
G4LogicalVolume(frontSide_3_box,material_dum,"frontSide_3_log");
                                    G4VisAttributes* frontSide_3_VisAtt=new
G4VisAttributes(G4Colour(0.1,0.2,0.6));
                                    frontSide_3_VisAtt->SetForceWireframe(true);
                                    frontSide_3_log->SetVisAttributes(frontSide_3_VisAtt);

                                    G4double frontSide_3pos_z=-1501*mm-0.1*mm-
115*mm+ThickShield3*0.5*mm;
                                    G4VPhysicalVolume* frontSide_3_phy=new G4PVPlacement(
                                    0,G4ThreeVector(0.0,frontSide_pos_y,frontSide_3pos_z)

        ,frontSide_3_log,"frontSide_3_phys",experimentalHall_log_dum,false,0);
//
//
//
                                    //frontSide_2 3 mm mat PbSb4
                                    G4Box* frontSide_2_box=new
G4Box("frontSide_2_box",451*0.5*mm,680*0.5*mm, ThickShield2*0.5*mm);
                                    G4LogicalVolume * frontSide_2_log= new
G4LogicalVolume(frontSide_2_box,material_Inner_dum,"frontSide_2_log");
                                    G4VisAttributes* frontSide_2_VisAtt=new
G4VisAttributes(G4Colour(0.2,0.2,0.6));
                                    frontSide_2_VisAtt->SetForceWireframe(true);
                                    frontSide_2_log->SetVisAttributes(frontSide_2_VisAtt);

                                    G4double frontSide_2pos_z=-1501*mm-0.1*mm-
115*mm+ThickShield3+0.1*mm+ThickShield2*0.5;
                                    G4VPhysicalVolume* frontSide_2_phy=new G4PVPlacement(
                                    0,G4ThreeVector(0.0,frontSide_pos_y,frontSide_2pos_z)

        ,frontSide_2_log,"frontSide_2_phys",experimentalHall_log_dum,false,0);
//
//
```

```
//                                      //frontSide_1 5 mm mat Steel
                                        G4Box* frontSide_1_box=new
G4Box("frontSide_1_box",451*0.5*mm,680*0.5*mm, ThickShield1*0.5*mm);
                                        G4LogicalVolume * frontSide_1_log= new
G4LogicalVolume(frontSide_1_box,material_dum,"frontSide_1_log");
                                        G4VisAttributes* frontSide_1_VisAtt=new
G4VisAttributes(G4Colour(0.2,0.2,0.6));
                                        frontSide_1_VisAtt->SetForceWireframe(true);
                                        frontSide_1_log->SetVisAttributes(frontSide_1_VisAtt);

                                        G4double frontSide_1pos_z=-1501*mm-0.1*mm-
115*mm+ThickShield3+0.1*mm+ThickShield2+0.1*mm+ThickShield1*0.5;
                                        G4VPhysicalVolume* frontSide_1_phy=new G4PVPlacement(
                                        0,G4ThreeVector(0.0,frontSide_pos_y,frontSide_1pos_z)

        ,frontSide_1_log,"frontSide_1_phys",experimentalHall_log_dum,false,0);
```

Acknowledgments

I would like to express my gratitude to Prof. Dr. Franco Casali (University of Bologna, Italy) that with his expertise he guided me during my graduate experience.

I wish to thank Dr. Urs Sennhauser (Empa, Dübendorf, Switzerland) for giving me the opportunity to carry out my thesis work in his research group, for the many fruitful discussions, and for his critical reviews.

I would like to thank Jürgen Hofmann (Empa, Dübendorf, Switzerland) for the implementation of the software to read STL-files and to parallelize the simulation, for his assistance in the development of the code, and for his efforts to modify the GEANT4 code, so it could run under Windows systems.

Special thanks to Dr. Raphael Thierry and Alexander Flisch (Empa, Dübendorf, Switzerland) for their time in reviewing manuscripts and presentations, for their suggestions and fruitful discussions.

I would like to express my thanks to the colleagues and friends of the group of non destructive testing of Empa and of the X-ray group of the Department of Physics of the University of Bologna for their help and support. Particular thanks go to Dr. Matteo Bettuzzi for his support in the calibration of the CdTe detector.

I would like to thank Peter Vontobel from PSI (Villigen, Switzerland) for supplying the radioactive sources for the calibration of the CdTe detector.

Thanks to Dr. Uwe Zscherpel from BAM (Berlin, Germany) for supplying the CdTe detector.

Thanks to the Swiss State Secretariat for Education and Research and the European Commission within the sixth framework project DETECT for financial support.

List of publications and patent

Publications

Journal papers

1. **Miceli, A**., Thierry, R., Flisch, A., Sennhauser, U., Casali F., Simon M., *Monte Carlo simulations of a high resolution X-ray CT system for industrial applications*, Nuclear Instruments and Methods in Physics Research Section A, Vol. 583/2-3, pp. 313-323, 2007.

2. **Miceli, A**., Thierry, R., Bettuzzi, M., Flisch, A., Hofmann, J., Sennhauser, U., Casali, F., *Comparison of simulated and measured spectra of an industrial 450 kV X-ray tube*, Nuclear Instruments and Methods in Physics Research Section A, Vol. 580, pp.123-126, 2007.

3. Thierry, R., **Miceli, A**., Hofmann, J., Flisch, A., Sennhauser, U., *Hybrid simulation of scatter intensity in industrial cone beam computed tomography*, submitted to Nuclear Instruments and Methods in Physics Research Section A (December 2007).

Conference proceedings

1. **Miceli, A**., Thierry, R., Flisch, A., Sennhauser, U., Casali F., *MC simulation for estimation of scatter intensities in a cone-beam CT system employing a 450 kV X-ray tube*, 4th International Workshop NDT in Progress, November 05-09, 2007, Prague, Czech Republic, ISBN 978-80-214-3505-6.

2. **Miceli, A**., Flisch, A., Thierry, R., Hofmann, J., *Tomografia computerizzata per applicazioni industriali*, AIPnD, 11.-13. October 2007, Milano (I), Conference Proceedings, ISBN 978-88-89758-03-8.

3. Thierry, R., Hofmann, J., **Miceli, A.,** Flisch, A., Simon M., *Schnelle und Genaue Abschätzung des Streusignals in Cone-Beam Computertomografie*, Wels (A), 2008.

4. Flisch, A., Thierry, R., **Miceli, A.,** Hofmann, J., Simon M., Sauerwein S, Casali, F, Bettuzzi, M., Morigi, *Neue Entwicklungen für schnelle Computertomografie zur Prüfung von Gussprodukten*, Wels (A), 2008.

5. Simon M., Tiseanu I., Hämmerle V., Sauerwein S., Flisch, A., Thierry, R., **Miceli, A.,** Casali, F, Bettuzzi, M., Morigi, *Erfahren zur verbesserten Computertomographie an großvolumigen Bauteilen*, Wels (A), 2008.

6. Thierry, R., **Miceli, A**., Hofmann, J., Flisch, *Fast estimation of single scattering projections: a simulation case in cone-beam CT*, 4th International Workshop NDT in Progress, November 05-09, 2007, Prague, Czech Republic.

7. Bettuzzi, M., Berdondini, A., Brancaccio, R., Casali, F., Flisch, A., **Miceli, A**., Morigi, M.P., *Tomografia industriale ad alta risoluzione con fasci di fibre ottiche coerenti*, AIPnD, 11.-13. October 2007, Milano (I), Conference Proceedings.

8. Flisch, A., Thierry, R., **Miceli, A**., *New developments for fast computed tomography inspection of foundry products*, International 47. Foundry Conference, 12.-14. Sept. 2007, Portorož, Slovenia, Conference Proceedings.

9. Bettuzzi, M., Brancaccio, R., Berdondini, A., Morigi, M.P., Casali, F., Flisch, A., **Miceli, A.**, *High resolution computed tomography for industrial applications based on coherent fiber optics ribbons*, 5th World Congress on Industrial Process Tomography, 3.-6. Sept. 2007, Bergen, Norway.

10. Thierry, R., Flisch, A., **Miceli, A**., Hofmann, J., *Hybrid simulation of projections in Industrial X-ray Cone Beam Computed Tomography*, DIR2007 25.-27. July. 2007, Lyon (F), Conference Proceedings.

11. Thierry, R., Flisch, A., **Miceli, A**., Hofmann, J., *Statistical Beam-Hardening Correction for Industrial X-ray Computed Tomography*, ECNDT, 25.-29. Sept. 2006, Berlin (D), Conference Proceedings We.3.7.2.

12. Thierry, R., Flisch, A., **Miceli, A**., Hofmann, J., *Fast simulation of first-order scattering in X-ray Imaging: application to cone-beam CT*, 8th XTOP, 19.-22. Sept. 2006, Baden-Baden (D), Conference Proceedings.

13. Flisch, A., Thierry, R., **Miceli, A**., *New developments for fast computed tomography inspection of foundry products*, International 47. Foundry Conference, 12.-14. Sept. 2006, Portorož, Slovenia, Conference Proceedings.

Empa and project reports

1. **Miceli, A**., Flisch, A., *Study on how the scan parameters influence the detection limits of 3D-CT scans*, DETECT project - Deliverable report D4.3, 2007.

2. **Miceli, A**., Flisch, A., Leroy, P., Genot, S., *Study on how the scan parameters influence the accuracy of 3D-CT scans*, DETECT project - Deliverable report D4.2, 2007.

3. **Miceli, A**., Thierry, R., Flisch, A., Hofmann, J., Sennhauser, U., Casali, F., *Monte Carlo simulation of a cone-beam CT system for industrial applications*, Empa Activity Report 2007.

4. Thierry, R., **Miceli, A**., Sennhauser, U., *Scattering correction and statistical reconstruction algorithm applied to polychromatic X-ray cone-beam CT*, Empa Activity Report 2006.

5. Wyss, P., **Miceli, A**., Sennhauser, U., Uggowitzer, P., *X-ray tomographic microscopy for 3D composite materials characterization*, Empa Activity Report 2005.

Patent

1. Thierry, R., **Miceli, A**., Sennhauser, U., Flisch, A., *A rapid estimation of photon scattering in X-ray Images,* European Patent Application, No. EP 07 012 409.4 (2007).